Diss. ETH No. 25798

Reference-Free Traction Force Microscopy: Experimental Platform and Algorithmic Analysis Pipeline for Complex Cell Studies

A thesis submitted to attain the degree of

DOCTOR OF SCIENCES of ETH ZURICH
(Dr. sc. ETH Zurich)

presented by

TOBIAS LENDENMANN

MSc ETH ME
born November 15th, 1987
citizen of Zurich, ZH

accepted on the recommendation of

Prof. Dr. Dimos Poulikakos, examiner
Prof Dr. Edoardo Mazza, co-examiner
Prof. Dr. Daniele Panozzo, co-examiner
Dr. Aldo Ferrari, co-examiner

2019

Summary

Single cells, the smallest living entities of the human body, are constantly interacting with each other and the surrounding tissue through mechanical, biochemical, and electrical signals. Out of these, the mechanical cues are the most widespread and emerge as the fastest information pathway cells can exploit. Contractile elements within the cells have the ability to generate forces. The physical adhesions that cells make to both their environment and neighbors propagate the internally generated forces. These same adhesions also act as mechanosensors for external forces to which cells are able to adapt. This mechanical communication pathway is the main interest of the field of mechanobiology, which makes use of specialized tools to measure the mechanical interaction between cells and their environment.

The methods to measure cellular forces have seen vast improvements in the last decades. The state-of-art protocols for measuring forces generated from cell collectives, single cells, and even single adhesions are generally summarized as traction force microscopy. The common procedure of all the traction force microscopy approaches is to visualize deformations of a mechanically characterized material. The deformations, in conjunction with the material characterization, can be used to calculate the produced cellular forces. The methods, however, differ strongly in how the forces are visualized and each comes with an inherent limitation. These range from the need for a load free reference image to measure displacements, the introduction of topography that alters cell behavior, or simplifying materials to the point where measurements are unreliable.

In this thesis, I will present a newly developed method for traction force microscopy and its application to several relevant biological processes. The new technology overcomes limitations from currently available methods. It does not need a reference image, which allows for live assessment of the forces and downstream processing, such as immunofluorescence. It uses an accurate material model in a finite element analysis to account for non-linearities of both material and geometry. And it employs a flat, non-intrusive substrate that does not impede the cellular behavior.

In the first part of the thesis at hand, I will explain how the new method termed confocal reference free traction force microscopy, or cTFM in short, works and why it does not require a reference image to determine the cellular forces. Next, I will demonstrate the usefulness of this property on relevant biological studies that require immunofluorescence to colocalize traction forces and the expression of proteins of interest.

In the second part, I will further expand the capabilities of cTFM by introducing a robust and fast analysis pipeline using new algorithms. The new computational pipeline proves fast enough to keep up with the pace of image acquisition of relevant biological processes. The speed of analysis and the reference free capabilities allow for a live assessment of forces. These capabilities are demonstrated during a study where cells are exposed to controlled shear stress in flow chambers. The cells have varying reactions to different magnitudes of shear, which is most evident in the cell shape, but also manifests itself in the measured forces. The characterization of the cells and their collective behavior under the influence of the external shear flow allows us to model the monolayer as polar nematic liquid crystals to make further prediction on its behavior.

Altogether this thesis presents a new traction force microscopy method with capabilities that have the potential to advance our understanding in the field of mechanobiology.

Zusammenfassung

Zellen sind die kleinste lebende Einheit des menschlichen Körpers. Durch mechanische, biochemische, und elektrische Signale interagieren sie ständig mit anderen Zellen und mit dem umgebenden Gewebe. Insbesondere die mechanischen Signale sind sehr vielseitig und stellen den schnellsten Kommunkationspfad zwischen Zellen dar. Kontraktile Elemente innerhalb der Zellen haben die Fähigkeit, Kräfte zu erzeugen. Die physikalischen Adhäsionen der Zellen zu ihrer Umgebung und zu benachbarten Zellen leiten die intern erzeugten Kräfte weiter. Diese Adhäsionen wirken auch als Mechanosensoren für äussere Kräfte, auf welche die Zellen reagieren und an die sie sich anpassen können. Der mechanische Kommunikationsweg ist das Hauptinteresse der Mechanobiologie, die spezielle Werkzeuge zur Messung mechanischer Interaktionen zwischen Zellen einsetzt.

Die Methoden zur Messung zellulärer Kräfte haben sich in den vergangenen Jahrzehnten stark verbessert. Modernste Verfahren zur Messung von Kräften aus Zellkollektiven, Einzelzellen und Einzeladhäsionen werden im Allgemeinen als Traction Force Microscopy (TFM) bezeichnet. Alle TFM-Verfahren visualisieren Verformungen eines mechanisch charakterisierten Materials. Die Verformungen können in Verbindung mit den Materialeigenschaften zur Berechnung der erzeugten Zellkräfte benutzt werden. Obschon alle TFM-Methoden Verformungen messen, unterscheiden sie sich stark in der Art und Weise, wie sie diese Verschiebungen visualisieren. Zudem haben all diese Methoden inhärente Einschränkungen. Diese reichen von der Notwendigkeit eines lastfreien Referenzbildes für die Messung von Verschiebungen, über die Einführung einer Topographie, die das Zellverhalten verändert, bis hin zur Vereinfachung von Materialien, sodass die Auswertung unzuverlässig wird.

In dieser Arbeit stelle ich ein neu entwickeltes TFM-Verfahren vor und wende es an mehreren relevanten biologischen Beispielen an. Die neue Technologie überwindet die Einschränkungen der derzeit verfügbaren Methoden. Das Verfahren benötigt kein Referenzbild, was eine Echtzeitüberprüfung der Kräfte und der nachgelagerten Prozesse, wie beispielsweise der Immunfluoreszenz, ermöglicht. Es verwendet ein genaues Materialmodell in einer finiten Elemente-Analyse, um Nichtlinearitäten von Material und von Geometrie zu berücksichtigen. Und es besteht aus einem flachen, nicht-intrusiven Substrat, welches das Zellverhalten nicht beeinträchtigt.

Im ersten Teil dieser Arbeit stelle ich die neu entwickelte Methode vor, welche die Einschränkung der derzeit verfügbaren Methoden überwindet. Das neue Verfahren, genannt Confocal Reference Free Traction Force Microscopy (cTFM), benötigt kein Referenzbild, um die Kräfte zu berechnen. In einem weiteren Schritt demonstriere ich den Nutzen dieser Eigenschaft an Beispielen, die Immunfluoreszenz erfordern, um Traktionskräfte und das Vorkommen eines Proteins zu kolokalisieren.

Im zweiten Teil dieser Arbeit erweitere ich die Möglichkeiten von cTFM, in dem ich eine robuste und schnelle Analysepipeline mit neuen Algorithmen einführe. Die neue Pipeline ist schnell genug, um mit der Bilderfassung relevanter biologischer Prozesse Schritt zu halten. Dies wird dann an einem Beispiel demonstriert, bei dem Zellen einer Scherkraft ausgesetzt sind. Die Zellen zeigen unterschiedliche Reaktionen auf die variierenden Scherkräfte, was sich am offensichtlichsten bei der Form der Zelle, aber auch in den erzeugten zellulären Kräften zeigt.

Insgesamt stellt diese Arbeit eine neue TFM-Methode vor, die das Potenzial hat, das Verständnis auf dem Gebiet der Mechanobiologie zu verbessern.

Resumaziùn

Las zelas en las ple pintgas unitads d'igl tgierp human. Ellas reageschan cuntstàntameing antras signals mecanics, biocemics ad electrics cun otras zelas a cun la tela digl conturn. Oravànttut en igls signals mecanics fetg polivalents ad en la ple sperta veia da comunicaziùn trànter las zelas. Igls elements da contracziùn andavains las zelas en capavels da crear forzas. Las adesiùns fisicalas da las zelas anviers igl sieus conturn a tier las zelas vaschinantas datan anavànt las forzas creadas agl intern. Quellas adesiùns opareschan ear sco mecanosensurs par forzas externas, sen qualas las zelas reageschan a pon s'adatar veda lezas. La veia da comunicaziùn mecanica e igl interess prinzipal da la mecanobiologeia, ca dovra guafens spezials par masirar las interacziùns mecanicas trànter las zelas.

Las metodas par masirar las forzas zelularas ân samigliuro igls davos ons fetg ferm. Igls ple moderns prozess par masirar las forzas or da colectivs da zelas, zelas singularas ad adesiùns singularas sanumnan generalmeing Traction Force Microscopy (TFM). Tut igls prozess TFM visualiseschan la defurmaziùn dad egn material cun caracteristicas mecanicas. Las defurmaziùns agl conex cun igl caracter d'igl material pon vagnir duvradas par masirar las forzas creadas an las zelas. Schagea ca tut las metodas TFM masiran las defurmaziùns, dat igl gràndas diferenzas an la moda a maniera da visualisar quellas defurmaziùns. Plenavànt ân tut quellas metodas restricziùns inerentas. Quellas tànschan d'igl basegn d'egn maletg referenzial sainza mulestis par masirar las dislocaziùns, sur l'introducziùn d'egna topografeia ca modifizescha igl cumportamaint da las zelas, antocen tar la simplificaziùn d'igls materials, ascheia ca la evaluaziùn vean malfidevla.

An quella lavur vignt jou a preschantar egn nov svilup d'egn prozess TFM cun la si'aplicaziùn veda plirs relevànts exaimpels biologics. La nova tecnologeia dumogna las restricziùns da las metodas c'en actualmeing disponiblas. Igl prozess dovra nign maletg referenzial, tge ca fa pussevel egna controla an tains real da las forzas ad igls prozess posteriurs, sco par exaimpel la imunofluorescenza. El dovra egn exact model da material an egna analisa finita d'igls elements par cunsiderar las nunlinearitads d'igl material a da la geometreia. Plenavànt cunsista igl prozess d'egn nunintrusiv substrat plat, ca disturba betga igl cumport da las zelas.

An l'amprema part da quella lavur preschaint' jou la nova metoda, ca riva da surmuntar las restricziùns da las metodas c'en actualmeing disponiblas. Igl nov prozess, numno Confocal Reference Free Traction Force Microscopy (cTFM), dovra nign maletg da referenza par masirar

las forzas. An egn savund zap demonstresch jou igl nez da quella caracteristica veda exaimpels, ca dovran la imunofluorescenza par colocalisar las forzas da tracziùn a l'existenza da proteins. An la savunda part da quella lavur schlargel jou las pussevladads da cTFM, antras ca jou introdutgesch egna pipeline d'analisa robusta a sperta cun algoritmus novs. La nova pipeline e avunda sperta par taner pass cun la registraziùn da maletgs da relevànts prozess biologics. Quegl vean demonstro veda egn exaimpel, noua ca las zelas vignan exponadas a la forza da stuschada. Las zelas mussan diferaintas reacziùns sen las forzas da stuschada ca varieschan. Quegl samussa igl ple cler veda la furma da la zela, mobagn ear veda las forzas zelularas creadas. Agl antier preschainta quella lavur egna metoda TFM, ca â igl potenzial da migliurar la capientscha an la sparta da la mecanobiologeia.

Acknowledgements

First, I would like to thank Prof. Dimos Poulikakos for giving me the opportunity to perform my doctoral research in his Laboratory of Thermodynamics in Emerging Technologies. My PhD thesis all started with him successfully putting up a fight to get funding for my project, which showed his immense support and bolstered my confidence in the project right from the start.

A huge thank you goes out to Aldo Ferrari, my mentor and friend. I could fully rely on him when I had questions and uncertainties. He is the one that kept bringing me back on board for new projects, which has now finally led to my PhD thesis. I enjoyed listening to and trying to realize his endless stream of, at times, crazy ideas. However, every now and then, he struck gold and that is how I got to where I am now. At this point, I also have to state how grateful I am to have had Costanza Giampietro around in our lab. She joined us half way through my PhD and really brought our work in the lab to a new level. I have never met a kinder and more helpful person.

On the way, I worked closely with several extraordinary people that I want to mention and thank here. Martin Bergert was my first collaborator. He mentored me early on in my PhD. We not only worked together, but also brought the LTNT Sola team to new competitive heights. At the same time, I also worked with Manuel Zündel. He was always good for a chat, or better, an instruction about mechanics. However, most of the time we discussed our other passion - biking. With Magdalini Panagiotakopoulou I had the pleasure to also work on a project. We spent many nights clicking away until one of us turned into a pumpkin and had to sign out. It was worth it. My last close collaborator was Georgios Stefopoulos. What an experience. He showed me what efficiency and dedication is. I hope some of it rubbed off on me. My office mate for almost all of my PhD deserves a shout-out as well. It was never boring with Patrik Rohner around, but I was definitely more productive when he was not.

And now to my friends over at NYU. Thank you, Daniele Panozzo, for inviting me to work with you and your team. I had a fantastic time and our longstanding collaboration brought forth two amazing projects. Of course this could not have been done without the help from Teseo Schneider, Marco Tarini, and Jeremie Dumas, who managed to teach a "biologist" at least some basic coding skills.

I would also like to thank Prof. Edoardo Mazza for accepting the co-examination and his thorough review of this thesis. Moreover, for collaborating on the cTFM project.

I also want to thank my family for their support during all these years, not just during my PhD. I could always rely on them to have my back, no matter what. For this thesis specifically, I would like to thank my brother Christoph for helping me transfer many documents to LaTeX and my dad Rolf for proofreading and helping me fix strange formulations and sentences.

Finally, I sincerely thank the Dolf Family from Wergenstein, Graubünden, who took it upon themselves to translate the summary of my thesis to Romansh.

Zürich, March 2019 Tobias Lendenmann

Contents

Part I

General Introduction

1 Cellular Forces

1.1 Mechanobiology

Collective cell activities play a fundamental role in tissue development, repair, and disease. But how can the underlying biological events, such as cell shape change and motion, which combine in space and time within the spatial boundary of a living organism, be accounted for by physics[1]? The answer to this question is what the field of mechanobiology, situated at the interface of biology, engineering, physics, computer science, and medicine is trying to answer[2,3]. The aim is to describe in physical terms the complex interplay between cells and their environment, which ranges vast scales in both space and time. From a molecular level where processes, such as protein unfolding, can occur in microseconds to macro-scale processes, such as the growth of embryos over months[4]. While the two-way communication of cells among one another or with the extra cellular matrix (ECM) can be of mechanical, biochemical, and electrical nature[5], mechanical forces are emerging as the fastest communication pathway between cells[5]. These inter- and intra-cellular forces are the focus of mechanobiology as they generate cues for cells to migrate individually or as a collective, to proliferate, and to differentiate[4].

In other words, mechanical stimuli that are presented to the cells by external forces or by the properties of the micro-environment critically affect cell functions, behavior, and overall biological identity. Indeed, cells are mechanosensitive, meaning that they are able to translate extracellular and intracellular mechanical forces into biochemical signals[6]. These signals, through the activation of diverse molecular pathways, modulate important cellular functions that are critical for the development and homeostasis, such as protein synthesis, secretion, proliferation, migration, viability, apoptosis, and differentiation. Understanding how cells sense these biophysical stimuli and ultimately translate them into specific biological outcomes is essential for advancing the field and for applying this knowledge to develop new clinical therapies. In this complex and exciting frame, new platforms are necessary to study the cellular reaction to physiological and pathological stimuli. These new technologies must have a temporal and spatial resolution sufficient to access the cellular processes under investigation and a sensitivity in the range of values comparable with cellular activities.

1.1.1 Mechanosensors

Cells generate and respond to many types of forces. Several mechanisms exist by which such forces are transduced to mediate different responses[4,7]. A selection is given in Figure 1.1, while a comprehensive review can be found here[8]. All cells respond to mechanical loadings by adapting their cellular functions[6]. These changes include short-term or long-term responses, which are triggered by multiple overlapping and cross-talking signaling pathways[9]. In addition, forces applied to cells are usually of dynamic nature, requiring a continuous adaptive response. Cellular mechanosensing is based on force-induced conformational changes in mechanoreceptor proteins[10]. These changes, such as protein unfolding, activate intra-cellular signaling[10]. In addition, over the last decade, numerous biological components have been identified to act as mechanosensors (Figure 1.2). Some of them are common among different cell types, while others are strictly specific to tissues functioning under mechanical load, such as the skin or the endothelium[11].

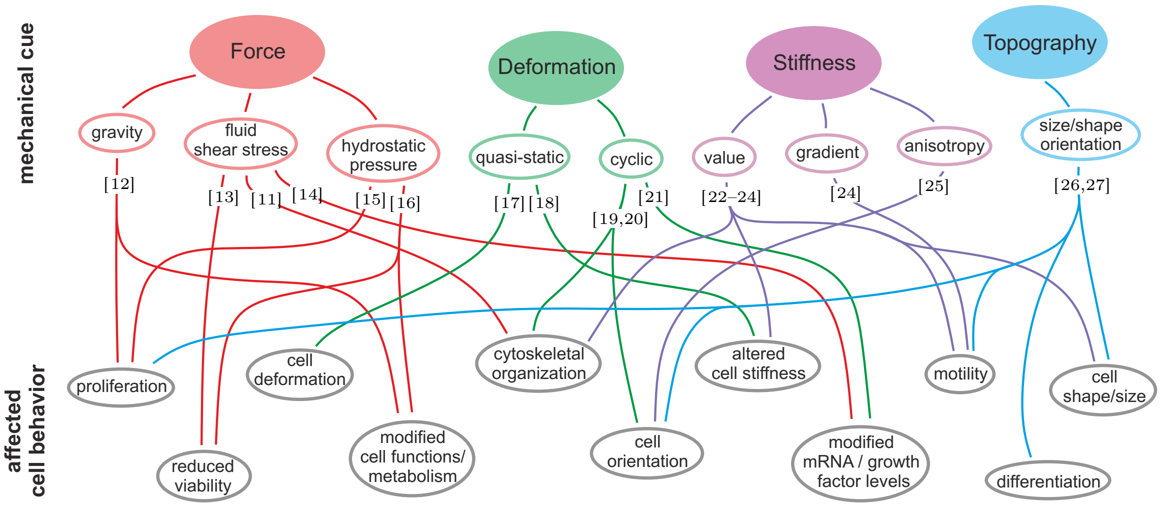

Figure 1.1: Mechanobiological Correlations. Flow chart of experimentally determined mechanical cues and cellular responses. Reprinted with permission from Manuel Zündel [28]

The core mechanical element in the cell and thus the primary mechanosensor is the cytoskeleton[29,30]. The cytoskeleton is comprised of fibrous protein polymer systems including actin, microtubules, and intermediate filaments[31–33]. Together, these proteins define the cell's structural integrity. Conformational changes of its elements activate intra-cellular signaling pathways[9]. Along the filaments, crosslinker and motor proteins can induce sliding movements, leading to contractions of the cytoskeleton and the cell as a whole[34]. In particular, acto-myosin contractility represents the main source of force generation in cells[35]. Actin filaments are linked to the ECM through transmembrane protein complexes and can transmit forces from or to the ECM over long distances[24,31,36]. As a response to external mechanical cues, micro-filaments assemble and disassemble, driving shape change of individual cells and behavioral change of cell collectives[37]. The interruption or inhibition of individual steps in the interplay of internal and external forces leads to complete failure of mechanotransduction[38].

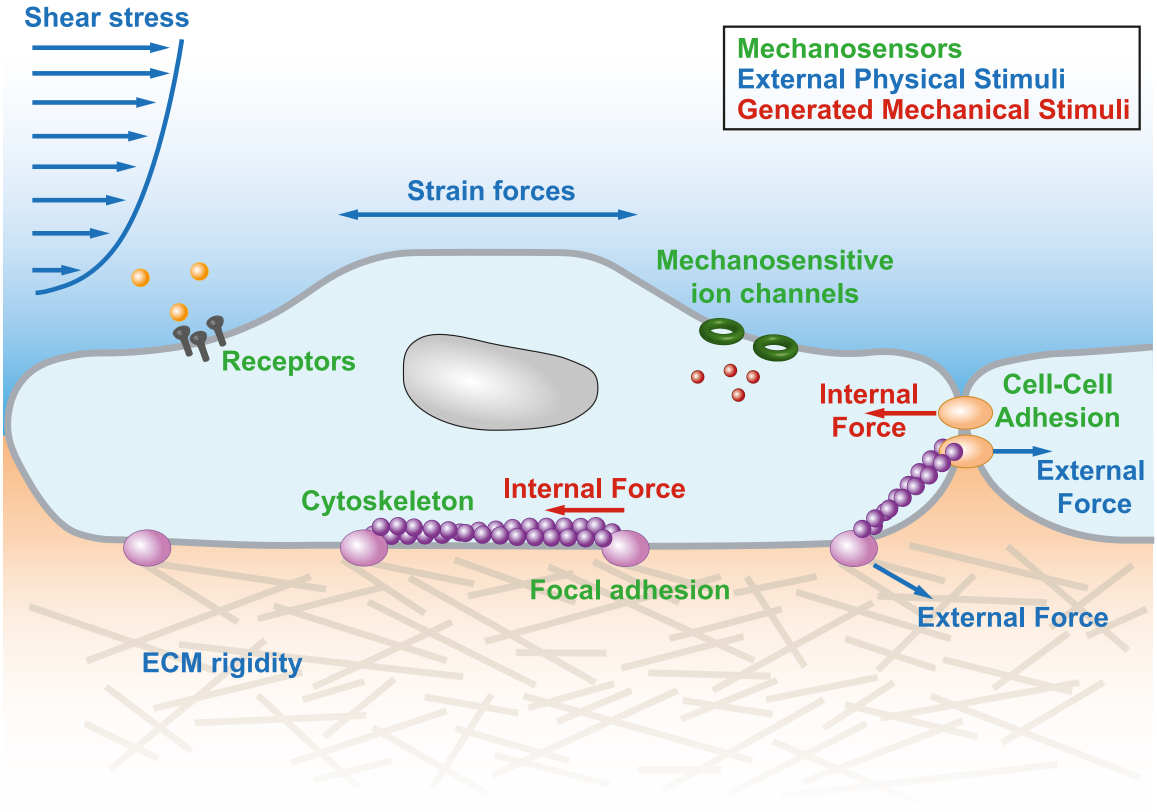

Figure 1.2: Cell Schematic. The most important mechanoreceptors, internal and external stimuli. cf. [39]

The connection of the cytoskeleton to the ECM is mediated by transmembrane proteins of the integrin family[40]. Clusters of integrins, along with other proteins, form adhesion complexes called focal adhesions (FAs)[41]. They enable the cells to exert traction forces on the ECM and simultaneously sense external forces or cues[40], such as ECM-rigidity and topography[42–44], to reinforce developing adhesions[45]. This allows the cell to sense the mechanical input, the response of its environment, and to react appropriately by softening, stiffening, reorientating, or polarizing the cytoskeleton and the cell as a whole. In all, this represents an adaptive remodeling of the cell functionality in response to the surrounding local stimulation[39,46]. Beyond integrins, the FA contains signaling proteins, such as focal adhesion kinase (FAK), phosphatases, and paxillin which, upon activation, induce biochemical intracellular signaling that are controlling gene expression[47,48].

Cells are rarely isolated in the body. Epithelial and endothelial cells in particular form continuous layers of cells. Epithelial cells line the boundaries of inner epithelial organs, such as lungs, mammary glands, kidneys as well as the outermost layer of the skin - the epidermis[49]. Endothelial cells line the inner boundaries of blood and lymphatic vessels[50]. They form single, continuous layers and separate two different media, exerting a control and filtering activity. These cell types form cadherin-based cell-cell junctions to ensure the integrity of the monolayer and its separating function[51]. Cadherins, like integrins, are transmembrane proteins. They are responsible for physically connecting to neighboring cells and integrating the cell into tissues[52,53]. In epi- and endothelia, cadherin-based adherens junctions couple the contractile cytoskeletons of cells together to generate tissue-scale contraction[54,55]. Junctional tension cascades through entire tissues as a form of communication between cells[56,57]. Examples of this are mechanical stress waves propagating from leader cells to the rear, driving collective migration during wound healing, and repulsive forces preventing the merger of epithelia during epithelial boundary convergence[58,59].

In addition to integrin and cadherin proteins, stretch-activated ion channels[60–62] and the glycocalix localized in the plasma membrane[63] complement the arsenal of cells' mechanosensitive elements. The ion channels open and close in response to membrane strain and allow the entry of calcium and other ions into the cytoplasm of the cells. These ions, acting as second intracellular messengers, also modulate cellular responses[64,65]. The glycocalix is a layer of carbohydrate-rich proteins localized on the cell surface that mediates mechanotransduction signaling in response to fluid shear stress in endothelial cells[66].

The nucleus itself has also been proposed to act as a mechanosensor[67]. Indeed, mechanotransduction events may occur at the nuclear envelope and within the nucleoplasm[68]. Forces applied at FAs propagate through the cytoskeleton and are transmitted to the nucleus primarily by actin stress fibers and intermediate filaments[69–71]. This way, ECM strains and loads deform the nucleus[72]. The alteration is associated with changes in gene expression profiles because nuclear deformations can alter chromatin conformation and modify the contact of transcription factors[73–75]. However, a direct evidence for this mechanism is still lacking.

1.1.2 Physiopathology of Mechanotransduction

Tissues *in vivo* are continuously under remodeling by changing their mechanical and biochemical properties[76]. The overall results of these changes influence morphogenesis and differentiation, which are crucial parts of the development of organisms. Indeed, key developmental processes are driven by mechanotransduction[77]. Conversely, malfunctioning of mechanotransduction often leads to pathological consequences due to genetic mutations or changes in the extracellular environment, in cell structure and organization, or in cellular sensing and signaling as summarized in Table 1.1[78].

For example, one of the first maladies that has been associated with defects in biomechanics and mechanotransduction is atherosclerosis, a disease that is the underlying cause of about 50% of all deaths in developed countries[89]. Briefly, in this pathology, the disturbed fluid shear stress at bifurcations correlates with sites of atherosclerotic plaque formation and dramati-

Disease	Primary cell/tissues affected	References
Arteriosclerosis	Endothelial and smooth muscle cells	[79,80]
Osteoporosis	Osteoblasts	[81]
Asthma	Endothelial cells	[82,83]
Cancer	Multiple cell types and tissues	[84–86]
Immune system disorders	Leukocytes	[87,88]

Table 1.1: Diseases in connection with mechanotransduction. cf. [78]

cally alters the endothelial cell organization, in particular, the cytoskeleton[90]. The plaque, which is a product of inflammation and a compromised endothelium, builds up and eventually impinges on the flow profile of blood[91]. In this case, the abnormal mechanical stress at cellular level affects cellular processes through normal and correct mechanotransduction signaling, which can result in failure of normal tissue functions. In another example, genetic mutation leading to the deficiency of dystrophin, a cytoskeletal protein responsible for connecting the cytoskeleton of each muscle fiber to the underlying basal lamina, increases muscle compliance and causes an aberrant mechanotransduction signal in muscles[92]. This leads to the development of Duchenne muscular dystrophy[93]. The full identification of the molecular components that are involved in normal and defective mechanotransduction will eventually lead to a better understanding of the mechanisms driving normal cellular function as well as disease development and could, in turn, provide new targets in the therapeutic approaches to these diseases[94–96]. For this, the study of cells' reaction to mechanical stimuli and their ability to produce such stimuli becomes fundamental.

1.2 Measuring Cellular Forces

When talking about cellular forces, it is important to distinguish between internal forces, such as those generated by acotmyosin contraction[35], and external forces like tension, compression, and shear stress stemming from exposure to flowing liquid[11,16,17]. These are closely linked, as internal forces are propagated to the environment and vice versa[14,35] (Section 1.1.1). There exists a vast variety of techniques to visualize and measure both internal and external cellular forces *in vitro*. However, the internal forces are typically measured after propagation to the extracellular environment. Far fewer techniques exist to directly measure the internal forces, such as Förster resonance energy transfer (FRET)[97], but they are typically less reliable and not part of this thesis.

The concept of forces is not difficult to understand. It is defined as an influence that accelerates mass or deforms bodies. In cellular environments, the Reynold's number, which relates the inertial to the viscous forces, is typically low[98]. In other words, inertia is not relevant on the cellular scale and acceleration can be neglected. This leaves deformations as the measurable quantity to infer forces. However, their measurement is less trivial than, for instance, distance or time and typically relies on the deformation of another mechanically characterized body. This is akin to a spring that deforms under load in macroscopic measurements[99]. Cellular forces, which are in the sub-micro-Newton range, pose an additional challenge that requires careful fine-tuning of the employed dynamometer.

Attempts to visualize and qualitatively assess cellular forces date back 40 years[100,101]. Early methods incorporated cells into 3D collagen lattices[101], which resemble closely the *in vivo* extra cellular matrix (ECM) produced by fibroblasts. The collagen lattices are detached from any underlying rigid surface and allowed to float in medium and thus deform freely. The cells within the lattice form adhesions to the collagen fibers and contract the lattice as a whole[102]. This method is a qualitative way to measure the contractility of a population of cells and is used to this day. It is, however, hardly quantitative and has poor spatial resolution, meaning that single cells cannot be resolved, let alone single adhesions. Another early method investigated how the contractile forces generated by cells deform and wrinkle a freely moving silicone disc surface (Figure 1.3 (a,b)). The wrinkles are indicators for the presence of contractile forces. Wrinkles, however, are hard to quantify and are additionally often larger than individual cells, thereby limiting also this method to purely qualitative statements.

More recent methods to measure cellular forces have been successful at making the forces quantitatively accessible (Table 1.2; [99]). This visualization of forces actuating cellular movements and shape change added a critical overlapping layer of information in the understanding of mechanotransduction. Especially in the context of cell collectives, breakthrough discoveries were made possible by works which extended classic traction force microscopy (TFM) techniques to whole epithelial sheets[103,104]. TFM refers to a family of optical methods capturing the deformations induced by cell generated tractions on compliant substrates[105]. A general classification separates discrete methods based on point-wise measurement of forces[25,106] and continuum methods exploiting elastic substrates doped with randomly dispersed fluorescent beads acting as deformation markers[103,107]. In the following sections, the existing, commonly used techniques to measure forces are introduced, along with their goals, their advantages, and their limitation.

1.2.1 Discrete Methods

The methods to measure forces point-wise are categorized as discrete methods. Here, the force measurement is decoupled into individual force sensors, such as pillars[106] (Figure 1.3 (c,d)) or molecular force sensors[110] (Figure 1.3 (e,f)). They typically report localized forces, for instance from single cells[111], or single adhesions[106].

Micropillar arrays are micro-fabricated from an elastic material. Given the high aspect ratio of the pillars, the apparent spring constant can be tuned such that the pillars are soft enough for cells to deflect them[108]. These deflections from the resting position point-wise reveal the

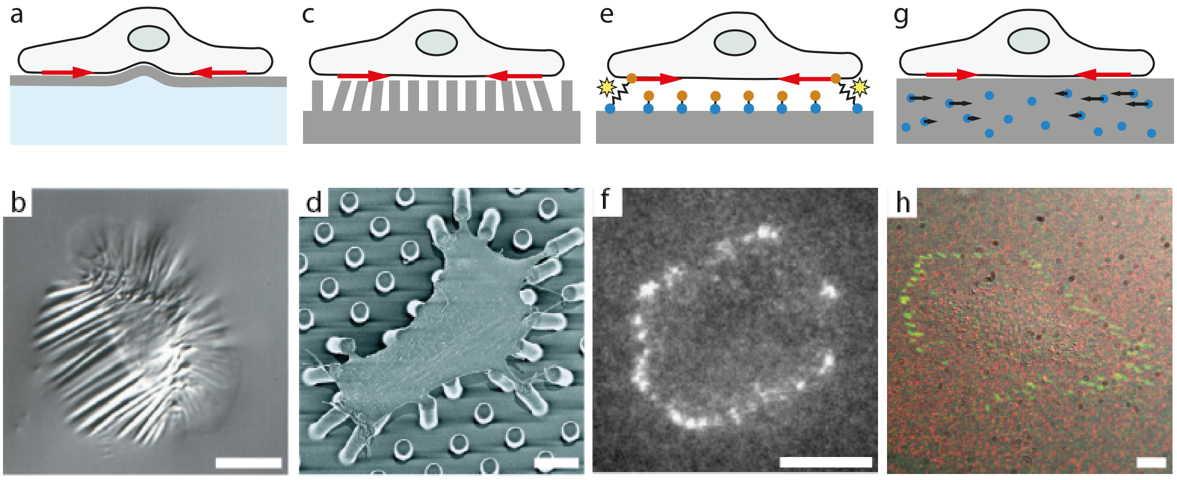

Figure 1.3: Force measurement methods. (a) Schematic of cell wrinkling a thin sheet of silicone. (b) An example of a cell generating traction forces and wrinkling a thin silicone sheet. (c) Schematic of a cell deflecting micro pillars from their resting position. (d) An example of a cell on micro pillars. (e) Schematic of molecular tension probes with the orange fluorophore and blue quencher. (f) Example of intensity map generated from molecular tension probes stretch by a cell. (g) Schematic of a cell displacing a continuous substrate incorporated with fluorescent bead. (h) Example of a cell expressing gfp-paxillin sitting on red fluorescent bead embedded in a compliant substrate. (a,c,e,g) cf. [108], (b,d,f) were reprinted from [106,109,110], respectively. Scale bars are $10\mu m$

generated cellular forces. The point-wise measurement of force is direct and thus very fast. An additional advantage of the micropillars stems from regularity of the array. The microfabrication is precise enough, such that the resting position of each pillar can be assumed. Thus, there is no need for a load-free reference image to measure the displacements of the pillars and subsequently the forces applied to them. While speed of analysis and being reference free are two advantages over other TFM methods, there is a major downside to pillar arrays. The micropillars introduce topography, which is known to influence cellular behavior by restricting their adhesion sites to a fraction of the area covered by the cell or enforcing shape-anisotropy of the adhesions[42,112].

The use of molecular force sensors is another prominent discrete method. Typically, a fluorophore is attached to a quencher molecule through an elastic link[108]. The quencher is fixed on a rigid surface and the cell can bind to the other end where the fluorophore is located (Figure 1.3 (e)). Upon force generation, the cell increases the distance between quencher and fluorophore, thereby increasing its quantum yield[113]. In other words, the intensity of the fluorescent signal is a function of the cell-generated forces (Figure 1.3 (f)). The linker is usually made from a protein or DNA strand, both of which lengthen step-wise at discrete force levels. A calibration of these force levels then links the fluorescent intensity to the generated forces[113]. This discrete method does not introduce topography, as the adhesion sites are continuously and abundantly available, thus not limiting the cell's adhesion. The method, however, comes with its own limitations. First, the output signal is a scalar field and does not reveal force direction. Second, there is background fluorescence from un-engaged sensors. And third, the number of engaged sensors per adhesion site may vary due to adhesion size and heterogeneously distributed sensor density. Thus, the calibration of the signal is not straight forward[108].

1.2.2 Continuum Methods

With continuum methods, unlike discrete ones, cells are adherent to either a continuous 2D environment or within an isotropic 3D environment. These approaches thus report a continuous and directional field of forces. The benefits come at the cost of more involved analysis.

2D Traction Force Microscopy. Despite many advances in the field, such as using super resolution microscopy techniques[114], the most commonly used technique is the in-plane TFM. Here, cells deform a soft elastic substrate with a stochastic pattern of fiducial markers, typically fluorescent beads (Figure 1.3 (g,h)). For higher resolution, two differently colored fluorescent beads are sometimes used[115]. Displacements of the markers are determined between a load free reference image and the deformed image using particle image velocimetry (PIV) or, in cases where the markers are easily distinguishable, with particle tracking velocimetry (PTV)[116]. The displacements of the markers are then used either in some form of Fourier Transform Cytometry (FTTC)[117,118] or a finite element (FE)[119] solver to determine the surface cellular traction forces. FTTC has fast computation times, but assumes both geometrical and material linearity, which does not hold for some materials and especially for large strains. In these cases FE analysis is used[108].

3D Traction force microscopy. Recently, the capabilities of 2D TFM have been expanded to not only detect out-of-plane displacements of the 2D substrate, but in fact embed cells in full 3D matrices. Here, the fluorescent markers are tracked in a 3D environment, revealing deformations in 3D[120]. The underlying technique, however, remains the same. A reference image must be taken without load to estimate the displacements. Additional complexity stems from the structure of the 3D matrices. They consist of a network of fibers to which the cells adhere. Local interactions between the fibers and the cells are highly complex, and fibrous materials are microscopically anisotropic. Even a single fiber, let alone an entire network, that is subject to different modes of deformation, like stretching, compressing, and bending, will have a different reaction in each case. However, when assuming isotropic material instead, these locally heterogeneous material parameters make current 3D TFM methods imprecise. They can be improved with the knowledge about the fiber orientation, density, and topology[121,122], which comes at high imaging and computational costs.

	Measured Quantity	Strengths	Limitations
2D Traction Force Micrscopy	Substrate displacement	Continuous 2D output	Computationally heavy; Requires a reference image
3D Traction Force Microscopy	ECM displacement	Measures forces in 3D	Computationally very heavy; Uniform ECM properties assumed
Micropillars	Pillar displacement	Fast; Reference free	Discrete measurement; Introduces topography
Molecular Force Sensors	Fluorescence signal	High Resolution; Reference free	No directional information; Difficult calibration

Table 1.2: Techniques to measure cellular force. cf. [99]

Even with the advances of continuum TFM, often times linear and homogeneous material parameters are chosen in both 2D and 3D models, which is known to be microscopically false for fibrous networks[121–123]. On top of that, the methods all suffer from the inherent limitation that the displacements of the markers must be determined after the removal of the cells. This renders any downstream processing of the experiment impossible. Anything that requires fixation of the cells, for instance immunofluorescence staining, is therefore not possible. Additionally, there can be no live assessment of the forces. On-the-fly measurements are only possible if the reference image can be calculated.

1.2.3 Inter-cellular Stresses

The above-described methods reveal the traction forces the cells apply to their environment through integrin mediated adhesions. Many cell types, prominent among them epi- and endothelial cells, grow cadherin-based cell-cell junctions. These junctions between cells have the capability to propagate forces among cells. A recently introduced computational method makes it possible to derive values of inter-cellular tension from maps of substrate tractions[124,125]. This protocol, termed monolayer stress microscopy (MSM), computes the inter-cellular tensions through a balance of forces within the cell monolayer (Figure 1.4). The process introduces several simplifying assumptions, like homogeneous properties throughout the cell layer, which limit its applicability to specific experimental conditions, such as model wound healing[125,126]. Access to this additional layer of information highlighted the existence of fundamental modes of migration typical of epithelial collectives. In particular, plithotaxis, by which each cell in the collective tends to migrate along a trajectory which minimizes the shear stresses exerted upon neighboring cells, and kenotaxis, by which cells proximal to a void exert a traction on the substrate which is aligned to the direction of the open space[124,125].

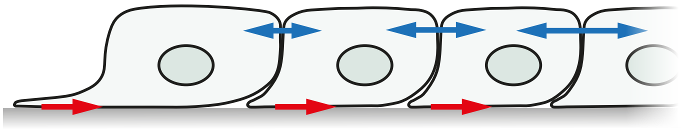

Figure 1.4: Inter-cellular stress. Cross-section of monolayer with side-view of cells. Red arrows depict the cellular traction forces. Integrating tractions leads to increasing inter-cellular stresses, depicted with blue arrows. cf. [127]

2 Aim and Content of this Thesis

The accurate measure of cellular forces has helped to identify and better understand cellular behaviors, responses and signaling pathways in mechanotransduction. While there are cells acting as individuals, the vast majority function as a collective in the human body. TFM has played a decisive role in studies of both and has, for instance, led to the definition of general patterns in the migratory behavior of epi- and endothelial cells[128,129].

The knowledge gained from TFM served as a platform to identify the role of cellular machineries establishing contact with the substrate (the integrin adhesions[130]), generating contractile forces (the actomyosin complex[131,132]), or responding to molecular (gradients of soluble molecules[133]) or physical (i.e. density of adhesion points[134], rigidity[24], surface topography[135]) directional stimuli. In addition, the established model of mesenchymal migration provided a reference to resolve alternative migration modalities, which are adopted by specific cell types[136,137]. The use of TFM was also instrumental to reveal unexpected force patterns propelling the advancement of epithelial edges during wound healing[103,138].

However, current TFM methods feature intrinsic limitations as they cannot detect out-of-plane forces and may introduce artifacts due to their structured and intrusive nature (Section 1.2.1,[105,139]) or require the acquisition of a reference image, which is captured upon cell removal and therefore precludes the generation of corresponding maps of molecular activities by immunofluorescence (Section 1.2.2).

The aim of my work has been is the development of a traction force platform that overcomes the limitations introduced in section 1.2. This includes the development of hardware and software, as well as testing the application on biologically relevant settings and processes. The hardware must be entirely reference free, must not introduce topography, and must be able to visualize forces in and out-of-plane (Chapter 3). The software must be able to robustly and accurately produce traction maps in a pace that keeps up with biological phenomena (Chapter 6). Together, this fulfills the criteria for high throughput traction force microscopy with capabilities for on-the-fly measurements. Finally, the method must be applicable to both single cells (Chapter 4) as well as cell collectives (Chapter 5 and 8) and be able to distill information to generate a cell model and make predictions.

Part II

Reference Free Traction Force Microscopy

As discussed in section 1.2, all the currently widely used TFM methods suffer from inherent limitations when extended beyond the application for which they were developed. Today's TFM cannot, at the same time, provide out-of-plane, high resolution, high sensitivity, and reference-free force detection at the single cell as well as at the multicellular level. The available continuum methods require a load-free reference image, which means that the cells need to be removed from the TFM platform before being able to compute the traction forces. The discrete methods either introduce topography that alters cell-behavior or the measurement is non-directional.

In this part of the thesis, Chapter 3: "*Confocal Reference Free Traction Force Microscopy*" shall introduce a novel technology, termed confocal reference-free TFM (cTFM) that overcomes these limitations. cTFM enables the direct calculation of traction forces generated by cells from a single fluorescent image. It is based on compliant silicone substrates with well characterized mechanical properties, onto which a highly regular triangular array of quantum dot nanodiscs is printed using electrohydrodynamic nanodrip printing[140]. The regular array is printed with nanometer-order precision, and provides a stable fluorescent signal, which can be tuned over the entire visible and infrared spectrum to be combined with other fluorescent reporters. The regular array is naturally deformed by cells upon interaction with the substrate. Imaging of this deformation renders both in plane and out of plane traction components without the need of cell detachment to obtain a load-free reference image. Calculation of cell-generated forces is very robust and shows a sensitivity of 200 Pa without the need of any arbitrary regularization steps. cTFM allows for the overlay of cell-generated traction fields with immunofluorescence, simultaneously revealing the location and activity state of proteins for which no live reporter is available.

Immunofluorescence is a technique used to mark the location of specific proteins in the cell. Fluorescently labelled antibodies attach to specific proteins through binding sites and make localization of proteins possible with fluorescence microscopy. The antibodies, however, do not penetrate the cell membrane and any proteins located in the cytoplasm cannot be accessed with this technique in live cells[141]. Therefore, the cells are fixed, meaning that any ongoing cell activity is stopped, and covalent chemical bonds are made between proteins. This keeps all proteins in place and links soluble proteins to the cytoskeleton[141]. Most importantly, however, the membrane becomes permeable to the antibodies and fluorophores. cTFM, in combination with immunofluorescence, can be used to gain insight in colocalization of proteins and the development of traction forces.

In addition to permitting downstream processing, with the cTFM platform, the cells are adherent to a continuous flat substrate, which eliminates any unwanted artifacts introduced by topography. The software that goes with the platform implements a robust finite element solution based on a non-linear elastic material model which was experimentally validated for the use of a soft silicone. The output from the solver is a continuous directional traction field. This goes beyond what any discrete method can achieve.

These advances are demonstrated on two biologically relevant examples. First, in Chapter 4: "*Cell Cycle-Dependent Force Transmission in Cancer Cells*", cTFM is employed to assess the force generation capabilities of single human epithelial cancer cells transfected with the cell-cycle reporter Fucci[142]. We therefore obtain a multiplexed set of data providing overlapping information on the cell cycle phase, the generated forces, and the activation state at the level of individual focal adhesions. Moreover, we demonstrate, through colocalization, the correlation of the generated traction forces with FAK-mediated paxillin phosphorylation.

Next we looked at MCF-10A epithelial cell monolayers. Isolated epi- and endothelial cells adhering to a flat substrate will spread and proliferate in the attempt to occupy the entire available space. The low level of interaction between cells supports a sustained motility, which in the absence of directional signals displays a gas-like diffusion. When cell density becomes sufficient to cover the entire substrate, and therefore achieve confluency, the migration speed begins to decrease[143]. Cells are now physically confined by the neighbors and cell-to-cell junctions are established[144,145] Collective motion, that is the coherent migration of groups of cells in the same direction at the same time, appears[146]. In this phase the monolayer dynamics is reminiscent of a fluid[147]. Collective movements decrease with increasing cell density eventually leading to the generation of a mature epithelium where cells assume a characteristic cobblestone shape[145], are stably confined, and largely immotile. This transition to a solid-like state, identified as jamming, is characteristic of mature and functional epithelia[148]. In specific conditions, collective cell motility can be re-activated and the system unjammed. This occurs during wound healing or upon invasion of healthy tissues by groups of carcinoma cells[149]. In Chapter 5: "*Endocytic Reawakening of Motility in Jammed Epithelia*", cTFM is used to compare the force generation of tissues in two different phases - Either in a *liquid* phase that manifests itself as highly dynamic cell collective that produces strong forces to the substrate, or in *solid* phase that is considered jammed with low cell motility and lower traction forces. Interestingly, ease of transitions between the two phases is increased by enhancing the expression of a single protein controlling endocytosis - Rab5.

3 Confocal Reference Free Traction Force Microscopy

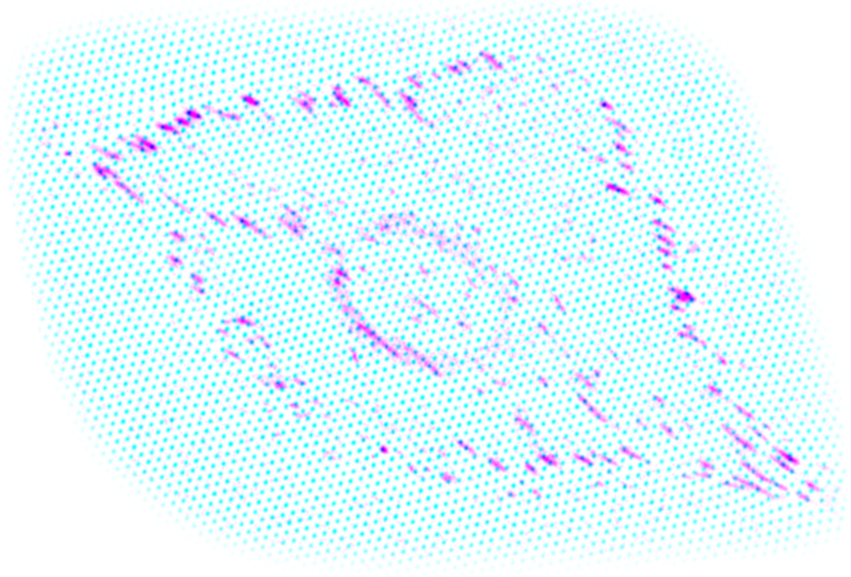

Parts of this chapter are published in: T. Lendenmann*, M. Bergert*, M. Zündel*, A. E. Ehret, D. Panozzo, P. Richner, D. K. Kim, S. J. P. Kress, D. J. Norris, O. Sorkine-Hornung, E. Mazza, D. Poulikakos and A. Ferrari, "Confocal Reference Free Traction Force Microscopy", *Nature Communications* 7 (2016): 12814. [150]

---

* These authors share first authorship of this contribution.

3.1 Introduction

Cells exert forces on their environment, mainly but not exclusively through the contractile acto-myosin machinery. These forces are transmitted to the extracellular surroundings through integrin-based adhesions (that is, focal adhesions) and enable shape changes and directional migration[151]. The biological function of this mechanical machinery goes beyond the simple physical anchoring and conveys environmental signals, which cells sense and respond to[152].

Traction force microscopy (TFM) provides a powerful tool to experimentally access cellular forces. In the last two decades multiple protocols for the measurement of cell-generated tractions have been developed, based on the optical detection of force-dependent deformations of compliant substrates[105,108,153]. Of these, lower-resolution discrete methods such as arrays of elastic micro-posts[106,154] allow the estimation of forces from a single image, yet carry significant limitations to the detection of out-of-plane components of traction forces, as well as artefacts due to their non-continuous, structured and intrusive nature[105,139,155,156]. Continuum TFM methods exploit elastic substrates containing randomly dispersed fluorescent beads[107,115,157]. These approaches yield high-resolution in- and out-of-plane force maps but require the additional acquisition of a reference (load-free) image, typically captured on cell removal and destruction, which markedly complicates experimental procedures and precludes post-processing such as the colocalization with immunofluorescence staining. Attempts to bypass these shortcomings, by applying micro-patterning of adhesive islands[158,159] or lithographic photoresist into ordered arrays[160], are hampered by major drawbacks such as the poor spatial resolution or the introduction of intrusive topographical features. Molecular methods, such as DNA-based force sensors[113], entail very high spatial resolution (about 200 nm) and one-shot force magnitude detection on flat, non-intrusive surfaces, but are unable to discern any force directionality.

Here we use highly precise electrohydrodynamic nanodrip-printing of quantum dots[140,161–163] (QDs) into monocrystalline, confocal arrays on elastomeric substrates and introduce a high-resolution and reference-free method (called confocal TFM or cTFM), capable of in- and out-of-plane force detection, which takes advantage of many assets of previously developed approaches while significantly advancing the landscape of reference-free force detection in cell biology and medicine.

3.2 Results

3.2.1 Design of the cTFM platform

The cTFM set-up in Figure 3.1a–c is comprised of a typical, 170µm glass coverslip spin-coated with a ≈ 30µm thick layer of a highly deformable CY52-276 silicone (Dow Corning)[164–167]. The CY52-276 silicone is a two-component elastomer yielding bulk elastic moduli ranging from 1 to 20kPa for mixing ratios close to 1:1 (Supplementary Figure A.2a). Standard PDMS (Sylgard 184) requires mixing ratios of around 1:60 to yield stiffnesses in the same range[168,169]. Silicones in general are very viscous and sticky before curing, and handling small amounts proves to be difficult. Thus, substrate preparation, especially for the small volumes required for spin-coating applications (ml regime), is simpler and more reliable with CY52-276 than for Sylgard 184. CY52-276 has a refractive index of $n_{632\mathrm{nm}} = 1.403$ (ref.[170]) and is optically transparent (Supplementary Figure A.2b). The point spread function measured in standard fluorescence wide-field microscopy is similar to the one obtained with commonly used polyacrylamide gels (Supplementary Figure A.2c–e). A unit of 0.05% poly(dimethyl-siloxane-b-ethylene oxide) is added during silicone fabrication to increase hydrophilicity[171], which aids nanodrip-printing precision[140,161]. All cTFM analyses shown in this work use a CY52-276 mixing ratio of 9:10, which provides an elastic modulus of ~ 12.6kPa according to our mechanical tests. A nonlinear hyperelastic material model, required for the analysis of large deformations of the substrate, is defined based on a comprehensive mechanical characterization of thin-cast samples in multi-axial mechanical tests[172] (Figure 3.1d and Supplementary Figure A.2f; for details see Methods). In addition, cyclic uniaxial strain rate sweep tests were performed between 0.3%s^{-1} and 5.2%s^{-1} at large strains, and showed negligible rate dependence of the material response (Supplementary Figure A.2g).

The silicone surface features a monocrystalline array of fluorescent nanodiscs, so that the lines connecting nearest neighbours form a grid of equilateral triangles (Figure 3.1e). Each printed fluorescent nanodisc contains a countable number of custom-made QDs[162] (Supplementary Movie 1). Individual nanodiscs are about 200nm in diameter (Figure 3.1e) and ≤ 30nm in thickness and thus represent confocal point sources of light, emitting a bright and stable fluorescent signal (Supplementary Figure A.1), without introducing intrusive surface topography[173]. By varying the size and composition of the QDs (see Methods for details), fluorescent nanodiscs with various and well-defined emission spectra can be created (Figure 3.1f), comparable and compatible with standard live-cell fluorescent proteins (for example, green fluorescent protein or mCherry). Sequential nanodrip-printing on a single substrate can interlace multiple arrays to yield a palette of emissions, without crosstalk between QDs of different colour (Figure 3.1g).

As previously demonstrated, electrohydrodynamic nanodrip-printing allows the generation of ordered nano-structures with spatial resolution of 100 – 200nm on dry surfaces[140]. As a first step in the adaptation of this technology to TFM and based on the requirements of the cases

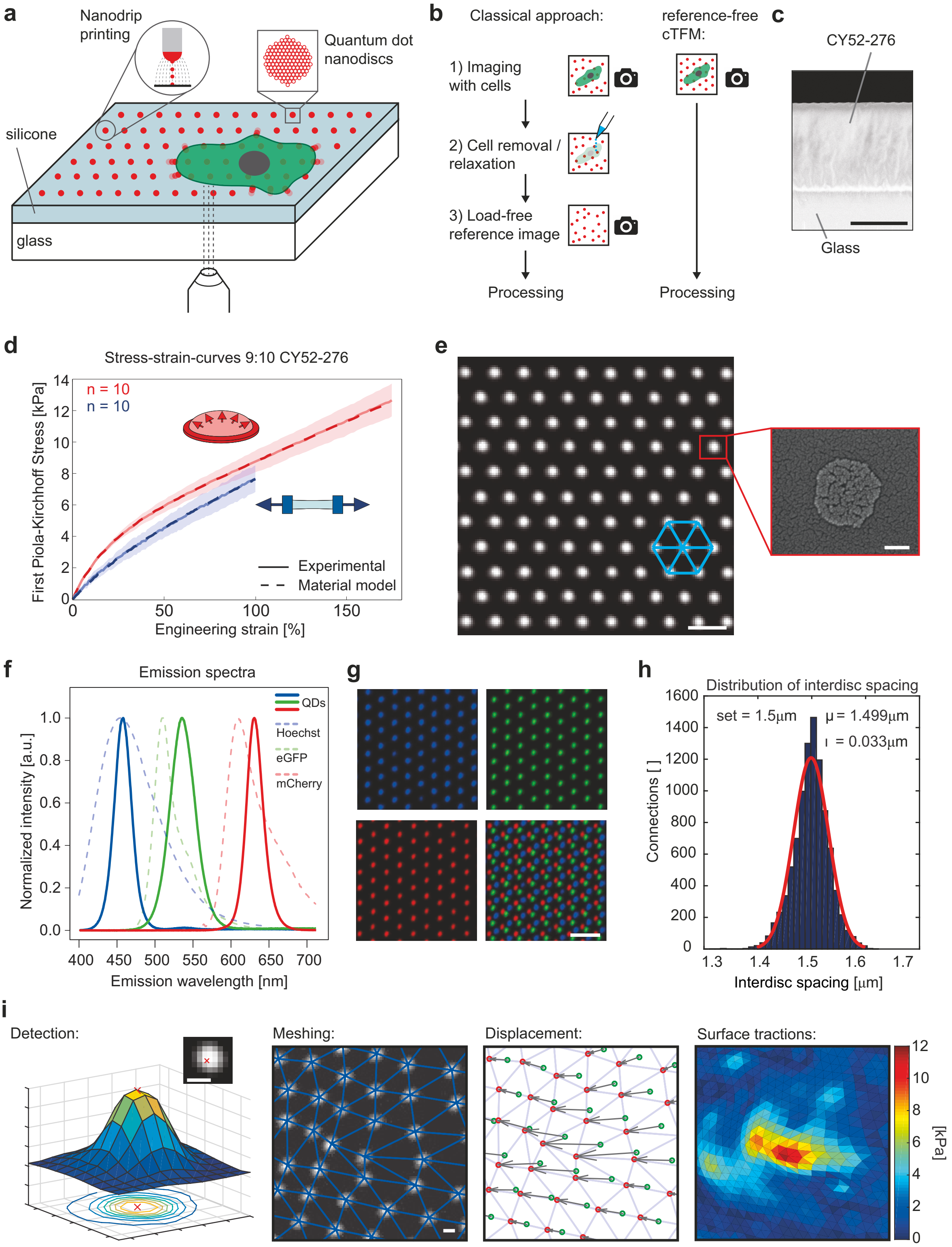
a
Nanodrip printing
Quantum dot nanodiscs
silicone
glass
b
Classical approach:
1) Imaging with cells
2) Cell removal / relaxation
3) Load-free reference image
Processing
reference-free cTFM:
Processing
c
CY52-276
Glass
d
Stress-strain-curves 9:10 CY52-276
n = 10
n = 10
First Piola-Kirchhoff Stress [kPa]
Engineering strain [%]
Experimental
Material model
0
2
4
6
8
10
12
14
0
50
100
150
e
f
Emission spectra
QDs
Hoechst
eGFP
mCherry
Normalized intensity [a.u.]
Emission wavelength [nm]
0.0
0.2
0.4
0.6
0.8
1.0
400
450
500
550
600
650
700
g
h
Distribution of interdisc spacing
set = 1.5μm
μ = 1.499μm
σ = 0.033μm
Connections [ ]
Interdisc spacing [μm]
0
200
400
600
800
1000
1200
1400
1600
1.3
1.4
1.5
1.6
1.7
i
Detection:
Meshing:
Displacement:
Surface tractions:
[kPa]
0
2
4
6
8
10
12

Figure 3.1: Overview and characterization of the cTFM platform (on page 22). (a) Schematic of the cTFM set-up and involved techniques. (b) Workflow of the classical continuum approach versus the one-step cTFM process. (c) Scanning electron microscopy (SEM) image of cross-section of elastic silicone layer on glass coverslip. Scale bar, 20µm. (d) Results of tensile (uniaxial) and inflation (equibiaxial) testing of CY52-276 silicone mixed at a 9:10 ratio. Free sample dimensions 40 × 10mm (uniaxial) and diameter 30mm (inflation). Thicknesses were in the range from 0.5 to 0.75mm; exact thickness was measured for each sample independently (see Methods). Shaded area: s.d.; $n = 10$ samples per test. (e) Representative example ($n = 20$) of QD nanodisc printing on elastic silicone substrates. Scale bar, 2µm. Red box: SEM image of QD nanodisc on glass. Scale bar, 100nm. (f) Emission spectra of blue, green and red QDs, as well as Hoechst, eGFP and mCherry for comparison. (g) Blue, green and red QDs were printed on the same substrate. Lower right image shows the merging of the three colours. Scale bar, 3µm. (h) Representative distribution of actual spacing between fluorescent QD nanodiscs after printing. (i) Overview of the analysis procedure. Subpixel detection of the QD nanodisc centre (Detection), followed by computational reconstruction of the triangular mesh (Meshing). From the displacement field (Displacement) the surface tractions are reconstructed using FEA (Surface tractions). Scale bars, 500nm.

we studied, we printed monocrystalline nanodisc arrays of custom-made QD dispersions on hydrophilic glass substrates with inter-disc spacing ranging from 0.75 to 3mm. This resulted in a positioning precision of 30 – 45nm, which was almost independent from the inter-disc spacing (Supplementary Figure A.3a). Printing of QDs was subsequently optimized for elastomeric substrates such as CY52-276 and yielded the same precision in nanodisc positioning (Figure 3.1h). In general, electrohydrodynamic nanodrip-printing is not limited to this particular silicone and can be equally applied to other silicones. Moreover, with future optimization of the chemistry to ensure stable binding of QDs to polyacrylamide, a cTFM substrate based on a hydrogel could be envisioned (Supplementary Figure A.4).

The achieved printing accuracy (Figure 3.1h) is a key enabler in omitting cell removal for the acquisition of a reference image (Figure 3.1b). An in silico analysis based on the defined material model (Figure 3.1d) revealed that with a printing error of 35nm the resulting noise in the calculated surface tractions increases from 100 to 500Pa as the inter-disc spacing decreases from 3 to 0.75mm (Supplementary Figure A.3b,c). We therefore applied monochromatic arrays featuring inter-disc spacing of 1.5mm to single cells and of 3mm to cell monolayers as an ideal trade-off between spatial resolution and force sensitivity.

After coating with fibronectin, adhering cells generate deformations of the substrate, which are captured as distortions of the fluorescent nanodisc array. A host of different cell types including, but not limited to, rat embryo fibroblasts (REF-Pax[174]), HeLa cells, human umbilical vein endothelial cells and MCF10A mammary epithelial cells proved compatible with the cTFM platform and induce dynamic deformations of the substrate to different extents (Figures 2a, 3a and 4b, and Supplementary Movies 2 and 3). In addition, the cTFM platform is fully compatible with biological applications, as no cytotoxicity is detected[175] (Supplementary Figure A.5).

On imaging of the cTFM platform in confocal or wide-field fluorescent microscopy, the position of individual nanodiscs on the deformed substrate is determined with sub-pixel resolution by calculating their weighted centroid (Figure 3.1i). An analyis using *in silico* generated images (for details see Methods) revealed that this detection algorithm has a precision of 4 – 8nm depending of the amount of imaging noise (Supplementary Figure A.6a,b). A custom-made algorithm is next utilized to construct the triangular mesh by identifying the six original neighbours for each individual QD nanodisc (Figure 3.1i; see Methods and Supplementary Methods for details). The corresponding (load-free) regular arrangement of the disc array is then computationally reconstructed by relaxing the triangular mesh back to an equilateral configuration (see Methods). This procedure tracks individual nanodiscs and allows to reliably extract displacement vectors (Figure 3.1i, Supplementary Figure A.6c–e, and Supplementary Movies 3 and 4). Analysis of the *in silico* generated images showed that the reconstruction algorithm is precise, resulting in positioning errors $\leq$ 30nm (Supplementary Figure A.6b), which are within the limit of our printing precision. On the basis of the displacement vectors obtained from the reconstruction algorithm, the kinematic boundary conditions of each node on the surface of a finite element mesh are defined by means of interpolation with radial basis functions (see Methods). Surface tractions, defined in the deformed configuration (Cauchy tractions), are finally obtained using nonlinear finite element analysis (FEA, Figure 3.1i, for details see Methods). The FEA accounts for both the nonlinear material properties of the substrate and the inherent geometrical nonlinearity associated with large deformations observed in cTFM experiments, typically with strains larger than 100%. For a 9:10 CY52-276 mixing ratio, this method provides a sensitivity of stress detection of 200Pa (Supplementary Figure A.7). Owing to the nanometre precision in the printing of nanodiscs and in the detection of their displacement, the calculation of generating traction fields does not require a regularization step, circumventing this difficulty present in particle image velocimetry (PIV)-based TFM procedures. cTFM is thus free from subjective parameterizations, which are prone to the underestimation of tractions in regions of the substrate where high deformations are detected[176,177].

3.2.2 High-resolution force detection at single focal adhesions

To validate our force detection system we plated REF-52 cells stably expressing YFP-Paxillin (REF-Pax) on a red-emitting cTFM platform. This allowed for simultaneous analysis of substrate deformations and imaging of cell adhesion structures (Figure 3.2a). The reconstructed traction peaks were mainly located at the cell perimeter, with nearly exact correspondence to focal adhesions (Figure 3.2b). The integral of surface tractions (ranging from 2 to 20kPa; Figure 3.2b) over the area defined by the Paxillin signal yields corresponding values for forces exerted per focal adhesion, which range from 1 to 30nN (Figure 3.2b,c). These results are in good agreement with values obtained on similar cells via classical continuum approaches[178,179], elastic PDMS pillars[106,154,180] or DNA-based force sensors[113]. Moreover, compared with other continuum reference-free methods based on lithographic or micropatterning approaches[158–160], cTFM features significant advantages: electrohydrodynamic

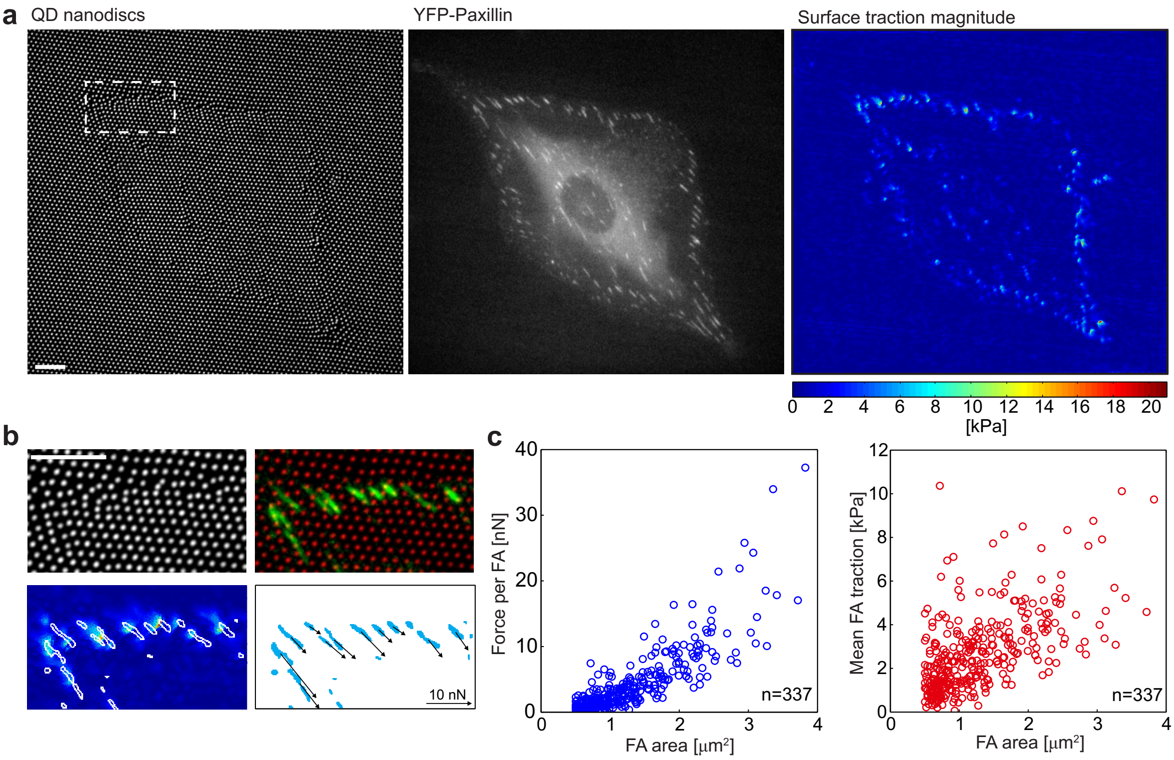

Figure 3.2: High-resolution detection of forces exerted at focal adhesions. (a) REF-Pax cell on cTFM substrate with red QD nanodiscs (spacing: 1.5μm). Scale bar, 10μm. Reconstructed surface tractions peaks are located at the cell circumference. (b) Surface traction peaks and focal adhesions colocalize. Scale bar, 10μm. The lower right panel depicts the magnitude and direction of forces exerted by individual focal adhesions. (c) Force and traction exerted by individual focal adhesions (only focal adhesions with an area $> 0.5\mu m^2$ were analysed). Data from $n = 337$ focal adhesions detected in four cells from independent experiments via integration of traction stress over focal adhesion area.

nanodrip-printing enhances spatial resolution, while simultaneously reducing the size of the fluorescent marker below optical resolution, allowing for a highly precise and robust spatial detection. In addition, cTFM provides a homogenously adhesive substrate with height differences $\leq$ 30nm (compared with 300nm; [160]), which is below the threshold at which substrate topography interferes with cells[173].

3.2.3 Out-of-plane force detection

Confocality of individual QD nanodiscs and of the nanodrip-printed disc array enables the monitoring of substrate deformations in all directions and with all fluorescent microscopy setups. Cells on planar substrates exert forces in all dimensions, with normal (out-of-plane) traction components typically being lower than in-plane ones[181]. Detection of these out-of-plane force components has led to fundamental findings in the field of cell adhesion biology[181,182]. To demonstrate the capability of cTFM in terms of out-of-plane force detection, we obtained three-dimensional (3D) image stacks of the fluorescent nanodisc array, deformed by spreading MCF10A cells. Intensity profiling along the Z axis was used to detect normal displacements (see Methods for details). We found that MCF10A cells generate significant normal displacements on spreading on the substrate, well above our vertical detection limit (Figure 3.3a–c and Supplementary Figure A.8). In line with previous work[181,182] cells pull upwards at the leading edge, and tend to push downwards towards the cell centre (Figure 3.3b,c). The detected vertical displacements are included in the reconstruction algorithm to calculate the volumetric traction field at the surface of the substrate, as well as corresponding principal traction vectors (Figure 3.3d,e). The ratio of out-of-plane and in-plane components of the tractions ranges from 0.1 to 0.5, illustrating the substantial magnitude of normal tractions[182]. Our results demonstrate that the cTFM platform is capable of separate detection of in-plane and out-of-plane components of cell tractions with high resolution. This is a remarkable advantage over other available discrete or continuum reference-free methods. PDMS pillars[106,154] have lower spatial resolution and only detect in-plane tractions, whereas molecular force sensors[113], despite their very high spatial resolution, cannot discriminate force direction. In addition, no out-of-plane force detection has been demonstrated using continuum reference-free methods[158–160], to the best of our knowledge. cTFM is thus the first reference-free TFM method based on a two-dimensional substrate capable of detecting cellular tractions exerted in all directions.

3.2.4 Correlative cTFM

The cTFM platform enables the direct correlative overlap of high-resolution continuous traction force fields with spatial localization of proteins via immunofluorescence methods. This capability has so far been limited to micropillar substrates[106,184–186], which geometrically constrain cell adhesion and might alter cell behaviour. cTFM thus expands the portfolio of possibilities, in addition to the use of live-cell reporters. Such capability is of unique value when addressing post-translational protein modifications such as site-specific phosphorylation, where, to the best of our knowledge, no live reporter exists that detects the presence of specific phospho-groups on target substrates. We illustrate this potential visualizing the phosphorylation pattern of the focal adhesion protein Paxillin[47] (Supplementary Figure A.9).

To further showcase the capability of cTFM, we applied it to a recently discovered molecular pathway implicated in the transduction of mechanical signals in epithelial monolayers. Signalling pathways activated by mechanical stimuli can drive whole sheet responses, while being active only in a subset of cells at specific locations within the cell layer, such as wound edges, replicative foci and others[187]. Perhaps the most prominent example is the mechano-sensitive pathway of Hippo[188], which controls the nuclear translocation of the transcription factor YAP (yes-associated protein). Gradients of YAP activation, commonly revealed by immunostaining, develop from the edge of the epithelium to the rear positions. Therefore, cells at the

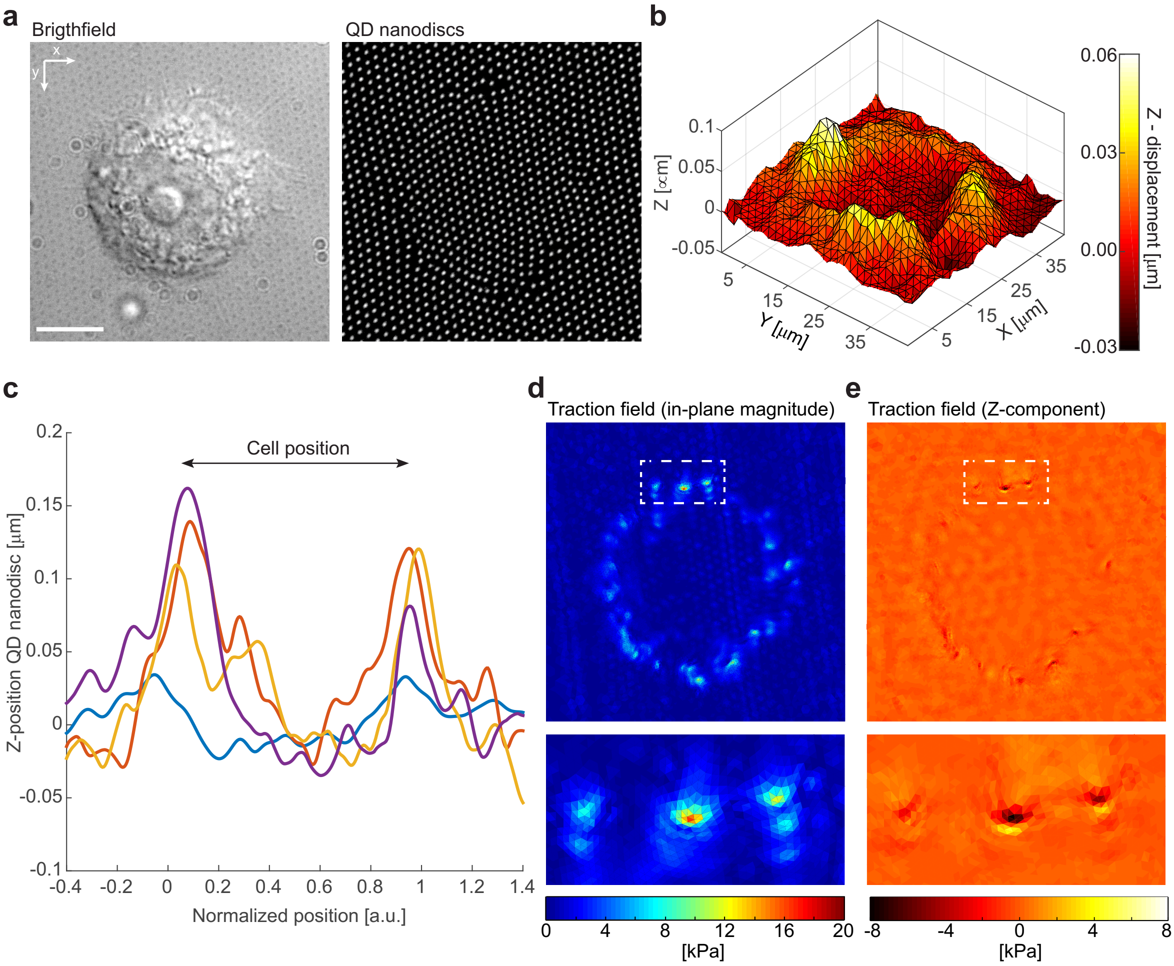

Figure 3.3: Detection of out-of-plane forces. (a) Spreading MCF10A cell on cTFM substrate with red QD nanodiscs (spacing: 1.5µm). Scale bar, 10µm. (b) Smoothed 3D surface plot of the area underneath the cell in a. For traction force reconstruction, the unsmoothed displacements in Z-direction are taken into account. (c) Z-profile of the substrate obtained from line scans underneath four independent cells. Cell dimensions were normalized so that cell outlines reach from 0 to 1. (d) Overall traction magnitude of the cell in a. (e) Out-of-plane ($Z-$) components of the traction field for the cell in a.

boundary retrieve positional information, which is assumed to be functionally linked with forces, including both intercellular and cell–extracellular (ECM) traction forces[183] (Figure 3.4a). We applied cTFM to directly correlate epithelial force generation and nuclear translocation of YAP. To this end, MCF10A mammary epithelial cells were seeded in dense clusters on red cTFM substrates. At the edge of the epithelial colony we detected traction forces within the cell monolayer (Figure 3.4b), followed by immediate fixation and immunofluorescence processing for YAP and Hoechst (Figure 3.4c,d). As suggested by previous literature, we found that cells in the proximity of the free, migrating edge of the colony display a strong cor-

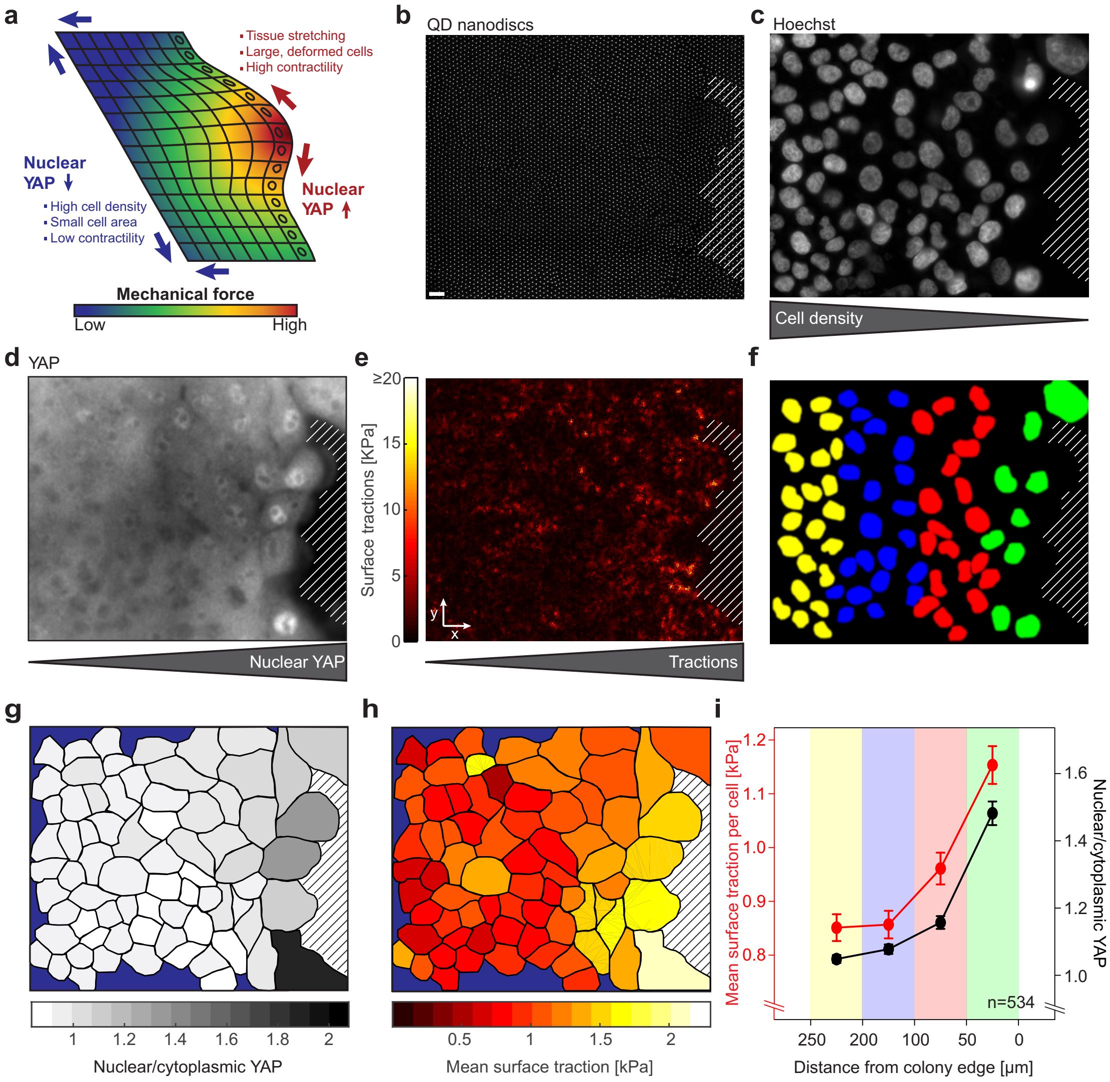

Figure 3.4: Correlative traction force microscopy. (a) Current model of YAP activation in epithelial monolayers (modified from ref. [183]). (b) Edge of a colony of epithelial MCF10A cells seeded on a cTFM substrate with red QD nanodiscs (spacing: 3µm). After live imaging of the fluorescent QD nanodiscs cells were immediately fixed and processed for immunostaining. Scale bar, 10µm. (c) Nuclei and decreasing cell density along the x axis. (d) Immunostaining for the transcription factor YAP. (e) Surface traction exerted by the MCF10A monolayer. (f) Binning of nuclei into 50µm regions of interest (ROIs) perpendicular to the colony edge. (g) On the basis of segmentation of the brightfield image, individual cell outlines were defined and nuclear/cytoplasmic YAP was quantified for each cell. (h) Mean surface traction per cell. Blue region corresponds to cells with cropped nuclei. Therefore no nuclear/cytoplasmic YAP could be quantified and cells were excluded. Hatched area corresponds to a region devoid of cells. (i) Cells from four independent colony edges were binned in four ROIs (as defined in f) and surface traction per cell and nuclear/cytoplasmic YAP ratio were determined. n=number of analysed cells; error: s.e.m.

relation between increased nuclear YAP signal and the magnitude of surface tractions[183,188] (Figure 3.4d–i).

We are not aware of any other studies and methods that have directly (for the same cells) and quantitatively correlated YAP localization with the magnitude of traction forces. Therefore, cTFM fully preserves the information on cell position and identity during downstream processing. This information enables the generation of colocalization maps and allows for spatially resolved quantitative analysis of traction forces and cellular signalling (Figure 3.4f–i). Further, the data show that cTFM is not limited to single-cell analysis but can be applied to cell cohorts and collectively migrating cell monolayers.

3.3 Discussion

The presented results establish cTFM as an easy-to-use, high-resolution force sensing method markedly advancing the state of the art over current TFM approaches. The highly deformable silicone-based substrate combined with a nanodrip-printed monocrystalline array of fluorescent landmarks constitutes an optically transparent, continuum environment, which can be adapted to a broad palette of biological applications. The selected two-component silicone allows for traction measurements over a wide range of physiological forces with straightforward fabrication requirements. For the cells and applications described here, the used 9:10 mixing ratio proved to be suitable in terms of magnitude of displacements and resulting material strains. Cell-induced displacements were well above nanodrip-printing noise ($\approx$ 30nm), while the resulting strains in the substrate were within the regime analysed in the mechanical tests (Figure 3.1d). For other cells or applications, fabrication and characterization of further CY52-276 mixing ratios can expand the force detection range of the cTFM platform in the future.

The well-defined and highly stable QD emission is homogenous across the nanodisc-lattice and can be tailored over a large palette of colours. Similar to conventional TFM, overlays of crystalline array with multiple colours could be used in the future to further increase spatial resolution of the cTFM platform[115]. The use of the nanodrip-printing technology enables the deployment of QDs into sub-resolution nanodiscs arranged in a confocal and crystalline triangular pattern. Therefore, it yields a substrate for cells, which is homogeneously adhesive and devoid of any intrusive topography. Finally, the corresponding fully nonlinear analysis enable application of the cTFM platform to highly deformable substrate materials and large strain problems, beyond the validity of linear methods[108].

The synergistic effect of the above-mentioned technologies enables a one-step-imaging process, which directly provides all necessary information to compute the intensity and direction of in- and out-of-plane traction forces produced by cells. This substantially simplifies the experimental workflow and supports a rapid and high-throughput analysis. Importantly, it removes the requirement for cell detachment and acquisition of a load-free reference image, enabling correlative visualization of traction forces and cellular signalling activity, and rendering cTFM a significant methodological advancement in cell force determination and activity for the biological and medical communities.

3.4 Materials and Methods

3.4.1 Cell culture

HeLa cells (American Type Culture Collection; ATCC) and rat embryonic fibroblasts stably expressing YFP-Paxillin (REF-Pax[174]) were grown in high-glucose Dulbecco's modified Eagle's medium (DMEM) supplemented with 2mM L-Glutamine, 10% FBS, 1% penicillin/streptomycin (all Sigma-Aldrich). Human Umbilical Vein Endothelial Cells (HUVECs, Life Technologies) were grown in M200 medium with Low Serum Growth Supplement (all Life Technologies). MCF10A cells (G. Scita, IFOM Milan, Italy) were grown in Dulbecco's modified Eagle's medium /F12 medium (Life Technologies) supplemented with 10% horse serum, 1% penicillin/streptomycin, $0.5\mu g\,ml^{-1}$ hydrocortisone, $10\mu g\,ml^{-1}$ insulin, $20\mu g\,ml^{-1}$ epidermal growth factor (all Sigma-Aldrich) and $100\mu g\,ml^{-1}$ Cholera toxin (List Biological Laboratories). All cells were cultured in a humid atmosphere containing 5% CO_2 at 37°C.

PC12 cells (ATCC) were grown in RPMI-1640 medium supplemented with 10% horse serum, 5% FBS, 2mM L-glutamine and 1% penicillin/streptomycin (all Sigma-Aldrich). Details on the cytotoxicity test are described elsewhere[175]. Briefly, PC12 cells were grown for 4 days in RPMI-1640 medium supplemented with 2% FBS, 2mM L-glutamine, 1% penicillin/streptomycin and $100\mu g\,ml^{-1}$ nerve growth factor (induction medium), followed by measuring the mean neurite length.

3.4.2 Substrate fabrication and nanodrip-printing

The two components of CY52-276 polydimethylsiloxane (Dow Corning) and 0.05% ($v\,v^{-1}$) poly(dimethylsiloxane-b-ethylene oxide) (Polysciences) were mixed thoroughly at the desired ratio for 5min, degased for 2min and spin-coated on 170mm thick coverslips for 1min at 1500 r.p.m. The silicone was then cured at 70°C for 30 min. Afterwards the substrates were kept at all stages in a clean, dust-free and dry environment to prevent fouling. With respect to ageing properties of polydimethylsiloxanes[172] , we always used CY52-276 samples of the same age for experiments (2 – 3 weeks). The red core-shell-shell CdSe-CdS-ZnS QDs with an emission peak at 627nm were synthesized following a published recipe[189] . The detailed recipe, as well as recipes for the blue and green QDs can be found in the Supplementary Methods. The QDs were transferred from hexane dispersions to tetradecane for the printing process. To ensure a reproducible printing process and reduce clogging at the printing nozzle, the optical density of the dispersion at the first absorption peak was adjusted to 0.5 for a 1mm path and then further diluted 1:1 in tetradecane. The deposition precision was further increased by adding 5% vol of octanethiol-capped gold nanoparticles[190] to the QD ink from a tetradecane dispersion with an optical density of 5 for a 1mm path. These gold nanoparticles enable a more stable printing process, leading to a reproducible droplet ejection and thus a higher placement precision, but do not adversely affect the fluorescence.

The QDs were deposited on the substrate by electrohydrodynamic nanodrip-printing, details of which have been published elsewhere[140,161–163]. Briefly, the substrate is placed on a conducting grounded plate. A gold-coated glass capillary with an opening diameter of 1 – 1.5µm is filled with the QD dispersion and brought within 5µm of the substrate using a piezoelectric stage with nanometre precision. By applying voltage pulses between the nozzle and the grounded plate, nanoscale droplets with a diameter of 50 – 100nm are rapidly ejected from the apex of a larger meniscus formed at the nozzle exit with frequencies of 100 – 200Hz. The droplets land softly on the substrate (no splashing or sizable spreading) and the tetradecane evaporates before the arrival of the next droplet, leaving behind only the nanoparticle content. To print one nanodisc of the triangular array, d.c. voltages of 200 – 250V are applied for 70ms. In this manner, the QDs of several nanodroplets land at the same location each time and form collectively one brightly emitting disc at a well-defined position. Arbitrary patterns can be created moving the substrate with the piezoelectric stage. Voltage, pulse length and stage position are controlled using a custom-built control unit. The electrohydrodynamic nanodrip-printing technology is freely available for laboratory research and, in addition, can be commercially obtained through an ETH Zurich spin-off company (http://www.scrona.ch).

3.4.3 Mechanical characterization of the substrate

The mechanical properties of the substrate were evaluated for thin cast samples loaded in different modes. Uniaxial-tension tests were performed on a tensile testing set-up mounted on a MTS 793 testing rig (MTS Systems, Eden Prairie, USA). Equibiaxial deformation behaviour of the material was characterized on a custom-built inflation set-up[172]. All measurements used for the evaluation of the elastic properties were performed at low strain rate ($\dot{\varepsilon} = 0.3\% s^{-1}$) and within the range of deformation expected to occur during cTFM (up to 175% strain). Strain was quantified by tracking optical features on the sample surface using a CCD (charge-coupled device) camera (Pike 100B Allied Vision Technologies GmbH) and a customized tracking algorithm[172]. The thickness of each sample was determined post testing by optical measurements of the cross-section of sliced samples in a microscope (LSM 5 PASCAL, Zeiss). The stress–strain data of the tests were used to fit the parameters of a hyperelastic Ogden material[191] with two terms (Table 3.1).

μ_1 (kPa)	α_1 (-)	μ_2 (kPa)	α_2 (-)
4.073	2.132	0.167	-0.600

Table 3.1: Ogden material parameters.

3.4.4 ECM coating and cell seeding

Before coating with the ECM protein fibronectin, substrates were incubated in a custom-built vacuum oven at 90°C for 1h, washed 1min in methanol and incubated for another 2h in the vacuum oven to remove ligands and anneal QDs to the silicone. Substrates were then glued in 35mm Petri dishes. For coating $50\mu g\,ml^{-1}$ fibronectin (Life Technologies) in PBS was applied to the substrates for 1h at room temperature. Substrates were washed twice with PBS before applying medium and seeding of cells at desired concentrations.

3.4.5 Live-cell imaging

Cells were allowed to spread from at least 3h till overnight before imaging (except otherwise noted) using an inverted Nikon-Ti wide-field microscope equipped with an Orca R-2 CCD camera (Hamamatsu Photonics, Japan) or an iXon Ultra 888 EMCCD (Andor, UK). Temperature, CO_2 and humidity were controlled during imaging using an incubation chamber (Life Imaging Services, Switzerland). Images were collected using a ×60 Plan Apo l 1.40 Oil or and ×60 Plan Apo VC 1.20 water objective. Focal drift during the experiments was avoided using the autofocus system of the microscope.

3.4.6 Image analysis

The pointspread function of individual 50nm fluorescent beads on polyacrylamide and CY52-276 silicone was distilled from 3D image stacks acquired with conventional wide-field fluorescent microscopy using Huygens software (Scientific Volume Imaging).

Focal adhesion structures were segmented based on a previously described method[192], except that the mathematical exponential step was omitted. Briefly, on background subtraction, the local contrast of the image was enhanced via Contrast Limited Adaptive Histogram Equalization. After applying a Laplacian of Gaussian filter, the image was manually tresholded and particles were analysed. Only focal adhesions with a size $> 0.5\mu m^2$ were considered for the analysis.

3.4.7 Immunofluorescence

Cells were fixed with 3% paraformaldehyde in PBS for 10min at room temperature and permeabilized via incubation in 3% paraformaldehyde with 0.1% Triton in PBS for 5 min. After blocking with 5% BSA in PBS for 2h, samples were incubated at 4°C overnight with a monoclonal primary antibody against YAP (Cell Signaling (D8H1X), dilution: 1:300) or phosphorylated Paxillin (Tyr118, Cell Signaling (#2541), dilution: 1:300). Alexa Fluor 647

Chicken anti-Rabbit (Thermofischer (#A-21443)) was used 1:200 as secondary antibody for 1h at room temperature. For staining of nuclei, Hoechst was added at $10\mu g\, ml^{-1}$ during a washing step.

3.4.8 *In-silico* image generation

A synthetic image that simulates a real image acquired in the microscope was created with the following procedure[193]. First, the positions of the QD nanodiscs in perfectly regular arrays and arrays with positioning errors of 35nm (recapitulating the printing error) were determined using MATLAB. Then, in some regions these positions were displaced to a maximum of 1.5µm to simulate cell tractions. A synthetic image was obtained by creating Gaussians with s.d. of 0.2µm at the exact positions of the nanodiscs, to simulate the signal convolution of the microscope. Finally, Gaussian noise with s.d. of 10 was added to the synthetic image in ImageJ to mimic imaging noise.

3.4.9 Data analysis and statistics

Data were analysed, tested for statistical significance, fitted and visualized using R or MATLAB (The MathWorks). No statistical method was used to predetermine sample size. No estimation of variance was performed. The Shapiro–Wilk test was used to test for normality of data. For non-normal distributed data, Mann–Whitney U-test was performed.

3.4.10 Data availability

cTFM software featuring algorithms for QD nanodisc detection, meshing, reference configuration estimation and displacement reconstruction, and surface traction evaluation is available as Supplementary Software (cTFM_Package_NatComm.zip and cTFM_Examples_NatComm-.zip) at https://dx.doi.org/10.6084/m9.figshare.3493685.v1. cTFM_Package_NatComm.zip contains the software package used to analyse cTFM images (including documentation).
cTFM_Examples_NatComm.zip contains example images to be analysed with the cTFM software. Further relevant data are available from corresponding authors on request.

4 Cell Cycle-Dependent Force Transmission in Cancer Cells

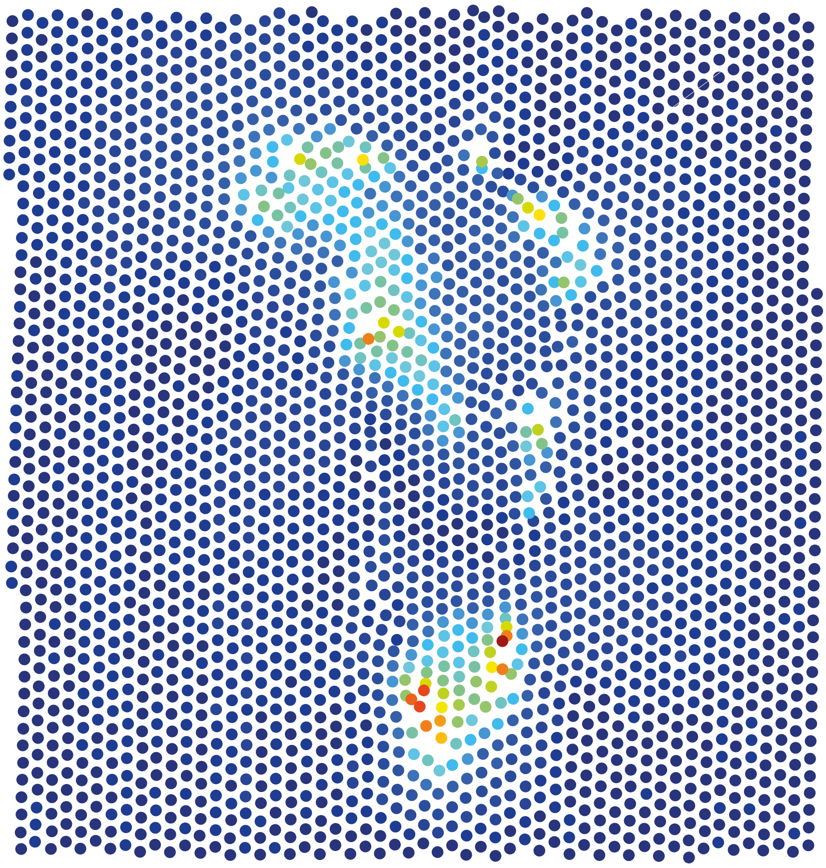

Parts of this chapter are published in: M. Panagiotakopoulou, T. Lendenmann, F. Pramotton, C. Giampietro, G. Stefopoulos, D. Poulikakos, A. Ferrari, "Cell cycle-dependent force transmission in cancer cells", *Molecular Biology of the Cell* 29 (2018): 2528. [194]

Contribution

I was partially involved in this project. My work involved the investigation of traction forces throughout the cell cycle of both HeLa and MCF-7 cells. Additionally, I developed algorithms for measuring the amount of phosphorylation in focal adhesions, and for the colocalization of phosphorylation and traction forces.

4.1 Introduction

Beyond their genetic heterogeneity, solid tumors display unique characteristics of size, shape, stiffness[86,195,196], and deformability[197]. This biophysical fingerprint depends on the composition, architecture, and type of cancer[198]. Within neoplastic lesions, cells are embedded in a complex three-dimensional (3D) environment, which contributes overlapping biological and mechanical signals impinging on the metastatic dissemination of cancer seeds. This mechanical interplay is of particular relevance in defining the ability of pervasive cells to migrate in dense interstitial tissues and proliferate in distant body locations[199,200]. In this context, traction forces exerted by cells on the surrounding environment via integrin contacts (i.e., the focal adhesions [FAs]) orchestrate a process of mutual evolution, during which metastatic cells remodel the extracellular matrix (ECM[201,202]), acquire the ability to repair DNA damage[203], and develop resistance to drugs[204].

A number of studies have evaluated the correlation between cell cycle progression and migration of cancer cells. In particular, the "go or grow" hypothesis postulated that the two activities are mutually exclusive in space and time[205–208]. Emerging evidence, however, shows that tumor cells do not defer proliferation for migration[209,210]. Along this line is the pathological observation that highly proliferative tumors are often likewise invasive[211]. This correlation is linked to frequent relapses and a very poor prognostic outcome.

The existence of a link between cell proliferation and migration remains elusive, yet a growing number of indications suggest that the key may be found in the way cells generate actomyosin-mediated traction forces and transmit them to the surrounding environment to propel migration[128]. We recently provided evidence that the efficiency of penetrative migration in small interstitial pores varies during the cell cycle progression of cancer cells[212]. Nuclear deformability increases immediately after division, a phase in which the biochemical decondensation of chromatin takes place (M/G1 phase). Cells can thus efficiently penetrate small openings due to the reduced physical resistance provided by the nucleus[213]. Nuclear stiffness increases in the ensuing G1 and S phases[214,215]. This, however, does not impede the pervasion of pores demanding a very large deformation. The same narrow openings become insurmountable obstacles as soon as the cell progresses from the early S to the late S/G2 phase[212].

A pivotal role in regulating both cell proliferation and migration is played by cell adhesions to ECM, which are established upon integrin activation[216–218]. Integrin contacts are partially lost during cell division[219] and gradually reassembled by daughter cells upon abscission. Cancer cells feature a greater number of large adhesions to the substrate in the G1 and S phase[212]. It is therefore logical to speculate that in these specific phases of the cell cycle, the transmission of cellular forces to the substrate is sufficient to actuate the necessary deformation and squeezing of a relatively stiff nucleus.

Actomyosin-generated contractility is transmitted to the substrate at the level of FAs[130]. Mature adhesions connect with actin stress fibers at their cytoplasmic sides (i.e., the adhesion plaque[40]). Beside actin dynamics[220,221], master regulators of this mechanical maturation are focal adhesion kinase (FAK) and paxillin[47,222–227]. In particular, FAK-mediated paxillin phosphorylation induces the recruitment of vinculin at the adhesion site, thus reinforcing the connection to the actin cytoskeleton[40]. This process may support the transmission of traction forces to the substrate in correspondence with individual integrin contacts, yet a direct demonstration is still missing.

Traction force microscopy (TFM) provides access to cellular forces transmitted to the substrate via FAs. TFM detects the resulting substrate deformations by tracking the displacement of optical landmarks[99]. To do this, classic TFM approaches, based on continuum hydrogels or silicon substrates, require the acquisition of a reference image[115], which renders them incompatible with the analysis of protein activity by immunohistochemistry. Discrete TFM methods do not require this disruptive step, yet introduce significant artifacts in the formation of integrin contacts[115]. A reference-free continuum TFM method, recently developed in our laboratory, allows the generation of spatially resolved overlapping maps of protein activity and traction forces[150]. Here, we exploit this approach to investigate the variation of force transmission to the substrate in cancer cells during their progression along the cell cycle and link it to the corresponding dynamics of FA maturation via FAK-mediated paxillin phosphorylation.

4.2 Results and Discussion

HeLa Fucci2 cells were adopted as a general model of cell cycle progression in human epithelial cancer. Their adhesion to the substrate and migratory behavior in standard culture and *in vitro* models of interstitial invasion are well established[228–230]. The cells stably express the Fucci two-color cell cycle reporter[142], which is characterized by the alternate nuclear expression of hCdt1-mCherry during the G1 phase (red fluorescent channel) and hGem-Azami Green during the S/G2/M phases (green fluorescent channel;[142]). Calibration of the relative signals from the two fluorescent channels and their correspondence to the cell transition in distinct cell cycle phases were previously reported for these cells. In particular, cells in M/G1 show no fluorescent emission, while the G1, early S, and S/G2 phases are identified by red, orange, or green emissions, respectively (Figure 4.1A[212]).

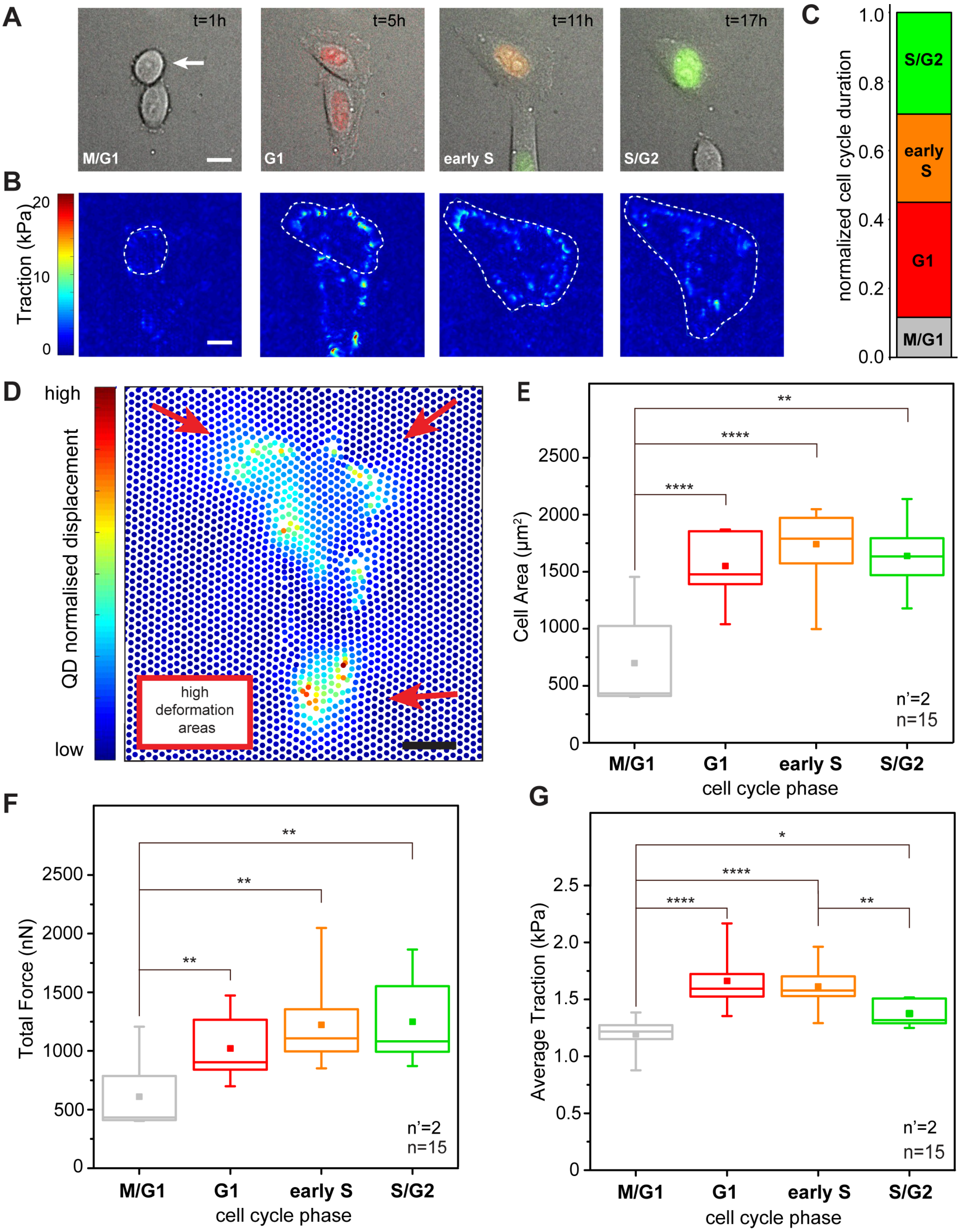
A
t=1h
t=5h
t=11h
t=17h
M/G1
G1
early S
S/G2
B
Traction (kPa)
20
10
0
C
normalized cell cycle duration
1.0
0.8
0.6
0.4
0.2
0.0
S/G2
early S
G1
M/G1
D
high
low
QD normalised displacement
high deformation areas
E
Cell Area (µm²)
2500
2000
1500
1000
500
0
**
****
****
n'=2
n=15
M/G1
G1
early S
S/G2
cell cycle phase
F
Total Force (nN)
2500
2000
1500
1000
500
0
**
**
**
n'=2
n=15
M/G1
G1
early S
S/G2
cell cycle phase
G
Average Traction (kPa)
2.5
2.0
1.5
1.0
0.5
0
*
****
****
**
n'=2
n=15
M/G1
G1
early S
S/G2
cell cycle phase

Figure 4.1: Cell cycle–dependent force transmission in cancer cells on page 38. (A) Merged transmission and fluorescence images of a HeLa Fucci2 cell over a complete cell cycle. The corresponding cell cycle phase, as defined by the Fucci2 reporter, is indicated in the bottom left corner of each panel. The elapsed time from the initial cell division is reported in the top right corner. Scale bar is 10 μm. (B) Corresponding maps of actuating traction obtained by cTFM. A white dashed line indicates the basal profile of the cell under analysis. (C) Relative duration of each cell cycle phase. (D) Typical displacement of the QD nanodisc array induced by a HeLa Fucci2 cell in G1. Scale bar is 10 μm. (E) Dynamics of absolute total forces along cell cycle progression. Force is averaged over all tracked cell cycles. (F) Corresponding phase-resolved dynamics of cell spreading and (G) traction transmitted to the substrate along individual cell cycles. *$p < 0.05$, **$p < 0.01$, ****$p < 0.0001$. n = number of cells and n' = number of independent experiments.

To access the forces imparted by cells to the substrate, HeLa Fucci2 cells were seeded at low density and care was taken to avoid the generation of large clusters, which interfere with the measurement of individual cell contractility (initial seeding density $4 \times 10^4/cm^2$). To measure the spatial and temporal variation of cellular traction as a function of the cell cycle phase, a red-emitting confocal TFM (cTFM[150]) platform was used. The force sensor array was based on a silicone substrate (9:10, CY52-276) yielding an elastic modulus of ~12.6 kPa, on the surface of which a triangular pattern of red quantum dot (QD) disk-shaped layers of diameter ~200 nm was printed, with a 2-μm pitch. This configuration provided sufficient spatial resolution and sensitivity to capture deformations induced by single FAs[150]. Individual cells were monitored through live-cell microscopy along the entire duration of their cell cycles, from one division to the next. The average duration of these cycles was 20.2 h; therefore a total observation period of 30 h made it possible to monitor a sufficient number of complete progressions. The resulting time lapses yielded stratified information on cell cycle and spreading dynamics and on corresponding deformation of the QD nanodisc array. From the latter, the actuating traction forces were derived by means of a dedicated algorithm (Figure 4.1B; [150]).

The average duration of each cell cycle phase was extracted as the first quantitative data layer (Figure 4.1C). During the recorded cycles, cells spent more time in the G1 phase, while their residence in M/G1 (early stage G1), early S, or late S/G2 phase was shorter. Similarly, phase-resolved values of cell spreading were obtained. The graph in Figure 4.1F reports the linear increase of basal area upon progression from the M/G1 to the G1 phase. The cell surface increment continued in the ensuing development to reach a plateau in late S/G2.

Cell-induced displacement of the QD nanodiscs from their original, perfectly-ordered position in the triangular array (through the deformation of the elastic substrate to which the nanodiscs firmly adhered) was automatically captured under each tracked cell and over the entire cell cycle (Figure 4.1, B and D). A finite element analysis of the resulting vectorial displacement field, based on the constitutive material model of the substrate[150], rendered spatially and temporally resolved maps of the actuating traction forces. Using the overlapping cell profiles, stress magnitudes were integrated under the entire cell surface, yielding the total force intensity exerted by the cell under analysis (Figure 4.1E). Forces transmitted by HeLa

Fucci2 cells increased from the M/G1 phase (699 ± 144 nN) to G1 and lasted through early S (1741 ± 89 nN), in line with previous reports establishing a linear correlation between cell area and force generation[86,231]. A slight decrease was instead measured toward the end of the cell cycle, in the late S/G2 phase (1638 ± 101 nN; Figure 4.1E).The same total force and cell area trends are well captured by measurements along individual cell cycles (Supplemental Figures C.2–C.5).

To better understand the link between cell spreading and force generation in cell cycle progression, the measured cellular force (Figure 4.1E) was divided by the cell basal area (Figure 4.1F) to obtain the average traction (Figure 4.1G). This derived descriptor corresponds to the density of force exerted by individual cells on the substrate and increased significantly from the M/G1 to the G1 phase (1.126 ± 0.2 kPa to 1.65 ± 0.2 kPa). It persisted upon transition to the S phase (1.54 ± 0.2 kPa) while dropping significantly when cells entered the S/G2 phase. In the S/G2 phase the average traction was only slightly higher than that measured in M/G1 (1.3 ± 0.2 kPa). These results suggest that the cellular machinery supporting force transmission matures during cell cycle progression along with cell spreading, but with different dynamics. The highest average traction is transmitted to the substrate before the cell surface reaches its full extension (Supplemental Figures C.2–C.5). Finally, no direct correlation between cell shape and exerted traction could be detected in individual cell cycles (Supplemental Figure C.6), suggesting that the small and rapid variations of cell shape recorded under our experimental conditions did not significantly impinge on the force generation dynamic.

cTFM provides a reference-free detection of cell-mediated substrate deformations from which a measure of transmitted cell contractility can be obtained directly without the necessity of disruptive cell removal[150]. The phase-resolved evolution of average traction obtained from fixed samples (Figure 4.2A), and thus from different cells, revealed the same temporal variation as that captured by the live cell analysis (Figure 4.1G). This result has a twofold value. First, it validates cTFM as conducive to endpoint sample processing (i.e., immunostaining) to reveal the level of activity of specific molecules as an additional layer of information. Second, it demonstrates that the G1 traction peak is significant beyond intercellular variability.

Hence, the total (total-pax) and phosphorylated paxillin (phospho-pax) distributions were visualized in cells contacting the cTFM substrate, providing a direct map of adhesions, paxillin activation, and resulting transmitted forces (Figure 4.2B). A first, qualitative analysis indicated that large FAs featuring prominent paxillin phosphorylation colocalized with regions of high transmitted force, while smaller adhesions with correspondingly lower phospho-pax levels were found in regions of low force transmission (Figure 4.2C).

Quantitative large-scale analysis confirmed this observation. HeLa cells do not display resolvable paxillin accumulation at the basal surface during M/G1[212], consistent with the absence of mature integrin contacts in this phase[232]. In the ensuing phases, FAs were mostly detected at the cell periphery (Figure 4.2B). Here, higher levels of phospho-pax correlated linearly with the size of individual adhesions (Supplemental Figure C.7), thus linking FA growth to their mechanical maturation[86,218]. Notably, phospho-pax levels were significantly higher in

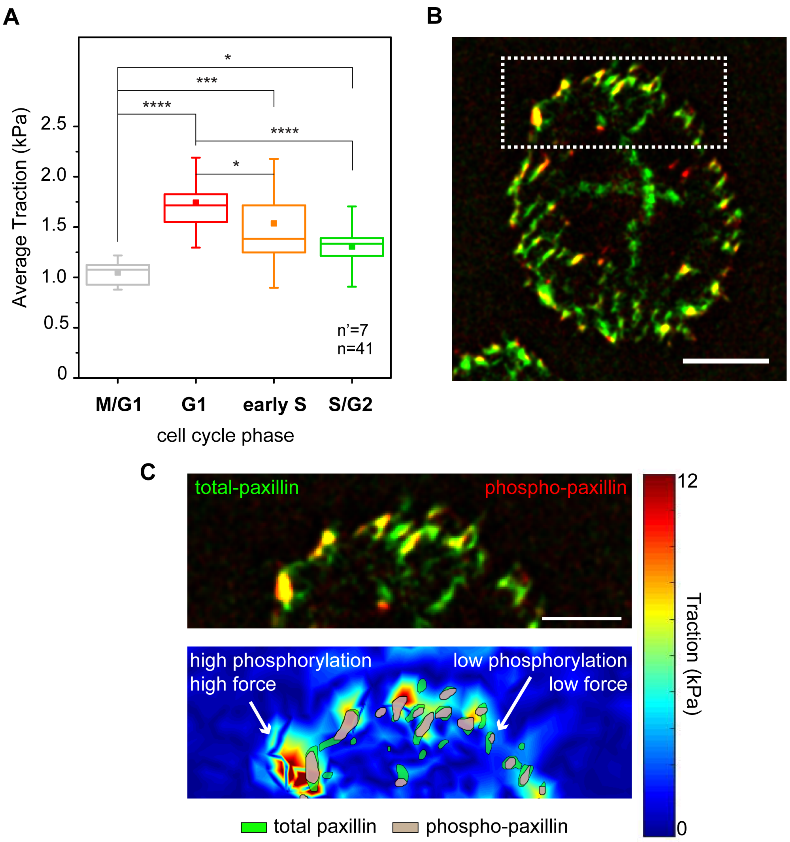

Figure 4.2: Combined analysis of forces and focal adhesion maturation. (A) Cell cycle–dependent variation of traction forces transmitted to the substrate in fixed samples. $^*p < 0.05$, $^{***}p < 0.001$, $^{****}p < 0.0001$. n = number of cells and n' = number of independent experiments. (B) Basal distribution of total (green) and phosphorylated (red) paxillin signals obtained from immunostaining. (C) Corresponding map of actuating stresses (top panel). Magnification of the cell periphery (bottom panel), including a group of individual focal adhesions. Green area outlines the total paxillin profile, and gray area outlines phosphorylated paxillin regions.

the G1 phase than for FAs of the same size detected in later phases of the cell cycle (Figure 4.3, A and B). Both the sizes of individual FAs and the corresponding phospho-pax levels were proportional to the amount of force exerted locally on the substrate (Figure 4.3, C and D). Yet the correlation slope was significantly steeper for cells in the G1 and early S phases. Thus, in the S/G2 phase, individual FAs of the same size exerted relatively less force.

Previous work has shown that the density of stresses is dependent on the shape of the cell and the location of focal adhesions[233,234]. Here, the specific biochemical inhibition of FAK activity (Figure 4.4A) greatly reduced the levels of paxillin phosphorylation detected at individual FAs and in all cell cycle phases (Supplemental Figure C.8). However, it did not perturb the overall size and number of integrin contacts (Supplemental Figure C.9). Consistently, the av-

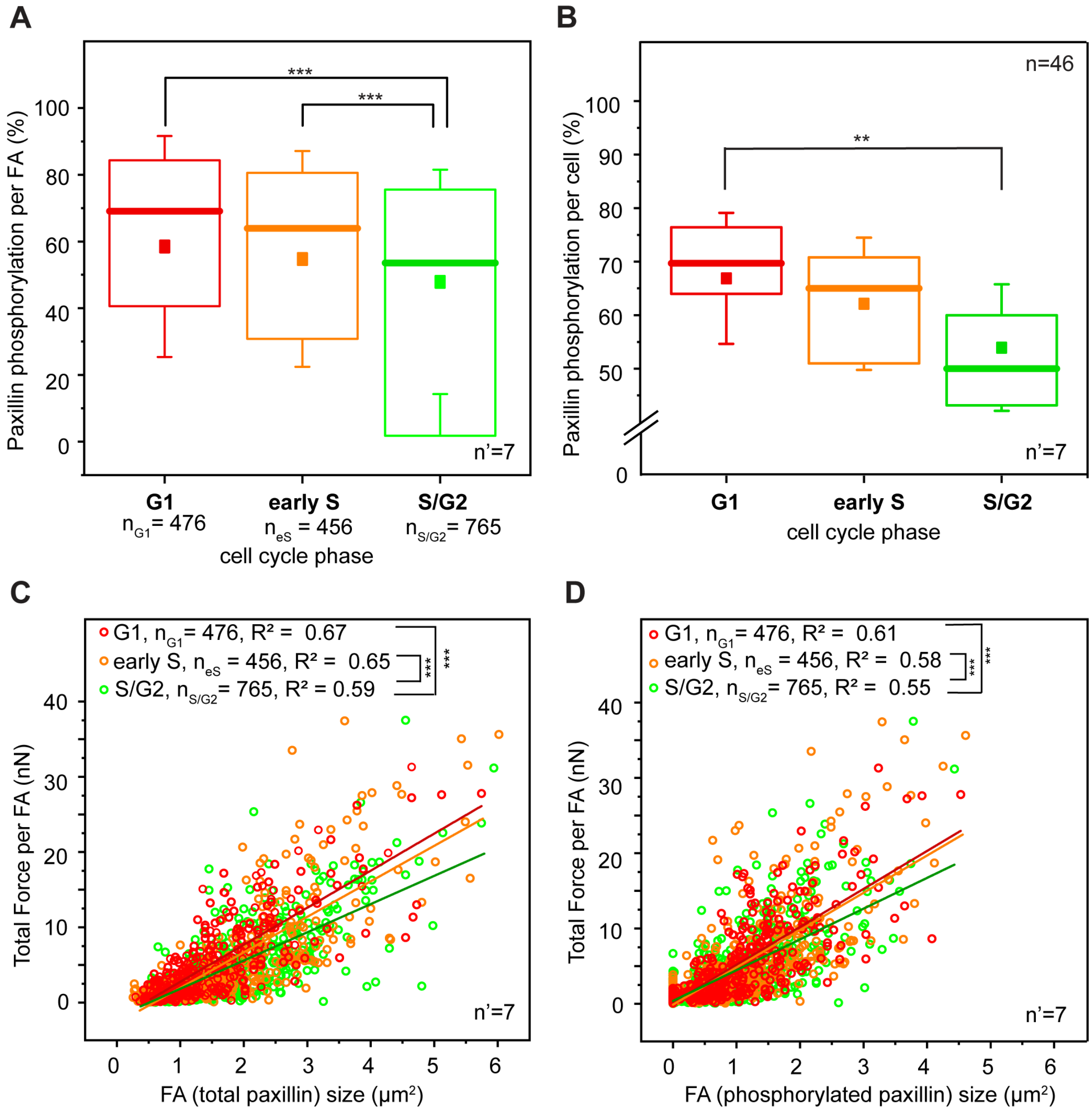

Figure 4.3: Paxillin phosphorylation and force transmission. (A) Cell cycle–dependent variation of paxillin phosphorylation at focal adhesion sites. (B) Global variation of paxillin phosphorylation during the cell cycle progression of HeLa Fucci2 cells. $^{**}p < 0.01$, $^{***}p < 0.001$. Correlation between force transmitted by individual focal adhesions and corresponding total focal adhesion size (C) and size of phosphorylated paxillin signal (D). Red, yellow, and green dots represent individual focal adhesions detected in G1, early S, and S/G2 cells, respectively. Lines of corresponding colors represent the linear fit to each data set. For panels A, C, and D, n = number of individual focal adhesions from seven independent experiments. For panel B, n = number of cells and n' = number of independent experiments.

erage tractions transmitted to the substrate dropped significantly in all analysed cells (Figure 4.4B). To further demonstrate that paxillin phosphorylation is necessary for the modulation of force transmission to the substrate during the cell cycle, the force analysis was extended to HeLa Fucci2 cells transfected with wild type (WT) and with nonphosphorylatable (Y2F) or phosphomimetic (Y2E) paxillin mutants[226]. Cells expressing either paxillin mutant displayed decreased average traction (as compared with the WT control) in the G1 phase. Moreover, Y2F mutants exhibited a reduction of average traction in the early S phase, while Y2E mutants exhibited a reduction in the S/G2 (Figure 4.4C). Altogether, these data indicate that the mechanical maturation of integrin contacts is supported by FAK-mediated paxillin phosphorylation regulating FA turnover. This process culminates in the G1 phase, thus colocalizing in space and time with higher transmission of actomyosin-mediated contractility.

To assess whether the cell cycle–dependent variation of force transmission to the substrate is a feature of epithelial cancer cells beyond the type already examined, we extended our analysis to highly metastatic human breast cancer cells MCF-7 and their tamoxifen- resistant (TamR) offspring (MCF-7 TamR; Figure 4.5). Tamoxifen is a widely used drug in chemotherapies against hormone-dependent breast carcinoma[235]. The molecule interacts competitively with the estrogen receptors on cancer cells, thereby blocking the estrogen activity[236]. Lack of estrogen stimulation halts cell cycle progression and directs cells toward apoptosis.

Interestingly, tamoxifen treatment arrests WT MCF-7 cells in G1[237]. TamR MCF-7 cells are insensitive to the abovementioned effects of the drug. In addition, they are characterized by dysregulated cell cycle progression and apoptotic pathway, which contribute to their survival under long-term tamoxifen treatment[217].

WT and TamR MCF-7 stably transfected with the Fucci2 sensor were generated by viral infection (see Materials and Methods). The introduction of the Fucci sensor did not affect the cell cycle duration of either cell type (Figure 4.5A). When compared, the two cancer strains displayed a significantly different cell cycle dynamic (Figure 4.5, A and B). In the absence of tamoxifen treatment, WT MCF-7 were characterized by faster proliferation (average cell cycle duration 27.3 and 32 h for MCF-7 WT and TamR, respectively; Figure 4.5A). In particular, WT cells lingered relatively longer in G1 and showed reduced permanence in all other cell cycle phases (Figure 4.5B). This observation indicates a delayed progression from the G1 to the S phase, consistent with the previously reported proliferative anomalies[238].

We aimed at investigating the dosage-dependent effect of tamoxifen (4-hydroxytamoxifen on ethanol vehicle) treatment on the Fucci transfected MCF7 strains, by means of live microscopy for a total period of 84 h. As expected[238,239]), the two strains had different responses to the drug (Supplemental Figure C.1). Treatment with a 5-μM dosage of 4-hydroxytamoxifen induced the apoptosis of WT MCF7, while the TamR population remained stable. In both strains, upon treatment with the drug, surviving cells accumulated in the G1 phase of the cell cycle. A dosage increase to 10 μM caused faster apoptosis in the WT population, while no significant change was detected in TamRcells. Again, in both strains, the remaining cells

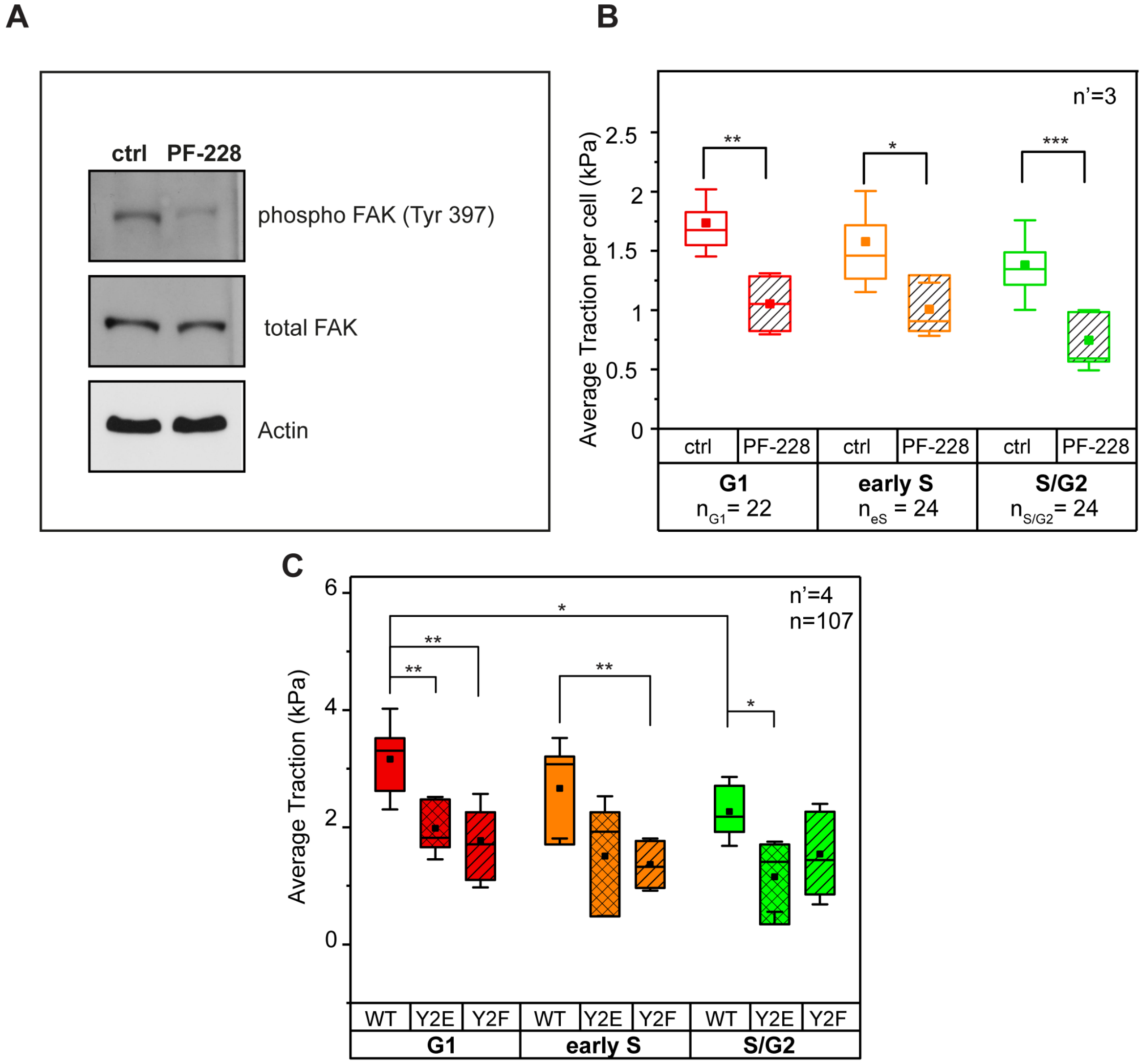

Figure 4.4: FAK activity and regulation of tractions. (A) Biochemical inhibition of FAK activity and (B) resulting phasedependent reduction of traction. (C) Average traction in phosphomimetic (Y2E) and nonphosphorylatable (Y2F) paxillin mutants. n = number of cells and n' = number of independent experiments. *p <0.05, **p <0.01, ***p <0.001.

mostly populated the G1 phase.Finally, a dose of 20 μM of 4-hydroxytamoxifen was cytotoxic for both strains, with rapid cell death starting after 1 d of exposure.

In both strains, the phase-resolved profiles of forces transmitted to the cTFM were obtained from complete cell cycle analyses of individual cells (Figure 4.6). The resulting trends reproduced the phasedependent dynamics measured for HeLa Fucci2 cells (Figure 1). In particular, the absolute total force peaked in the G1 and early S phases for the WT (Figure 4.6, A and

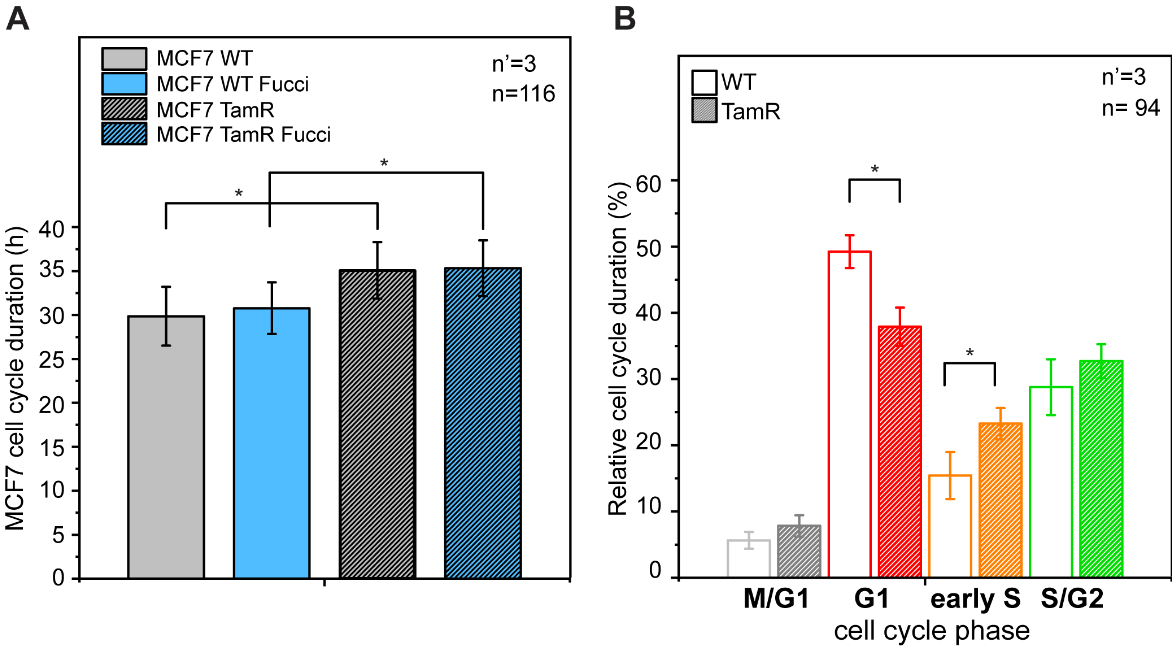

Figure 4.5: Proliferation dynamics in WT and tamoxifen-resistant MCF-7 cells. (A) Average duration of cell cycle in WT and tamoxifen-resistant (TamR) MCF-7 cells. (B) Relative duration of each cell cycle phase. *p <0.05. n = number of cells and n' = number of independent experiments.

D). A significant drop in force transmitted in the late S/G2 phase was detected both in WT MCF-7 and in TamR cells. Effects of traction upon cell cycle progression were obtained by integrating the corresponding cell spreading dynamics (Figure 4.6, C and F) and confirmed the presence of a peak in G1 for both cell strains. Altogether, these data contribute to establishing the presence of a periodic variation of traction forces exerted by cancer cells on the substrate during their proliferative cycles. In addition, they individuate the G1 phase as the most mechanically intense, during which the cells are able to impart the highest levels of force at the interface with the surrounding extracellular environment.

To assess whether this finding is linked to a specific phenotype in MCF-7 cells, we performed two independent evaluations of cell invasiveness. The Boyden chamber assay (Figure 4.7A; [240]) revealed a more efficient pervasive invasion of TamR MCF-7 cells than of the WT population. This difference was further increased by the addition of 10 μM of tamoxifen. The drug treatment almost completely ablated the pervasive invasion of WT cells while showing a minor effect on the invasion of the resistant counterpart. In addition, a 2D invasion assay was performed to evaluate cell migration within a dense array of vertical obstacles generating narrow constrictions[241]. The patterned area was planar and conducive to live-cell microscopy, thus allowing the detection of pervasive migration and the concomitant resolution of the cell cycle phase (Figure 4.7, B–E). Directional movements were pronounced in the G1 phase in

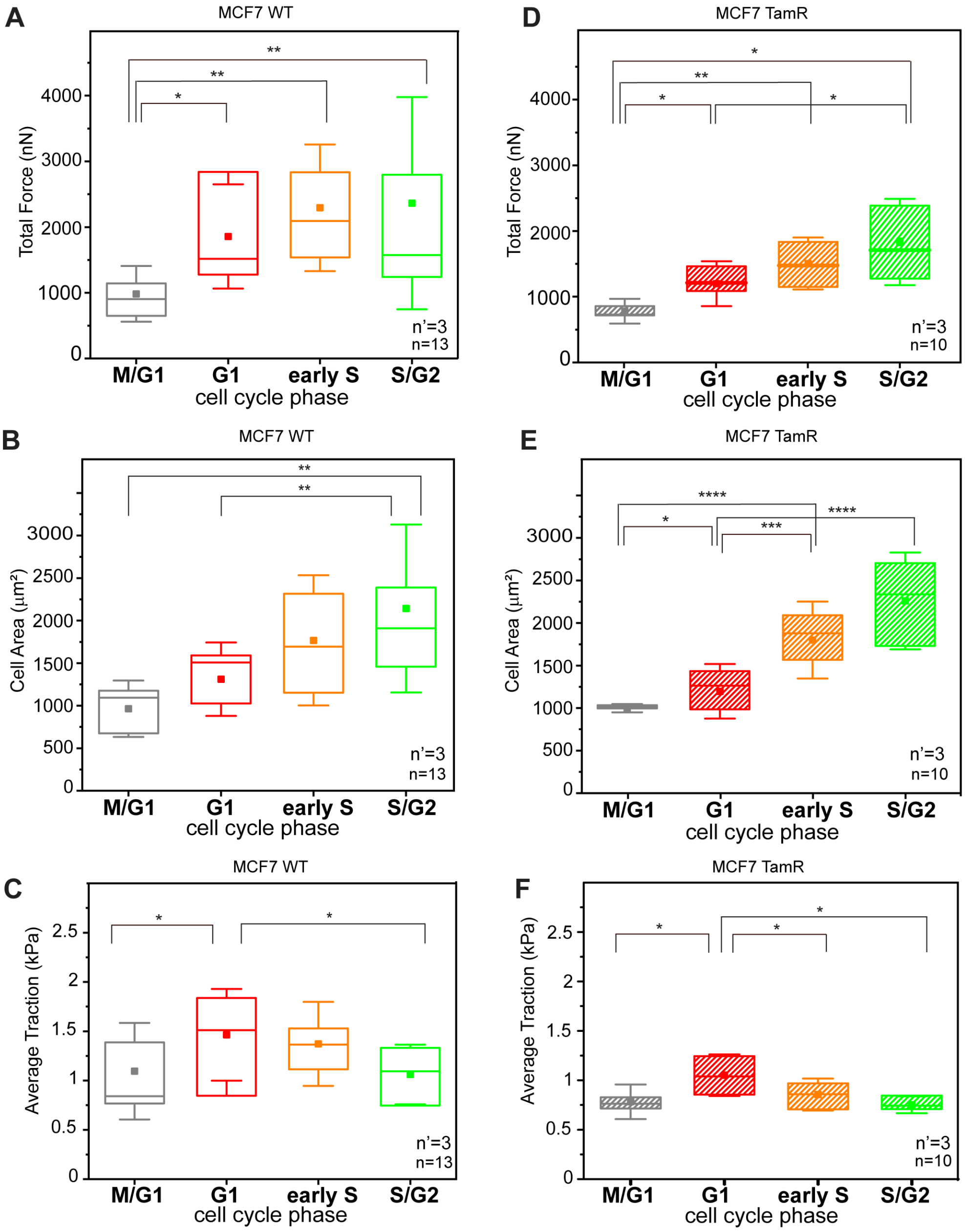

Figure 4.6: Cell cycle–dependent force transmission in MCF-7 cells. (A, D) Phase-resolved dynamics of absolute forces during cell cycle progression for WT (A) and TamR (D) MCF-7 cells, respectively. (B, E) Corresponding dynamics of cell spreading over the cell cycle. (C, F) Tractions transmitted to the substrate during individual cell cycles for WT (left) and TamR cells (right), respectively. $^{*}p < 0.05$, $^{**}p < 0.01$, $^{***}p < 0.001$, $^{****}p < 0.0001$. n = number of cells from four independent experiments per cell line variant and n' = number of independent experiments.

both WT and TamR MCF-7 cells, yielding more efficient advance in the dense array of vertical obstacles in this phase of the cell cycle. Enhanced invasiveness in G1 was also measured upon treatment with tamoxifen, which induced, however, an overall reduction of cell motility.

In summary, the results presented here demonstrate a significant, periodic variation of tractions transmitted to the substrate by proliferating cancer cells. Force transmission in correspondence with integrin contacts is low immediately after division, a phase in which focal adhesions are not yet fully reassembled. A rapid increase in transmitted forces is detected in the G1 and early S phases. The mechanical activity of cells changes trend in the S/G2 phase, during which transmitted forces are reduced. These measurements obtained on different strains of human epithelial cancer are in line with what reported for nontransformed epithelial cells from the human retina (RPE-1; [242]), indicating that this pattern of mechanical activity may be a conserved feature beyond the analysed cell types.

It is generally accepted that cell-generated tractions increase with cell spreading. Therefore, cells with a larger surface should transmit more force to the substrate. This assumption is confirmed by the correlative analysis of individual cells over the entire cell cycle. However, the correlation is not linear, as the two cellular activities, force transmission and spreading, follow different dynamics. In fact, the density of transmitted forces is maximal in G1. During this phase, cancer cells are able to exert tractions concentrated on a limited surface, a behavior that may be conducive to higher efficiency in the penetration of complex environments requiring a major deformation of the cell nucleus[212,243–245].

Finally, the use of a recently developed reference-free approach[150] to monitor the mechanical activity of cells during their progression in the cell cycle offered the possibility of investigating the role of focal adhesion maturation. The involvement of FAK-mediated paxillin phosphorylation is supported by the direct spatial and temporal covariance between the protein activity and the local variation of traction forces transmitted to the substrate. Using this experimental framework, future analysis may reveal the full mechanism linking cell migration, proliferation, and force transmission.

4.3 Materials and Methods

4.3.1 Confocal traction force microscopy

Substrate traction was measured using cTFM substrates with redemitting QDs with an interdisc spacing of 2 μm[150]. After being coated with fibronectin, adhering cells generated deformations of the substrate, which were captured as distortions of the fluorescent nanodisc array. The subpixel detection of the QD nanodisc center was followed by computational reconstruction of the triangular mesh. From the displacement field, the surface tractions were reconstructed using FEA, as previously reported[150].

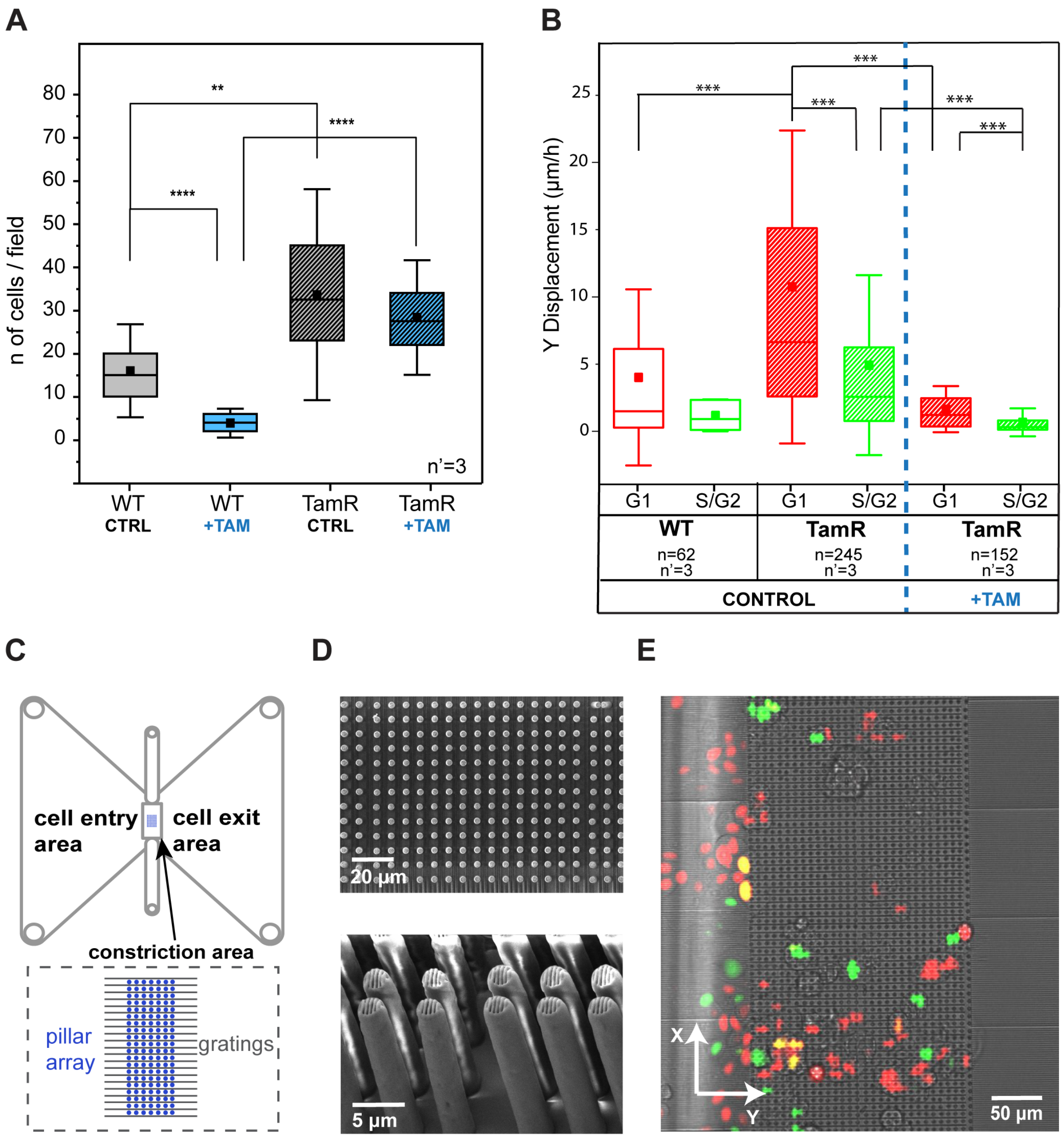

Figure 4.7: Migratory and invasive phenotypes of MCF7-WT and MCF7-TamR cells. (A) Comparison of invasion capacity of WT and TamR MCF-7 cells, with and without tamoxifen, using a Boyden chamber–based invasion assay. The results come from three independent experiments, each performed in triplicate. **p <0.01, ****p <0.0001. (B) Migratory properties of MCF7-WT and MCF7-TamR cells in a 2D invasion assay. ***p <0.001. n = number of cells and n' = number of independent experiments per condition. (C) Schematic of the device as reported in Corallino et al.[241]. (D) Scanning electron microscope pictures (top panel, top view; bottom panel, side view) of the pillar array. (E) Merged transmission and fluorescent pictures from the live microscopy experiments.

4.3.2 Absolute force per adhesion calculation

The absolute force per adhesion was determined based on three elements: the focal adhesion area (pixels in an image belonging to an individual adhesion), the overall traction forces, and the conversion from pixels to micrometers. To determine the area of the adhesions, a threshold was applied to the paxillin signal as previously reported in[150]. This yielded the positions and sizes of individual adhesions, as well as a list of pixels belonging to each of them. For the calculation of the forces per adhesion, traction forces acquired from the FEA were interpolated onto a quadratic grid corresponding to the pixels in the paxillin image. For each pixel, the Euclidean norm of the traction was calculated. Based on the adopted magnification and the pixel size of the microscope camera, the actual pixel's size (in micrometers) was defined. Finally, traction magnitudes multiplied by the area of one pixel were summed for all the pixels within the adhesion area to compute the absolute force per adhesion.

4.3.3 Cell lines and culture conditions

MCF-7 WT and tamoxifen-resistant cells, a kind gift of Stefan Wiemann (German Cancer Research Center, Heidelberg, Germany), have been extensively characterized previously[218,238,246]. HeLa Fucci2 cells stably expressing a Fucci construct[142] were purchased from Riken Bioresource Center (Japan) and previously characterized[212].

MCF7 and MCF7-TamR cells expressing the Fucci reporter system were obtained by lentiviral infection of mKO2-hCdt1(30/120) and mAG-hGem (1/110) probes[142]. HeLa cells were maintained in DMEM (Sigma-Aldrich, St. Louis, MO) supplemented with 100 U/ml penicillin, 100 μg/ml streptomycin, and 10% fetal bovine serum (FBS) at 37°C under a 5% CO_2 humidified atmosphere. WT and TamR MCF-7 cells were maintained in DMEM phenol red free medium (Sigma-Aldrich, St. Louis, MO) supplemented with 100 U/ml penicillin, 100 μg/ml streptomycin, and 10% FBS at 37°C under a 5% CO_2 humidified atmosphere. Cells were routinely analysed by reverse transcriptase-PCR for mycoplasm contamination.

4.3.4 Lentiviral production and infection

HEK293T packaging cells (1 × 106) in a 10-cm (diameter) dish were transfected with equimolar ratios of pMD2, psPAX2 (Invitrogen), and Fucci expression vectors. Transfection was performed with LipofectAMINE 3000 (Invitrogen) in OPTIMEM in accordance with the manufacturer's instructions. After transfection, cells were incubated for 18 h, and then the medium containing the transfection reagent has been removed and replaced with fresh culture medium. After 24 h, culture medium containing lentiviral particles was collected and passed through a 0.45-μm filter, 8 μg/ml polybrene was added, and the culture was immediately used to infect the target cells.

4.3.5 Live microscopy

Cell cycle movies were acquired using an inverted Nikon-Ti widefield microscope (Nikon, Japan) equipped with an Orca R-2 CCD camera (Hamamatsu Photonics, Japan) or a Nikon-Ti spinning disk confocal microscope (Nikon, Japan) equipped with an Andor DU-888 camera (Oxford Instruments, United Kingdom), both with an incubation chamber (Life Imaging Services, Switzerland) to control temperature, CO_2, and humidity. Images were collected using a 40× objective (Plan Fluor 40× Oil DIC H N2). Multiple nonoverlapping fields capturing all positions with quantum dots were recorded in parallel ($\Delta T = 1$ h, total duration ~30 h for HeLa Fucci and ~48 h for MCF7).

At each time of measurement, a transmission and two fluorescent images of the nuclei of the cells were acquired using differential interference contrast (DIC), an FITC (fluorescein isothiocyanate) filter set, and a TRITC (tetramethylrhodamine isothiocyanate) filter set. Focal drift during the experiments was avoided using the autofocus system of the microscope.

For the analysis of the effect of tamoxifen on the phase partition and viability of the cells, cells were seeded in the presence of 4-hydroxytamoxifen in ethanol solvent (Sigma-Aldrich, St Louis, MO) or ethanol solvent control.

4.3.6 Image analysis

Cell cycle duration was quantified as the time between birth and division of the same randomly chosen cell. The cell cycle phase of Fucci2 transfected cells was determined from the ratio of the absolute intensities of red and green fluorescence of the nucleus. Absolute intensities were calculated by subtracting the intensity of the background from the relative intensity of the nucleus, both measured in ImageJ. Transparent cells (M/G1) were distinguished from the rest of the population because their relative intensity was equal to that of the background.

For the quantification of cell adhesions during the cell cycle, cells were seeded on cTFM substrates, incubated overnight (O/N), and stained for paxillin and phosphorylated paxillin (see Immunofluorescence).

Fluorescent Z-stacks of the signals emitted by the focal adhesions ($\Delta z = 0.3 \mu m$) were collected using a Nikon-Ti spinning disk confocal microscope (Nikon, Japan) equipped with an Andor DU-888 camera (Oxford Instruments, United Kingdom). Focal adhesions (total paxillin) were quantified as described in the paper by Horzum et al.[192]. After the regions of interest (ROIs) of all adhesions were registered, the phosphorylation amount per adhesion was calculated by dividing the area of the total paxillin ROI of each adhesion site by the area of the phosphorylated paxillin ROI. A designated Matlab script was used to colocalize the ROIs of total and phosphorylated paxillin that belonged to the same adhesion site by comparing their centroid coordinates.

4.3.7 Immunofluorescence

Cells were fixed with 4% paraformaldehyde in phosphate-buffered saline (PBS) for 10 min at room temperature (RT) and permeabilized via incubation in 3% paraformaldehyde with 0.1% Triton in PBS for 5 min. After being blocked with 5% bovine serum albumin (BSA) in PBS for 2 h, samples were incubated at 4°C O/N with monoclonal primary antibodies.

The following commercial antibodies were used: mouse antipaxillin, BD Bioscience (#610051), dilution: 1:200[247] and rabbit anti-paxillin Tyr118, Cell Signaling (#2541S), dilution: 1:200[231]. Secondary antibodies Alexa Fluor 647 chicken anti-rabbit (LifeTechnologies #A-21443) or DyLight 405 donkey anti-mouse (Javkson Immunofluorescence) were used at 1:200 for 1 h at RT.

4.3.8 FAK inhibition

HeLa cells were treated O/N with 10 μM of FAK inhibitor PF-573228 ([248]; SIGMA Aldrich) diluted in dimethyl sulfoxide (DMSO). The control samples were incubated with the same amount of DMSO. After the treatments, cells were immediately processed for immunofluorescence and Western blotting analyses.

4.3.9 Plasmids and transfection

YFP-paxillin WT and two YFP-phosphorylation mutants, in which both tyrosine 31 and 118 were replaced either by glutamic acid (Y2E, phosphomimetic) or by phenylalanine (Y2F, nonphosphorylatable), were a generous gift of Benjamin Geiger (Weizmann Institute of Science; [226]). Transfection was performed using Lipofectamine 3000 (Invitrogen) in accordance with manufacturer's instructions and transfected cells were selected with 800 μg/ml G418.

4.3.10 Invasion assay

The invasive potential was tested using Transwell chambers (pore size 8 μm; Corning, Corning, NY) precoated with fibronectin (100 μg/ml; Sigma-Aldrich). Briefly, MFC7 WT and MCF7 TamR cells (5 × 104 cells/well) in 100 μl of serum-free DMEM were placed in the upper chamber, and 600 μl of culture medium containing 10% FBS was added to the lower chambers as a chemoattractant, in the presence or absence of tamoxifen (10 μM). After being incubated for 24 h, the cells remaining on the upper membrane were carefully wiped off with cotton swabs, while the cells that had invaded through the membrane were fixed in 4% paraformaldehyde and stained with 4',6-diamidino-2-phenylindole (DAPI). The stained cells were imaged and counted from five random visual fields/experiment. For the experiments with tamoxifen, 10 μM tamoxifen was added 24 h prior to starting.

4.3.11 Cell migration through the pillar array

The array of pillars was fabricated with two-photon polymerization on glass substrates, as previously reported in Corallino et al.[241]. The structure consisted of two components: a dense micropillar array and gratings with ridges of depth 1 μm and width 1 μm. The structure components were designed using CAD software (Autodesk Inventor, Autodesk). The interpillar distance was set to 2.5 μm after parametric testing of various dimensions to ensure the mechanical constriction of the cells during their migration through the array. The pillar thickness was set to 2.5 μm to provide the necessary mechanical stability to the structure. The structural elements of the pillars and barriers (mesh slicing and hatching) and the printing parameters of the whole structure (laser power, scan speed) were designed with the program DeScribe v.2.4.4 (Nanoscribe GmbH), which creates a file readable by the laser lithography system. The sample fabrication was completed with a 3D laser lithography system (Photonic Professional GT, Nanoscribe GmbH, Germany) used in conventional oil-immersion mode. This involved passing a two-photon laser (780-nm laser, laser power 12.5 mW, scan speed 800 μm/s) from a ×63 objective lens through a layer of oil beneath the glass substrate, polymerizing the photoresist on the top side of the glass substrate. The photoresist chosen was a biocompatible organic–inorganic hybrid polymer (Ormocomp, MicroResist Technology GmbH). The resist was drop-cast on the glass substrates and prebaked at 80°C for 2 min. After laser writing, the resist was baked at 130°C for 10 min, developed in OrmoDev developer (MicroResist Technology GmbH) for 10 min to remove the unpolymerized resist, and rinsed in isopropanol (IPA), followed by drying in a critical point dryer (Automegasamdri R 915B, Tousimis).

The glass substrate with the microstructures printed on top was attached on the self-adhesive underside of a commercially available microfluidic chamber (sticky-Slide Chemotaxis, Ibidi), with the micropillar array placed in the middle area. The chamber was filled with 70% ethanol for 1 h for sterilization and washed three times with 1× PBS for 5 min, and substrates were coated with 0.01% poly-llysine (PLL; Sigma) according to the manufacturer's specification. Afterward, poly-l-lysine was gradually replaced with 1× PBS and finally with cell medium. Cells (104) were seeded from the inlets of the cell pool area (Figure 4.7C) and were gently distributed over the cell pool area, with attention that they did not float over the pillars. The chambers were incubated O/N at 37°C and once the cells were spread, cell motion was recorded using a Nikon-Ti spinning disk confocal microscope (Nikon, Japan) equipped with an Andor DU-888 camera (Oxford Instruments, United Kingdom) with a 20× objective over a 40 -h period, with pictures taken every 30 min. All the assays were performed using an environmental microscope incubator set to 37°C and 5% CO_2 perfusion. For the experiments with tamoxifen,10 μM tamoxifen (4-hydroxytamoxifen on ethanol vehicle) was added 24 h prior to imaging.

The velocity of the cells was quantified using the particle tracking algorithm of Imaris (Bitplane Scientific Software, Switzerland). Timelapse videos were uploaded into Imaris, and the voxel size and time interval were adjusted before particle tracking.

For the quantification, the component of the velocity that was parallel to the gratings and perpendicular to the pillar forest was taken.

4.3.12 Western blotting

Total proteins were extracted by solubilizing HeLa cells in boiling Laemmli buffer (2.5% SDS and 0.125 M Tris-HCl, pH 6.8). Lysates were incubated for 5 min at 100°C to allow protein denaturation and then spun for 5 min at 13,200 rpm to discard cell debris. Supernatants were collected and the concentration of proteins was determined using a BCA Protein Assay Kit (Pierce) according to manufacturer's instructions. An equal amount of proteins (30 μg) was loaded on gel and separated by SDS–PAGE, transferred to a Protran nitrocellulose hybridization transfer membrane (pore size 0.2 μm; Whatman), and blocked for 1 h at RT in 1X TBST (150 mM NaCl, 10 mM Tris-HCl, pH 7.4, and 0.05% Tween)–5% BSA. The membranes were incubated O/N at 4°C with primary antibodies diluted in 1× TBST–5% BSA.

The following primary antibodies were used: FAK (Rb polyclonal 1:1000, 3285S Cell Signaling;[213]) and p-FAK Y397 (Rb polyclonal 1:1000, 3283S Cell Signaling;[213]). Next, they were rinsed three times with 1× TBST for 5 min each and incubated for 1 h at RT with horseradish peroxidase–linked secondaryantibodies (diluted in 1× TBST–5% BSA). Membranes were rinsed three times with TBST for 5 min each, and specific binding was detected by an enhanced chemiluminescence (ECL) system (Amersham Biosciences) using Hyperfilm (Amersham Biosciences). The molecular masses of proteins were estimated relative to the electrophoretic mobility of the cotransferred prestained protein marker Broad Range (Cell Signaling Technology).

4.3.13 Statistical analysis

Boxes in all box plots extend from the 25th to the 75th percentile, with a line at the median and a square representing the mean. Whiskers extend to the SD of the data. Data were analysed, tested for statistical significance, fitted, and visualized using Origin or Matlab (The MathWorks). The total number of recorded events from three or more independent experiments is shown in the top or bottom right-hand corners of the presented graphs. The Shapiro–Wilk test was used to test for normality of data. For nonnormal distributed data, a nonparametric Kolmogorov–Smirnov test was performed ($\alpha = 0.05$). Significant differences between slopes included in Figure 4.3 were calculated using the Akaike information criterion and F-test analysis.

5 Endocytic Reawakening of Motility in Jammed Epithelia

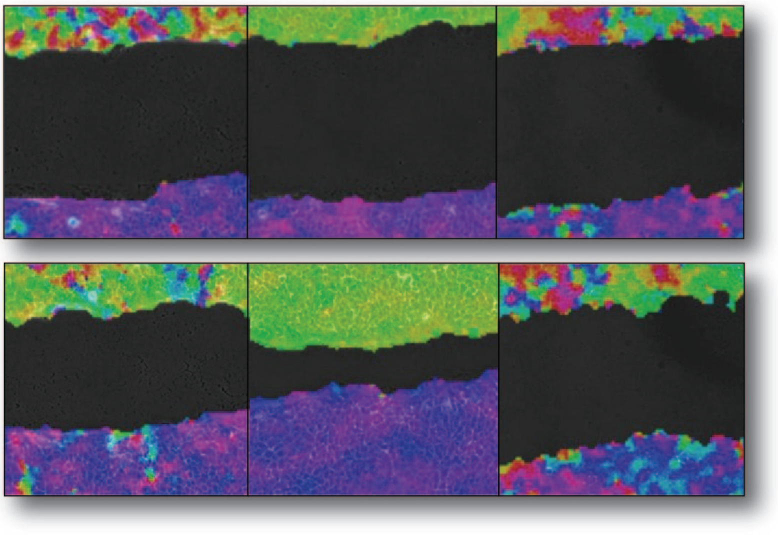

Parts of this chapter are published in: C. Malinverno, S. Corallino, F. Giavazzi, M. Bergert, Q. Li, M. Leoni, A. Disanza, E. Frittoli, A. Oldani, E. Martini, T. Lendenmann, G. Deflorian, G. V. Beznoussenko, D. Poulikakos, K. Haur Ong, M. Uroz, X. Trepat, D. Parazzoli, P. Maiuri, W. Yu, A. Ferrari, R. Cerbino & G. Scita, "Endocytic reawakening of motility in jammed epithelia", *Nature Materials* volume 16 (2017), 587. [249]

Contribution

I was partially involved in this project. Only what I worked on is displayed in this thesis. For the full content check Malinverno, et al. (2017). My work involved the investigation of traction forces and migration for the jammed and unjammed states of epithelial MCF-10A monolayers. This resulted in traction maps and collective migration correlation lengths for both states.

5.1 Introduction

Collective cell migration is essential for tissue morphogenesis during development and repair, and also for tumour dissemination[149]. Most aspects of multicellular migration are ruled by the physical interactions that cells establish among each other and with their environment. For example, during collective migration within confluent monolayers, cell sheets flow like a fluid yet remain fixed and solid-like at short timescales, with the motion of each cell constrained by the cell crowding due to its neighbours[146,250,251]. As cell density rises, neighbouring cells restrict the motion of each cell, forcing them to move in groups, surprisingly similar to what is observed in systems of inert particles that undergo a jamming or rigidity transition at large density[146,148,252,253]. However, while the transition in inert systems invariably occurs at a critical particle packing ϕ_c[254], epithelial monolayers display limited density fluctuations. Therefore, material parameters that encode cell properties such as cell–cell adhesion and cortical tension, rather than density alone, have been proposed to govern the rigidity transition in cell monolayers[252,253,255–257]. However, the general validity of this theoretical framework remains to be investigated. Even less understood are the molecular determinants and cellular processes that regulate multicellular dynamics by impacting on physical properties.

A cellular process that influences cellular and multicellular motility strategies is membrane trafficking[258,259]. Here, we report that perturbation of endocytosis by altering the levels of its master regulator RAB5A[260,261] is sufficient to reawaken the motility of jammed epithelial monolayers. RAB5A causes large, anisotropic and spatially correlated motility streams by globally enhancing endosomal trafficking and macropinocytic internalization. These variations impact on junctional tension, topology and dynamics of junctional proteins, facilitating coherent cell motion over long distances. RAB5A further promotes the extension of protrusions aligned to the local velocity of migratory cohorts. RAB5A-induced reawakening of motility is associated with a growing length scale, precluding an understanding of monolayer dynamics simply in terms of an increase in local rearrangements. A self-propelled Voronoi model that includes an active cell reorientation mechanism accounts for RAB5A-induced multicellular dynamics. The model identifies a motility regime that we define as flowing liquid, where local and long-range collective motility coexist. As a consequence of these emerging material properties, RAB5A monolayers are not only efficient in directed locomotion during wound closure or epiboly gastrulation movement in zebrafish development, but also display a high degree of plasticity that allows them to migrate under physical constraints typical of interstitial tissues architecture. These properties may be exploited in tumorigenic settings to escape the intrinsic motility-suppressive environment of jammed epithelial tissues.

5.2 Results

5.2.1 RAB5A promotes coherent and ballistic collective motility.

To test the role of endocytic tracking on collective epithelial locomotion, we perturbed the levels of RAB5A by generating doxycycline-inducible, RAB5A-expressing populations of human mammary epithelial MCF-10A cells. These cells form polarized monolayers and, upon reaching confluence, display a typical collective locomotion mode characterized by the emergence of large-scale, coordinated motility streams, involving tens of cells. As cells keep on dividing, density increases, causing a near complete kinetic arrest akin to a jamming or rigidity transition[252,262]. Unexpectedly, under these latter conditions, elevation of RAB5A reawakened motility of kinetically arrested monolayer by promoting large and heterogeneous multicellular streams (Figure 5.1b). RAB5A expression had marginal effects on the rate of cell division of confluent monolayers, and collective motility was unperturbed by inhibition of cell division. Finally, RAB5A expression did not alter the migration of individual MCF-10A cells in random migration assays (Figure 5.1a). Thus, RAB5A effects on motility are emergent properties of cell collectives that elicit reawakening of locomotion of kinetically arrested, jammed epithelia.

Collective locomotion depends on complex cell-cell interactions and communication occurring during the migration of epithelial sheets[263]. To characterize the phenotype induced by RAB5A in MCF-10A cells, we analysed movies by cell image velocimetry (CIV)[264] and particle image velocimetry (PIV)[265], focusing on the time window where the full availability of soluble epidermal growth factor (EGF) enables locomotion. We found that RAB5A expression robustly enhances cell coordination (Figure 5.1b). A simple indicator of the collective nature of cell motion is obtained by calculating the velocity correlation length L_{corr} as the width of the correlation function $C_{VV}(r) = (\langle\langle(x_0 + r) \cdot v(x_0)\rangle\rangle)/\langle\|v(x_0)\|^2\rangle$ of the (vectorial) velocity $v(x0)$. We observe a 20-fold increase of L_{corr} from $55 \pm 5\mu m$ (control) to $1.1 \pm 0.3mm$ (RAB5A), which corresponds to about 50 cell diameters (Figure 5.1c).

5.2.2 RAB5A induces polarized cell protrusions and traction forces.

One striking feature of RAB5A-induced large-scale streaming flows is their persistent and ballistic motility, suggesting that individual cells must efficiently orient their motion with the local direction of migration. Actin-based, polarized protrusions are a proxy of cell-oriented locomotion. In monolayers, these protrusions extend underneath neighbouring cells and are called cryptic lamellipodia. By monitoring the dynamics of EGFP-LifeAct-expressing cells

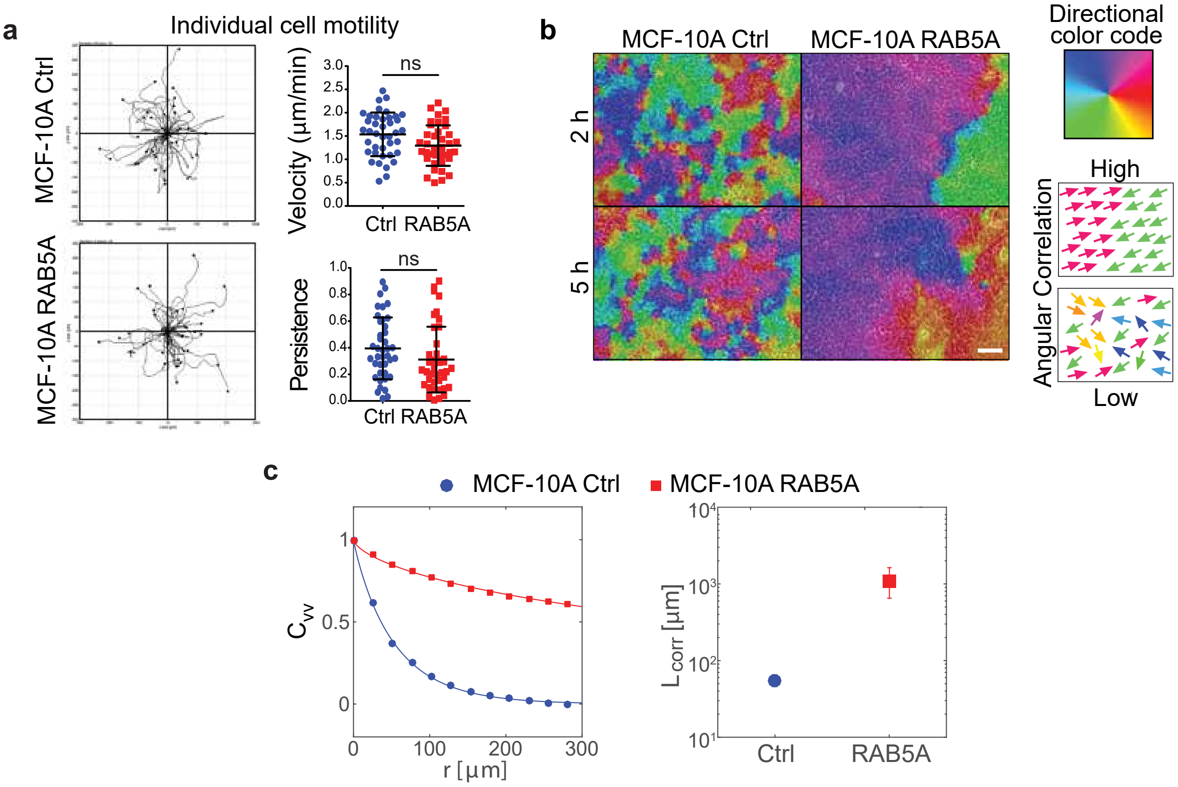

Figure 5.1: RAB5A promotes coherent, ballistic motion of jammed epithelia. **(a)**, Left plots: migration paths of control and RAB5A-MCF-10A cells seeded sparsely to monitor individual cell motility and analysed using the Chemotaxis Tool ImageJ software plugin. Right plots: velocity and persistence of the locomotion of cells. Data are the mean ± s.d. (n = 40 single cells/experiment/genotype of three independent experiments); NS, not significant. **(b)**, Snapshots depicting the angular velocity of control and RAB5A-MCF-10A cells seeded at jamming density and monitored by time-lapse microscopy. Angular velocity vectors are calculated by CIV analysis. The colour code indicates the direction of migration. Homogeneous and inhomogeneous scattered colours indicate regions with high and low migration coherence, respectively. Scale bar, 100 μm. Representative images from nD5 time-lapse series. **(c)**, PIV analysis of motion of doxycycline-treated control and RAB5A-MCF-10A cells seeded at jamming density. Left: velocity correlation functions C_{VV} evaluated in the time window comprised between 4 and 12 h during which the availability of EGF allows migration. The continuous lines are best fits of C_{VV} with a stretched exponential function. Right: correlation lengths L_{corr} (five movies/experimental condition out of three to eight independent experiments).

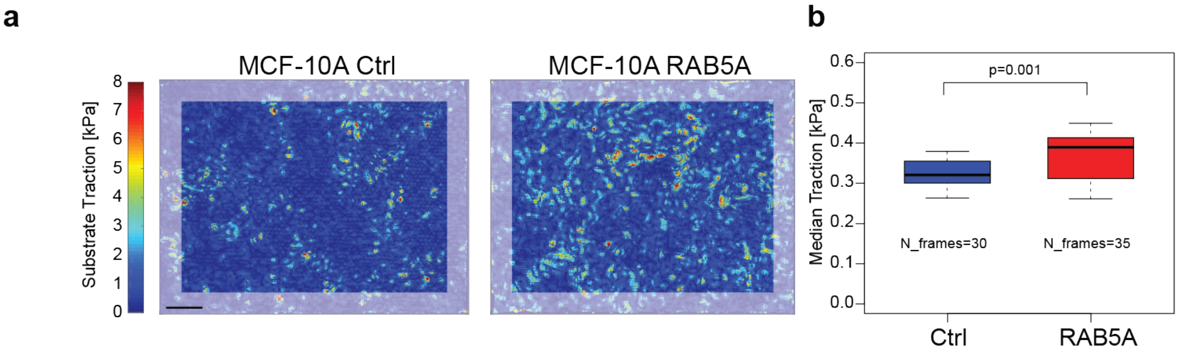

Figure 5.2: RAB5A promotes polarized cell protrusions and traction forces. **(a)**, Left images: substrate tractions of control and RAB5A monolayers measured using cTFM[150]. Grey frames correspond to areas excluded from analysis due to boundary effects. Scale bars, 25 μm. **(b)** the median traction analysed from n time points, obtained from five to six fields of view out of two independent experiments. p-value calculated with Mann–Whitney-U-Test.

interspersed with non-fluorescent cells, we detected, only in RAB5A monolayers, the formation of cryptic lamellipodia oriented along the motility direction of supra-cellular motility streams. RAB5A-induced cryptic lamellipodia are RAC1-dependent, consistent with the role of RAB5A endo/exocytic cycles in spatially restricting RAC1 signalling for protrusions extension[266]. Indeed, a pharmacological inhibitor of RAC1 activation reduced cryptic lamellipodia formation, and impaired the motility of RAB5A monolayers.

These findings indicate that RAB5A monolayers might exert large traction forces on the substrate during locomotion. To directly assess this possibility, we measured surface tractions of control and RAB5A monolayers using a novel confocal reference-free traction force microscopy (cTFM)[150]. We found that RAB5A monolayers exert significantly higher and more dynamic substrate tractions (Figure 5.2a,b) that moved with the flow tracking velocity fields. We obtained higher traction forces of RAB5A than control monolayers also by measuring the displacements of fluorescent beads embedded into polyacrylamide gel substrates[125].

Thus, RAB5A promotes the extension of aligned cell protrusions in combination with increased and more dynamic substrate tractions, both of which combine to promote monolayer unjamming and collective motility.

5.3 Conclusion

We found that RAB5A controls a diverse set of collective motility processes *in vitro* and *in vivo* by re-awaking the directional, coordinated locomotion of jammed and kinetically arrested monolayers. RAB5A exerts this function by promoting the formation of polarized, actin-based, lamellipodia that generate traction forces, which can be efficiently transmitted at long ranges through enhanced junctional contact and stresses. The increased mechanical coupling also enables a cell to obtain directional guidance cues from their neighbours, forcing adjacent cells to align their front-rear polarity, resulting in a positive feedback between polarity and net displacement. This, combined with increased dynamic of junctional E-cadherin to accommodate for cell neighbouring exchange, volume, density and strain fluctuations, collaboratively enable multicellular entities to acquire a fluid-like character. These alterations appear primarily to be the results of mechanical changes caused by global membrane trafficking perturbations. However, given the inextricable link between endocytosis and signalling, we cannot exclude that amplification and rewiring of specific biochemical pathways, particularly those emanating from EGF receptors, underpins some of the altered mechanical properties—a possibility that is currently under investigation. Importantly, these changes of plasticity promote the motility of otherwise jammed and glassy-like monolayers, leading to invasive, collective migration under physical confinement and accelerated multicellular directed migration during embryonic development.

5.4 Materials and Methods

5.4.1 Cell image velocimetry

Cell image velocimetry (CIV) analysis of monolayer and wound healing time series was performed as previously described[44,264,267]. Overlays of phase-contrast images and coloured migration direction were exported from the software. Uniform colour indicates a homogeneous migration direction, and thus high coherence between cells. Angular correlation during wound healing was quantified for each frame between cells at a distance of 100 μm.

5.4.2 Traction force microscopy

Substrate tractions were measured using cTFM with an interdisc spacing of 3 μm (ref. [150]). During the reference configuration reconstruction step, the position of the outermost quantum dot (QD) nanodiscs plus a region of 2 μm towards the inside was fixed. QD nanodiscs inside this fixed frame were then relaxed to original positions as described in ref. [150]. As the fixed QD nanodiscs themselves are distorted, displacement reconstruction is prone to errors close to the image border. Therefore, final traction analysis was restricted to data originating from an area more than 15 μm from the image border.

Part III

Live Traction Force Microscopy

The cTFM platform described in Chapter 3 advances the capabilities of traditional traction force microscopy. The regularity of the pattern of quantum dot nanodiscs in the undisturbed state enables the computation of a reference image, without having to detach the cells and thus terminate any ongoing experiment. This paves the way for identifying traction forces during live microscopy. Regions of interest can be determined on the fly and imaging be adjusted, for example to a higher frame rate or higher magnification.

Live calculation of continuum traction forces needs a robust and fast implementation of the analysis algorithms. In Chapter 6: "*Cellogram - On-the-fly Traction Force Microscopy*" and Chapter 7: "*Cellogram - Software and Algorithms*" I shall introduce a novel traction force microscopy (TFM) analysis software, which named Cellogram which converges at the pace of data acquisition. It is therefore compatible with the online evaluation of an ongoing experiment.

Using the Cellogram software, TFM images are analysed one to two orders of magnitude faster than with all other available software, and the large majority of images does not require any user interaction. When the method is applied to images generated by reference-free TFM, for example cTFM or micropillars, displacement maps are rendered in seconds. I shall provide evidence that the newly developed pipeline, tackling image processing, reference image estimation, and finite element analysis at once, is sufficiently efficient to buffer data acquisition at 10 images per minute. High-throughput and high-resolution investigations of mechanically driven cellular processes become compatible with the online evaluation of actuating forces. This extraordinary advancement opens to a range of new applications in biology and medicine.

A further application of Cellogram is provided in Chapter 8: "*Bistability of Polar Liquid Crystals in the Collective Adaptation of Endothelia*". Here, I studied endothelial cell monolayers exposed to physiological values of flow-generated wall shear stress. In this experimental set-up, endothelia were grown on cTFM substrates and exposed to laminar flow within a flow chamber yielding physiological (1.4 Pa) or supraphysiological (8 Pa) values of WSS. The high WSS values resemble those experienced by endothelial cells upon stenosis or at the luminal surface of cardiovascular devices. Cell alignment with respect to the flow direction undergoes a binary switch between the two regimes, while polarization remains facing the flow direction. The transitions from the same initial condition to the two perpendicular end points produce strong mechanical deformation energies, which could be measured using cTFM. Simulations which model the cells as polar liquid crystals exposed to an electrical field show good congruence in behavior and free energy during transitions.

6 | Cellogram - On-the-fly Traction Force Microscopy

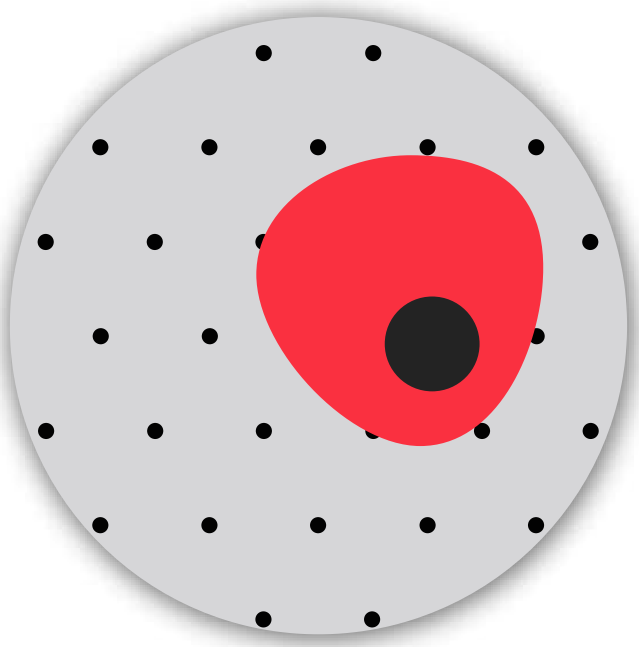

6.1 Introduction

Forces transmitted by mammalian cells to the extracellular environment contribute fundamental signals and actuation mechanisms to complex biological processes, including migration, organogenesis and tissue repair[104,268]. Among cellular forces, actomyosin-generated cell contractility can be estimated by means of optical methods which capture the deformation imposed by cells to the substrate[99]. These experimental approaches have evolved from simple qualitative observations[104] to the current family of traction force microscopy (TFM) protocols yielding force maps with high spatial resolution[114].

Despite these advancements, the accurate measurement of substrate deformations from optical images remains challenging. In particular, classical TFM techniques[114,269] use stochastic patterns generated by randomly dispersed fluorescent beads in a continuous, compliant substrate[177]. Their intrinsic limitation is in the requirement of a reference, load-free image of the same field of view, to reveal the displacement of optical landmarks[99]. This is obtained upon de-adhesion of cells, implying that the force map can only be computed after the experiment is terminated. For this reason, reference-based TFM methods are not compatible with on-the-fly computation of tractions during an ongoing experiment.

In reference-free methods, randomly dispersed fluorophores are replaced by precisely arranged, regular patterns of markers or force sensors[106,150]. Specifically, beds of silicone pillars or needles provide a well-established and scalable approach, which has seen its best application in the study of forces applied by individual adhesion points[106,270,271]. Upon force generation, flexible pillars are bent from their resting position and the ensuing deformation can be observed using fluorescence or transmission microscopy[272]. The resulting quantification provides a time-resolved force vector in correspondence of each pillar[106]. Tractions maps with sub-adhesion resolution can similarly be obtained in reference-free modality, using the, by comparison, novel confocal TFM (cTFM), an approach based on the decoration of a compliant, continuum elastomeric substrate with a regular distribution of electrohydrodynamic printed quantum dot (QD) nanodiscs[150,194]. Based on the high precision patterning of either pillars or QD nanodiscs, their load-free configuration can be numerically computed[150]. Reference-free approaches are therefore conducive to the online determination of force maps from a single image, in turn opening the way to the iterative education of the ongoing experiment. Such innovative approach is particularly appealing for high-throughput applications where the user may restrict the experimental evaluation to mechanically-active samples. This breakthrough development is, however, hampered by the poor automation of currently available in silico approaches, which are practically non-compatible with the online processing of large data sets acquired at high frequency.

Here, we provide a novel analysis pipeline for reference-free TFM images, including automated image processing, reference state determination, and finite element analysis. An estimate of the displacements is computed in seconds, while the accurate force reconstruction is completed offline in minutes. The combination of these three steps is a black-box analysis pipeline with unprecedented efficiency, compatible with the online generation of force maps in long-term and/or high time resolution live cell experiments. These features are showcased by two challenging examples. First, using a cTFM approach, we explore the temperature dependence of cellular force generation in cancer cells and define a threshold value for thermally-induced mechanical annihilation. Second, using micro-pillar arrays, we detect the time correlation between forces exerted by cells on individual adhesions, which provides a direct estimation of the typical length of basal stress fibers. Altogether, these experimental settings yield an online information flow, which provides access to additional layers of information and is far beyond the reach of the existing state of the art.

6.2 Results

6.2.1 The analysis algorithm

Cellogram automatically converts images featuring optical landmarks (pillars or QD nanodiscs[106,150]) into traction forces. Specifically, the algorithm detects the fiducial markers in the image, estimates their reference positions, and runs a finite element analysis to calculate the actuating tractions (Figure 6.1 a-b). For most experimental images (more than 95%), the processing is fully automatic. Minimal user interaction is required in the remaining cases in which high local deformations, substrate defects, or low image quality create ambiguities.

When compared to existing solvers[150,273–276], Cellogram proves superior in terms of calculation time for all sub-processes (Figure 6.1 c-g) and is overall at least one or several orders of magnitude faster (Figure 6.1 h). Considering the application to cTFM, the new computational approach is compatible with imaging at a time resolution of 5 s for the online estimation of displacements (for approximately 3,000 landmarks). This enables the generation of full traction maps fully automatically in less than 2 min. This time resolution compares with an average of more than 20 min for the previous method, which requires lot of user input[150]. For the application to the analysis of forces on arrays of deformable pillars, the fully automatic processing time is reduced to less than a second. This compares with 5 min of manual interaction for previous methods[276].

In addition to the fast and automatic generation of force maps, which can run in parallel with the ongoing image acquisition at high temporal and spatial resolution, Cellogram extends the analysis to all available images, including those featuring large substrate deformation. This includes data, which proved unsolvable using previous approaches. In these settings, reference-free TFM becomes a routine technique (Figure 6.1 i,k), which can be applied to study transient processes, without investing large amounts of time or requiring trained users. Together, the increase in speed and robustness opens up reference-free platforms to high throughput TFM and high temporal resolution online TFM. In what follows, examples are presented, in which the new capabilities are fully exploited.

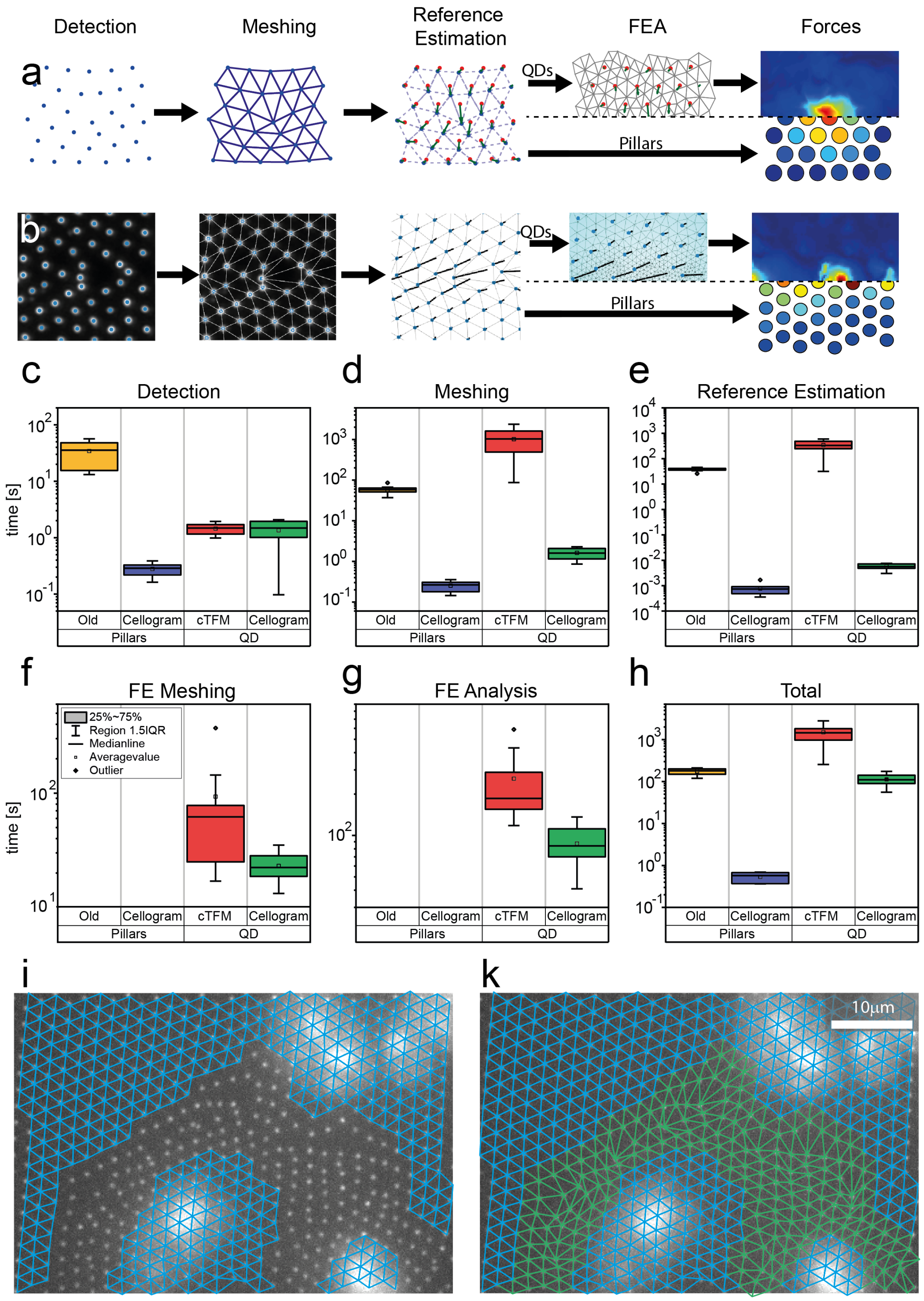

Figure 6.1: Processing pipeline improvements (a) Schematic of the Cellogram processing pipeline. (b) Software screenshots of the Cellogram pipeline corresponding to the steps in (a). (c-g) comparison of computation times for individual pipeline stages in Cellogram and previously used softwares on 10 images each. (h) Computation time comparison for the total analysis time per image. (i) Unsuccessful meshing attempt in cTFM (k) Completed meshing in Cellogram

6.2.2 Temperature dependence of traction forces generated by cancer cells

Localized temperature increase provides an efficient and non-invasive mechanism to ablate unresectable tumors in soft tissues[277]. A safe application of thermal ablation must ensure the complete eradication of the metastatic seeds, while minimizing the collateral damage to the surrounding healthy tissues. In this context, it is relevant to evaluate the sensitivity of cancer cells to increasing temperatures, up to the definition of a threshold value, at which adhesion and force generation are compromised. A state which, together with genetic and metabolic damage[278], irreversibly leads to cell death[279]. The response of cancer cells to hyperthermia is therefore a clinically-relevant biological phenomenon which requires a statistically significant number of observations with high temporal and spatial resolution to distil a reliable trend of temperature dependency from a cell population.

Some information is available regarding the integrity of the cell cytoskeleton and integrin mediated adhesion at low temperatures (i.e. below 37°C; [280]). However, a time-resolved evaluation of the mechanical cell response to supraphysiological temperatures remains unexplored. We approached this problem using cTFM to visualize substrate deformations induced by HeLa cells in a temperature-controlled environment. This cell line was selected as its biochemical and adhesion properties are very well described[281]. In particular, to visualize the actin cytoskeleton, we used a cell strain stably expressing mCherry-actin. Environmental temperature was gradually increased from 37°C to 45°C with a $\Delta T/t$ of 1°C/h. Multiple individual cells were imaged in parallel with a time resolution of 30 min. Cells initially (i.e. at 37°C) conveyed different levels of mechanical strain energy U to the substrate[117]. Yet, following a sufficient number of individual cells (n = 43), a general trend could be obtained (Figure 6.2 g-h). Cell-generated substrate deformation remained $<$10% until the temperature of 42°C was reached. Interestingly, all cells increased significantly ($>$25%) their contractility during the time period in which temperature increased from 42 to 44°C. In this phase cell surfaces started to shrink, while actin structures could still be detected (Figure 6.2 a,b,f). Above 44°C, the mechanical activity of all monitored cells rapidly decreased (Figure 6.2 c) yielding an evident cell rounding which was accompanied by the disassembly of the actin cytoskeleton (Figure 6.2 e). These results indicate that a threshold for the mechanical annihilation of HeLa cells is reached at 45°C, a value that is in good agreement with clinical reports[277]. The concomitant remodeling of the membrane protrusions, actin fibers and focal adhesion was evaluated through an endpoint immunofluorescence analysis (Figure 6.2 d,e). In thermally-annihilated cells, the actin cytoskeleton appeared completely dismantled, while peripheral integrin adhesions could still be detected (Figure 6.2 e). This observation suggests that the ablation mechanism initially affects membrane fluidity and permeability, as previously reported[282], leading to cell volume and surface reduction. In this phase the cell adhesion and contractile machinery may still be intact, yielding a transient increase of substrate deformation due to the concomitant membrane retraction (Figure 6.2 g,h). Only when the actin fibers are thermally destabilized (at 45°C), force generation is impaired. Interestingly, integrin-based substrate adhesions represent the last component of the force transmission chain to be disassembled.

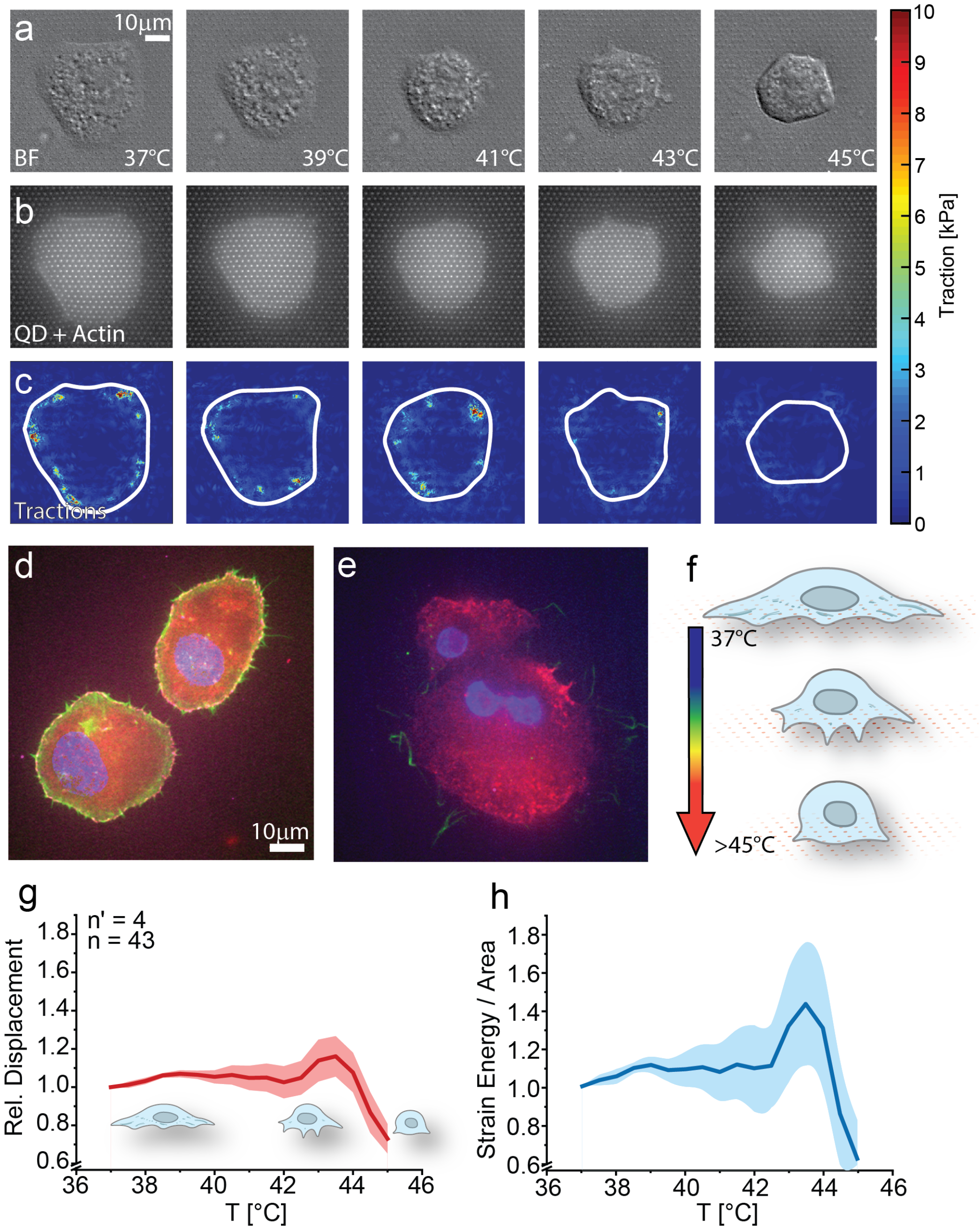

Figure 6.2: Temperature series (a) brightfield images of HeLa cells in increasingly hyperthermic environment from left to right. (b) Quantum dots and mcherry actin (c) cellular traction maps (d,e) HeLa WT cells immunostained for actin (green), paxillin (red), dapi and phosphorylated paxillin (magenta) at 37°C and 45°C, respectively. (f) Schematic of a cell retracting under hyperthermia. (g) Average relative displacements on substrate surface wrt to displacements at 37°C. (h) Ratio of strain energy over area wrt to said ratio at 37°C.

6.2.3 Functional evaluation of correlation length between individual focal adhesions

The contractile machinery of cells is able to transmit tractions to the underlying substrate in a process that regulates cell spreading and migration[151]. Acto-myosin generated contractility is coupled to the extracellular environment by the physical interaction between ventral stress fibers and focal adhesions[283]. At the basal side of adherent cells, single stress fibers define linear connections between two oppositely growing focal adhesions, therefore establishing tension across the cells body. While the typical architecture of these structural elements has been described, the mechanism of interaction and the resulting cell shape adaptation remains poorly understood[283].

Force sensor arrays featuring elastomeric posts with diameter and pitch of few microns offer a structured substrate to adhering cells, allowing the establishment of a single focal adhesion on the upper surface of individual pillars[106]. The resulting one-to-one interaction renders therefore a digital representation of the dynamic mechanical activity of adhesions opening to the investigation of the pattern of force transmission that cells are actuating during the cell cycle[194]. In this direction, a spatial and temporal analysis of focal adhesion activity is possible, which however requires an agile and efficient approach to define the cross-correlation among several mechanical elements, at high frequency and over long periods of observation. We approached this application using an array of deformable pillars ($4\mu m$ pitch, $1.83\mu m$ diameter, 7.1 μm height and 2.5 MPa Young's modulus) on which HeLa cells expressing a Fucci2 cell-cycle phase sensor were seeded (Figure 6.3 a; [142,194]). Individual cells were imaged for 160 min with a time resolution of $\Delta t = 4$ min, thus compatible with the typical dynamic activity of focal adhesions[283]. The global analysis of pillar bending yielded values of deformation for individual pillars at each time point. The pair-wise Pearson correlation coefficient of these plots (on average 38 pillars per cell) was calculated. Pillar couples on which force transmission increased or decreased at the same time received a positive correlation score (+1). Pillar couples which on the contrary displayed an antithetic behavior received a negative correlation score (-1). Pairs of pillars which behaved independently had zero correlation. This analysis was extended to all possible couples of pillars interacting with individual cells, and to multiple cells in different cell cycle phases, yielding a total of 22 thousand pillar pairs analysed. Significantly negative correlation (i.e. smaller than -0.75) was very seldom detected (0.01%). This result indicates that force generation in cells does not use sliding or oscillation of rigid bodies. On the other hand, significant positive correlation (i.e. larger than 0.75) was evident for specific couples of pillars (17.2%), which increased or decreased deformation at the same time (Figure 6.3 f). Correlated pillars moved at the same time and along the same direction, but in opposite sense, compatibly with the increase or decrease of contractile actuation. Based on this global analysis, a plot of correlation score as a function of the distance between pillars was obtained (Figure 6.3 b,d). It is interesting to note that the frequency of correlation between pillar couples decreases exponentially at increasing distance (Figure 6.3 c,e). For cells in the G1 phase of the cell cycle, the most mechanically active[283], this yielded a correlation distance up to 40 μm, and with average values of 18 μm. The

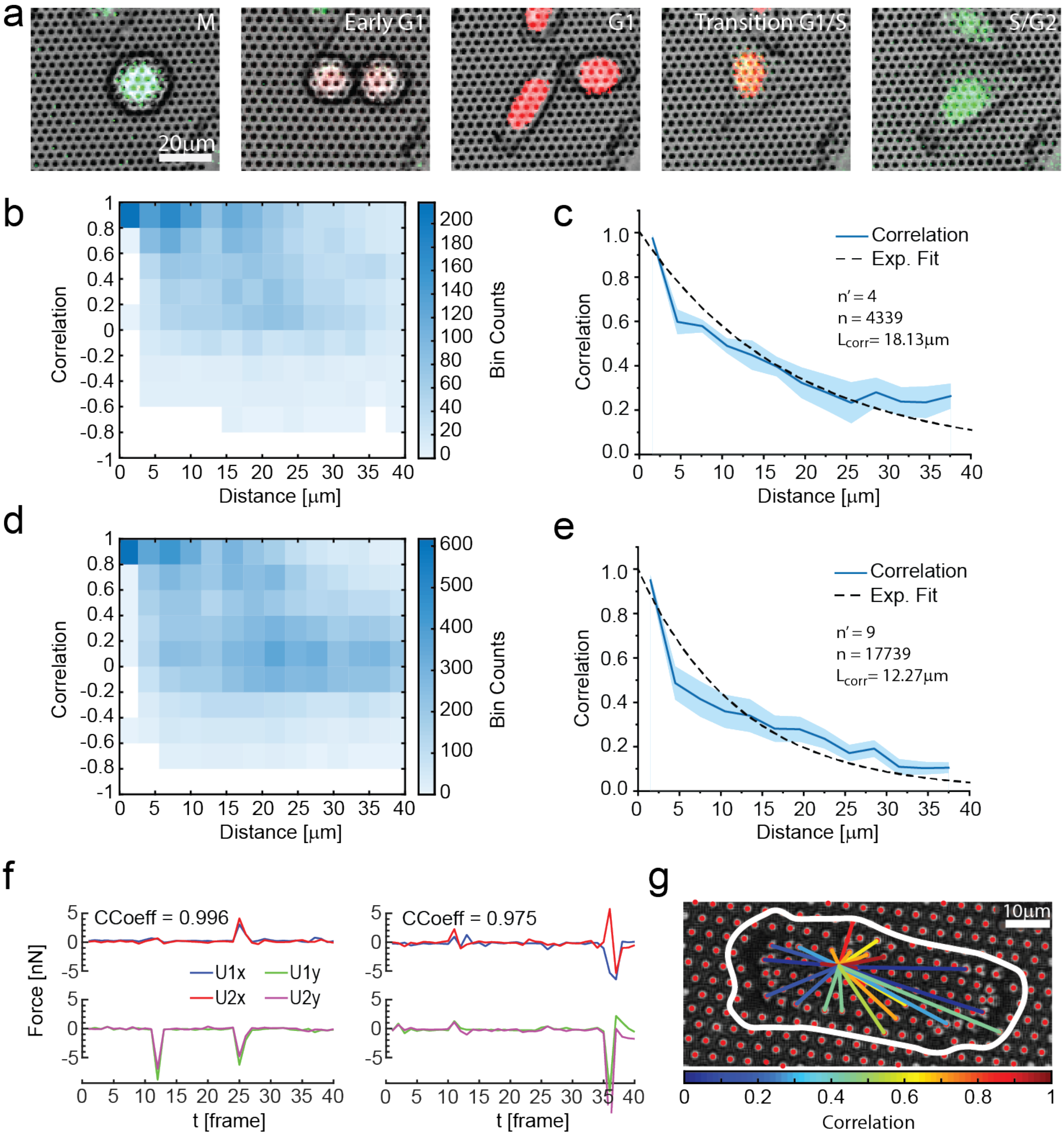

Figure 6.3: Cell cycle. (a) HeLa Fucci cell cycle phase dependent nucleus coloring. (b,d) Binned scatter plot of pairwise force correlation between micro-pillars displaced by cells in G1 and G2, respectively. (c,e) Force correlation as a function of distance between micro-pillars. Shaded area is the ste. The exponential fit (dashed) reveals a correlation length for cells in G1 and G2, respectively. (f) Two examples of force development of highly correlated micro-pillars. (g) Schematic showing force correlations of several micro-pillars wrt to a central pillar

transition to the ensuing S phase significantly reduced this length to 12 μm (Figure 6.3 c,e). When the correlation map is overlapped with the cell profile, this yields a representation of its contractile polarity, whereas correlated pillars are aligned along the cell's short axes (Figure 6.3 g). Mechanically active stress fibers have a typical length between 10 and 100 μm, depending on the cell type and activity[283]. This specific architecture was never linked to the cell cycle phase and overall cell shape anisotropy. The resolved cross-correlation obtained through the application of Cellogram allows for a deeper insight into force generation and transmission in adhering cells, which could be easily upscaled to multiple cells and tissues.

6.3 Materials and Methods

6.3.1 Cell culture

Cells were cultured in an incubator at 37°C and in 5% CO_2 humidified atmosphere. For the temperature series on the QD nanodisc array substrates HeLa and HeLa expressing mCherry-actin were used. They were maintained in DMEM (Sigma-Aldrich, St. Louis, MO, USA) supplemented with 100 U/ml penicillin, 100 $\mu g/ml$ streptomycin, and 10% fetal bovine serum at 37°C in a 5% CO_2 humidified atmosphere. For cell cycle synchronization, HeLa cells were pre-incubated overnight with the G2/M blocker RO-3306[284] at a final concentration of 10 μm. The experiments were started at a temperature of 37°C degrees. The rate of temperature increase was set to one Celsius per hour. The temperature of the cell culture medium was measured with TSic temperature sensors (IST AG, Switzerland) and cells were imaged every 30 min. For the cell cycle experiments we used HeLa cells stably transfected with the Fucci2 biomarker[142] and seeded them on micro-contact printed micropillars. The cells were seeded onto the pillar array 12 to 18 h prior to the experiment. Images were taken every 4 min for a total of 160 min.

6.3.2 Live-cell imaging

Cells were allowed to spread on the target substrates overnight before imaging. Temperature, CO_2 and humidity were controlled during imaging using an incubation chamber. QD nanodisc array imaging was done with a Nikon TI N DIC with a 60x oil immersion objective with 1.35 NA. Micropillar array imaging was done with a Zeiss Axio Observer. Z1 and 40X (EC Plan-NEOFLUAR 40x/0.75) objective with 0.55 NA.

6.3.3 Substrate preparation

Arrays of QD nanodiscs were generated as reported in[150]. Briefly, the QDs were deposited on the substrate by electrohydrodynamic nanodrip-printing[140]. The colloidal ink containing the QDs is ejected from a micro-sized gold-coated nozzle in an electric field onto the elastomeric substrate. By modulating the electric field and position of the substrate the QDs are deposited in a controlled orderly fashion. The electro-hydrodynamic nanodrip-printing technology can be commercially obtained through an ETH Zurich spin-off company (http://www.scrona.ch). Before performing the experiments, the temperature dependence of the substrate mechanical properties was evaluated, resulting perfectly stable within the analysed temperature range[285]. The PDMS micropillar array was manufactured by a two-step molding process[154,286–288]. First, a Si, master mold was created using photo lithography. The master mold was used to create a negative mold using a 10:1 Polydimethylsiloxane (PDMS) solution, (w/w, base: curing agent Sylgard 184, Dow, Corning). This negative mold was functionalized with oxygen plasma and Trichloro(1H,1H,2H,2H-perfluorooctyl) silane and placed it on top of a cover glass with a drop of 10:1 PDMS and cured for 40 hours in 110 °C. The PDMS negative mold was then peeled off to recover the PDMS micropillar arrays. Micro-contact printing[154,288] was used to visualize the PDMS pillar tops using a fluorescent ECM proteins to promote cell attachment. Briefly, 30:1 PDMS stamps were treated with a mixed solution of Alexa-Fluor 647-conjugated fibrinogen (25 $\mu g/ml$; Life Technologies) and fibronectin (50 $\mu g/ml$; Sigma-Aldrich) for an hour at room temperature. The treated stamps were rinsed with DI water, dried and then placed in contact with the top of the pillar array (pre-treated with ultraviolet light for 7 min), which transferred the proteins on the pillar tops. The pillars were washed with pure ethanol, 70% ethanol and DI water. The unstamped regions were then blocked with 0.2% Pluronic (Sigma-Aldrich) solution for 60 minutes and finally washed with DI water. Functionalized pillars were stored in DI water before loading the cells. To visualize and functionalize the PDMS micropillar, micro-contact printing was used to modify the top of PDMS micropillar with fluorescent ECM proteins to promote cell attachment. 7 mm x 7 mm 30:1 PDMS stamp were treated with 30 μL of mixed solution drops comprising of fibronectin (50$\mu g/ml$; Sigma-Aldrich) and Alexa-Fluor 647-conjugated fibrinogen (25 $\mu g/ml$; Life Technologies) for 1 hour at room temperature. Treated PDMS stamps were rinsed with distilled (DI) water and blown dry with nitrogen gas. Meanwhile, PDMS micropillar arrays were pre-treated with ultraviolet (UV) ozone for 7 min in a UVO cleaner (Jelight). Functionalized PDMS stamp was placed in contact with the top of the PDMS micropillar arrays. Through this process, the functionalization proteins were transferred from the PDMS stamps to the tops of PDMS micropillar. PDMS stamp was removed and the PDMS micropillar array was washed by pure ethanol, 70% ethanol and DI water.0.2% Pluronic (Sigma-Aldrich) solution was used to block the un-stamped regions of the PDMS micropillar array. After 60 min of immersion, DI water and PBS (Life Technologies) was used to wash away the excess Pluronic solution.

6.3.4 Immunofluorescence

Cells were fixed with 4% paraformaldehyde in phosphate-buffered saline (PBS) for 10 min at room temperature (RT) and permeabilized with 0.5% Triton in PBS for 10 min. After blocking with 5% bovine serum albumin (BSA) in PBS for 1h, samples were incubated at 4°C overnight with primary antibodies. The following commercial antibodies were used: mouse anti-paxillin, BD Bioscience (#610051), dilution: 1:100[247] and rabbit anti-phospho-paxillin Tyr118, Cell Signaling (#2541S), dilution: 1:100[231]. Secondary antibodies Alexa Fluor 647 chicken anti-rabbit, LifeTechnologies (#A-21443) or Alexa Fluor 555 donkey anti-mouse, LifeTechnologies (#A-31570), were used at 1:200 for 1h at RT. Actin cytoskeleton has been stained with Alexa Fluor 488 phalloidin, Life Technologies (#A12379), while nuclei were stained with Hoechst, Sigma (#H6024).

7 Cellogram - Software and Algorithms

This document provides a detailed description of the algorithms used in the image processing pipeline, which is composed of 4 steps: (1) markers detection, (2) inference of reference graph topology, (3) computation of displacements, and (4) traction force reconstruction. The 4 steps are illustrated in Figure 7.1.

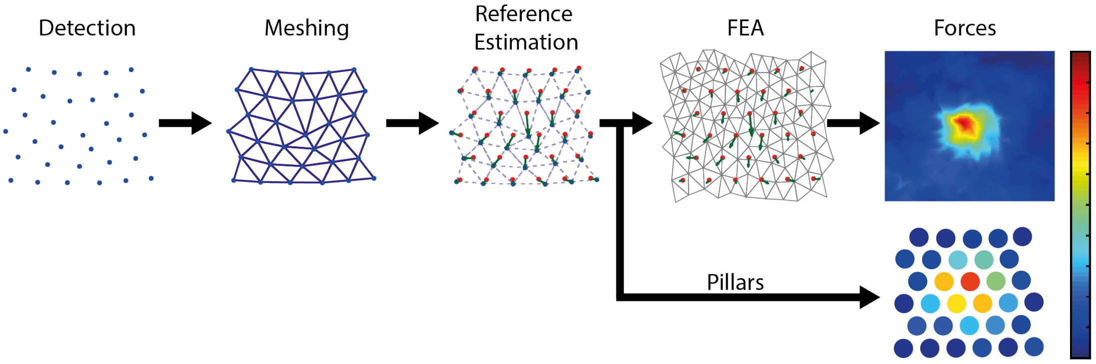

Figure 7.1: The 4 pipeline stages, which automatically convert images of reference-free TFM markers to traction forces.

7.1 Markers Detection

The algorithm input is a gray scale image acquired by fluorescence microscopy (Figure 7.2a). It contains either quantum dots[150] or micropillars[106] as markers. The first step of the algorithm analyses the image to extract the 2D position of each marker. First, a Gaussian filter with a user-defined sigma is applied to the image to reduce noise, i.e. the image is convoluted with a 2D-Gaussian (Figure 7.2b). This image is then binarized at the intensity level determined algorithmically[289] to generate a mask with candidate regions where the markers could potentially be located (Figure 7.2c). In parallel a Laplacian of Gaussian (LoG) filter is applied to the original image. Here, the image is convoluted with a LoG kernel. The result is an image with low values in locations where originally there was no gradient of intensity, i.e. the center of markers, and high values where intensity gradients were strong (Figure 7.2d).

The LoG image then is subtracted from the Gaussian image to generate a new frame with sharper peaks at the position of the markers. In this resulting image the local maxima are determined. A pixel is considered a local maxima if it displays the highest intensity value among its eight neighboring pixels (Figure 7.2e). If a pixel is a local maxima and is in the candidate region of the mask, then the pixel's position is used to least square fit a 2D Gaussian in its vicinity (Figure 7.2f, [290]) in the original unfiltered image. The fitted Gaussian has a single user-controlled parameter: sigma. Duplicate detections that can arise from two maxima located close together, for which the Gaussians merge, are eliminated after the fitting.

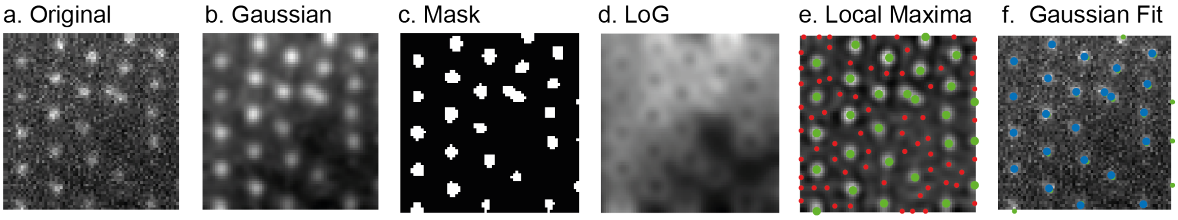

Figure 7.2: Detection. (**a**) Original image, (**b**) Gaussian filter (**c**) Mask generated from thresholded image in (b) using Otsu-Threshold, (**d**) Laplacian of Gaussian (LoG), (**e**) Detected local maxima in resulting image from LoG subtracted from Gaussian image. The maxima detected in the mask and outside of the mask are in green and red, respectively. (**f**) Least square fit of Gaussians at the detected local maxima

7.2 Inferring Graph Topology

The previous step generates a set of 2D position of the markers: the regular lattice connectivity between them shall now be reconstructed. The challenge lies in the fact that the grid is deformed by the traction forces, which are unknown. The only prior is that, before the displacement induced by the cells, the markers were positioned over an unknown subset of a regular triangular lattice of unknown size and orientation. Crucially, for every marker we only use its position and do not require any additional information. Differently from previous methods, our reconstruction shall be tolerant to occasional errors in the detection of markers, correcting false negatives (markers missed by the detection procedure) as well as false positives (markers "hallucinated" by the detection procedure). For example, false negatives and positives may be induced by noise, or arise by the misinterpreting two adjacent markers as a single one.

7.2.1 Formal problem definition

The input of this step is a set of *detected* 2D points D, each point represented by a pair of coordinates. The output is a set $P \subset D$ of *false positives*, a set N of *false negatives* (new 2D points which are inferred to exist although they were never directly observed), and a permutation α of 2D points $(D/P \cup N)$ into the position of a regular triangular grid. Once the permutation is known, the relaxed positions can be inferred by smoothing the grid (Section 7.3) and the displacements are then defined by the difference.

Among all potential choices of N, P, α (for a given observation D), the one minimizing its *unlikelihood* is defined as

$$k_1|N| + k_2|P| + E(\alpha(D/P \cup N)), \tag{7.1}$$

where $|X|$ denotes the cardinality of the set X, k_1 and k_2 are fixed scalar parameters weighting the penalty associated to different factors (determining how much false positives and negatives impact the likelihood of a solution), and $E(X)$ is an approximation of the potential elastic energy which would be required to deform a regular pattern into the given pattern X (on the ground that the least energetic configuration is the most plausible).

To define E, the elastic substrate is approximated as a network of Hookean linear springs connecting each pair of direct neighbors on the lattice, resulting in:

$$E(X) = \sum_{i=0}^{|X|} \sum_{x_j \in N_i} (|x_i - x_j|_2 - L)^2, \tag{7.2}$$

where L is the step length of the regular lattice, and N_i is the set pf neighbours of x_i.

7.2.2 Problem analysis

This formulation makes the complexity of the problem apparent: it is a combinatorial optimization over a large space, with a strict set of constraints that must be enforced to obtain valid solutions. As observed in[150], an exhaustive search of the optimal solution via a branch and bound algorithm would be practical only for tiny problem instances (up to around 20 vertices).

We propose an algorithm to efficiently find a low energy solution. While the approach is not guaranteed to find the optimal solution, in the large majority of cases, it indeed finds the same solution obtained by an exhaustive search, while being orders of magnitudes faster and scaling to tens of thousands of markers.

The proposed approach is incremental: an initial guess for permutation is initially proposed, and then iteratively improved until convergence.

The key novelty of the algorithm is the use of two complementary representation for an intermediate solution for α: a *Mesh*-based and a *Lattice*-based representation. The two representations are equally capable of expressing any consistent permutations α into a lattice, but crucially, each can also represent certain inconsistencies of different nature. Switching from one to the other allows reducing these inconsistencies very efficiently.

Overview. The initial guess of α is expressed as a Mesh-based representation. This solution is then converted back and forth between Lattice and Mesh representation, applying an optimization step after every conversion. The optimization step improves the solution, greedy applying a sequence of local operations (i.e. operations affecting only a small, constant portion of the representation). In both representations, a local operation lowers the number of inconsistencies and the energy term for E in Equation 7.2.

At the end of the process, residual inconsistencies in the final α are interpreted as false positive and negatives, creating sets P and N respectively.

In summary, the algorithm can be written as:

```
• Variables: Mesh, Lattice

1. Mesh ← initial_guess( $D$ )                                Section 7.2.3
2. loop:
     a) local_operations( Mesh )                              Section 7.2.4
     b) convert: Mesh → Lattice                               Section 7.2.5
     c) local_operations( Lattice )                           Section 7.2.6
     d) if converged then exit loop                           Section 7.2.8
     e) convert: Lattice → Mesh                               Section 7.2.7
3. $(P, N)$ ← fix_residual_inconsistencies( Lattice )         Section 7.2.9
```

First, the two representations are described, and then the other parts of the algorithm are described in more detail.

Mesh representation. In this representation, the permutation into a lattice is represented as a two-manifold, triangular, mesh whose vertices are D. In other words, a Mesh consists of all points in D connected by a set of triangles; the sides of the triangles are termed edges. This structure is the ubiquitous way to represent piecewise linear surfaces, and has been deeply studied for example in Geometry Processing (e.g. see [291] for an overview). The meshes are open and simple, meaning that they have an unique loop of boundary edges and vertices (i.e. there are no internal “holes”). They are two-manifold, meaning that that every edge of each triangle is either a boundary edge or is shared by exactly another triangle. The valency of a vertex is defined as the number of triangles sharing that vertex. A mesh is called regular when each boundary vertex has valency < 6, and each other vertex has valency 6.

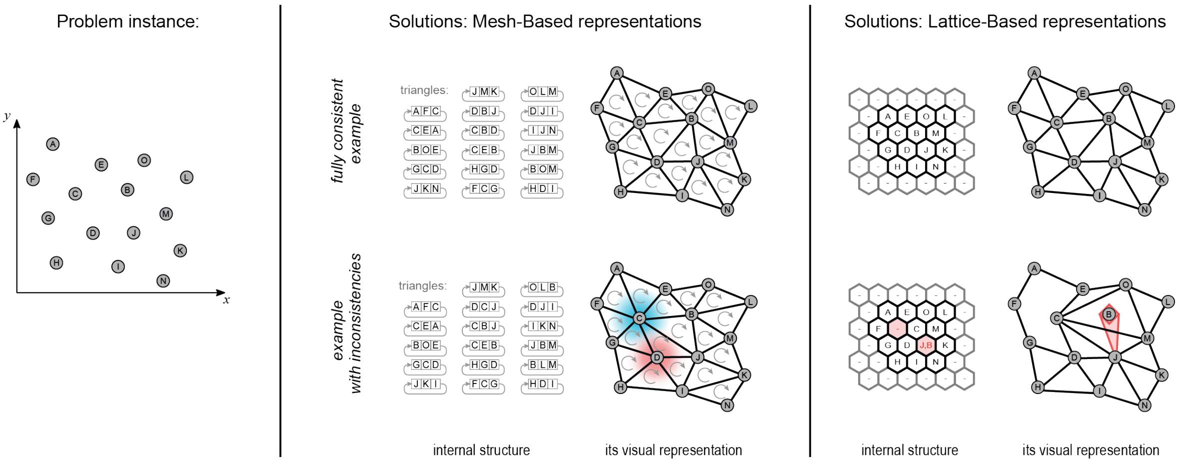

Figure 7.3: An instance of the graph-topology problem consists of a set of 2D points, like in this toy example (left most). In our system, a solution is represented in either of two alternative representations: mesh-based, and lattice-based. Mesh-based representation consists of a two-manifold, well-oriented and simple triangular mesh (middle column), whose vertices are the given set of points. A lattice-based solution consists of a regular honeycomb grid of cylindrical cells which can be assigned to one (or multiple) vertices (rightmost column). Either representation is capable of expressing any permutation into a lattice, like the one depicted on top (which is, in this case, the energy minimizer, and therefore the optimum). Each representation is also subject to include inconsistencies of different types. In the mesh representation, for example, internal vertices can have a valency different from 6 (in the example on bottom: a valency-5 vertex is highlighted in red, and valency-7 vertex in blue). In the lattice-based representation, there can be internal "holes" in the regular grid, or multiple nodes assigned to the same grid cell, (bottom-right).

A regular mesh can be interpreted as a permutation α of its vertices D into a lattice, since it encodes a regular lattice. A mesh which is not regular, conversely, does not correspond to any such permutation. The inconsistencies of a Mesh representation are, therefore, vertices breaking the above requirement on the valency (termed "irregular" vertices).

Lattice representation. Our lattice, or matrix, is a 2D regular grid of hexagonal cells (honeycomb tiling). Each element of D is hosted in one cell. A cell can be empty, or host one or more elements. In the lattice, non-empty cells always form a contiguous subset of the grid, and all cells on the boundary of the grid are empty.

Ideally, each non-empty cell hosts only a single element of D. Also, empty cells are all found in one continuous set around the lattice (i.e. there is no island of empty cells completely surrounded by non-empty cells). A lattice with these properties can be trivially converted to a valid permutation α. The inconsistencies of a lattice representation are, therefore, cells hosting more than one element of D (these elements are called "colliding"), or empty cells that are not connected to the boundary of the grid by a sequence of empty cells (these cells are called "holes").

7.2.3 Step 1: Mesh initialization

The algorithm is initialized by computing the 2D Delaunay triangulation[292] of the set of vertices D. This process is fast and guarantees to produce a two-manifold, simple mesh. In undeformed areas, this mesh reproduces the connectivity and the shape of a regular grid and it is thus a correct solution. However, in distorted regions, irregular vertices are introduced. The next steps address these inconsistencies.

7.2.4 Step 2: Mesh local operations

An edge-flip[292] is a standard local operation commonly used in the context of mesh optimization and simplification. In the represented context, edge-flips are used to improve the quality of the mesh, striving to obtain a regular connectivity on the entire mesh and a decreased energy.

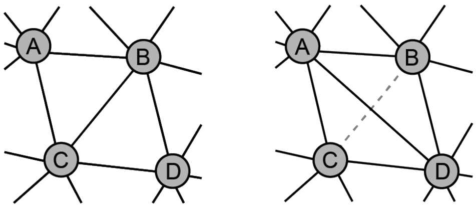

Figure 7.4: An example of an edge-flip operation: in this mesh, flipping the edge B-C decreases the valency of vertices B and C by one, and increases the valency of vertices A and B by one.

Specifically, the effect of an edge-flip is scored by two numbers (e_a, e_b). e_a is the induced increase in the number of regular vertices (or decrease if negative): as an edge-flip increases the valency of two vertices by one, and increases the valency of other two vertices by one (Figure 7.4), it can either increase, decrease or leave unaffected the total number of irregular vertices on the mesh. e_b is the induced decrease is on energy E: only the edge being flipped changes its length and thus its contribution to the energy E (Equation 7.2). An edge-flip is beneficial either when $e_a > 0$, or when $e_a = 0$ and $e_b > 0$.

All potential edge-flips (there is exactly one per edge) are tested, and the ones that are beneficial are performed. In a second pass, the algorithm tests all the possible pairs of consecutive edge flips affecting a common vertex that have a *combined* (summed) beneficial effect.

Edge-flip operations which would reduce an internal vertex valency below 3, are always disallowed as it would compromise the two-manifoldness of the mesh.

While this step is effective at solving many locally inconsistent configurations, it might fail at identifying the long sequences of flips that may be necessary in images with large displacements. The mesh is therefore converted to a lattice representation, to continue the optimization.

7.2.5 Step 3: Mesh to lattice conversion

Starting from an empty lattice, the mesh is explored, copying the indices of the encountered vertices into the lattice cells, one by one. The mesh is visited with a “flood-fill” approach, i.e. from a “seed” triangle and iteratively proceeding by expanding the visit to neighboring triangles, until the entire mesh is visited. Crucially, the parts of the mesh which are more regular are explored first; in this way, the less ambiguous parts of the mesh, which can be interpreted with higher confidence, serve as a guidance to settle the more ambiguous parts. In practice the problematic parts of the mesh are surrounded by the visit (thus isolated) and then conquered from the exterior inwards.

A precise description of the employed algorithm is given below. In the following, we define the “equilateral factor” of a triangle with sides lengths a, b, c, with $a > b > c$, as the real number $((c + b)/a - 1)$. A perfectly equilateral triangle has factor 1, a completely degenerate triangle has factor 0, and any intermediate case has values in between.

Identifying the seed triangle. Every triangle of the mesh is labelled as either reliable or not reliable. A reliable triangle fulfills three conditions: (i) it is not on the mesh boundary, (ii) its three vertices are regular (valency 6), and (iii) its shape is sufficiently equilateral (equilateral factor larger than 0.85). The seed is selected as the furthest reliable triangle (under hop distance) from any unreliable triangle; in other words, the triangle which is surrounded by the maximal number of reliable triangles. The three vertex indices of the seed triangle are copied into a group of three reciprocally adjacent grid cells.

Enumerating and prioritizing the expansion moves. An expansion move potentially enlarges the set of visited triangles by one element, traversing one mesh edge adjacent to an already visited triangle. There is one expansion move for each internal mesh edge. At any given time, an expansion move is available if at least one of the triangles shared by the corresponding edge has been visited (note that this includes edges with visited triangles on both sides). During the fill, all available moves are kept in a set, and prioritized, from highest to lowest confidence, according to summed equilateral factors of the two triangles sharing the edge. The set of available expansion moves is kept in a *priority queue*, and is initialized with the three edges of the seed triangle.

Iteratively, the element with the highest priority is extracted from the set of potential moves, removed from the set, and the move executed. After the move, up to two new available expansion moves are added to the set to reflect the expansion of the set of visited triangles (and evaluate their priority). Traversed edges are flagged as such and never added to the set of available moves a second time. The procedure terminates when the set is empty (i.e. when each internal mesh edges has been traversed exactly once).

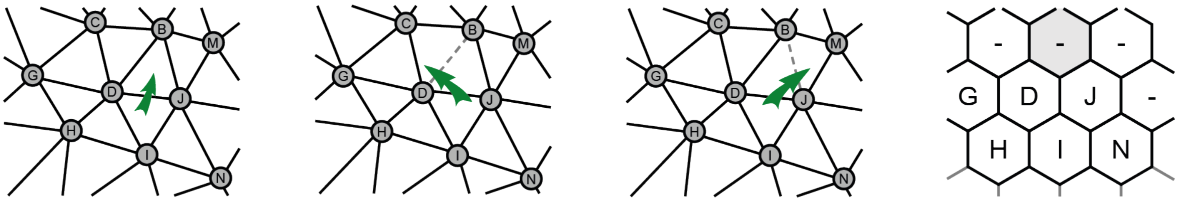

Figure 7.5: An example of the execution of an expansion-move. Executing the move crossing the edge DJ and visiting triangle DJB (left-most diagram), would have the effect of filling the grayed square of the lattice with the vertex labelled as B (right-most diagram). If that square is already filled by a vertex other than B, or if vertex B is already allocated anywhere else on the lattice, then this move would cause an inconsistency. In this case, an edge-flip of one of the other two edges of DJB is attempted first: flipping the BD edge causes the grayed square to be filled with vertex C instead of B (mid-left diagram); flipping the JB edge causes it to be filled with vertex M instead of B (mid-right diagram). If either edge-flip avoids the conflict, then it is performed before the move executed.

Executing an expansion move. An expansion move consists of expanding the visit from the visited triangle t_A, over edge e_0, into the (potentially not yet visited) triangle t_B. Let v_i be the vertex of t_B opposite to edge e_0. Executing the move consists of copying v_i into a given cell of the grid with index c_i (see Figure 7.5). The cell index c_i is fully determined by the cell position on the grid, of the vertices of t_A. Note that, due to previous expansion moves, it is possible that cell c_i is already occupied by a vertex; likewise, and independently, it is possible that vertex v_i is already allocated in a grid cell. Therefore, three cases can arise:

- **Expand**, when vertex v_i is not currently allocated anywhere in the grid, *and* cell c_i is currently vacant;
- **Confirm**, when vertex v_i is already present in cell c_i (i.e. cell c_i already contains vertex v_i);
- **Contradiction**, when vertex v_i is already allocated in some other cell position different from c_i, or cell c_i is already occupied by some vertex different from v_i, or both.

In the Expand case, cell c_i is filled with vertex v_i. In the Confirm case, nothing needs to be done; when that case arises, it means that the current expansion moves is consistent with the lattice layout as inferred from the already visited triangles. This can happen, for example, because vertex v_i was previously reached from a different direction, possibly along a completely different triangle paths from the seed. Vice-versa, the third case happens because the starting mesh is not fully regular. Executing the move would create an inconsistency. At this point, it is checked whether the conflict can be avoided by means of edge flips performed on the mesh. There are two potential edge flips, corresponding to 2 edges of t_B that are not e_0. If either edge flip is viable, it would result in a different vertex indices v_i' and v_i'' in place of v_i (see Figure 7.5), and therefore in a different case. The edge-flip is performed if it is viable and results in the removal of the contradiction (if the extremely rare case when both edge-flips qualify, the one resulting in the highest summed equilateral factors of the two affected triangles is selected). Note that the edge flips are performed, in this phase, regardless of their local effect on the valency of the vertices or the energy.

After the expansion move, assuming no contradiction arose or that it could be resolved, the two external edges of t_B are added to the set of potential moves, unless these edges have been already processed.

Rationale. Importantly, triangles can be assigned to the grid by independently assigning their three vertices to grid cells, before that triangle is explicitly visited. This happens for example when the boundary of the visit meets with itself after that the flood-fill encircled a problematic region (e.g. a region containing irregular vertices) from the two different sides. Eventually, these triangles will be explicitly visited also. When that happens, the visit can only either confirm or contradict the previously found grid layout. In case of contradiction, the grid values are not overwritten, because earlier moves are, by design, considered more reliable than later moves. Instead, the existing grid values are used to correct the mesh connectivity (by means of flips). In conclusion, the flip operations which are performed in this phase are driven by the global grid structure of the mesh, rather than by its local configurations, differently from the local optimization on the mesh (Section 7.2.4). In this sense, this flip identification strategy is drastically more "long sighted" and capable of avoiding local minima.

7.2.6 Step 4: Lattice greedy optimization

A Lattice admits three local operations: (1) permutation of a small subset of the vertex indexes stored in the cells, (2) hole filling and (3) conflicts resolution. A set of local operations is tested, and all the ones with a positive effect on the global energy are performed (Equation 7.1).

Operation 1: Greedy permutations. Given a set of n vertices $v_0 \dots v_{n-1}$ assigned to cells $c_0 \dots c_{n-1}$, a cycle permutation is the reassignment of each vertex v_i to $c_{(i+1)\%n}$ (% being the modulo operator). A cycle permutation is beneficial if it results in an overall decrease of the energy. A brute force approach, where each set of 2, 3, and 4 adjacent cells are tested for all potential cycles is used. Cycles of size 2 (that is, swaps between pairs of cells) are also tested between any pairs of cells separated by a single cell. In total, 48 cycles are tentatively tried around each non empty grid cells, in a fixed pattern. The resulting algorithm is linear with the number of cells and fast, because testing for the effect of a cycle requires to sum up only a limited number of addendum to the energy in Equation (7.2).

Operation 2: Hole filling. A Lattice "hole" is defined as an empty grid cell that is not connected to the lattice boundary by a path of empty cells. Each disconnected empty cell is a hole, and is evaluated for removal. In order to remove a hole, first, the vertex from a neighboring non-empty cell must move to fill its position, thus shifting the hole to that cell; then, the process has to be repeated until the hole ends up neighboring one boundary empty cell, or the moving vertex is a conflicting vertex (i.e. was one of the two vertices allocated in the same cell). In the latter case, that “conflict” inconsistency is also removed. Each movement of a vertex into the empty position comes with an associated increase (rarely, a decrease) of the energy E. In other terms, in order to fix a hole, a path from that position to a either a connected empty cell, or to a conflicting vertex needs to be found.

The problem can be cast as a minimum cost path, which is solved using the Dijkstra algorithm (seeded at the cell presenting the hole, and targeted at any eligible destination of the path). The cost of every step is defined as the increase (rarely, the decrease) of the energy for the corresponding swap. Additionally, the cost of the final step is further decreased (possibly down to a negative number) by the value k_0 (Equation (7.1)), to reflect the decrease of the number of holes. In case that the final destination of the graph is a conflicting vertex, the cost is also decreased by the additional value k_1, to reflect the decrease of the number of conflicts.

When the minimum cost path is identified, it is applied it if and only if its total cost sum up to a negative number. Otherwise, the total likelihood of the found solution would decrease (in other words, a more likely justification for the hole is to assume that an existing point was undetected). To optimize, we abort the Dijkstra search over paths which results in a total cost larger than $(k_0 + k_1)$.

Operation 3: Conflict resolution. For conflicts inconsistencies, the situation is conceptually similar. A conflict is a situation where two vertex indices are located in the same lattice cell. It can be solved by, first, moving either vertex index to a neighboring cell, thus shifting the position of the conflict to that cell, and repeating this step until an empty cell is reached. If the final empty cell is also labelled as disconnected from the boundary (i.e. it is a hole), this has the additional side effect of simultaneously fixing that hole. Again, the problem is cast as a minimal cost path search, solved via the Dijkstra algorithm. This time, the path starts from the conflicted cell and terminates into any empty cell, either connected or disconnected to the boundary. The cost associated to the move terminating the path is decreased by k_1 or by $k_0 + k_1$, to reflect the fixing of either one or two inconsistencies. Similarly to the previous case, the resulting fix is considered profitable if the found path has a negative total cost (otherwise, it is concluded that the inconsistency would be more parsimoniously explained by assuming the conflicting vertex to result from a false positive in the point detection).

7.2.7 Step 5: Lattice to mesh conversion

This step is implemented as a variant to Step 4, that is, the mesh is visited again using a flood-fill seeded at an appropriate starting location. The only difference is that this time, the lattice is not initialized as empty, but kept unmodified at its current values. Consequently, the only two possible outcome for expansion moves are "confirm" or "contradiction" (and never "expand") and the only sought effect is to perform edge flips in the latter case.

Rationale. The objective is to modify the current mesh configuration to make it more similar to the current lattice configuration, but only by means of valid local mesh operations (the lattice is only used to guide these operations); this ensures that the mesh representation is kept consistent. The aim is not to obtain a mesh configuration perfectly mirroring the one represented by lattice, because inconsistencies which are potentially left in the lattice ("collisions" and "holes") cannot be represented in the mesh representation.

7.2.8 Step 6: Convergence detection

The algorithm stops when an entire iteration (2 conversions and 2 sets of local operations) are not changing the lattice representation. In our experience, this never takes more than 4 iterations.

7.2.9 Step 7: Removal of lattice inconsistencies

For every set of points in D allocated to the same cell, one is selected to occupy that cell, and the others are considered false positives and added to P. Similarly, every set of isolated empty cells (i.e. separated from the boundary by non-empty cells) are considered false negatives and added to N. Their position is computed as the average position of their neighbors (the averaging is repeated until convergence, for islands of two cells of more).

7.3 Displacement Computation

At this stage, the markers in the input image have been detected, and the connectivity between them computed. The next step is to reconstruct the marker displacements from the rest configuration, to the configuration captured in the image. This is achieved with a relaxation process that warps the markers in the image into a regular grid: the displacements are then computed by taking the difference between the initial and relaxed positions. The relaxation process is modeled using the graph Laplacian

$$L_{ij} = \begin{cases} \Sigma_j L_{ij} & i == j \\ 1 & \text{i is a neighbor of j} \\ 0 & \text{otherwise} \end{cases} \tag{7.3}$$

which, for a perfectly regular mesh, satisfies

$$Lx = 0, \tag{7.4}$$

where x are the coordinates of the vertices in the mesh. The vertices are split into two groups - the inner vertices, which need to be relaxed to their original position, and the boundary vertices which are fixed. The Laplacian L is split accordingly:

$$x = \begin{bmatrix} x_i \\ x_b \end{bmatrix} \quad L = \begin{bmatrix} L_{ii} & L_{ib} \\ L_{bi} & L_{bb} \end{bmatrix} \tag{7.5}$$

The system of equations is reduced to

$$\begin{bmatrix} L_{ii} & L_{ib} \end{bmatrix} \begin{bmatrix} x_i \\ x_b \end{bmatrix} = 0 \tag{7.6}$$

and solving

$$x_i = -L_{ii}^{-1} L_{ib} x_b \tag{7.7}$$

yields the relaxed positions of the inner vertices. With the boundary vertices fixed, this has the effect of simultaneously moving all the vertices to the barycenter of their on-ring neighborhood, thus creating a regular hexagonal grid.

7.4 Force Reconstruction

The displacements computed in the previous step are already a good proxy for the traction forces. The conversion of the markers' displacements into traction forces depends on the type of image. For pillars, the forces are discretely applied to each pillar and can be reconstructed directly from the displacements. For quantum dots, the forces are applied continuously on the substrate, and thus their reconstruction requires a finite element method.

7.4.1 Pillars

For pillars, the forces can be directly computed from the displacement field u obtained in the previous steps as

$$F = \frac{3EI}{L^3} u, \tag{7.8}$$

where E is the Young's modulus, I is the moment of inertia, and L is the length of the pillars[106]. Results of this procedure are shown in Figure 6.3 in the main paper.

7.4.2 Quantum dots

For quantum dots, we have to solve a volumetric deformation problem, which given the target displacements of the vertices on the surface, finds the traction forces inducing such displacement.

Volumetric Meshing. To set up our physical simulation problem, it is necessary to first discretize the substrate, decomposing it into a mesh composed of tetrahedra. The tetrahedral mesh is adaptive, with a higher density in the regions corresponding to the higher displacement. The meshing proceeds in 4 steps. The meshing proceeds in 4 steps.

Step 1. A background 2D mesh is created as the Delaunay triangulation of the displaced markers, plus a few additional points on an extended bounding box whose size is user-controlled. In the following, we will distinguish the inner box (the substrate) from the outer box (substrate + padding).

Step 2. A sizing field is computed in 2D to indicate the target edge length of the mesh to be used in the simulation. First, the "source" of the sizing field is determined as the mesh triangles whose vertices have a displacement larger than a user-given threshold (set as percentage of the max displacement across all dots – 18% by default in our application). The target size for the source region is then set as a user-defined percentage of the median distance between adjacent quantum dots – 30% by default in our app. If no marker falls within this threshold, the whole inner-box is set to be the "source", and the target size is set to the median distance between adjacent dots. The sizing field is then propagated from the source region to the rest of the background mesh so that the ratio between adjacent vertices follow a user-given ratio (a gradation of 1.2 is used by default).

Step 3. A dense tetrahedral mesh of the outer box is computed in 3D using TetGen[293]. Let $s_{\max}$ be the maximum target size of the 2D sizing field computed above. The 2D sizing field is extended through the dense 3D volume so that it is equal to the original field on the top (the surface), and equal to $s_{\max}$ on the bottom.

Step 4. The dense tetrahedral mesh is remeshed with mmg[294] to follow the 3D sizing field.

Finite Element Method. We propose two approaches, one for creating a quick preview of the forces using a linear elastic material model, and a second one for accurate reconstruction using a neo-Hookean material model. For both modes the material parameters are obtained through material testing (Figure 7.6; [150]) and assume no additional external forces, which is a realistic approximation for most experimental setups. We solve for the displacement u

$$-\operatorname{div}(\sigma(u)) = 0 \qquad \text{and} \qquad u = g \text{ on the boundary}, \tag{7.9}$$

where $\sigma(u)$ is the stress tensor and g are the boundary conditions. Note that, the form of $\sigma(u)$ depends on the material model: for linear elasticity

$$\sigma(u) = 2\mu\epsilon(u) + \lambda \operatorname{Tr} \epsilon(u) I, \tag{7.10}$$

with $\epsilon(u) = \frac{1}{2}\left(\nabla u^T + \nabla u\right)$, for Neo-Hookean

$$\sigma(u) = \mu(F - F^{-T}) + \lambda \ln(\det F) F^{-T}, \tag{7.11}$$

with $F(u) = \nabla u + I$.

In both cases, the same boundary conditions g are specified. For the bottom side g is zero, while the for the top side it corresponds to the displacement field reconstructed in Section 7.3. Note that, since a planar displacement field is measured in the xy-direction, we leave the z-direction free to move to account for buckling effects. Since the displacement field is defined only on the vertices of the detected points, radial basis function is used for interpolation with Gaussian kernel[295,296] to extend it to the whole plane. Finally, to obtain the traction forces from the solution of the partial differential equation, we multiply the stress σ with the face normal. We use isoparametric linear Lagrangian elements in both cases.Results of this procedure are shown in Figure 6.1 in the main paper.

7.5 Material Characterization

In a previous publication the mechanical properties of the material was thoroughly characterized[150]. Fitting of the hyperelastic Ogden model[191] achieved a very close recreation of the uniaxial and biaxial material tests. Here, for the sake of implementation and computation speed a linear model and Neo-Hookean model were fitted to the test data. The data was least-square fitted for both uniaxial and biaxial simultaneously. Given the incompressible properties of the silicone used, Poisson ratio was fixed at 0.49 and the only free parameter was the Young's modulus E. The Neo-Hookean model shows a very good fit and deviates only slightly from the Ogden model for large stretches (Figure 7.6). The best overall fit for the linear model was achieved at a lower stiffness off $E = 10.05kPa$, in which case the uniaxial did not match well (Figure 7.6 (a)). Using the same stiffness as for the Neo-Hooke, the uniaxial fit was better, but the biaxial fit quite off (Figure 7.6 (b)). Hence, for accuracy the Neo-Hookean model is chosen, whereas for speed the linear model can be used.

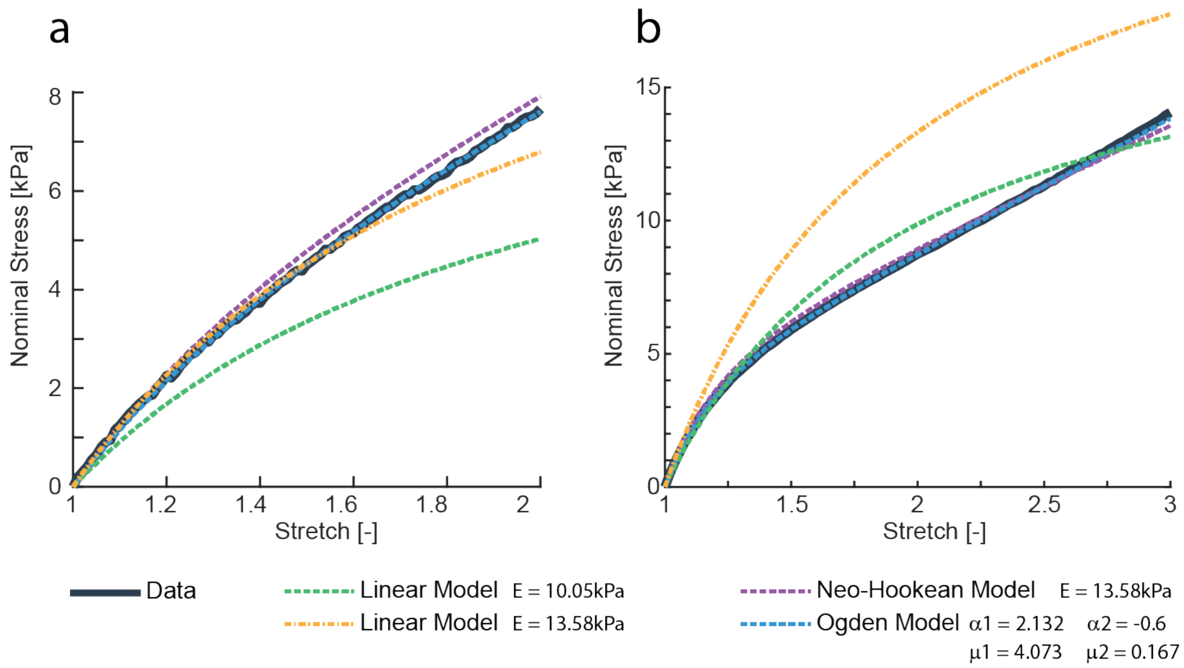

Figure 7.6: Material model fitting. (a) Uniaxial test data and fitted curves. (b) Equibiaxial test data and fitted curves.

8 Bistability of Polar Liquid Crystals in the Collective Adaptation of Endothelia

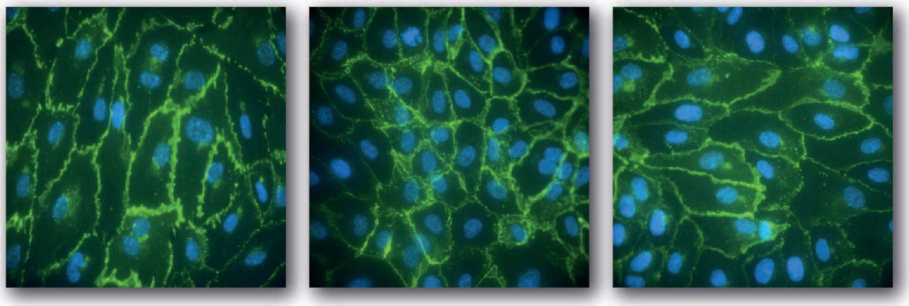

8.1 Introduction

Understanding how cells interact with each other and with their external environment is pivotal in describing the collective nature of multicellular assemblies such as embryos, tissues, and organs[103,297]. Simple physical models stemming from inert soft matter behavior have been successfully proposed to describe such interactions and formulate testable predictions relying on key control parameters[298]. This can be viewed as a form of inverse bio-inspiration where inanimate matter knowledge inspires the explanation of the more complex behavior of animate matter.

A paradigm that proved effective in describing high-density epithelial cell layers comes from liquid crystals: a combination of intrinsic anisotropy and self-propulsion can generate local order within an epithelium, akin to nematic systems comprising rod-shaped molecules[298]. As in inert liquid crystals, the nematic order of epithelia can be locally frustrated yielding topological defects that trigger the apical extrusion of cells from the monolayer[299]. The presence of nematic alignment and topological defects was also observed in other cell types including fibroblasts[300,301]. In this system, analogies with the Freedericksz transition of liquid crystals[302] were useful to explain spontaneous shear flows arising in confined monolayers and their dependence on the confinement width[302].

Human endothelia are an exquisite example of a dense cell system actively responding to flow[303]. Endothelial cells, like epithelial ones, grow to confluence and mature forming a mechanically and biologically-connected monolayer[144]. In *vivo*, endothelia occupy the interface between the lumen of blood and lymphatic vessels and the surrounding tissues[304]. They are naturally exposed to unidirectional flow and flow-generated wall shear stress (WSS). The local hemodynamics provides anisotropic signals fundamentally contributing to tissue maturation and function[305].

Flow induces coordinated planar cell polarity (PCP), whereby cells coherently re-localize cellular compartments, such as the Golgi, and functions[306]. In addition, they adaptively elongate and orient the cell body[307]. Endothelia exposed to unidirectional flow in vitro, polarize to the upstream direction (i.e. against the flow)[306]. Parallel cell elongation is typically observed under low WSS values[308]. At WSS levels higher than 6 Pa, collective cell arrangement falls in a different regime, and perpendicular (to flow) orientation emerges[43,309]. These two orthogonal orientations are similarly observed *in vivo*. The specific angle of alignment and the direction of PCP vary depending on the vascular bed, age, and local hemodynamic conditions[310], with perpendicular alignment observed in locations of the body exposed to high flow, as on the surface of heart valves[311]. Disturbed hemodynamics can compromise this coherent multicellular adaptation[303]. In vivo, regions of vessel stenosis or bifurcation, prone to flow recirculation or reversal, typically feature cells with random PCP and orientation. These locations represent hotspots for the development of inflammatory processes, and are exposed to endothelial denudation and atherosclerosis[310].

Little has been done to explain the collective endothelial adaptation to external physical stimuli, for example by constructing soft matter inspired models. To describe the endothelial response to flow we employed a custom-developed bioreactor[43] and exposed human cells to laminar flow generating low (1.4 Pa) or high (8 Pa) WSS. We monitored two alternative transitions yielding orthogonal collective cell alignment but identical PCP. In both cases, the achievement of coherent organization required dynamic force generation and a transient increase of junctional tension in the monolayer[312].

To explore the physics of this complex behavior, we propose a simple basic description, relying on polar liquid crystal observations. The model features a collection of polar anisotropic active units and incorporates the key symmetries of the problem. Adaptation of polar nematic elements to an external electric field generates two distinct ordered phases characterized by identical polarization but orthogonal alignment. The model enables to simulate the transition between these two ordered phases, revealing the existence of an intermediate state featuring high nematic disorder and slowly relaxing to the alternative ordered configuration. The emergence of such metastable configuration in endothelial monolayers was experimentally verified. A switch in the WSS level or flow directionality induced a randomization of both ordered states, which evolved into an isotropic configuration where collective alignment was lost. This development was rapidly followed by disassembly of cell-to-cell junctions and loss of monolayer integrity. Based on the analogy with polar nematic elements, the transition to an intermediate disordered state can be explained by the inability of cells to simultaneously satisfy requirements of shape and orientation on the one hand, and polarity with respect to the external field, on the other hand.

The resulting physical picture has its origin on the active nature of cells and on the intrinsic functional polarity of endothelia, piecing together a generic mechanism to interpret the effects of hemodynamic perturbations on human tissues.

8.2 Results

To investigate the self-organization ability of human endothelia we monitored their response to flow (Figure 8.1). Monolayers developed in static culture featured cells with weak shape anisotropy and random planar cell polarity (PCP; Supplementary Figure D.1), a condition that represented the starting point for the flow experiments (Figure 8.1a). Fully developed laminar flow coupled to the monolayers of interest was generated in an optically conducive bioreactor[43]. Endothelia were exposed to wall shear stress (WSS) of 1.4 or 8 Pa. Onset of flow prompted a fast response, which induced cell shape elongation and collective orientation (Figure 8.1b-g). During the adaptation to flow, PCP was visualized by the position of Golgi relative to the nucleus[306]. Coherent cell polarity was accomplished within ~2 h (Figure 8.1h-j). Cell shape change and collective alignment proceeded with slower dynamics reaching a plateau after ~6 h (Figure 8.1b-g). At this point, cell ensembles featured a statistically stable collective organization that was maintained for extended exposures to unaltered flow.

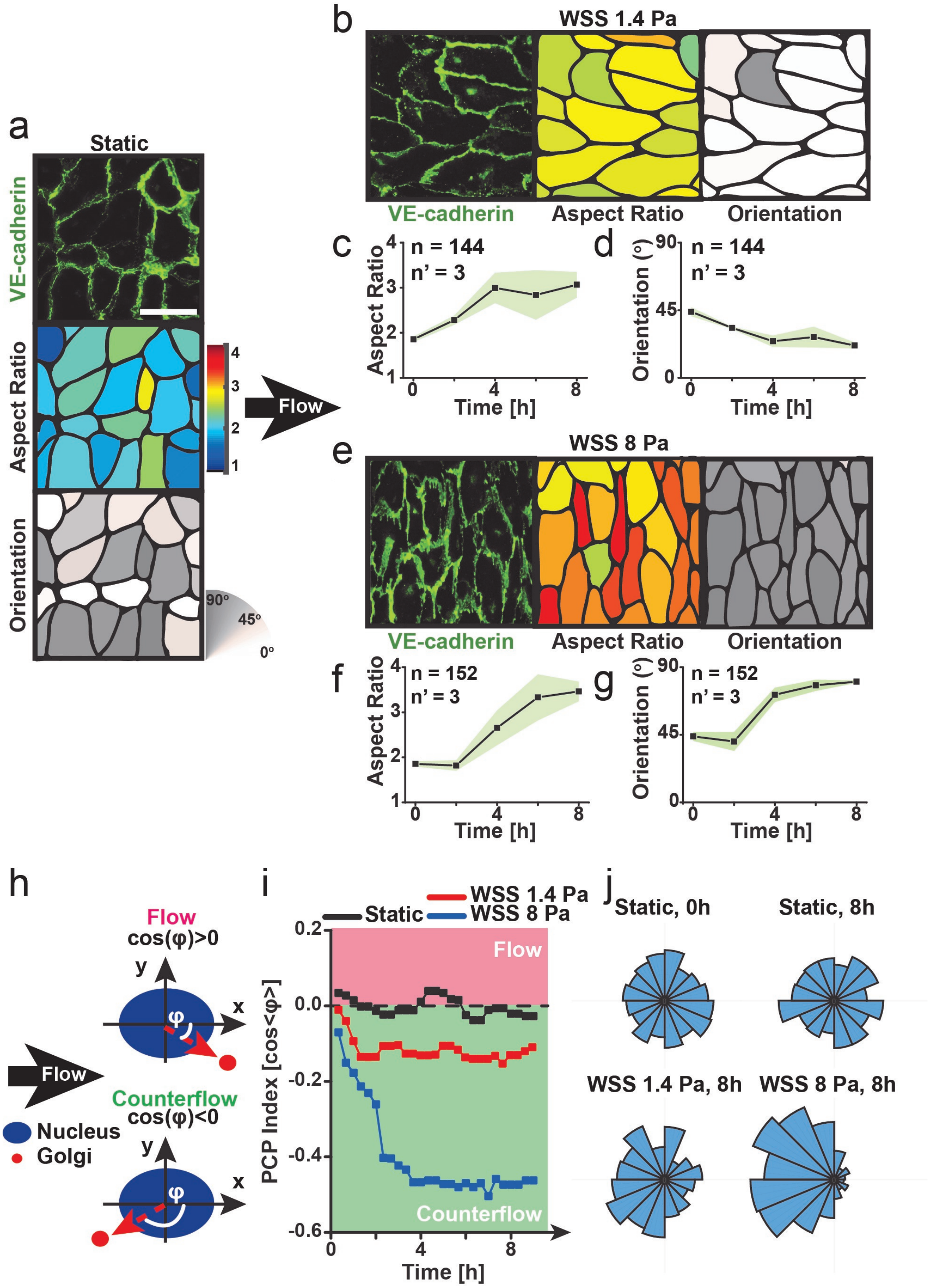
a
Static
VE-cadherin
Aspect Ratio
Orientation
4
3
2
1
90°
45°
0°
Flow
b
WSS 1.4 Pa
VE-cadherin
Aspect Ratio
Orientation
c
n = 144
n' = 3
Aspect Ratio
Time [h]
d
n = 144
n' = 3
Orientation (°)
Time [h]
e
WSS 8 Pa
VE-cadherin
Aspect Ratio
Orientation
f
n = 152
n' = 3
Aspect Ratio
Time [h]
g
n = 152
n' = 3
Orientation (°)
Time [h]
h
Flow
cos(φ)>0
Counterflow
cos(φ)<0
Nucleus
Golgi
x
y
φ
i
Static
WSS 1.4 Pa
WSS 8 Pa
Flow
Counterflow
PCP Index [cos<φ>]
Time [h]
j
Static, 0h
Static, 8h
WSS 1.4 Pa, 8h
WSS 8 Pa, 8h

Figure 8.1: Alternative transitions in endothelial monolayers under flow. Figure on page 96 (**a**) Isotropic state in static conditions and (**b-g**) adaptation to unidirectional flow generating physiological (i.e. 1.4 Pa) or supraphysiological (i.e. 8 Pa) wall shear stress (WSS). Fluorescent images of VE-cadherin distribution (green) at cell-to-cell junctions (top panel in (a), leftmost panel in (b) and (e)). Scale bar is 50 μm. Cell profiles with color-coded aspect ratio (middle panel in (a), (b), and (e)) and cell orientation (bottom panel in (a) and rightmost panel in (b) and (e)) as encoded by corresponding color scale bars . (b) Anisotropic state featuring cell alignment along the direction of flow. Corresponding evolution of cell aspect ratio (c) and orientation. (e) Anisotropic state featuring cell alignment orthogonal to flow. Evolution of cell aspect ratio (f) and orientation (g). The number of analysed fields of view is reported as n and the number of independent experiments as n'. The shaded area indicates the standard deviation. (**h**) Cartoon defining planar cell polarity (PCP) under flow. (**i**) Evolution of PCP in static conditions and upon exposure to unidirectional flow generating WSS values of 1.4 Pa or 8 Pa. (**j**) Radial distribution of PCP (i.e. φ as defined in (h)) in static conditions at 0 h (top left panel) and 8 h (top right panel) and under flow generating WSS of 1.4 Pa (bottom left panel) or 8 Pa (bottom right panel), both at 8h.

Under low WSS (i.e. 1.4 Pa) cell bodies elongated along the flow (parallel alignment at ~0°; Figure 8.1b-d). Exposure to high WSS (i.e. 8 Pa), prompted instead a faster remodeling yielding perpendicular cell alignment (~90° to the direction of flow; Figure 8.1e-g). Interestingly, despite orthogonal orientation, both ordered states featured identical PCP with Golgi positioned upstream of the nucleus (counterflow polarity; Figure 8.1i-j). These emerging responses were not observed in isolated endothelial cells exposed to the same hydrodynamic conditions.

Taken together, these results confirm that endothelial cells in confluent monolayers coordinately adapt shape, alignment and polarity in response to flow. Collective cell body elongation and alignment depend on the WSS level. On the other hand, PCP reflects flow directionality (Figure 8.1). To assess whether cell orientation and polarity represent independent collective properties of mature endothelia, we generated monolayers on anisotropic substrates in static conditions[43]. Topographic contact guidance was effective in inducing cell elongation and alignment along the direction of the gratings. Notwithstanding the strong and coherent orientation of cell shape, PCP remained randomly distributed (Supplementary Figure D.2) demonstrating that the two properties can be fully decoupled.

We next investigated the dynamics of monolayer transition to either of the two flow-driven ordered states (Figure 8.2). Confocal traction force microscopy (cTFM), a recently introduced method to obtain a direct visualization of cell tractions on compliant substrates[150,194,249], was employed. Cells transmitted distinctive patterns of traction to the substrate during collective orientation and polarization (Figure 8.2a and d). A force peak was measured between 2 and 6 h from the onset of flow (Figure 8.2a-b and d-e). The system relaxed as soon as the majority of cells reached the final orientation, shape, and PCP. In addition, using monolayer stress microscopy[125], intercellular stresses were mapped (Figure 8.2c and f), further revealing tension maxima during the adaptation phase. Traction and stress peaks were significantly higher during evolution to perpendicular alignment (WSS = 8 Pa), yet the trend and dynamics were similar between the two orthogonal transitions. Intercellular stresses similarly relaxed upon attainment of global order[313].

Liquid crystal models have proven helpful in describing state transitions in epithelial monolayers, as function of cell density, anisotropy (i.e. a nematic index), and self-propulsion[314]. Such models however, do not include the effect of an external field and can therefore not distinguish states with orthogonal collective orientation. On the contrary, polar liquid crystal models[315] contemplate alternative transitions of nematic particles with positive or negative dielectric anisotropies (i.e. $\Delta\varepsilon$).

A monolayer of polar and weakly nematic elements with positive (Figure 8.3a) or negative (Figure 8.3b) dielectric anisotropy was initially allowed to spontaneously relax. In this phase, the nematic index increased as a function of time (from time = 0 to 100), enabling the attainment of nematic order, akin to what described in epithelial monolayers[300]. The switch of an external electric field triggered a global configuration change, with a sharp increase of disorder (time = 102) followed by a monotonous relaxation to a highly ordered state (time = 102). Specifically, nematic elements with $\Delta\varepsilon > 0$ aligned along the field direction, while orthogonal alignment was obtained with $\Delta\varepsilon < 0$. Both ordered states featured the same polarization.

The qualitative agreement with the reported response of endothelial monolayers exposed to flow (Figure 8.1) was further validated by the direct measurement of the energy landscape characterizing the alternative transitions. Free energy was computed from the number of nematic defects present in each intermediate configuration (see Supplementary Information, section ‘Modeling Nematic Liquid Crystals’). For both transitions (Figure 8.3a-b), a free energy peak, indicative of a non-equilibrium state, was reached upon the field switch and was relaxed (decreased) as soon as a high level of order was obtained (Figure 8.3c-d). These trends were compared with the relative strain energy measured upon endothelial adaptation to flow, yielding similar bimodal energy increase and relaxation (Figure 8.2c and f and Figure 8.3c-d). This analogy suggests that the phase of instability experienced by nematic systems responding to an external field may correspond to the observed peaks of junctional tension in endothelia adapting to flow (Figure 8.2c and f).

We next inquired the model about the evolution of either ordered states when forced to develop into the orthogonal configuration (Figure 8.4). This transition was induced by switching the sign of $\Delta\varepsilon$ (at time = 160), from positive to negative (Figure 8.4a) or from negative to positive (Figure 8.4b). In both cases, the nematic system rapidly evolved to a configuration with higher disorder, from which it slowly escaped (at time = 250) relaxing into the alternative ordered state. The energy profile of these evolutions indicate the transition into a persistent, metastable state characterized by a high level of free energy (Figure 8.4c-d). This metastable state similarly appeared when the system was perturbed by a switch in the field direction (Supplementary Figure D.3).

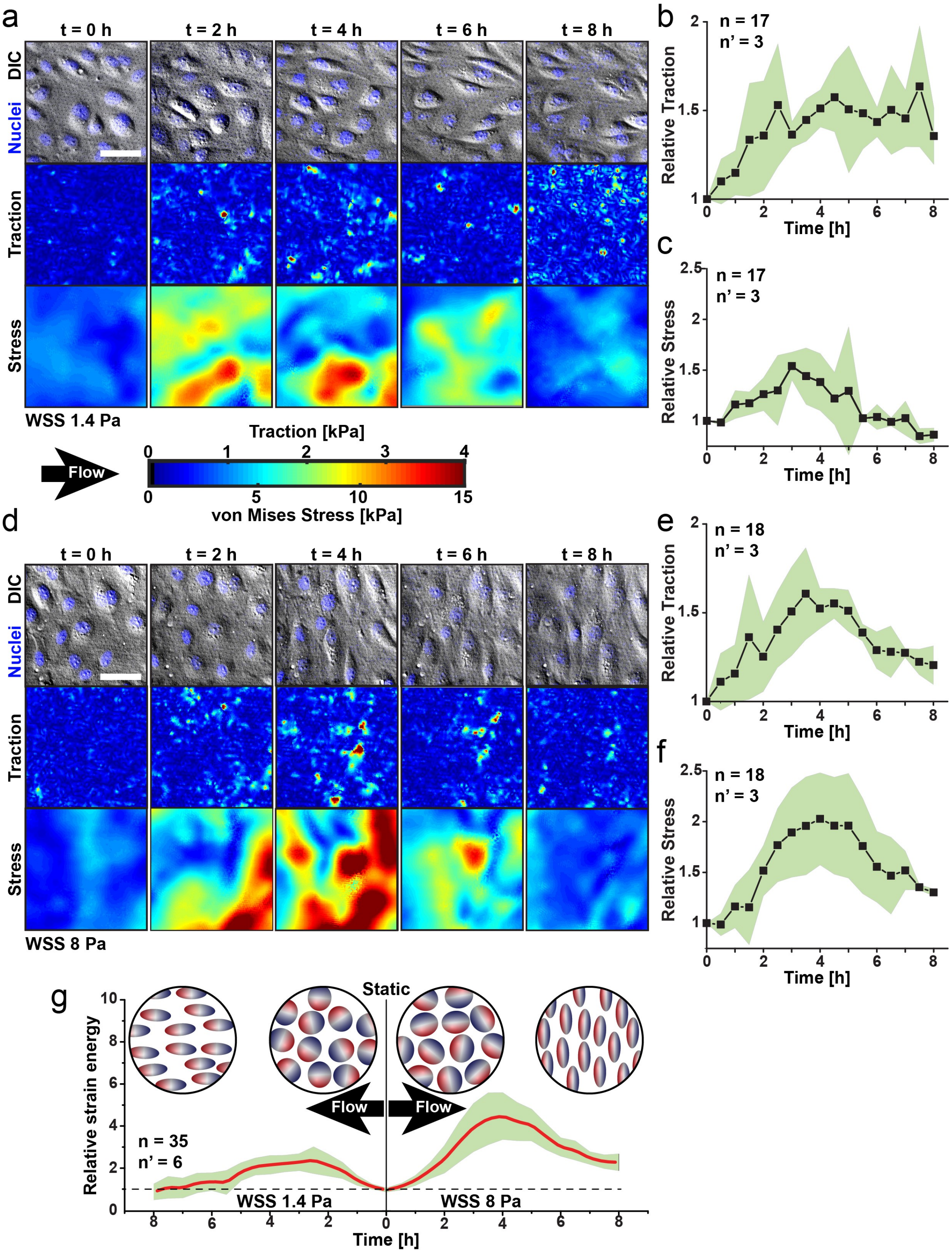
a
t = 0 h
t = 2 h
t = 4 h
t = 6 h
t = 8 h
DIC
Nuclei
Traction
Stress
WSS 1.4 Pa
Traction [kPa]
0
1
2
3
4
Flow
0
5
10
15
von Mises Stress [kPa]
b
n = 17
n' = 3
Relative Traction
Time [h]
c
n = 17
n' = 3
Relative Stress
Time [h]
d
t = 0 h
t = 2 h
t = 4 h
t = 6 h
t = 8 h
DIC
Nuclei
Traction
Stress
WSS 8 Pa
e
n = 18
n' = 3
Relative Traction
Time [h]
f
n = 18
n' = 3
Relative Stress
Time [h]
g
Static
Flow
Flow
Relative strain energy
n = 35
n' = 6
WSS 1.4 Pa
WSS 8 Pa
Time [h]

Figure 8.2: Traction and stress during alternative transitions in endothelial monolayers under flow. Figure on page 99 (**a**) DIC images and fluorescent nuclei (top row), traction force (middle row) and intercellular stress (bottom row) maps for endothelia exposed to unidirectional flow generating WSS of 1.4 Pa. Scale bar is 50 μm. Relative evolution of (**b**) traction force and (**c**) intercellular stress (bottom plot). (**d**) Corresponding DIC and nuclei (top row) and traction and stress maps (middle and bottom rows; respectively) for endothelial exposed to unidirectional flow generating WSS of 8 Pa. The flow direction is indicated by a black arrow. The magnitude of traction and intercellular stress is indicated by the color scale bar. (**e**) Relative evolution of traction and (**f**) stress. Mean values (black squares) are plotted (b-c, and e-f). (**g**) Relative strain energy produced by the endothelium during the transition from the initial isotropic state (static) to the alternative anisotropic states. The shaded green area correspond to the standard deviation. A corresponding representation of the polar nematic states is displayed in the circular cartoons. The number of analysed fields is reported as n and the number of independent experiments as n'.

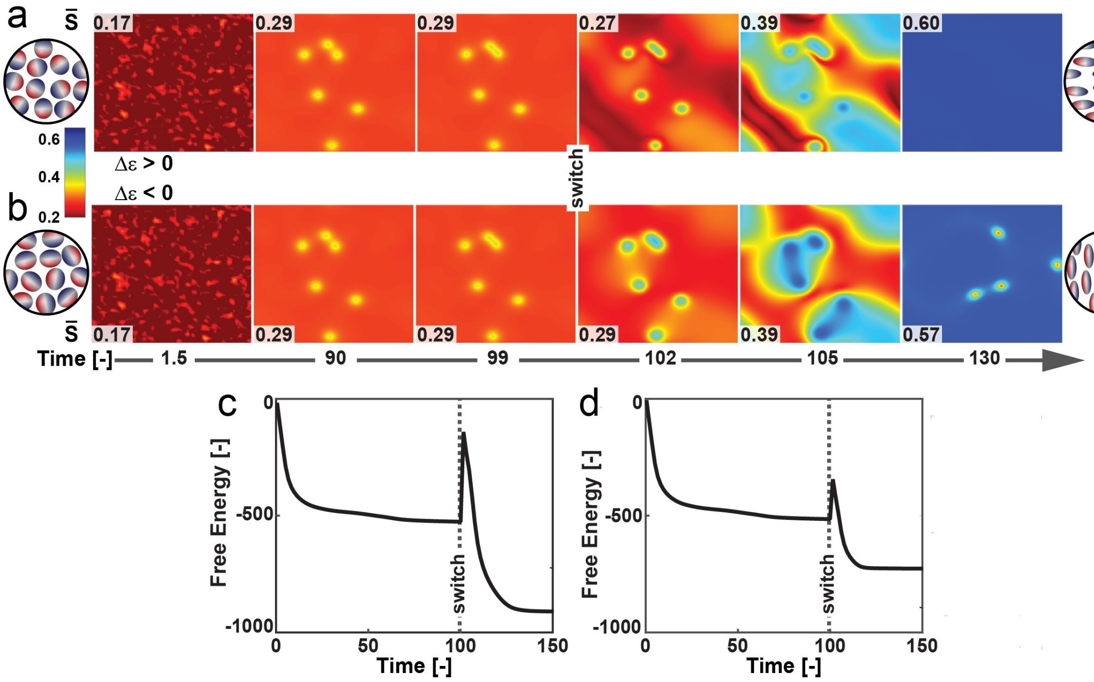

Figure 8.3: System transitions in polar nematic crystals. (**a**) Heat maps of the transient order parameter $\bar{S}$ for nematic particles with polarity along the long their axis ($\Delta\varepsilon > 0$). (**b**) Corresponding heat maps for nematic particles with polarity along their short axis ($\Delta\varepsilon < 0$) Both (a) and (b) are initiated with the same random configuration. At t = 100 the electric field is switched on. (**c**) Free energy of the transition depicted in (a). (**d**) Free energy of the transition depicted in (b).

The same transitions were experimentally reproduced in endothelial monolayers. Perturbation of fully aligned endothelia (Figure 8.4e and i) were obtained by increasing (Figure 8.4e-h) or decreasing (Figure 8.4i-l) the WSS. The multicellular systems quickly reacted evolving towards an isotropic state where coherent cell alignment and elongation were lost (Figure 8.4f-h and j-l). Cell polarity was not significantly affected by the perturbation. The same transition

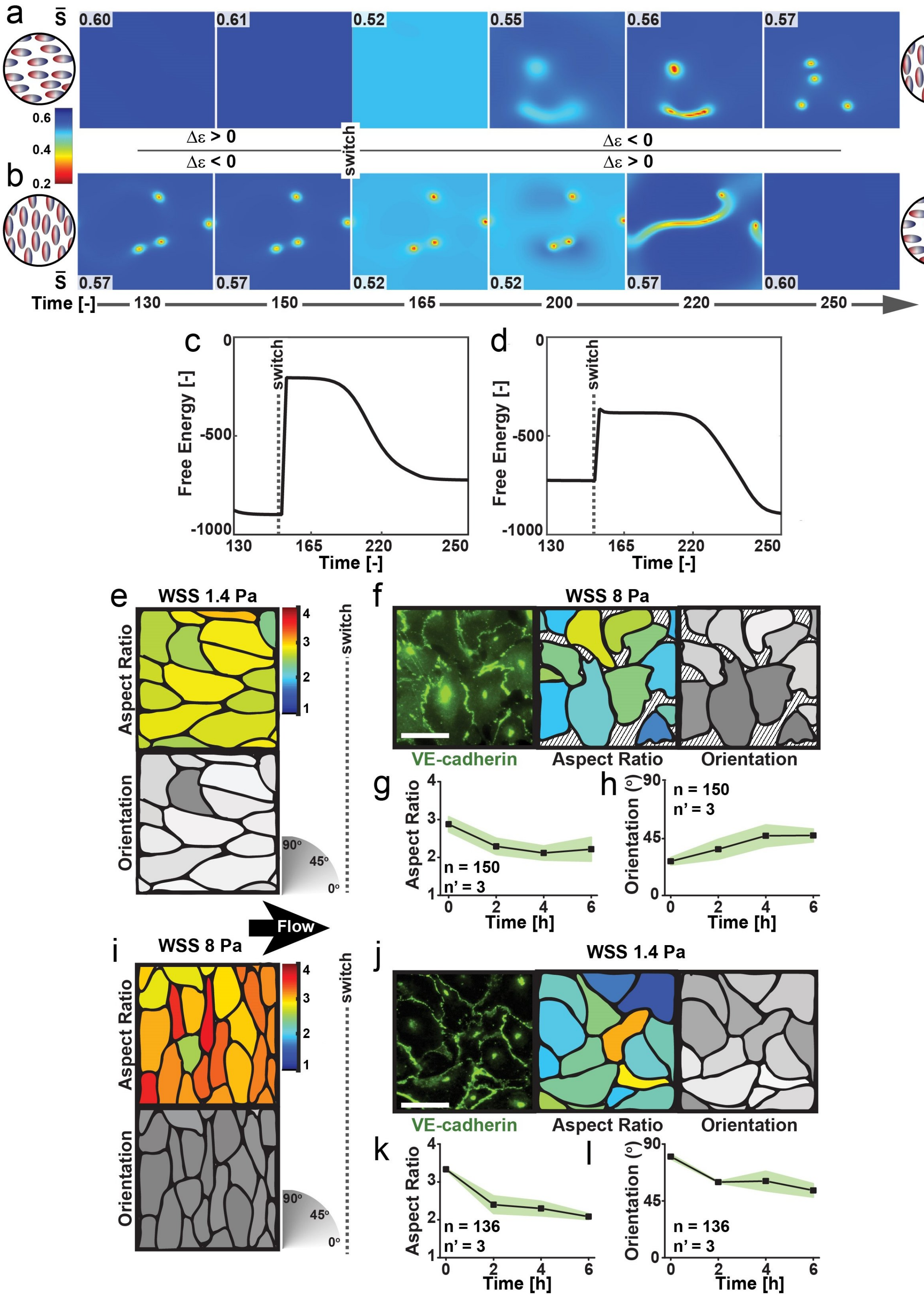
a
s̄
0.60
0.61
0.52
0.55
0.56
0.57
0.6
0.4
0.2
Δε > 0
Δε < 0
switch
Δε < 0
Δε > 0
b
s̄
0.57
0.57
0.52
0.52
0.57
0.60
Time [-]
130
150
165
200
220
250
c
Free Energy [-]
0
-500
-1000
switch
130
165
220
250
Time [-]
d
Free Energy [-]
0
-500
-1000
switch
130
165
220
250
Time [-]
e
WSS 1.4 Pa
Aspect Ratio
4
3
2
1
Orientation
90°
45°
0°
switch
f
WSS 8 Pa
VE-cadherin
Aspect Ratio
Orientation
g
Aspect Ratio
4
3
2
1
n = 150
n' = 3
0
2
4
6
Time [h]
h
Orientation (°)
90
45
0
n = 150
n' = 3
0
2
4
6
Time [h]
Flow
i
WSS 8 Pa
Aspect Ratio
4
3
2
1
Orientation
90°
45°
0°
switch
j
WSS 1.4 Pa
VE-cadherin
Aspect Ratio
Orientation
k
Aspect Ratio
4
3
2
1
n = 136
n' = 3
0
2
4
6
Time [h]
l
Orientation (°)
90
45
0
n = 136
n' = 3
0
2
4
6
Time [h]

Figure 8.4: Disruptive transitions in endothelial monolayers upon variation of flow intensity. Figure on page 101 **(a,b)** Transient order parameter $\bar{S}$ for aligned nematic particles with switching polarity from $\Delta\varepsilon > 0$ to $\Delta\varepsilon < 0$ for (a), vice-versa for (b). The switch of polarity occurs at t = 165. **(c)** Free energy of the transition depicted in (a). **(d)** Free energy of the transition depicted in (b). **(e)** Anisotropic state featuring cell alignment along the direction of flow generating physiological (i.e. 1.4 Pa) wall shear stress (WSS) and **(f-h)** maladaptive rearrangement to WSS increase (from 1.4 Pa to 8 Pa). Fluorescent images of VE-Cadherin distribution (green) at cell-to-cell junctions (top panel in (a) and (i), leftmost panel in (f) and (j)). Scale bar is 50 μm. Cell profiles with color-coded aspect ratio (middle panel in (e), (f), and (j)) and cell orientation (bottom panel in (e) and (i) and rightmost panel in (f) and (j)) as encoded by corresponding color scale bars. (f and j) Isotropic intermediate states featuring intercellular gaps (regions identified by black lines). Corresponding evolution of cell aspect ratio (g and k) and orientation (h and l). **(i)** Anisotropic state featuring cell alignment perpendicular to the direction of flow generating supraphysiological (i.e. 8 Pa) wall shear stress (WSS) and **(k-m)** maladaptive rearrangement to WSS decrease (from 8 Pa to 1.4 Pa). The number of analysed fields of view is reported as n and the number of independent experiments as n'. The shaded area indicates the standard deviation.

was observed upon switching the flow direction (Supplementary Figure D.3c-f). The strength of cell-to-cell junctions during the transition was evaluated through the immunostaining of VE-cadherin distribution and phosphorylation[305]. This analysis revealed that hydrodynamic perturbations significantly decreased the junctional stability along with the loss of collective order (Supplementary Figure D.5). The intermediate disordered state was, in fact, non-conducive to further development and led to a loss of monolayer integrity, with the formation of gaps between cells and ensuing cell loss.

8.3 Discussion

Coordinated movement of epithelial sheets, observed during tissue morphogenesis, manifests itself through the collective organization of cell shape and orientation. Explaining these complex activities can be facilitated by rationally adapting physical models developed for dense nematic systems of inanimate particles[268,297]. This analogy extends to capture specific tissue properties, such as the emergence of local topological defects that, in mature tissues, enable the control of global density and homeostasis[299,316]. Adult epithelia retain a functional level of plasticity to respond to external mechanical stimuli, whereby tissue fluidity can be transiently reactivated adapting to a dynamic physical environment[317]. At the fundamental level, subtle variations of cell shape and junctional tension can stir the system towards a pathological response, as observed in asthma[317] and cancer[318].*In silico* models are able to reproduce these maladaptive processes and individuate their key control parameters.

Much of this largely unexpected behaviour can also manifest itself as collective coordination in endothelial ensembles, naturally developed to interact with a mechanical environment dominated by hemodynamic loads. Onset of autonomous circulation at birth exposes the vasculature to a complex mechanical landscape, in which the tissue must develop to serve a growing body. The control of shape changes and cell orientation renders a vascular tree, which radiates larger vessels from the heart and tapers in the body periphery. Yet, the intrinsic endothelial plasticity proves insufficient to adapt to local flow perturbations, such as those induced by stenosis or deployment of cardiovascular implants. Excessive flow intensity increase or decrease, or regions of flow recirculation represent hotspots for inflammatory processes mining the stability of endothelial junctions[305], and therefore of the overall monolayer. These are locations where endothelial denudation precedes the development of atherosclerotic lesions[319].

Such behaviour generates important and extremely interesting questions, such as, why does a distinctive global order emerges in different locations of the vasculature? Or, why do adult endothelia fail to adapt to variations of flow directionality or intensity? It is clear that the physical description of endothelial monolayers poses new challenges, which go beyond the capabilities of models developed for epithelial tissues. The explanation lies in the unique nature of the stimulus instructing endothelial adaptation: A vector quantity encoding at once directionality, which drives cell polarization, and intensity, for structural remodelling. Two information that are processed independently, yielding distinct multicellular configurations.

Polar liquid crystals provide a physical description, which, as we observed in the endothelial cell layer, incorporates alternative responses to an external directional stimulus. The model includes constitutive elements with opposite dielectric anisotropies and resolves nematic states with orthogonal collective alignment but identical polarization. On the resulting phase diagram, the transition between the two distinct ordered states crosses an intermediate non-nematic phase characterized by high levels of disorder. When this model is applied to describe endothelial systems, it predicts the emergence of a random tissue configuration upon variations of flow direction or intensity. Experimentally, the transition comes to an end by a disruptive junctional remodelling and eventually leads to loss of tissue integrity.

This catastrophic event may not be considered as a maladaptive response *per se*, and thus rooted in the downstream biological signalling, but rather an intrinsic property of a system that once primed by an external (mechanical or electric) field, loses plasticity and thus adaptability. In this line of thinking, the pathological trigger would be encoded by the variation of local hemodynamics. Endothelial tissues, like polar nematic crystals, may only be able to adapt once, but not several times.

8.4 Materials and Methods

8.4.1 Cell culture, substrate coating and seeding

Primary human umbilical vein endothelial cells (HUVECs; Invitrogen, USA) were grown in medium 200PRF supplemented with fetal bovine serum 2% v/v, hydrocortisone 1 mg/ml, human epidermal factor 10 ng/ml, basic fibroblast growth factor 3 ng/ml and heparin 10 mg/ml (all reagents from Invitrogen) and were incubated at 37°C and 5% CO_2. All reported experiments were performed using cells with less than six passages *in vitro*.

Silicone substrates were incubated in a custom-built vacuum oven at 90°C for 4 h, washed 1 min in methanol and incubated for another 2 h in the vacuum to remove ligands. They were subsequently coated with 1,5% gelatin (104070, Merck Millipore, USA). Finally, the surfaces were washed twice with warm PBS before applying medium and seeding cells at desired concentrations. To generate a confluent monolayer, cells were seeded on the surfaces at high density (3.5-5 x 10^4 cell/cm^2) and cultured for three days (Supplementary Figure D.1)[320]. In developing endothelial monolayers, cell motility decreased and collective motion emerged as a function of local density. However, even upon proliferation arrest, endothelial cells continued to be motile and exchange neighbors (Supplementary Figure D.1).

8.4.2 cTFM

The two components of CY52-276 polydimethylsiloxane (Dow Corning) and 0.05% (v /v) poly(dimethylsiloxane-b-ethylene oxide; Polysciences) were mixed thoroughly at a ratio of 9:10 (A:B) which provides an elastic modulus of ~12.6 kPa[150] for 5 min, degased for 2 min and spin-coated on 170 μ thick cyclic olefin copolymer (COC) for 1 min at 1500 rpm to achieve a target thickness of ~35 μm. The silicone was then cured at 70°C for 30 min. Substrates were then maintained in a clean, dust-free and dry environment to prevent fouling until use. To avoid ageing, samples were used 2 weeks after fabrication.

Red quantum dot nanodiscs were deposited on the substrate by electrohydrodynamic nanodrip printing with a spacing of 3-5 , as previously reported[150].

8.4.3 Flow experiments

A custom-designed parallel plate flow chamber was used to apply a unidirectional laminar flow yielding a constant shear stress of 1.4 or 8 Pa to endothelial monolayers as reported previously[43,321,322].

To analyse planar cell polarity, endothelial cells were incubated for 16 h at 37°C with the CellLight Golgi RFP (Bac Mam, Invitrogen) for visualization of the Golgi apparatus (2 μl/10^4 cell in media). Media was then exchanged and cells were stained with NucBlue (2 drops/ml of media; NucNlue Live ReadyProbes Reagent, R37605, ThermoFisher) 35 min before the experiment. The substrates supporting fluorescently labeled monolayers were then placed mounted in the flow bioreactor.

8.4.4 Antibodies

The following primary antibodies were used: goat polyclonal anti-VE-cadherin (1:200, sc-6458, Santa Cruz Biotechnology), mouse monoclonal anti-YAP/TAZ (1:100, sc-101199, Santa Cruz Biotechnology), rabbit polyclonal anti-pY658-VEC[305] (1μg/ml), mouse monoclonal anti-vinculin (1:400, V9131, SIGMA Aldrich). The secondary antibodies were donkey anti-goat–Alexa 488 (Invitrogen, A11055) and donkey anti-mouse-Alexa 555 (Invitrogen, A21202) and chicken anti-rabbit- Alexa 647 (Invitrogen, A21443).

8.4.5 Immunostaining

HUVECs were fixed for 20 min with 2% paraformaldehyde (PFA) at room temperature. Next, the cells were permeabilized with 1% Triton x-100 in PBS for 5 min. After washing the samples three times for 5 min with PBS, they were incubated in 5% w/v bovine serum albumin (Sigma-Aldrich, USA) in PBS for 2 h at room temperature. The samples were incubated with the respective antibodies (See Antibodies section) or with TRITC-phalloidin (Sigma Aldrich), overnight at 4°C.

Subsequently, the samples were rinsed 2 times for 30 min with PBS and then 2 times for 30 min with 5% BSA in PBS. They were then incubated with the corresponding secondary antibodies for 45 min at room temperature. Finally, the samples were washed 4 times for 30 min with PBS. For staining of nuclei, Hoechst was added at 10 μg ml^{-1} during a washing step.

8.4.6 Cell microscopy

Cell adaptation to flow was monitored using an inverted Nikon-Ti wide-field microscope (Nikon, Japan) and an incubation chamber (Life Imaging Services, Switzerland). Both the flow bioreactor and the medium reservoir were maintained at a controlled temperature of 37°C and CO_2 concentration of 5%. Images were collected with a 20x, 0.45 NA long-distance objective (Plan Fluor, Nikon, Japan). Time-lapse experiments were set to routinely collect images, in different spatial positions of the sample, in the DAPI (nuclei) and TRITC (Golgi apparatus or fluorescent QDs) channel with a time resolution of 20 or 30 min.

VEC, Actin, and cell nuclei distribution were acquired in immunostained samples using a 60X, 1.4 NA oil immersion objective (Plan Fluor, Nikon, Japan), and the FITC, TRITC and DAPI filter; respectively. Samples were images with an inverted Nikon-Ti spinning disk confocal microscope (Nikon, Japan) equipped with an Andor DU-888 camera (Oxford Instruments, UK) and a pE-100 LED illumination system (CoolLED Ltd, Andover, United Kingdom).

8.4.7 Modeling of nematic system transitions

We adapted and used a publicly available, previously published algorithm for modeling the nematic system transitions[315]. We looked at both positive (dipole moment along the long molecular axis, $\Delta\varepsilon > 0$) and negative (dipole moment along the short molecular axis, $\Delta\varepsilon < 0$) dielectric anisotropies and two different electric field orientations ($\mathbf{E} = [E_x, E_y.E_z] = [1,0,0]$; $\hat{\mathbf{E}} = [0,1,0]$). What follows below is a brief summary of the model and the parameters we used in the simulations. Please see Ref[315] for full details.

The orientational order of the nematic liquid crystal is given by the tensor $\mathbf{Q}$. For a uniaxial system whose molecular orientation is defined by the unit vector $\mathbf{u}$, the we can write, $\mathbf{Q} \equiv S(\mathbf{n}\mathbf{n}^T - \frac{1}{3}\mathbf{I})$, where $S = \langle cos^2\Theta\rangle - \frac{1}{3}$ is the scalar order parameter,$\mathbf{n}$ is the director (in nematic liquid crystals, the rod-like molecules orient themselves in space along an arbitrary direction called the director), I is the identity matrix, and Θ is the angle of the rods with respect to the director ($cos\Theta = \mathbf{n}\cdot\mathbf{u}$).

8.4.8 Image analysis

A measure for cell orientation and aspect ratio was obtained from the DIC images using the “Freehand selection” tool of Fiji (National Institute of Health, USA). The initially obtained values, in degrees, have a range of 0° to 90°. A value of 0° indicates perfect, parallel to the flow alignment, whereas an alignment of 90° corresponds to an alignment perpendicular to the flow. A value of 45° depicts that no preferential alignment of the structures exists in the image and therefore such values where calculated for randomly oriented endothelia under static conditions (i.e. isotropic endothelia). For the calculation of the aspect ratio, an ellipsoidal fit was used. The ratio of the long to the short axis yields the cell aspect ratio.

The evolution of planar cell polarity (PCP) in monolayers was monitored using a custom developed algorithm utilizing Imaris and MATLAB (Supplementary Figure D.4). First, fluorescent time lapse images of the cell nuclei and Golgi were imported in Imaris (Bitplane). Structures were individuated using the spot detection frame-wise in Imaris. The coordinates of the cellular structures were then imported to MATLAB, where they were processed with the following protocol: from the detected nuclei a Voronoi tessellation was generated. Detected Golgi that are located within a Voronoi cell of a nucleus, are associated to that respective nucleus. For cases that more than one Golgi was detected, the final position was determined by averaging their weighted positions. The weight for the positions decreased with increasing distance from the nucleus. Last, a vector from the center of the nucleus to the weighted Golgi position was created. The vector's angle with the direction of flow (φ)was then used to calculate the PCP index (cos φ).

For the migration experiments, the nuclei were initially detected using Imaris. The position of the nuclei over time was then tracked in MATLAB using a custom made algorithm. The lower detection limit for actual migration was set to 10 μm/h, below which the cells were considered stationary. Data for migration velocity were automatically extracted using MATLAB.

Pathfinding measures were performed using cell tracking software Imaris (Bitplane Scientific Software, Switzerland). Time-lapse videos were uploaded into Imaris, and the voxel size and time interval were adjusted before particle tracking. The velocity and density of the cells was obtained by tracking the migration of individual cells over time until confluency.

Cell image velocimetry (CIV)[264] toolbox was used for the correlation length calculation. The velocity fields (u and v) in the two direction (x and y) were provided by the CIV analysis.

The magnitude of the velocity M was calculated with Matlab using the velocity fields: $M = (u(x,y)^2 + v(x,y)^2))^{\frac{1}{2}}$. For all purposes, the mean velocity was subtracted from calculated velocity field to avoid any drift-related bias and to get the fields.

To estimate the distance over which movements are correlated, the velocity spatial correlation function C_{vv} was calculated. The velocity correlation function C_{vv} were fitted with a decreasing exponential function of the form $f(r) = e^{-(r/CL)}$ in order to extract the velocity correlation length C_L.

Traction forces were calculated frame-by-frame utilizing the cTFM software[150]. The detection and meshing was done in MATLAB, as described previously[150]. For the calculation of intercellular stresses, the protocol suggested from Tambe et al[125] was used. According to this, for each spatial and temporal position the intracellular stresses were calculated. The total strain energy was calculated according to Butler et al.[117] by integrating over the surface the dot product of tractions and displacements.

For the colocalization analysis, the Pearson's coefficient was extracted from each image stack using the colocalization section of Imaris (Bitplane, Switzerland). Before the colocalization analysis, the "Background Subtraction" function of Imaris was applied to both the blue and red channels. During the colocalization analysis, threshold values calculated based on[323] were imposed for both channels.

8.4.9 Proliferation assay

The DNA synthesis–based cell proliferation assay was performed using a commercially available Click-iT EdU Imaging Kits Protocol (Thermo Fisher Scientific) and following the manufacturer recommendations. 3.5-5 x 10^4 cell/cm^2 endothelial cells were seeded on the substrates and incubated overnight with 10 μM 5-Ethynyl-2'-deoxyuridine (EdU) labeling solution before the fixing (day 0, 1, 2, 3 and 6). After fixation with 4% formaldehyde and permeabilization with 0.5% Triton X-100 in PBS, samples were stained and imaged using a fluorescence microscope.

8.4.10 Statistical analysis

The Shapiro-Wilk test was used to test for normality of data. For non-normal distributed data, Mann–Whitney U test or Wilcoxon signed-ranked test was performed. Boxes in all box plots extend from the 25^{th} to the 75^{th} percentiles, with a line at the median and a square representing the mean. Whiskers extend to 1.5x IQR (inter-quantile range) or the max/min data points if they fall within 1.5xIQR. The total number of events counted is shown in the graphs. The number of independent experiments is reported as n' and the number of total fields of view or cells analysed is shown as n.

Part IV

Conclusion and Outlook

9 Conclusion

The aim of this thesis is to describe the development of a traction force platform that overcomes limitations of available methods and demonstrate its use to distill information, generate cell models, and make predictions. With cTFM such a tool becomes available. It enables entirely reference free measurement of directional cellular traction forces without introducing topography.Downstream processing is now possible, for example to colocalize protein expression and force generation through immunofluorescence or for the live assessment of forces in an ongoing experiment.

My follow-up project to cTFM saw the development of Cellogram - a stand-alone software with robust and fast analysis algorithms for the calculations of traction forces. The two technologies combined permit high throughput traction force microscopy and have the capacity for on-the-fly measurements.

The cTFM platform demonstrated its capabilities on multiple use-cases for single cells. First, on fibroblasts, where we measured the forces that single focal adhesions (FAs) can generate. A correlation between adhesion size and force generated was found, by colocalizing paxillin and tractions. For HeLa and MCF-7 cancer cells we measured the tractions that FAs generated as a function of phosphorylated paxillin and cell cycle phase. For HeLa cells we also determined the correlation length of force generation in a high throughput data analysis. In a further study, we found the temperature dependence of mechanical activity in HeLa cells.

The platform can also be applied to the study of cell collectives. We successfully employed cTFM with MCF-10A epithelial cells. Here, we measured different levels of tractions depending on the population's collective phase. Monolayers that exhibited liquid phase properties generated higher tractions than monolayers in a solid-like phase. cTFM was also easily used in combination with flow chambers. There we exposed human umbilical vein endothelial cell (HUVEC) monolayers to varying levels of wall shear stress induced by the flow of medium across the cell surface. The measurements of tractions, as well as cell polarity and alignment, gave us a good foundation for the application of a sophisticated simulation. This simulation successfully modelled the monolayer of HUVECs as polar, nematic liquid crystals.

10 Outlook

cTFM was developed as a complete package containing both the hardware to collect data as well as the software to analyse the collected data. Since its commissioning, the cTFM package has been applied to several use cases, ranging from single cell experiments to monolayer, and from static single images to time series. With the development of Cellogram, cTFM received an upgrade on the software side. Not only is Cellogram much faster than its previous software package versions, but it is completely stand alone. This means it does not require any third-party commercial software. On top of that, Cellogram is also applicable to other reference free traction force methods. This software will be released for the public use upon publication.

While there has been an iteration and an upgrade on the software side of cTFM, the hardware side is still as it was when cTFM was published. The next iteration of improvement should therefore focus on improving the physical cTFM platform, that is the silicone layer with the printed quantum dot (QD) nanodisc arrays on top.

Printing. Currently the QDs are deposited through electrohydrodynamic (EHD) nanodrip printing. This printing process has the advantage of being versatile with respect to the inks used, as well as the geometry printed. However, both these advantages are not crucial for cTFM. Furthermore, the printing is restricted to an area of 300 x 300 μm^2. For cTFM the printed geometry is always identical, with only the spacings between the QD nanodiscs varying from sample to sample. Here, instead of EHD printing, lithography could be a very useful process for repeatedly producing the same geometry. It is inherently faster than a printing process. With modern techniques, the error of positioning the QD nanodiscs through lithography could be kept at a similar or even lower level as compared to EHD printing. Developing a protocol for manufacturing cTFM substrates with a lithography step would permit larger QD nanodisc arrays and production time would decrease.

Mechanical characterization. Currently, there exists one material fully characterized and soft enough for cTFM. Cellogram already accommodates different materials and models, but in order to expand the capabilities of cTFM to both weaker and stronger cells, new materials need to be characterized. Developing a larger arsenal of precisely characterized materials is desirable. At this point, it would also be interesting to investigate these materials on microscale instead of using macroscopic tests. The scale at which materials are probed has been shown to influence the results, especially for fibrous materials.

3D TFM. For the cell types tested in this thesis, the 2D platform with the capacity to measure out-of-plane forces suffices. Not all cells, however, form planar structures like epi- and endothelial cells do. For these cell types, a 3D reference free traction force method has yet to be developed. This is a very challenging task, as every step in the pipeline becomes more difficult. Fabrication needs entirely new processes to build 3D scaffolds, and imaging within these scaffolds requires good resolution in all three spatial dimensions. Reference position reconstruction and force calculation also become much more involved. Nevertheless, this would be an interesting project, which would enable approaches to measure cellular forces in realistic environments for many more cell types.

Appendices

A Supplementary Information: Confocal Reference Free Traction Force Microscopy

A.1 Stability of QDs

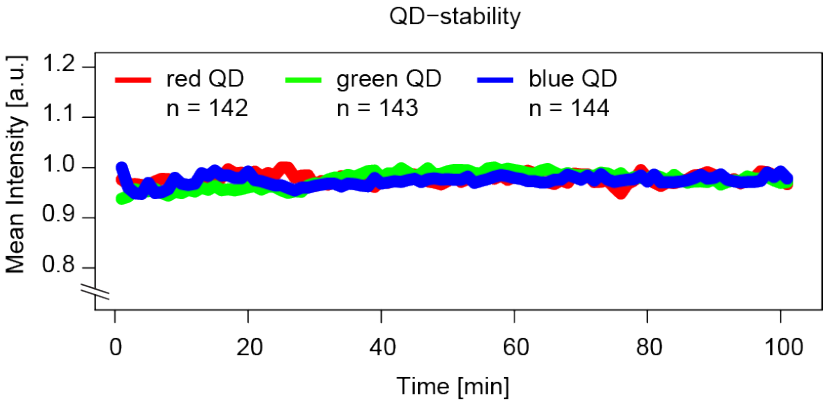

Figure A.1: Stability of QDs. Red, green and blue QD nanodiscs were printed on elastic silicone, post treated and immersed in cell culture medium for 30min. Imaging of the fluorescent array was then performed every 1min for 100 time steps and mean intensity of QD nanodiscs was measured. Small fluctuations are caused by focal drift during imaging. n: number of analysed QD nanodiscs.

A.2 Mechanical and optical properties of CY52-276 silicone

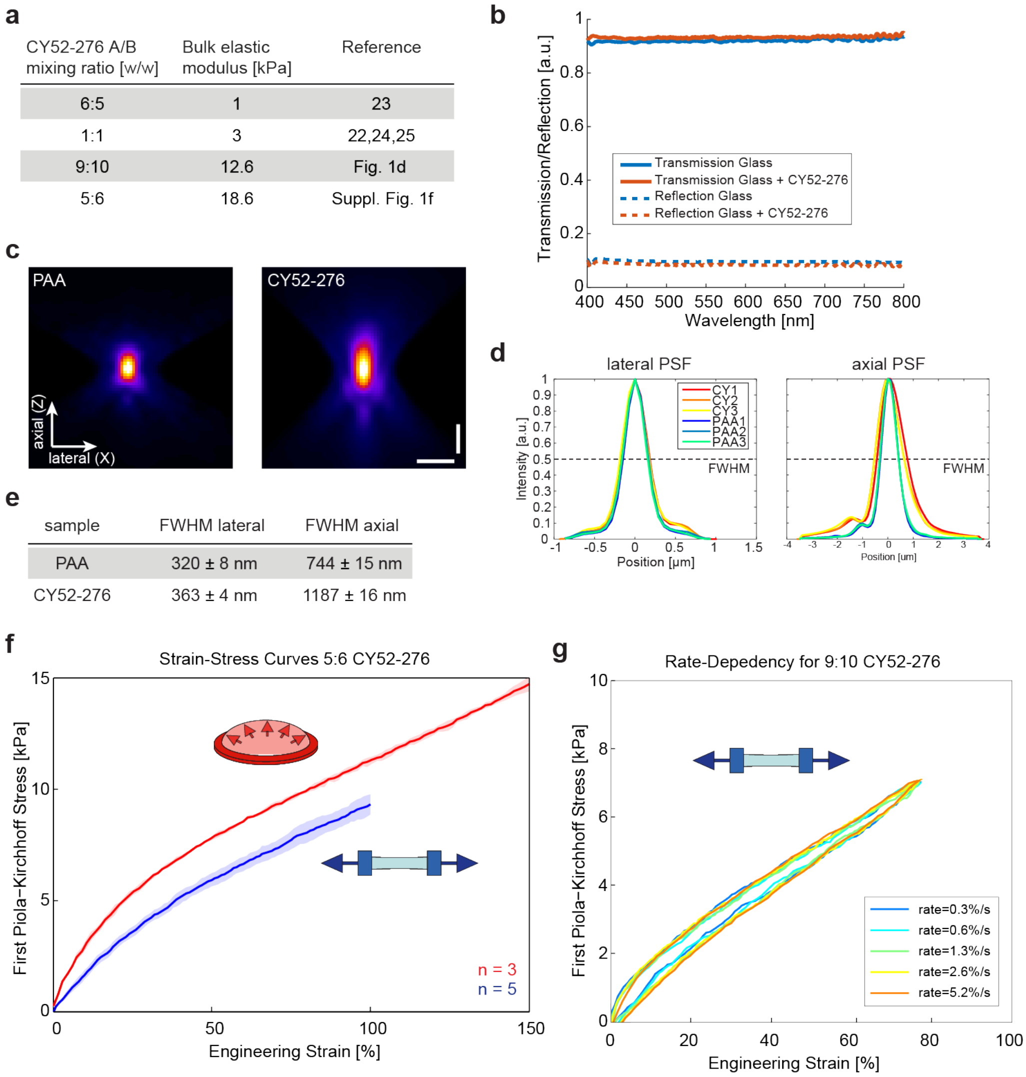

a

CY52-276 A/B mixing ratio [w/w]	Bulk elastic modulus [kPa]	Reference
6:5	1	23
1:1	3	22,24,25
9:10	12.6	Fig. 1d
5:6	18.6	Suppl. Fig. 1f

e

sample	FWHM lateral	FWHM axial
PAA	320 ± 8 nm	744 ± 15 nm
CY52-276	363 ± 4 nm	1187 ± 16 nm

Figure A.2: Mechanical and optical properties of CY52-276 silicone. (a) Elastic moduli of CY52-276 silicone for different mixture ratios. (b) Transparency measurements of glass and glass coated with a 30µm thick CY52-276 layer. (c) Examples for PSF of 50nm fluorescent beads on Polyacrylamide and CY52-276 silicone, imaged with conventional widefield fluorescent microscopy. Scale bars: 1µm. (d,e) Lateral and axial extensions of the PSF, determined from 3 independent beads for each condition. Error: standard deviation (s.d.). (f) Results of tensile (uniaxial) and inflation (equibiaxial) testing of CY52-276 silicone mixed at a 5:6 ratio. Free sample dimensions 40mm10mm (uniaxial) and diameter 30mm (inflation). Thicknesses were in the range from 0.5mm – 0.75mm; Exact thickness was measured for each sample independently (see Methods). Shaded area: standard deviation (s.d.); $n_{\text{uniaxial}} = 5$, $n_{\text{equibiaxial}} = 3$ samples per test. (g) Result of a cyclic uniaxial strain rate sweep test with CY52-276 silicone mixed at 9:10 ratio.

A.3 Inter-disc spacing of the cTFM platform

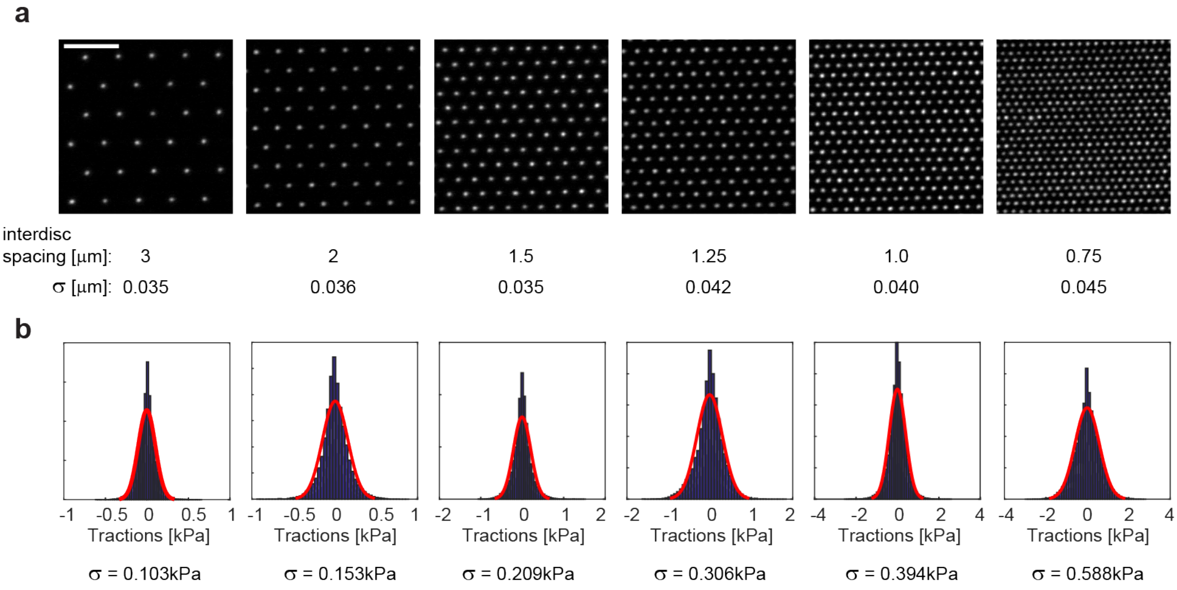

c

Interdisc spacing [µm] (simulated)	Printing noise [µm] (simulated)	Traction sensitivity [Pa]
3	0.035	100
2	0.035	159
1.5	0.035	223
1.25	0.035	279
1.0	0.035	360
0.75	0.035	495

Figure A.3: Inter-disc spacing of the cTFM platform. (a) Red QD nanodiscs were printed on glass with inter-disc spacing ranging from 3 to 0.75µm and the resulting standard deviation (s.d.) for the inter-disc spacing was measured based on fluorescent images (σ). Representative data of $n = 2-3$ nanodisc arrays. Scale bar: 5µm. (b) Images of the undistorted as-printed arrays (a) were analysed applying the algorithm for estimation of surface tractions (see Methods for details) and the resulting standard deviation (s.d.) of the obtained tractions, which corresponds to the sensitivity in force detection, was determined. (c) Simulated undistorted arrays with various inter-disc spacing and a constant printing noise of 35 nm were used to estimate surface tractions and resulted in similar traction force noise levels than the as-printed arrays in (a).

A.4 Electrohydrodynamic nanodrip-printing on polyacrylamide substrates

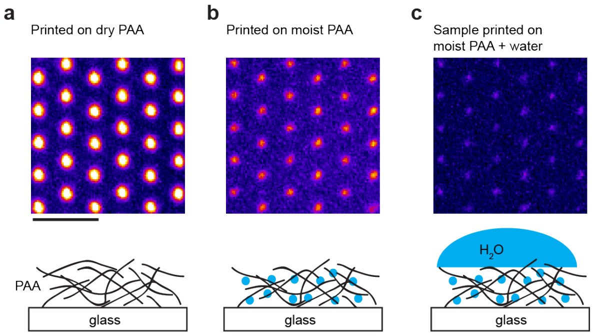

Figure A.4: Electrohydrodynamic nanodrip-printing on polyacrylamide substrates. (a) Red QD nanodiscs printed on dry polyacrylamide (PAA) (spacing: 1.5µm). Scale bar: 3µm. (b) Red QD nanodiscs printed on moist polyacrylamide. (c) The sample from B upon immersion in water.

A.5 Cytotoxicity assay

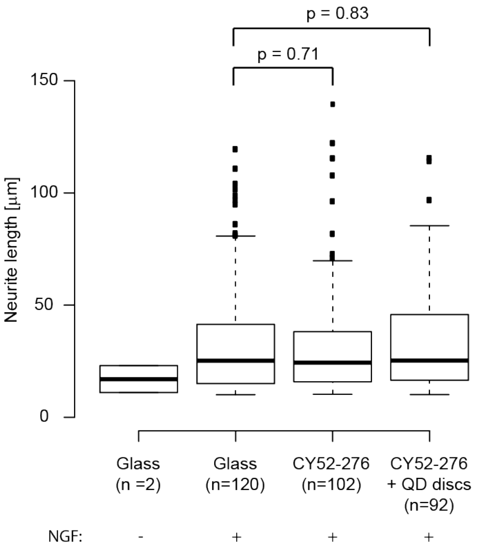

Figure A.5: Cytotoxicity assay. Biocompatibility of the cTFM platform. Plots shows the average length of neurites generated by PC12 cells after 4 days in culture. In the four tested conditions the cells were alternatively plated on control glass substrates, on substrates coated with a thin layer of CY52-276 or on a cTFM platform (CY52-276 + QD nanodiscs). Upon stimulation with NGF, PC12 cells underwent neuronal differentiation with no significant differences between control glass substrates and substrates with CY52-276 or CY52-276 + QD nanodiscs (Mann-Whitney-U-Test). n = number of neurites analysed on 2 independent substrates for each condition, except for a single substrate for glass without NGF.

A.6 Reconstruction of the displacement field

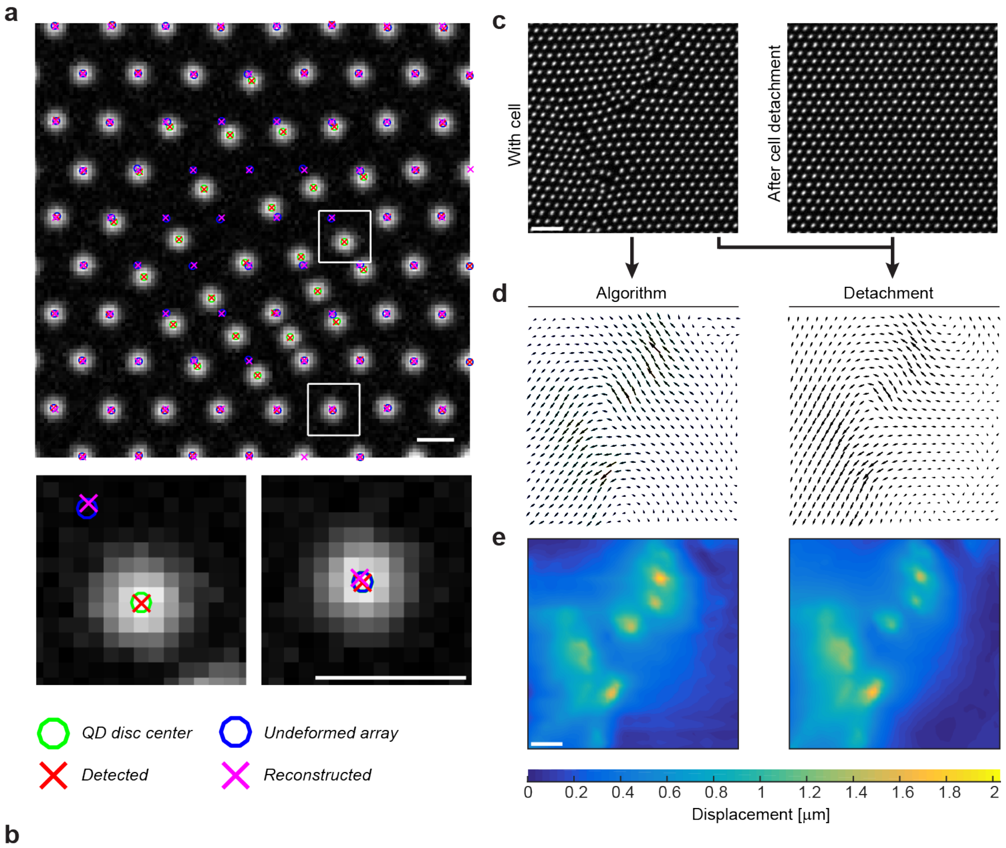

b

Input Data	Detection	Reconstruction	Combined
no noise	4.75 ± 3 nm	0.18 ± 0.16 nm	4 ± 2.4 nm
with 35 nm printing error	6.4 ± 2.7 nm	27.6 ± 17.7 nm	28.8 ± 16 nm
with imaging noise	7.4 ± 3.7 nm	N/A	3 ± 2.4 nm
with 35 nm printing error & imaging noise	8 ± 4.2 nm	N/A	29.1 ± 15.7 nm

Figure A.6: Reconstruction of the displacement field. (a) Synthetic images with known imposed initial and displaced positions were used to estimate errors in QD nanodisc detection and displacement field reconstruction. QD disc center: imposed center of QD nanodisc, Detected: position of QD nanodisc after detection, Undeformed array: Position in the initial, undeformed array. Reconstructed: Reconstructed initial position of the QD-nanodisc. Scale bars: 1µm. (b) Errors of the detection, the reconstruction and the combined algorithm used to estimate the cTFM displacement fields. Data quantifies mean ± standard deviation (s.d.) of the distances between the following positions: Detection: QD disc center - Detected; Reconstruction/ Combined: Undeformed array - Reconstructed. Data for Reconstruction uses QD disc center as input, data for Combined uses Detected as input. (c) Part of a QD nanodisc array on cTFM substrate with HeLa cells, on the left in distorted configuration and on the right after cell detachment (see Supplementary Movie 3). Scale bar: 5µm. (d) Displacement fields obtained with the reconstruction algorithm (see Methods) and from classical relaxation upon cell detachment. (e) Corresponding displacement magnitude maps. Scale bar: 5µm.

A.7 Sensitivity of the cTFM platform

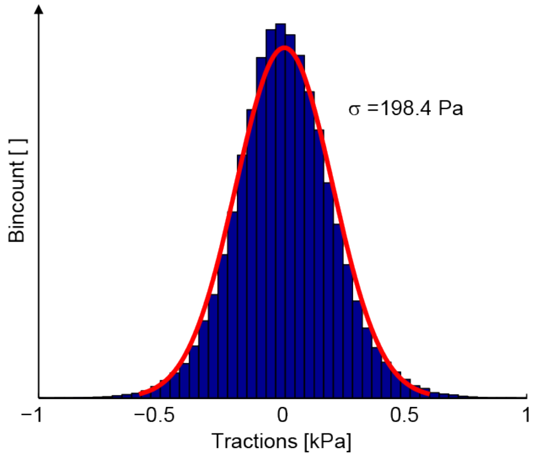

Figure A.7: Sensitivity of the cTFM platform. A representative (n = 5) as-printed array of fluorescent QD nanodiscs on the elastic silicone with a spacing of 1.5μm and a printing error of σ = 0.033μm (Figure 1h) was used to estimate the sensitivity of the cTFM platform. After the analysis procedure (Figure 1i), tractions were distributed around 0kPa with a standard deviation (s.d.) of 0.198kPa.

A.8 Detection of Z-position of QD nanodiscs.

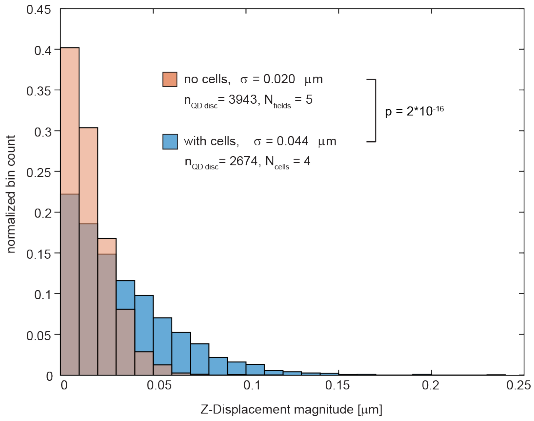

Figure A.8: Detection of Z-position of QD nanodiscs. Flat, undeformed fluorescent nanodisc arrays (n = 5) with spacing of 1.5μm were imaged as 3D stack using conventional wide-field microscopy (Z-spacing: 100nm). After evaluation of the Z-position of each QD nanodiscs (see Methods), a standard deviation (s.d.) of about 20nm was found for the detection of the Z-position, which includes possible minor deviations from perfect flatness of our spin coated CY substrate as well as imaging noise. Upon spreading of MCF10A cells, significantly larger Z-displacements were detected. P-Value: Mann-Whitney-U-Test.

A.9 Correlative traction force microscopy using anti-phospho-antibodies

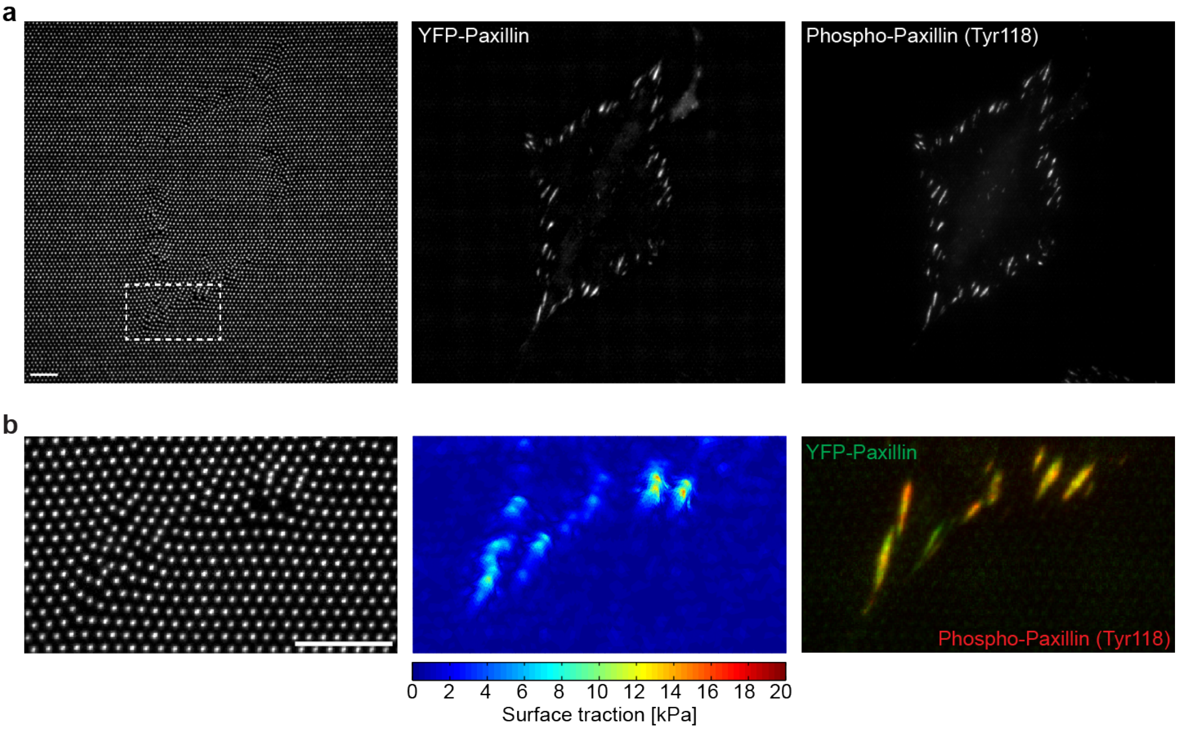

Figure A.9: Correlative traction force microscopy using anti-phospho-antibodies. (a) REF-Pax cell on cTFM substrate with red QD nanodiscs (spacing: 1.5µm). Upon imaging of the QD nanodiscs, the cell was fixed and immunostained for phosphorylated Paxillin. Scale bar: 10µm. (b) Zoom of the region outlined in a. Scale bar: 10µm.

B Deprecated Traction Force Analysis

The initial software developed to analysis cellular traction forces was overhauled and replaced through Cellogram (Chapter 6). Here, the analysis pipeline used in several studies and published in Confocal reference free traction force microscopy[150] is described. It follows the same pipeline of detecting the QD nanodiscs, reconstructing the mesh, calculating the reference positions and running the finite element analysis, albeit with different implementation compared to Cellogram.

B.1 QD nanodisc detection and meshing

Traction evaluation starts with the detection of the XY positions of the QD nanodiscs. A threshold was applied to the image and the connected pixel islands were identified as the QD nanodiscs. The exact position of the QD nanodisc was calculated by taking the weighted centroid of the grey scale value of the connected pixel islands. To evaluate the deformation along the Z axis, 3D image stacks were acquired (≥ 30 slices, spacing 100µm). The spot detection function of Imaris (Bitplane) was used to detect the Z position of the QD nanodiscs (spot size: XY, 0.717µm; Z, 1.434µm). By fitting a plane through all points (Matlab, Mathworks) and taking the difference between the plane and the measured Z coordinates, a tilt correction was applied to filter for skewness between the sample and the focal plane.

B.2 Triangular mesh reconstruction

The next step in the analysis procedure was the construction of the triangular mesh with a two-step custom-built algorithm, achieved by identifying the original six neighbours for each individual QD nanodisc (for a detailed description see Supplementary Information). Briefly, in a first step the regions of the image with no or low distortion were identified. In the non- or low-deformed configuration each QD nanodisc has exactly six neighbouring QD nanodiscs at equal distances and forming angles of 60°. Each QD nanodisc is locally checked for this condition and connected to its six neighbours only if this condition holds, up to a tolerance of ≤ 250nm and 10° to account for small deformations. At the end of this analysis, the regular parts of the image are meshed, that is, connected to an array of triangles, whereas the QD nanodiscs in regions with high deformation remain unmeshed, forming voids in the mesh (Supplementary Figure B.1). The boundary of each void gives sufficient information to generate a perfect mesh with the same geometry as the void and has the same number of vertices as there are unconnected QD nanodiscs in void. The algorithm then computes the optimal assignment of vertices of the perfect mesh to positions of QD nanodiscs by minimizing the overall mesh distortion.

The regular pattern printed on the substrate is a perfect triangular mesh whose vertices are the QD nanodiscs (Figure 3.1e). A custom built algorithm was used to define a mesh whose connectivity is identical to the original mesh (i.e. each vertex with exactly 6 neighbors). The algorithm proceeds in two steps, by firstly identifying regions with low distortion (where the original connectivity is easily recovered), and then filling the remaining regions through an advanced and computationally more expensive procedure:

B.2.1 Step 1

The low distortion regions are identified based on the properties of the as-printed mesh. Each QD nanodisc has exactly six neighbors at equal distance and forming angles of 60° between them. Each individual nanodisc is checked for this condition, and connected to its 6 neighbors only if the condition holds, up to a predefined tolerance to account for small deformations. Let p^i be the position of a nanodisc and p^i_1, $p^i_2, \ldots, p^i_6$ be its 6 closest neighbors (with respect to Euclidean distance) ordered counterclockwise around p^i. A nanodisc vertex is regular if and only if the standard deviation of all six angles and all six edge-lengths is smaller than 10 degrees and 250 nm respectively. Each detected regular vertex is now connected to its 6 neighbors, leading to a mesh that partially covers the image, as displayed in Figure B.1a. This step robustly detects areas of the image featuring low distortions, while skipping the regions where the deformations are large (voids). At the end of this phase, all edges incident with non-regular vertices are removed.

B.2.2 Step 2

To fill the remaining regions, a procedure that finds the most uniform regular tessellation fitting the void, while snapping to the positions of nanodiscs, is used. Each void is a sequence of coordinates of vertices $b_1, \ldots, b_n$ at the boundary of the meshed region, in addition to a set of QD nanodisc positions $d_1, \ldots, d_m$ in its interior. For each boundary vertex b_i the number of regular vertices around it is known and denoted by n_i. The notation is illustrated in Figure B.1b. The void filling algorithm proceeds in 3 phases: First, it identifies the connectivity of a triangulation that can fill the void (Figure B.1c(II)), then warps the mesh to perfectly match the given boundary (Figure B.1c(III)) and finally snaps its internal vertices to the nanodisc positions, while preserving the regularity of the mesh (Figure B.1c(IV)).

Connectivity. The connectivity of the mesh required to fill the void is uniquely identified by the number of neighbors of the vertices on the boundary of the void and can be extracted with a simple algorithm that walks over a regular triangulation. Since the number of regular vertices that need to be inserted to make the vertex regular is known, we can uniquely decide which part of the mesh needs to be copied. The boundary walk is described in Figure B.1d: The first boundary edge connects to a boundary vertex with 4 connected neighbors. Thus a straight walk is necessary to find the next boundary vertex. The next vertex along the boundary has 5 neighbors implying a left turn. The next boundary vertex has two connections, therefore a sharp right must be taken. The entire boundary can be walked following this procedure. At the end of the walk, a regular mesh with the same boundary geometry is cut out of the perfect grid.

Boundary fitting. Connectivity alone is not sufficient to close the void, since generally it overlaps with other triangulated regions of the original image. The regular mesh is thus deformed solving the following linear system:

$$Lx = 0 \text{ s.t. } x_i = b_i \in 1 \ldots n \tag{B.1}$$

where x is a vector containing the coordinates of the mesh vertices. The constraint fixes the boundary vertices to match the void boundary and L is the uniform Laplacian[324], defined as follows:

$$L_{ij} = \begin{cases} \Sigma_j L_{ij} & i == j \\ 1 & \text{i is a neighbor of j} \\ 0 & \text{otherwise} \end{cases} \tag{B.2}$$

The boundary of the deformed mesh matches (due to the constraints) the boundary of the void, while each interior vertex is placed at the barycenter of its neighbors, thus keeping the shape as similar as possible to a regular grid, where this property trivially holds.

QDs snapping. After the boundary fitting, the interior vertices will not necessarily overlap with the internal nanodisc positions (Figure B.1c(III)). The optimal assignment of vertices of the mesh to the position of nanodiscs is obtained through an algorithm that preserves their regular structure. This is done by explicitly encoding the assignment between the internal vertices of the mesh and the position of the internal nanodisc positions in a permutation matrix P. The optimal permutation minimizes the following energy:

$$min_P \left\| LPD \right\|_2, \tag{B.3}$$

where D is a matrix containing the position of one of the internal nanodiscs in each row, and P is a permutation matrix (i.e. each row and column sum to 1, and each entry can be either 0 or 1). The energy can be rewritten to explicitly highlights the variables, which correspond to the entries of P.

$$\|LPD\|_2^2 = \sum_i \|LPD_i\|_2^2 = \sum_i D_i P^T L^T L P D_i = \tilde{P}\left(\sum_i (I \otimes D_i)^T L^T L (I \otimes D_i)\right)\tilde{P} \tag{B.4}$$

Where $M_i = \tilde{P}\begin{bmatrix} (P^T)_1 \\ (P^T)_2 \\ \dots \end{bmatrix}$.

This is a binary integer optimization in its canonical form and the globally optimal solution is found with the Gurobi solver[325]. The running time of the solver varies from a tenth of a second for small voids to a few minutes for large voids, but increases dramatically for regions containing more than 150 vertices. When such regions occasionally appear in our experiments the operator is asked to manually split them in two parts drawing a straight line (Figure B.1e).

In all, this approach is a good approximation of the material behavior and it is very robust, as demonstrated in examples featuring a high deformation (Figure B.1f). Each void is independently filled and if at the end of this procedure a void is multiply connected, the internal islands are removed to obtain simply connected regions.

B.3 Reference configuration reconstruction

The regular initial arrangement of the QD nanodiscs permits the reconstruction of the reference configuration without acquiring a load-free image, exploiting the fact that the reference distance between two neighbouring nanodiscs is known (L_0) and equal for all nanodiscs. For this procedure, the QD nanodiscs are idealized as point masses and connected to their neighbours (identified in the previous step, see paragraph above) with pre-stretched springs of reference length L_0. Minimization of the potential energy relaxes the deformed spring-mass network towards the steady-state solution, which corresponds to the stress-free configuration where all the springs have length L_0. To stabilize the computation an inconsequential damping component is added and the differential equation describing the dynamics of the damped mass-spring network is solved explicitly using a fourth-order Runge–Kutta integration scheme.

B.4 Nonlinear FEA-based traction reconstruction

To account for both large deformations and material nonlinearity, a custom high-resolution nonlinear TFM framework was developed based on Python scripts (Python Software Foun-

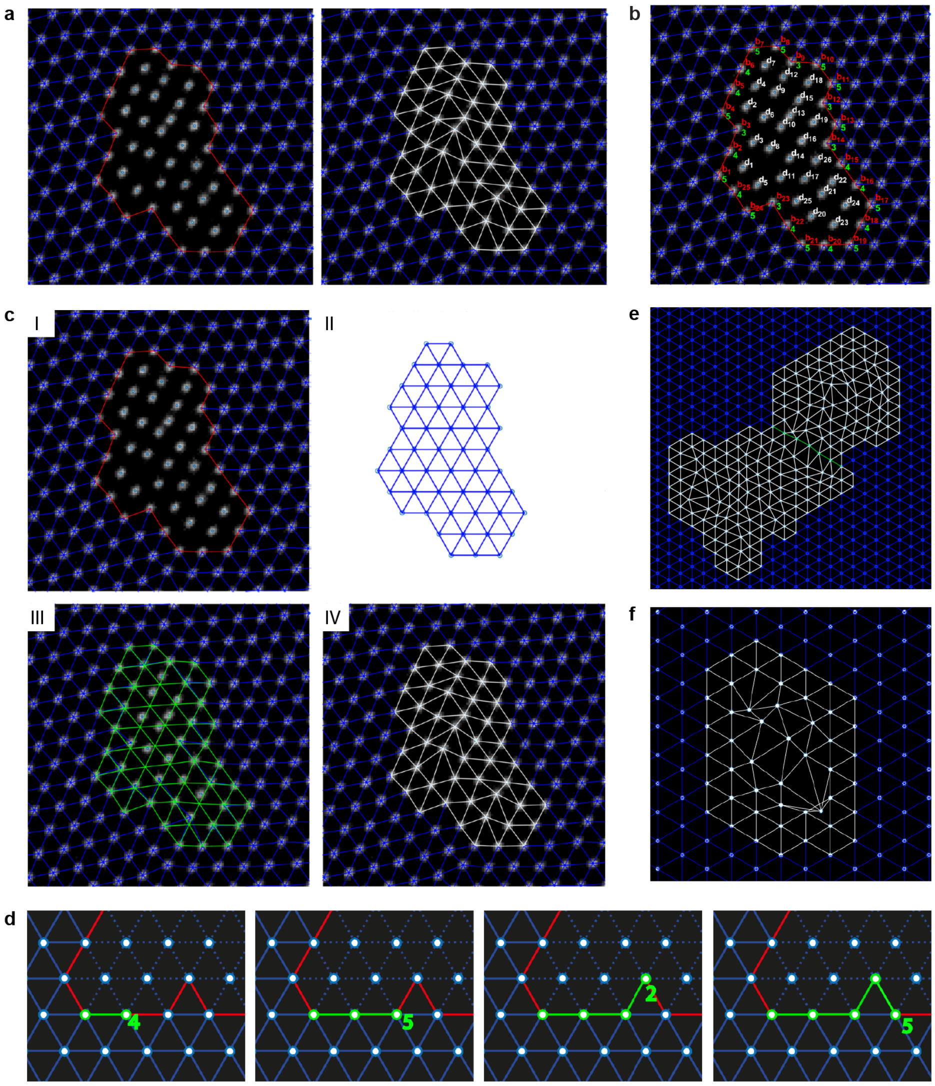

Figure B.1: Triangular mesh reconstruction. a - (left) Only regular regions of the image are meshed (blue) in the first stage of the algorithm. (right) Each void is separately meshed (white) and finally combined to obtain the final mesh. b - Notation for the boundary vertices (red), the number of their connections (green), and internal vertices (white) of a void. c - The three phases of the void meshing pipeline. Unmeshed region (I), perfect flattening (II), boundary fitting (III) and internal snapping (IV). d - Walking along the boundary vertices and taking turns according to the number of connected neighbors. e - Large voids with more than 150 vertices are slow to process. In these cases, the user shall split the cluster in two parts (green edges), and then process them independently. f - Even in cases with extreme deformations, the algorithm reliably reconstructs the original mesh. Note that in certain cases, self-intersection between the edges must be introduced.

dation) and a commercial finite element code (Abaqus, Dassault Systèmes). The framework contains three principal steps: (I) model creation and finite element meshing; (II) application of displacement boundary conditions; and (III) computation of the traction stress field.

In the first step (I), the finite element geometry models a cuboid section of the substrate, whose height is equal to the actual substrate. In-plane dimensions are chosen larger than the analysed cell, so that the border zones of the section contain undeformed regions. An adaptive meshing algorithm was implemented that selects the QD nanodiscs with high displacement magnitude and automatically meshes with linear hybrid tetrahedral elements the corresponding regions with a fine mesh (elements five times smaller than QD nanodisc interspacing), whereas the other regions are meshed by elements of increasing size (up to QD nanodisc spacing). Material properties were defined based on the nearly incompressible implementation of the Ogden model (Poisson's ratio 0.49) provided by the software, with parameters given in Table 3.1 obtained by fitting the experimental data (Figure 3.1d).

To determine the displacement boundary conditions (II), an interpolation based on thin-plate spline radial basis functions[326] is applied to prescribe the displacement at each node of the finite element mesh on the cell sided surface of the substrate. This is necessary, since image analysis provides the displacements only at the position of the QDs. To account for the bonding of the substrate to the glass coverslip and the embedding of the model into a larger portion of the substrate, the degrees of freedom of nodes on the lateral and bottom sides of the section were fixed.

Finally (III), the implicit FEA solver is used to compute the strain and stress states in the substrate, taking into account the applied boundary conditions and the nonlinear material behaviour. The computed solution includes reaction forces for all the nodes that are constrained by displacement boundary conditions. These forces are subsequently related to the deformed surface area of the elements, finally providing the traction field induced by the cell. It is important to note that, as required in the case of large deformations, tractions are defined in the deformed configuration (Cauchy tractions).

C Supplementary Information: Cell Cycle-Dependent Force Transmission in Cancer Cells

C.1 Effect of 4-hydroxytamoxifen

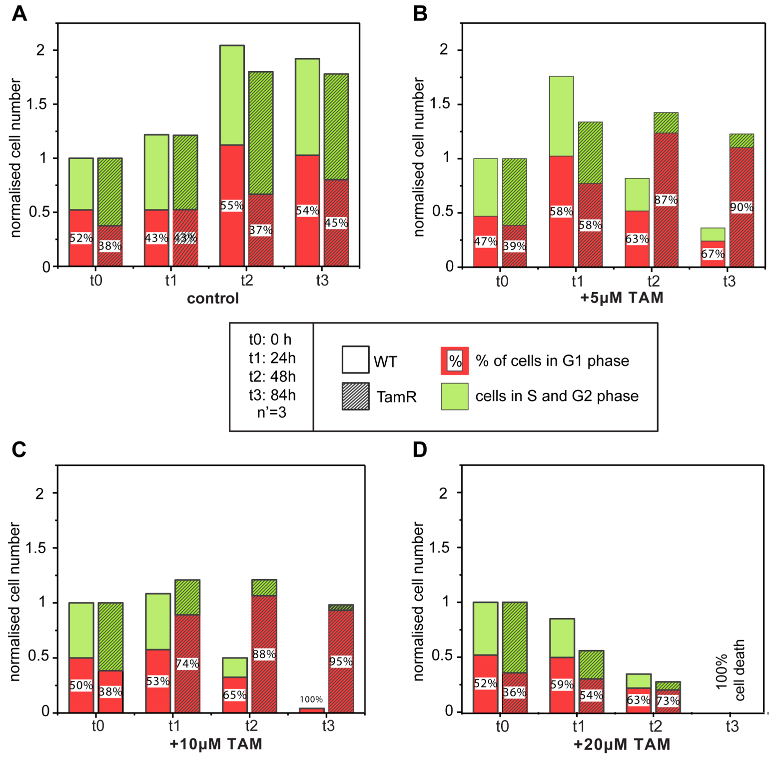

Figure C.1: The effect of 4-hydroxytamoxifen on the cell cycle partition and viability for wild type and Tamoxifen-resistant MCF7 cells. Control (ethanol vehicle) (A), 5 μM (B), 10 μM (C), and 20 μM (D) was added and monitored by live microscopy for a total duration of 84h.

C.2 Individual cell variability

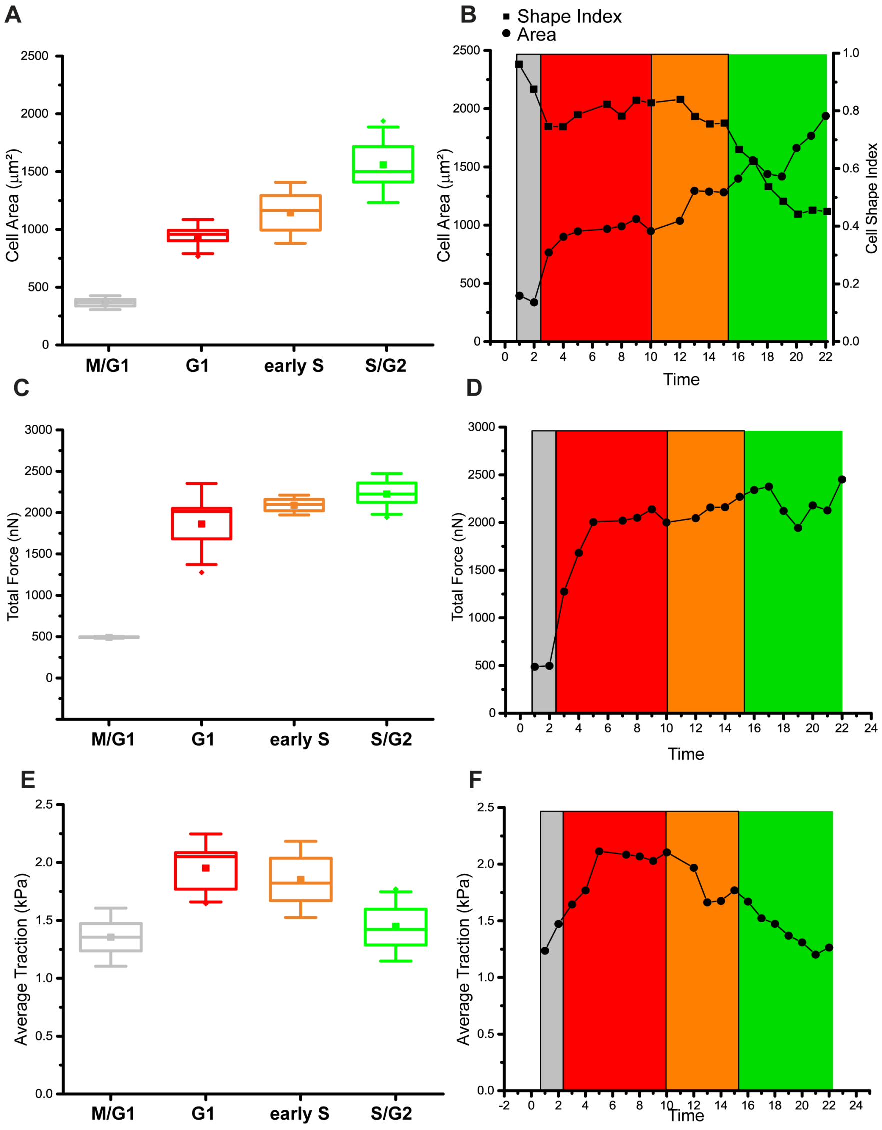

Figure C.2: Individual cell variability for cell area (A, B), forces (C, D) and tractions (E, F) for 4 distinct cells

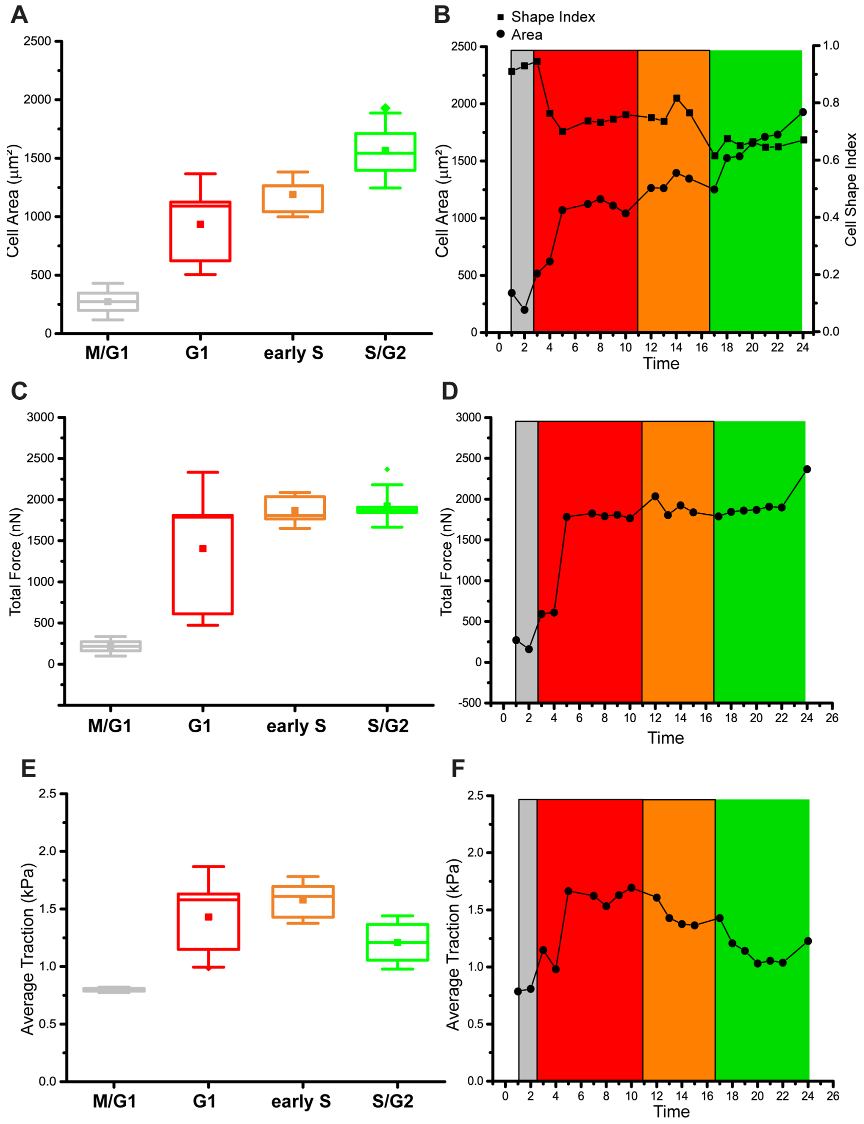

Figure C.3: Individual cell variability for cell area (A, B), forces (C, D) and tractions (E, F) for 4 distinct cells

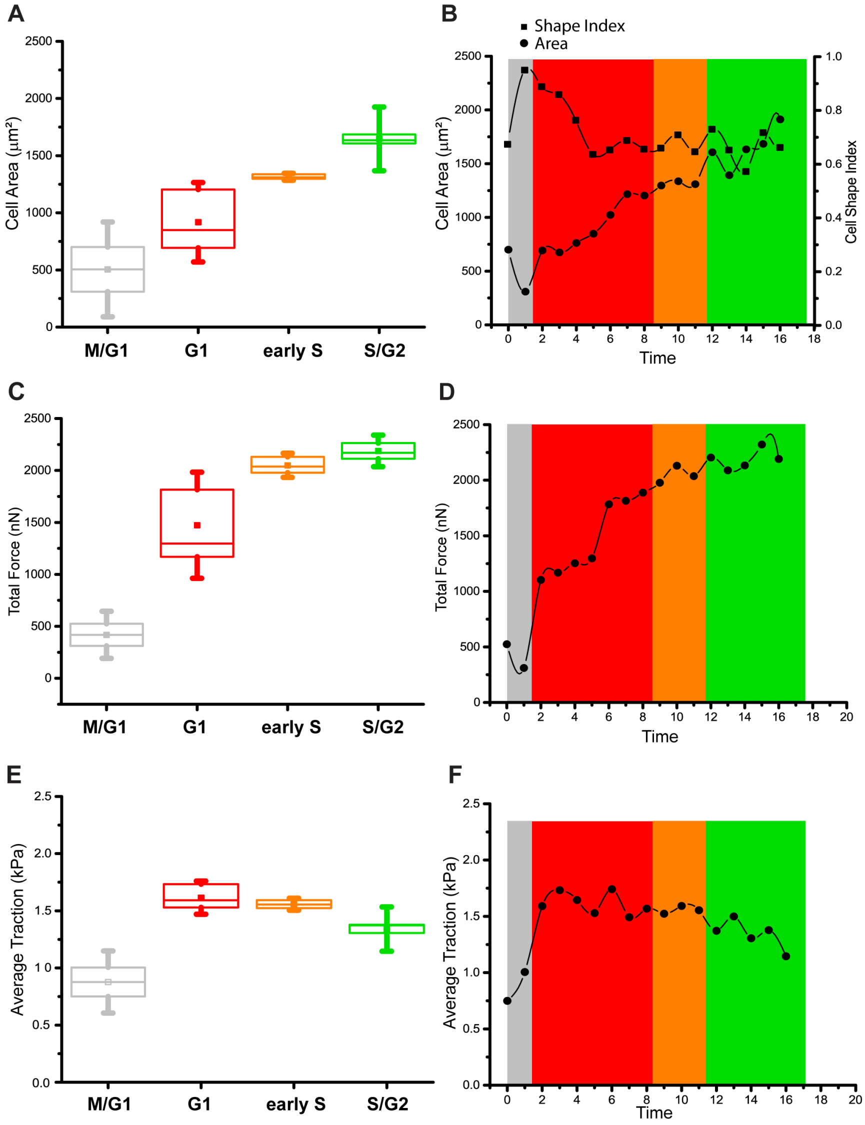

Figure C.4: Individual cell variability for cell area (A, B), forces (C, D) and tractions (E, F) for 4 distinct cells

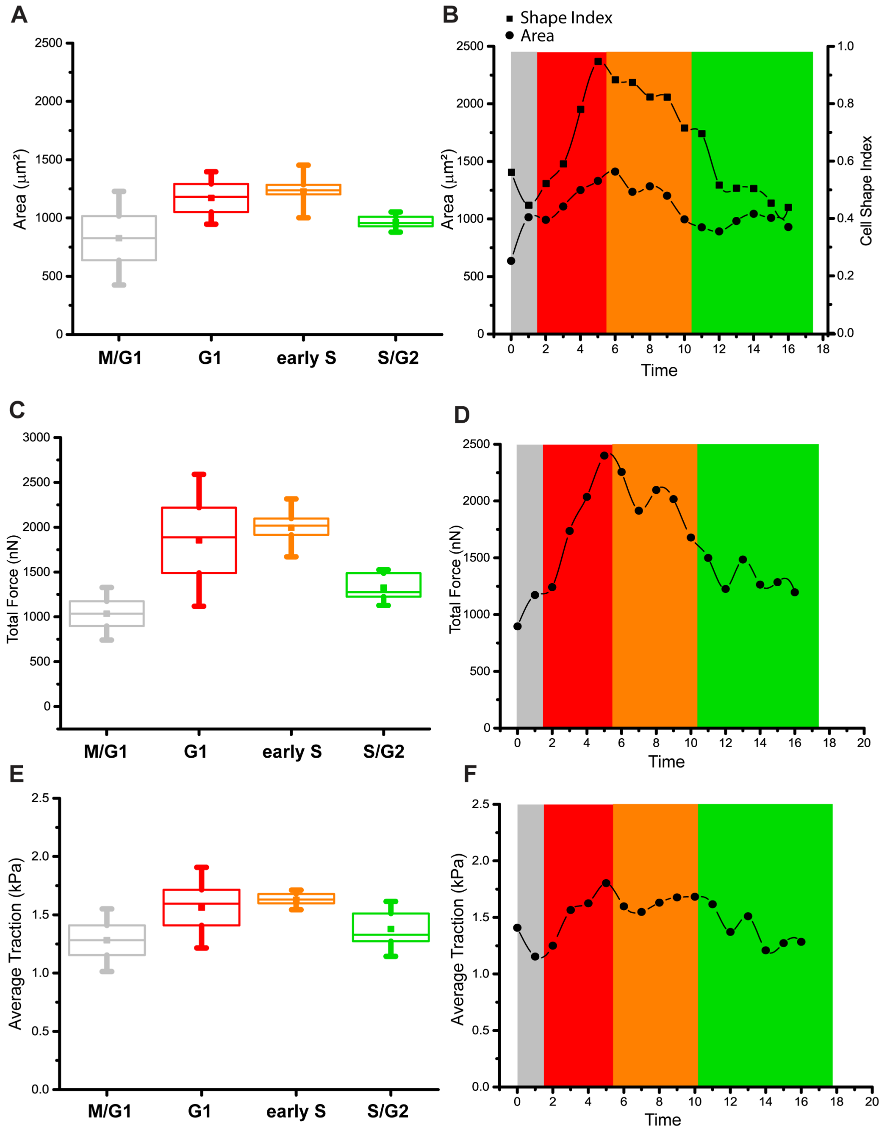

Figure C.5: Individual cell variability for cell area (A, B), forces (C, D) and tractions (E, F) for 4 distinct cells

C.3 Correlation between cell shape and traction

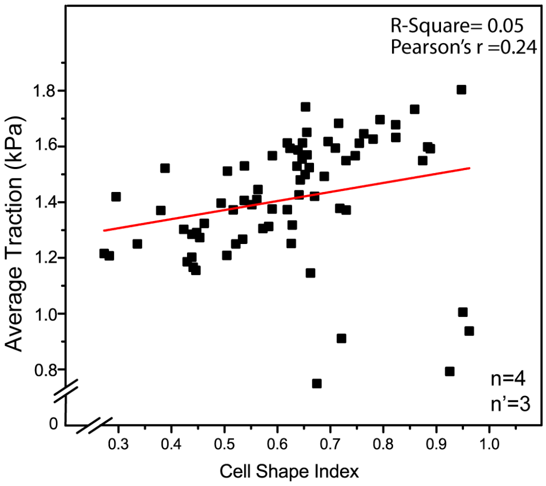

Figure C.6: Correlation between cell shape and traction: The R-Square and Pearson's r values indicate that the two variables are not linearly correlated. n= number of cells and n'= number of independent experiments.

C.4 Correlation between the focal adhesion size (total paxillin) and the size of phosphorylated paxillin

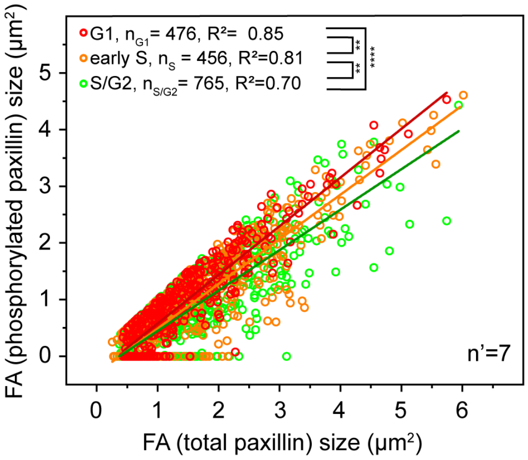

Figure C.7: Correlation between the focal adhesion size (total paxillin) and the size of phosphorylated paxillin. $^{**}p<0.01$. $^{****}p<0.0001$. n=number of individual focal adhesions for 7 independent experiments. n= number of cells and n' = number of independent experiments.

C.5 The effect of FAK inhibition on paxillin phosphorylation per focal adhesion and per cell

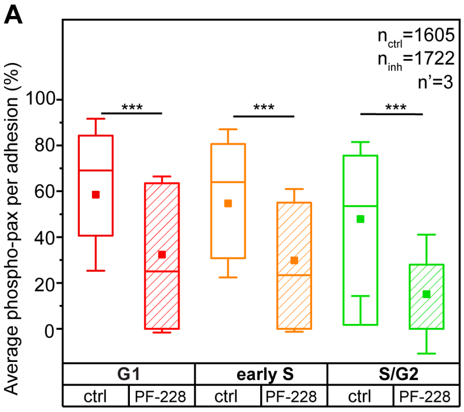

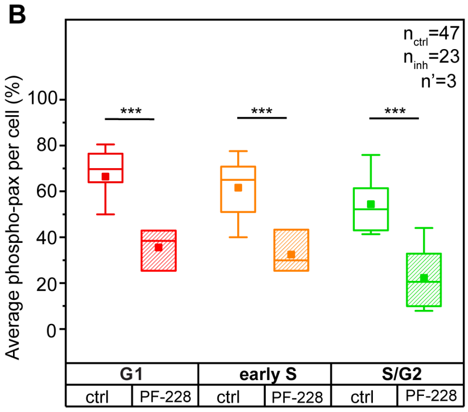

Figure C.8: The effect of FAK inhibition on paxillin phosphorylation per focal adhesion (A) and per cell (B) ***p<0.001. Panel A: n=number of individual focal adhesions, Panel B: n= number of cells and n' = number of independent experiments.

C.6 The effect of FAK inhibition

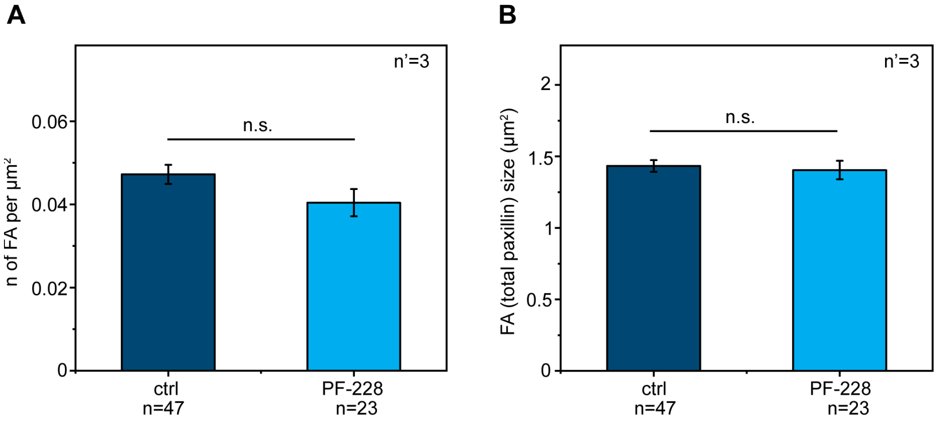

Figure C.9: The effect of FAK inhibition on the number of focal adhesions per μm^2 (A), and the average size of focal adhesions (B) n= number of cells and n' = number of independent experiments.

D Supplementary Information: Bistability of Polar Liquid Crystals in the Collective Adaptation of Endothelia

D.1 Modelling nematic liquid crystals

For the polar nematic liquid crystal simulations, the free energy is defined as

$$F = \int d^3r(F_I + F_{II} + F_{III}), \tag{D.1}$$

where r is position and the three terms are defined as

$$F_I = \frac{A}{2}\mathrm{tr}Q^2 + \frac{B}{3}\mathrm{tr}Q^3 + \frac{C}{4}(\mathrm{tr}Q^2)^2 + \frac{D}{6}(\mathrm{tr}Q^3)^2, \tag{D.2}$$

and is obtained from a local expansion of the rotationally invariant powers of the order parameter where A (nematic vs. isotropic), B (rod vs. disk molecules), C (greater than zero; ensures that the free energy density functional is bounded from below;[327]), and D (uniaxial vs biaxial) are nematic material parameters and

$$F_{II} = \frac{R_1}{2}\delta_\alpha Q_{\beta\gamma}\delta_\alpha Q_{\beta\gamma}, \tag{D.3}$$

(Einstein notation) which is non-local and is obtained rotationally invariant combinations of gradients of the order parameter where R1 is an elastic constant and

$$F_{III} = -\Delta\epsilon Q_{\alpha\beta}E_\alpha E_\beta, \tag{D.4}$$

which is due to the effect of the electric field.

For the simulations, we worked with a $[N_x, N_y, N_z] = [256, 256, 1]$ grid; the constants A, B, C, D, and R_1, were set to -1, -1, 2.67, 0, and 1, respectively. All other values that were used are given in the figures. The kinetic coefficient, Γ, was set to 1.0. To calculate the global free energy, we computed the local value at each point and summed at every time point until the final time t_{end}, which was set to 1000. The spatial steps, dx, dy, dz were set to 1.0, 1.0, and 1.0, respectively, and the time step dt was 0.1. For this model, we made one of the above constant B inversely proportional to the strength of the electric field and we were able to turn the field on and off as well as change its direction. When E=0, B=1, and when E=1, B=-1, and the values vary linearly in between. In some cases, we also made the value of $\Delta\varepsilon$ variable in time.

D.2 Generation of mature endothelial monolayers

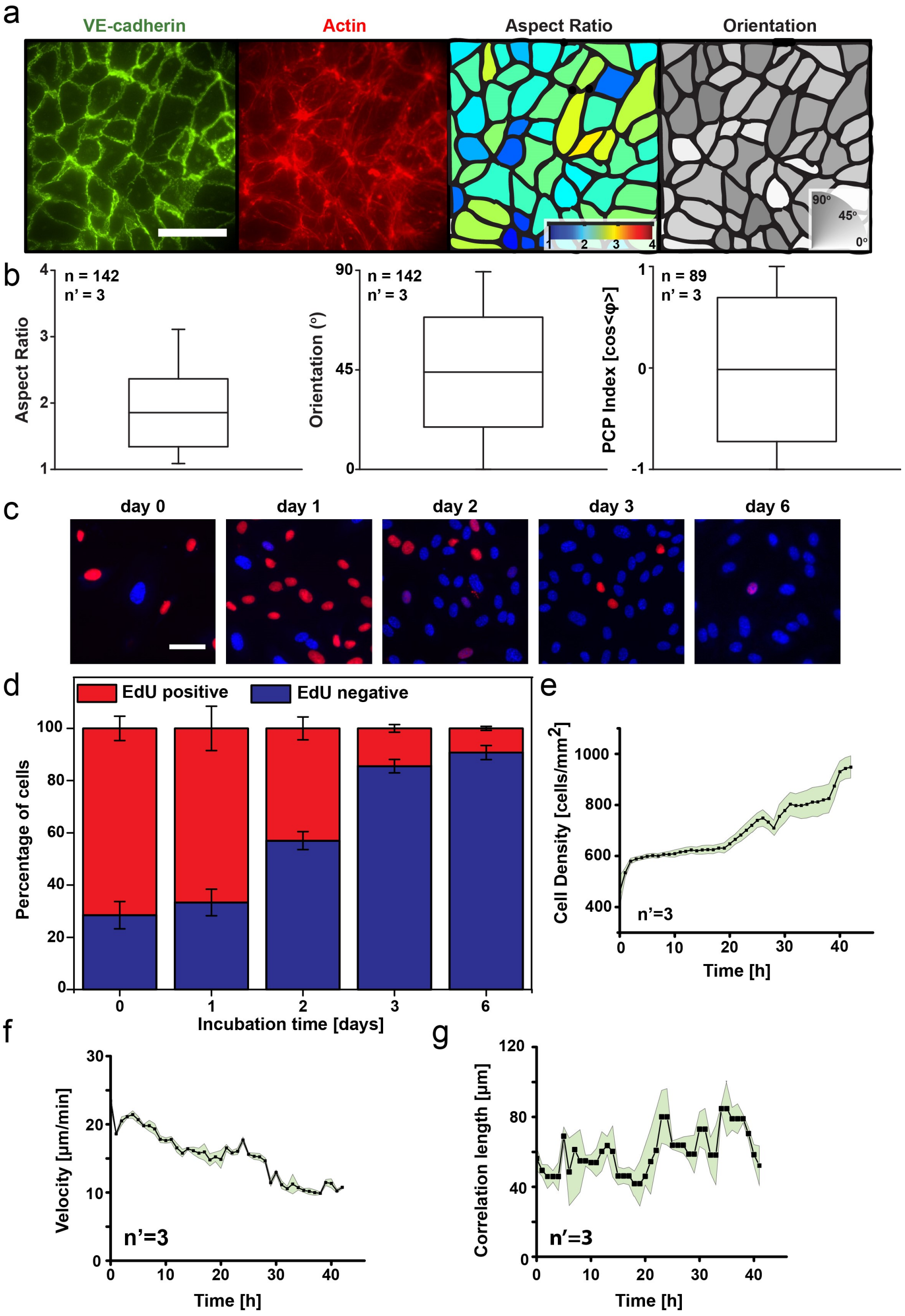

Figure D.1: Generation of mature endothelial monolayers. Figure on page 141 (a) Isotropic state obtained in static conditions. Fluorescent images of VE-cadherin distribution (green) at cell-to-cell junctions, and actin cytoskeleton (red). Scale bar is 50 μm. Cell profiles with color-coded aspect ratio, and cell orientation as encoded by corresponding color scale bars. (b) Corresponding boxplots reporting the quantification of cell aspect ratio (left), orientation (middle) and PCP index (right). (c-d) Cell proliferation during maturation. (c) Fluorescent images and (d) quantification of EdU assay. Time evolution of (e) cell density, (f) velocity, and (g) correlation length. The shaded area indicates the standard deviation. The number of independent experiments is indicated as n'.

D.3 Anisotropic endothelial monolayer generated in static conditions on microstructured gratings

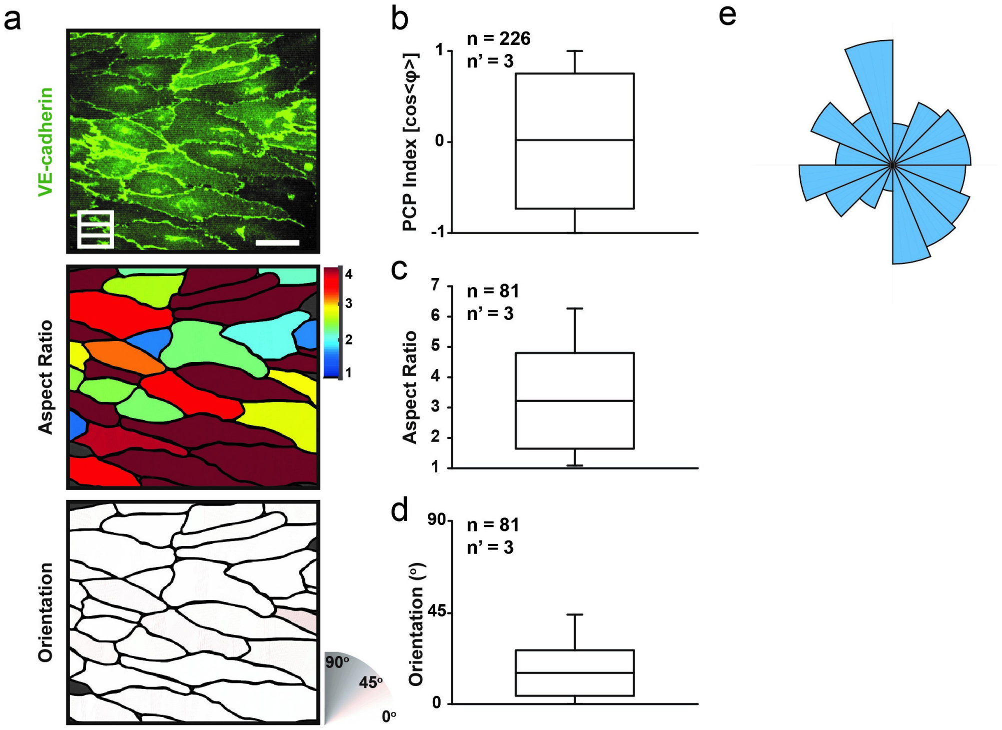

Figure D.2: Anisotropic endothelial monolayer generated in static conditions on microstructured gratings. (a) Fluorescent images of VE-cadherin distribution (green; top) at cell-to-cell junctions. Scale bar is 50 μm. The orientation of the gratings is reported in the lower left corner. Cell profiles with color-coded aspect ratio (middle), and cell orientation (bottom) as encoded by corresponding color scale bars. Corresponding boxplots reporting the quantification of (b) PCP index, (c) cell aspect ratio, and (d) orientation. (e) Radial distribution of PCP (i.e. φ as defined in Figure 8.1h). The number of analysed fields of view is reported as n and the number of independent experiments as n'.

D.4 Anisotropic endothelial monolayer exposed to flow reversal

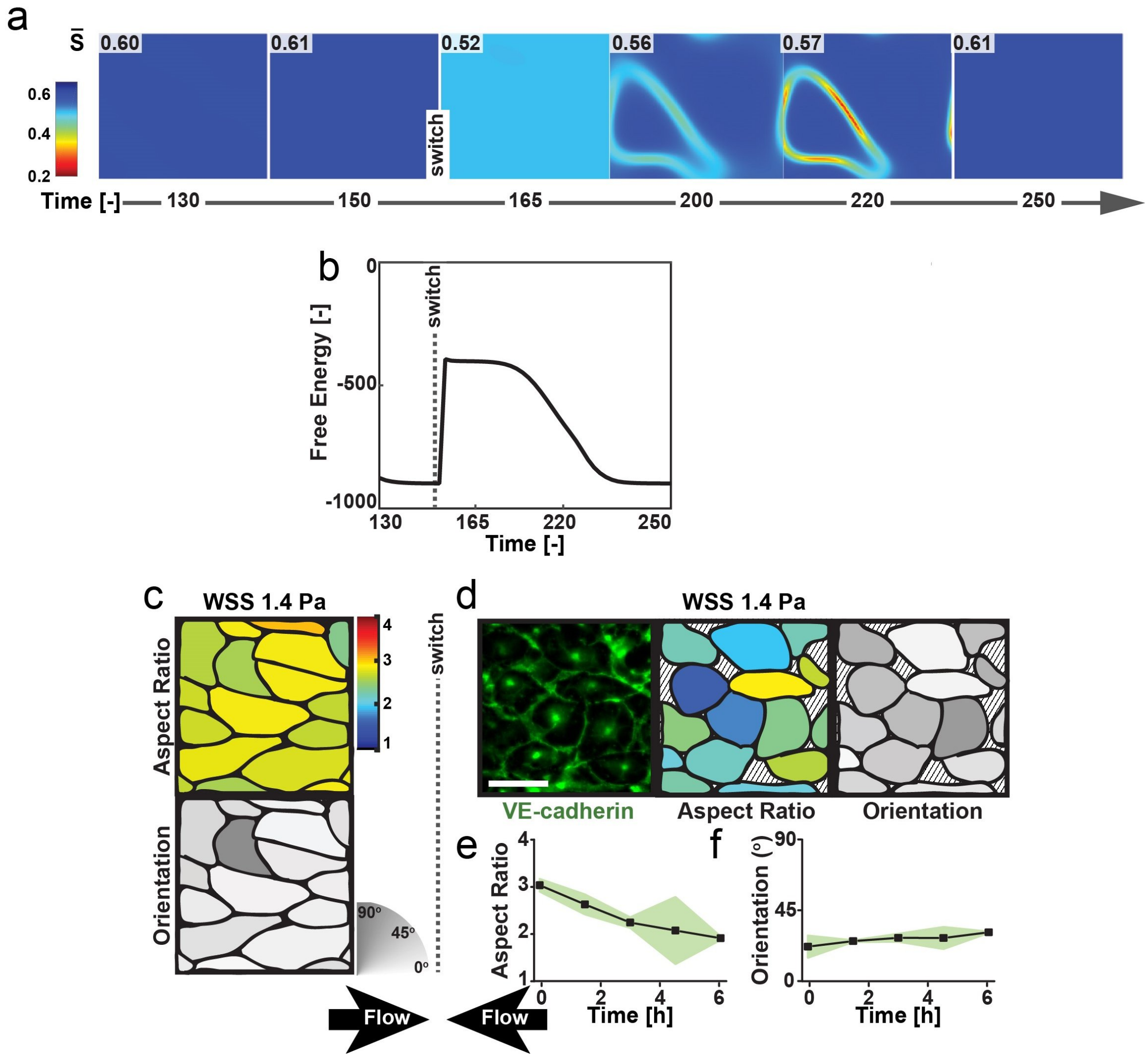

Figure D.3: Anisotropic endothelial monolayer exposed to flow reversal. **(a)** Transient order parameter $\bar{S}$ for aligned nematic particles preconditioned in a field in x-direction (E = [1,0,0]). At time t = 165 the field switches to be in y-direction (E=[0,1,0]). (**b**) Corresponding free energy development of the transition depicted in (a) **(c)** Cell profiles with color-coded aspect ratio (top), and cell orientation (bottom) as encoded by corresponding color scale bars for anisotropicly aligned cell (1.4 Pa) **(d-f)** after flow reversal. Fluorescent images of VE-Cadherin distribution (green) at cell-to-cell junctions (leftmost panel in (d)). Scale bar is 50 μm. Cell profiles with color-coded aspect ratio (middle panel in (d)) and cell orientation (rightmost panel in (d)) as encoded by corresponding color scale bars. (f) Isotropic intermediate states featuring intercellular gaps (regions identified by black lines). Corresponding evolution of cell aspect ratio (e) and orientation (f).

D.5 Planar Cell Polarity Evolution

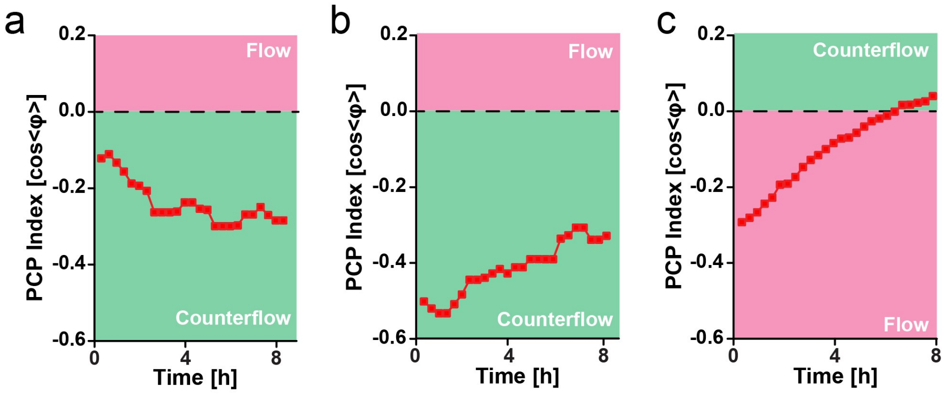

Figure D.4: PCP evolution. **(a)** Evolution of PCP upon flow intensity increase (WSS values from 1.4 Pa to 8 Pa) or **(b)** decrease (WSS values from 8 Pa to 1.4 Pa). **(c)** Evolution of PCP upon flow reversal. All switches occur at t = 0

D.6 Flow-mediated phosphorylation of VE-cadherin (VEC) reporting on the dynamic instability of cell-to-cell junctions

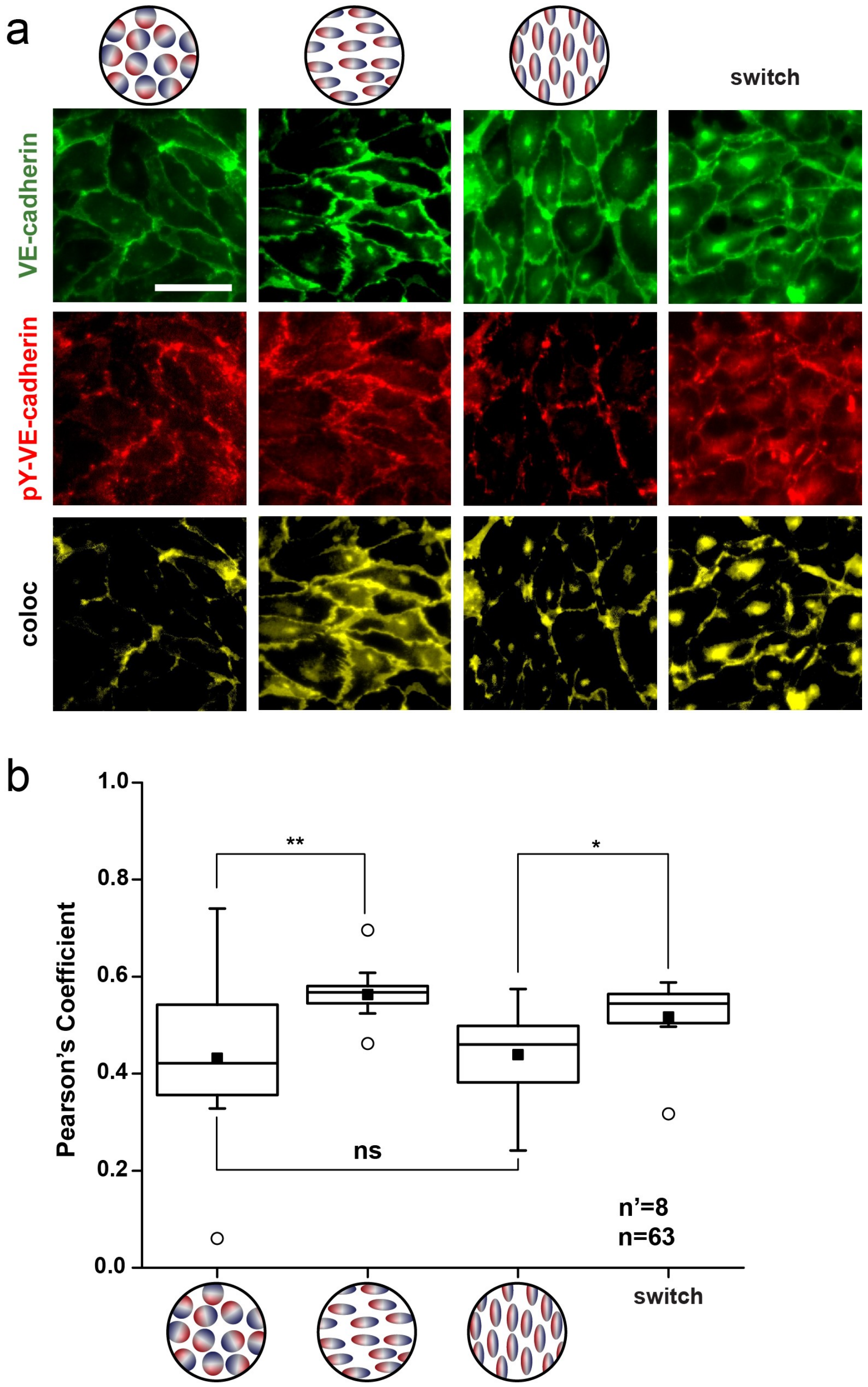

Figure D.5: Flow-mediated phosphorylation of VE-cadherin (VEC) reporting on the dynamic instability of cell-to-cell junctions. Figure on page 145 (a) Fluorescent images depicting the distribution of total VE-cadherin (green, top row), pY658-VE-cadherin (red, middle row) and of the colocalization (yellow, last row) between total and Y658-phosphorylated VE-cadherin. Panels from left to right display endothelia under static conditions (static), or exposed to flow yielding WSS of 1,4 Pa (parallel) or 8 Pa (perpendicular), or to the maladaptive transition upon flow reversal (reverse). Flow direction is defined by a white arrow. (b) Boxplots reporting the measured Pearson's correlation coefficient between VE-cadherin and phosphorylated VE-cadherin (py-VEC) channels for each condition. The number of analysed fields of view is reported as n and the number of independent experiments as n'.

E | References

[1] E. Schrödinger. What is life? the physical aspect of the living cell. erwin schrodinger. *The American Naturalist*, 79(785): 554–555. doi: 10.1086/281292. 1945.

[2] K. A. Jansen, D. M. Donato, H. E. Balcioglu, T. Schmidt, E. H. Danen and G. H. Koenderink. A guide to mechanobiology: where biology and physics meet. *Biochimica et Biophysica Acta (BBA)-Molecular Cell Research*, 1853(11): 3043–3052. 2015.

[3] J. Eyckmans, T. Boudou, X. Yu and C. S. Chen. A hitchhiker's guide to mechanobiology. *Developmental cell*, 21(1): 35–47. 2011.

[4] B. Ladoux and R.-M. Mège. Mechanobiology of collective cell behaviours. *Nature Reviews Molecular Cell Biology*, 18(12): 743. 2017.

[5] S. Na, O. Collin, F. Chowdhury, B. Tay, M. Ouyang, Y. Wang and N. Wang. Rapid signal transduction in living cells is a unique feature of mechanotransduction. *Proceedings of the National Academy of Sciences*, 105(18): 6626–6631. 2008.

[6] A. G. Kamkin and I. S. Kiseleva. *Mechanosensitivity in cells and tissues*. Springer. 2005.

[7] M. Behrndt, G. Salbreux, P. Campinho, R. Hauschild, F. Oswald, J. Roensch, S. W. Grill and C.-P. Heisenberg. Forces driving epithelial spreading in zebrafish gastrulation. *Science*, 338(6104): 257–260. 2012.

[8] A. W. Orr, B. P. Helmke, B. R. Blackman and M. A. Schwartz. Mechanisms of mechanotransduction. *Developmental cell*, 10(1): 11–20. 2006.

[9] P. K. Mattila, F. D. Batista and B. Treanor. Dynamics of the actin cytoskeleton mediates receptor cross talk: An emerging concept in tuning receptor signaling. *J Cell Biol*, 212(3): 267–280. 2016.

[10] A. E. Brown and D. E. Discher. Conformational changes and signaling in cell and matrix physics. *Current Biology*, 19(17): R781–R789. 2009.

[11] C. Galbraith, R. Skalak and S. Chien. Shear stress induces spatial reorganization of the endothelial cell cytoskeleton. *Cell motility and the cytoskeleton*, 40(4): 317–330. 1998.

[12] D. Mesland. Possible actions of gravity on the cellular machinery. *Advances in Space Research*, 12(1): 15–25. 1992.

[13] L. Leverett, J. Hellums, C. Alfrey and E. Lynch. Red blood cell damage by shear stress. *Biophysical journal*, 12(3): 257–273. 1972.

[14] A. M. Malek and S. Izumo. Mechanism of endothelial cell shape change and cytoskeletal remodeling in response to fluid shear stress. *Journal of cell science*, 109(4): 713–726. 1996.

[15] A. D. Acevedo, S. S. Bowser, M. E. Gerritsen and R. Bizios. Morphological and proliferative responses of endothelial cells to hydrostatic pressure: role of fibroblast growth factor. *Journal of cellular physiology*, 157(3): 603–614. 1993.

[16] F. Abe. Exploration of the effects of high hydrostatic pressure on microbial growth, physiology and survival: Perspectives from piezophysiology. *Bioscience, Biotechnology, and Biochemistry*, 71(10): 2347–2357. doi: 10.1271/bbb.70015. 2007.

[17] N. Caille, Y. Tardy and J.-J. Meister. Assessment of strain field in endothelial cells subjected to uniaxial deformation of their substrate. *Annals of biomedical engineering*, 26(3): 409–416. 1998.

[18] T. Mizutani, H. Haga and K. Kawabata. Cellular stiffness response to external deformation: tensional homeostasis in a single fibroblast. *Cell motility and the cytoskeleton*, 59(4): 242–248. 2004.

[19] J. H.-C. Wang, P. Goldschmidt-Clermont, J. Wille and F. C.-P. Yin. Specificity of endothelial cell reorientation in response to cyclic mechanical stretching. *Journal of biomechanics*, 34(12): 1563–1572. 2001.

[20] B. Liu, M.-J. Qu, K.-R. Qin, H. Li, Z.-K. Li, B.-R. Shen and Z.-L. Jiang. Role of cyclic strain frequency in regulating the alignment of vascular smooth muscle cells in vitro. *Biophysical journal*, 94(4): 1497–1507. 2008.

[21] A. A. Lee, T. Delhaas, A. D. McCulloch and F. J. Villarreal. Differential responses of adult cardiac fibroblasts to in vitro biaxial strain patterns. *Journal of Molecular and Cellular Cardiology*, 31(10): 1833–1843. doi: 10.1006/jmcc.1999.1017. 1999.

[22] S.-Y. Tee, J. Fu, C. S. Chen and P. A. Janmey. Cell shape and substrate rigidity both regulate cell stiffness. *Biophysical Journal*, 100(5): 25–27. doi: 10.1016/j.bpj.2010.12.3744. 2011.

[23] T. Yeung, P. C. Georges, L. A. Flanagan, B. Marg, M. Ortiz, M. Funaki, N. Zahir, W. Ming, V. Weaver and P. A. Janmey. Effects of substrate stiffness on cell morphology, cytoskeletal structure, and adhesion. *Cell motility and the cytoskeleton*, 60(1): 24–34. 2005.

[24] C.-M. Lo, H.-B. Wang, M. Dembo and Y.-l. Wang. Cell movement is guided by the rigidity of the substrate. *Biophysical journal*, 79(1): 144–152. 2000.

[25] A. Saez, M. Ghibaudo, A. Buguin, P. Silberzan and B. Ladoux. Rigidity-driven growth and migration of epithelial cells on microstructured anisotropic substrates. *Proceedings of the National Academy of Sciences*, 104(20): 8281–8286. 2007.

[26] C. J. Bettinger, R. Langer and J. T. Borenstein. Engineering substrate topography at the micro-and nanoscale to control cell function. *Angewandte Chemie International Edition*, 48(30): 5406–5415. 2009.

[27] M. Nikkhah, F. Edalat, S. Manoucheri and A. Khademhosseini. Engineering microscale topographies to control the cell–substrate interface. *Biomaterials*, 33(21): 5230–5246. 2012.

[28] M. Zündel. *Mechanical Interactions of Cells with Soft Synthetic Substrates: A Computational Analysis.* Ph.D. thesis, Eidgenössische Technische Hochschule Zürich. 2018.

[29] N. Wang, J. P. Butler and D. E. Ingber. Mechanotransduction across the cell surface and through the cytoskeleton. *Science*, 260(5111): 1124–1127. 1993.

[30] F. J. Alenghat and D. E. Ingber. Mechanotransduction: all signals point to cytoskeleton, matrix, and integrins. *Science Signaling*, 2002(119): pe6–pe6. 2002.

[31] D. E. Ingber. Mechanical control of tissue growth: function follows form. *Proceedings of the National Academy of Sciences*, 102(33): 11571–11572. 2005.

[32] D. E. Ingber. Tensegrity-based mechanosensing from macro to micro. *Progress in biophysics and molecular biology*, 97(2-3): 163–179. 2008.

[33] N. Wang and Z. Suo. Long-distance propagation of forces in a cell. *Biochemical and biophysical research communications*, 328(4): 1133–1138. 2005.

[34] A. C. Martin, M. Kaschube and E. F. Wieschaus. Pulsed contractions of an actin–myosin network drive apical constriction. *Nature*, 457(7228): 495. 2009.

[35] P. Pandya, J. L. Orgaz and V. Sanz-Moreno. Actomyosin contractility and collective migration: may the force be with you. *Current opinion in cell biology*, 48: 87–96. 2017.

[36] Z. Sun and Y. Toyama. Three-dimensional forces beyond actomyosin contraction: lessons from fly epithelial deformation. *Current opinion in genetics & development*, 51: 96–102. 2018.

[37] X. Trepat, L. Deng, S. S. An, D. Navajas, D. J. Tschumperlin, W. T. Gerthoffer, J. P. Butler and J. J. Fredberg. Universal physical responses to stretch in the living cell. *Nature*, 447(7144): 592. 2007.

[38] A. S. Torsoni, T. M. Marin, L. A. Velloso and K. G. Franchini. Rhoa/rock signaling is critical to fak activation by cyclic stretch in cardiac myocytes. *American Journal of Physiology-Heart and Circulatory Physiology*, 289(4): H1488–H1496. 2005.

[39] Y. Sun, C. S. Chen and J. Fu. Forcing stem cells to behave: a biophysical perspective of the cellular microenvironment. *Annual review of biophysics*, 41: 519–542. 2012.

[40] P. Kanchanawong, G. Shtengel, A. M. Pasapera, E. B. Ramko, M. W. Davidson, H. F. Hess and C. M. Waterman. Nanoscale architecture of integrin-based cell adhesions. *Nature*, 468(7323): 580. 2010.

[41] A. Bershadsky, M. Kozlov and B. Geiger. Adhesion-mediated mechanosensitivity: a time to experiment, and a time to theorize. *Current opinion in cell biology*, 18(5): 472–481. 2006.

[42] A. Ferrari and M. Cecchini. *Cells on Patterns*, chapter 12, 267–290. John Wiley & Sons, Ltd. ISBN 9783527633449. doi: 10.1002/9783527633449.ch12. 2011.

[43] F. Robotti, D. Franco, L. Bänninger, J. Wyler, C. T. Starck, V. Falk, D. Poulikakos and A. Ferrari. The influence of surface micro-structure on endothelialization under supraphysiological wall shear stress. *Biomaterials*, 35(30): 8479–8486. 2014.

[44] D. Franco, M. Klingauf, M. Bednarzik, M. Cecchini, V. Kurtcuoglu, J. Gobrecht, D. Poulikakos and A. Ferrari. Control of initial endothelial spreading by topographic activation of focal adhesion kinase. *Soft Matter*, 7(16): 7313–7324. 2011.

[45] C. S. Chen. Mechanotransduction–a field pulling together? *Journal of cell science*, 121(20): 3285–3292. 2008.

[46] B. R. Sarangi, M. Gupta, B. L. Doss, N. Tissot, F. Lam, R.-M. Mege, N. Borghi and B. Ladoux. Coordination between intra-and extracellular forces regulates focal adhesion dynamics. *Nano letters*, 17(1): 399–406. 2016.

[47] A. M. Pasapera, I. C. Schneider, E. Rericha, D. D. Schlaepfer and C. M. Waterman. Myosin ii activity regulates vinculin recruitment to focal adhesions through fak-mediated paxillin phosphorylation. *The Journal of cell biology*, 188(6): 877–890. 2010.

[48] R. Zaidel-Bar, S. Itzkovitz, A. Ma'ayan, R. Iyengar and B. Geiger. Functional atlas of the integrin adhesome. *Nature cell biology*, 9(8): 858. 2007.

[49] J. S. Lowe and P. G. Anderson. Chapter 3 - epithelial cells. In J. S. Lowe and P. G. Anderson (Editors), *Stevens & Lowe's Human Histology (Fourth Edition) (Fourth Edition)*, 37 – 54. Mosby, Philadelphia, fourth edition edition. doi: doi.org/10.1016/B978-0-7234-3502-0.00003-6. 2015.

[50] E. A. Jaffe. Cell biology of endothelial cells. *Human Pathology*, 18(3): 234 – 239. ISSN 0046-8177. doi: doi.org/10.1016/S0046-8177(87)80005-9. 1987.

[51] M. Takeichi. The cadherins: cell-cell adhesion molecules controlling animal morphogenesis. *Development*, 102(4): 639–655. 1988.

[52] T. Lecuit and A. S. Yap. E-cadherin junctions as active mechanical integrators in tissue dynamics. *Nature cell biology*, 17(5): 533. 2015.

[53] D. Leckband and J. De Rooij. Cadherin adhesion and mechanotransduction. *Annual review of cell and developmental biology*, 30: 291–315. 2014.

[54] C. Bertet, L. Sulak and T. Lecuit. Myosin-dependent junction remodelling controls planar cell intercalation and axis elongation. *Nature*, 429(6992): 667. 2004.

[55] J. T. Parsons, A. R. Horwitz and M. A. Schwartz. Cell adhesion: integrating cytoskeletal dynamics and cellular tension. *Nature reviews Molecular cell biology*, 11(9): 633. 2010.

[56] E. Bazellières, V. Conte, A. Elosegui-Artola, X. Serra-Picamal, M. Bintanel-Morcillo, P. Roca-Cusachs, J. J. Muñoz, M. Sales-Pardo, R. Guimerà and X. Trepat. Control of cell–cell forces and collective cell dynamics by the intercellular adhesome. *Nature cell biology*, 17(4): 409. 2015.

[57] M. Takeichi. Dynamic contacts: rearranging adherens junctions to drive epithelial remodelling. *Nature reviews Molecular cell biology*, 15(6): 397. 2014.

[58] P. Rodríguez-Franco, A. Brugués, A. Marín-Llauradó, V. Conte, G. Solanas, E. Batlle, J. J. Fredberg, P. Roca-Cusachs, R. Sunyer and X. Trepat. Long-lived force patterns and deformation waves at repulsive epithelial boundaries. *Nature materials*, 16(10): 1029. 2017.

[59] X. Serra-Picamal, V. Conte, R. Vincent, E. Anon, D. T. Tambe, E. Bazellieres, J. P. Butler, J. J. Fredberg and X. Trepat. Mechanical waves during tissue expansion. *Nature Physics*, 8(8): 628. 2012.

[60] S. E. Murthy, A. E. Dubin and A. Patapoutian. Piezos thrive under pressure: mechanically activated ion channels in health and disease. *Nature Reviews Molecular Cell Biology*, 18(12): 771. 2017.

[61] S. Katta, M. Krieg and M. B. Goodman. Feeling force: physical and physiological principles enabling sensory mechanotransduction. *Annual review of cell and developmental biology*, 31: 347–371. 2015.

[62] C. E. Morris, E. A. Prikryl and B. Joós. Mechanosensitive gating of kv channels. *PloS one*, 10(2): e0118335. 2015.

[63] J. Liu, H. Kang, X. Ma, A. Sun, H. Luan, X. Deng and Y. Fan. Vascular cell glycocalyx-mediated vascular remodeling induced by hemodynamic environmental alteration. *Hypertension*, 71(6): 1201–1209. doi: 10.1161/Hypertensionaha.117.10678. 2018.

[64] E. J. Kodis, R. J. Smindak, J. M. Kefauver, D. L. Heffner, K. L. Aschenbach, E. R. Brennan, K. Chan, K. K. Gamage, P. S. Lambeth, J. R. Lawler *et al.* First messengers. *e LS*. 2001.

[65] T. D. Pollard, W. C. Earnshaw, J. Lippincott-Schwartz and G. Johnson. Chapter 26 - second messengers. In T. D. Pollard, W. C. Earnshaw, J. Lippincott-Schwartz and G. T. Johnson (Editors), *Cell Biology (Third Edition)*, 443 – 462. Elsevier, third edition edition. doi: 10.1016/B978-0-323-34126-4.00026-8. 2017.

[66] M. Y. Pahakis, J. R. Kosky, R. O. Dull and J. M. Tarbell. The role of endothelial glycocalyx components in mechanotransduction of fluid shear stress. *Biochemical and biophysical research communications*, 355(1): 228–233. 2007.

[67] J. Lammerding, J. Hsiao, P. C. Schulze, S. Kozlov, C. L. Stewart and R. T. Lee. Abnormal nuclear shape and impaired mechanotransduction in emerin-deficient cells. *J cell biol*, 170(5): 781–791. 2005.

[68] C. Uhler and G. Shivashankar. Regulation of genome organization and gene expression by nuclear mechanotransduction. *Nature Reviews Molecular Cell Biology*, 18(12): 717. 2017.

[69] N. Wang, J. D. Tytell and D. E. Ingber. Mechanotransduction at a distance: mechanically coupling the extracellular matrix with the nucleus. *Nature reviews Molecular cell biology*, 10(1): 75. 2009.

[70] J. L. Kadrmas and M. C. Beckerle. The lim domain: from the cytoskeleton to the nucleus. *Nature reviews Molecular cell biology*, 5(11): 920. 2004.

[71] R. Pawłowski, E. K. Rajakylä, M. K. Vartiainen and R. Treisman. An actin-regulated importin α/β-dependent extended bipartite nls directs nuclear import of mrtf-a. *The EMBO Journal*, 29(20): 3448–3458. 2010.

[72] C. Lanctôt, T. Cheutin, M. Cremer, G. Cavalli and T. Cremer. Dynamic genome architecture in the nuclear space: regulation of gene expression in three dimensions. *Nature Reviews Genetics*, 8(2): 104. 2007.

[73] R. S. Gieni and M. J. Hendzel. Mechanotransduction from the ecm to the genome: are the pieces now in place? *Journal of cellular biochemistry*, 104(6): 1964–1987. 2008.

[74] K. Fal, A. Asnacios, M.-E. Chabouté and O. Hamant. Nuclear envelope: a new frontier in plant mechanosensing? *Biophysical reviews*, 9(4): 389–403. 2017.

[75] G. Shivashankar. Mechanosignaling to the cell nucleus and gene regulation. *Annual review of biophysics*, 40: 361–378. 2011.

[76] D. Eder, C. Aegerter and K. Basler. Forces controlling organ growth and size. *Mechanisms of development*, 144: 53–61. 2017.

[77] E. Farge. Mechanotransduction in development. In *Current topics in developmental biology*, volume 95, 243–265. Elsevier. 2011.

[78] D. E. Jaalouk and J. Lammerding. Mechanotransduction gone awry. *Nature reviews Molecular cell biology*, 10(1): 63. 2009.

[79] M. A. Gimbrone Jr, J. N. Topper, T. Nagel, K. R. Anderson and G. Garcia-Cardeña. Endothelial dysfunction, hemodynamic forces, and atherogenesis a. *Annals of the New York Academy of Sciences*, 902(1): 230–240. 2000.

[80] G. García-Cardeña, J. Comander, K. R. Anderson, B. R. Blackman and M. A. Gimbrone. Biomechanical activation of vascular endothelium as a determinant of its functional phenotype. *Proceedings of the National Academy of Sciences*, 98(8): 4478–4485. 2001.

[81] J. Klein-Nulend, R. Bacabac, J. Veldhuijzen and J. Van Loon. Microgravity and bone cell mechanosensitivity. *Advances in Space Research*, 32(8): 1551–1559. 2003.

[82] D. A. Affonce and K. R. Lutchen. New perspectives on the mechanical basis for airway hyperreactivity and airway hypersensitivity in asthma. *Journal of applied physiology*, 101(6): 1710–1719. 2006.

[83] S. Uhlig. Ventilation-induced lung injury and mechanotransduction: stretching it too far? *American Journal of Physiology-Lung Cellular and Molecular Physiology*, 282(5): L892–L896. 2002.

[84] S. Huang and D. E. Ingber. Cell tension, matrix mechanics, and cancer development. *Cancer cell*, 8(3): 175–176. 2005.

[85] S. Suresh. Biomechanics and biophysics of cancer cells. *Acta Materialia*, 55(12): 3989–4014. 2007.

[86] M. J. Paszek, N. Zahir, K. R. Johnson, J. N. Lakins, G. I. Rozenberg, A. Gefen, C. A. Reinhart-King, S. S. Margulies, M. Dembo, D. Boettiger *et al.* Tensional homeostasis and the malignant phenotype. *Cancer cell*, 8(3): 241–254. 2005.

[87] J. Y. Ji, H. Jing and S. L. Diamond. Hemodynamic regulation of inflammation at the endothelial–neutrophil interface. *Annals of biomedical engineering*, 36(4): 586–595. 2008.

[88] M. F. Coughlin, D. D. Sohn and G. W. Schmid-Schönbein. Recoil and stiffening by adherent leukocytes in response to fluid shear. *Biophysical journal*, 94(3): 1046–1051. 2008.

[89] W. Herrington, B. Lacey, P. Sherliker, J. Armitage and S. Lewington. Epidemiology of atherosclerosis and the potential to reduce the global burden of atherothrombotic disease. *Circulation research*, 118(4): 535–546. 2016.

[90] W. Insull Jr. The pathology of atherosclerosis: plaque development and plaque responses to medical treatment. *The American journal of medicine*, 122(1): S3–S14. 2009.

[91] P. L. da Luz, A. C. P. Chagas, P. M. M. Dourado and F. R. Laurindo. Chapter 33 - endothelium in atherosclerosis: Plaque formation and its complications. In P. L. D. Luz, P. Libby, A. C. Chagas and F. R. Laurindo (Editors), *Endothelium and Cardiovascular Diseases*, 493 – 512. Academic Press. doi: doi.org/10.1016/B978-0-12-812348-5.00033-7. 2018.

[92] A. Kumar, N. Khandelwal, R. Malya, M. B. Reid and A. M. Boriek. Loss of dystrophin causes aberrant mechanotransduction in skeletal muscle fibers. *The FASEB Journal*, 18(1): 102–113. 2004.

[93] L. Nicholson, M. A. Johnson, K. Bushby, D. Gardner-Medwin, A. Curtis, I. B. Ginjaar, J. T. den Dunnen, J. Welch, T. Butler and E. Bakker. Integrated study of 100 patients with xp21 linked muscular dystrophy using clinical, genetic, immunochemical, and histopathological data. part 2. correlations within individual patients. *Journal of medical genetics*, 30(9): 737–744. 1993.

[94] L. Chin, Y. Xia, D. E. Discher and P. A. Janmey. Mechanotransduction in cancer. *Current opinion in chemical engineering*, 11: 77–84. 2016.

[95] Z. Mohri, A. D. R. Hernandez and R. Krams. The emerging role of yap/taz in mechanotransduction. *Journal of thoracic disease*, 9(5): E507. 2017.

[96] D. Ingber. Mechanobiology and diseases of mechanotransduction. *Annals of medicine*, 35(8): 564–577. 2003.

[97] A.-L. Cost, P. Ringer, A. Chrostek-Grashoff and C. Grashoff. How to measure molecular forces in cells: a guide to evaluating genetically-encoded fret-based tension sensors. *Cellular and molecular bioengineering*, 8(1): 96–105. 2015.

[98] E. Lauga and T. R. Powers. The hydrodynamics of swimming microorganisms. *Reports on Progress in Physics*, 72(9): 096601. 2009.

[99] P. Roca-Cusachs, V. Conte and X. Trepat. Quantifying forces in cell biology. *Nature cell biology*, 19(7): 742. 2017.

[100] A. K. Harris, P. Wild and D. Stopak. Silicone rubber substrata: a new wrinkle in the study of cell locomotion. *Science*, 208(4440): 177–179. 1980.

[101] E. Bell, B. Ivarsson and C. Merrill. Production of a tissue-like structure by contraction of collagen lattices by human fibroblasts of different proliferative potential in vitro. *Proceedings of the National Academy of Sciences*, 76(3): 1274–1278. 1979.

[102] T. D. Allen and S. L. Schor. The contraction of collagen matrices by dermal fibroblasts. *Journal of ultrastructure research*, 83(2): 205–219. 1983.

[103] X. Trepat, M. R. Wasserman, T. E. Angelini, E. Millet, D. A. Weitz, J. P. Butler and J. J. Fredberg. Physical forces during collective cell migration. *Nature physics*, 5(6): 426. 2009.

[104] A. Brugués, E. Anon, V. Conte, J. H. Veldhuis, M. Gupta, J. Colombelli, J. J. Muñoz, G. W. Brodland, B. Ladoux and X. Trepat. Forces driving epithelial wound healing. *Nature physics*, 10(9): 683. 2014.

[105] W. J. Polacheck and C. S. Chen. Measuring cell-generated forces: a guide to the available tools. *Nature methods*, 13(5): 415. 2016.

[106] J. L. Tan, J. Tien, D. M. Pirone, D. S. Gray, K. Bhadriraju and C. S. Chen. Cells lying on a bed of microneedles: an approach to isolate mechanical force. *Proceedings of the National Academy of Sciences*, 100(4): 1484–1489. 2003.

[107] M. Dembo, T. Oliver, A. Ishihara and K. Jacobson. Imaging the traction stresses exerted by locomoting cells with the elastic substratum method. *Biophysical journal*, 70(4): 2008–2022. 1996.

[108] U. S. Schwarz and J. R. Soiné. Traction force microscopy on soft elastic substrates: A guide to recent computational advances. *Biochimica et Biophysica Acta (BBA)-Molecular Cell Research*, 1853(11): 3095–3104. 2015.

[109] K. Burton, J. H. Park and D. L. Taylor. Keratocytes generate traction forces in two phases. *Molecular biology of the cell*, 10(11): 3745–3769. 1999.

[110] Y. Zhang, C. Ge, C. Zhu and K. Salaita. Dna-based digital tension probes reveal integrin forces during early cell adhesion. *Nature communications*, 5: 5167. 2014.

[111] D. R. Myers, Y. Qiu, M. E. Fay, M. Tennenbaum, D. Chester, J. Cuadrado, Y. Sakurai, J. Baek, R. Tran, J. C. Ciciliano *et al.* Single-platelet nanomechanics measured by high-throughput cytometry. *Nature materials*, 16(2): 230. 2017.

[112] A. Marmaras, T. Lendenmann, G. Civenni, D. Franco, D. Poulikakos, V. Kurtcuoglu and A. Ferrari. Topography-mediated apical guidance in epidermal wound healing. *Soft Matter*, 8(26): 6922–6930. 2012.

[113] B. L. Blakely, C. E. Dumelin, B. Trappmann, L. M. McGregor, C. K. Choi, P. C. Anthony, V. K. Duesterberg, B. M. Baker, S. M. Block, D. R. Liu *et al.* A dna-based molecular probe for optically reporting cellular traction forces. *nature methods*, 11(12): 1229. 2014.

[114] H. Colin-York, D. Shrestha, J. H. Felce, D. Waithe, E. Moeendarbary, S. J. Davis, C. Eggeling and M. Fritzsche. Super-resolved traction force microscopy (stfm). *Nano letters*, 16(4): 2633–2638. 2016.

[115] S. V. Plotnikov, B. Sabass, U. S. Schwarz and C. M. Waterman. High-resolution traction force microscopy. In *Methods in cell biology*, volume 123, 367–394. Elsevier. 2014.

[116] R. J. Adrian. Twenty years of particle image velocimetry. *Experiments in fluids*, 39(2): 159–169. 2005.

[117] J. P. Butler, I. M. Tolic-Nørrelykke, B. Fabry and J. J. Fredberg. Traction fields, moments, and strain energy that cells exert on their surroundings. *American Journal of Physiology-Cell Physiology*, 282(3): C595–C605. 2002.

[118] B. Sabass, M. L. Gardel, C. M. Waterman and U. S. Schwarz. High resolution traction force microscopy based on experimental and computational advances. *Biophysical journal*, 94(1): 207–220. 2008.

[119] Z. Yang, J.-S. Lin, J. Chen and J. H. Wang. Determining substrate displacement and cell traction fields—a new approach. *Journal of theoretical biology*, 242(3): 607–616. 2006.

[120] T. M. Koch, S. Münster, N. Bonakdar, J. P. Butler and B. Fabry. 3d traction forces in cancer cell invasion. *PloS one*, 7(3): e33476. 2012.

[121] K. Bircher, A. E. Ehret and E. Mazza. Microstructure based prediction of the deformation behavior of soft collagenous membranes. *Soft matter*, 13(30): 5107–5116. 2017.

[122] M. Zündel, A. E. Ehret and E. Mazza. The multiscale stiffness of electrospun substrates and aspects of their mechanical biocompatibility. *Acta biomaterialia*. 2018.

[123] S. Domaschke, M. Zündel, E. Mazza and A. E. Ehret. A 3d computational model of electrospun networks and its application to inform a reduced modelling approach. *International Journal of Solids and Structures*. 2018.

[124] J. H. Kim, X. Serra-Picamal, D. T. Tambe, E. H. Zhou, C. Y. Park, M. Sadati, J.-A. Park, R. Krishnan, B. Gweon, E. Millet *et al.* Propulsion and navigation within the advancing monolayer sheet. *Nature materials*, 12(9): 856. 2013.

[125] D. T. Tambe, C. C. Hardin, T. E. Angelini, K. Rajendran, C. Y. Park, X. Serra-Picamal, E. H. Zhou, M. H. Zaman, J. P. Butler, D. A. Weitz *et al.* Collective cell guidance by cooperative intercellular forces. *Nature materials*, 10(6): 469. 2011.

[126] D. T. Tambe, U. Croutelle, X. Trepat, C. Y. Park, J. H. Kim, E. Millet, J. P. Butler and J. J. Fredberg. Monolayer stress microscopy: limitations, artifacts, and accuracy of recovered intercellular stresses. *PloS one*, 8(2): e55172. 2013.

[127] X. Trepat and J. J. Fredberg. Plithotaxis and emergent dynamics in collective cellular migration. *Trends in cell biology*, 21(11): 638–646. 2011.

[128] D. A. Lauffenburger and A. F. Horwitz. Cell migration: a physically integrated molecular process. *Cell*, 84(3): 359–369. 1996.

[129] A. J. Ridley, M. A. Schwartz, K. Burridge, R. A. Firtel, M. H. Ginsberg, G. Borisy, J. T. Parsons and A. R. Horwitz. Cell migration: integrating signals from front to back. *Science*, 302(5651): 1704–1709. 2003.

[130] B. Geiger, J. P. Spatz and A. D. Bershadsky. Environmental sensing through focal adhesions. *Nature reviews Molecular cell biology*, 10(1): 21. 2009.

[131] L. Ji, J. Lim and G. Danuser. Fluctuations of intracellular forces during cell protrusion. *Nature cell biology*, 10(12): 1393. 2008.

[132] R. J. Petrie and K. M. Yamada. Fibroblasts lead the way: a unified view of 3d cell motility. *Trends in cell biology*, 25(11): 666–674. 2015.

[133] R. Keller. Physical biology returns to morphogenesis. *Science*, 338(6104): 201–203. 2012.

[134] M. Arnold, V. C. Hirschfeld-Warneken, T. Lohmuller, P. Heil, J. Blummmel, E. A. Cavalcanti-Adam, M. López-García, P. Walther, H. Kessler, B. Geiger *et al.* Induction of cell polarization and migration by a gradient of nanoscale variations in adhesive ligand spacing. *Nano letters*, 8(7): 2063–2069. 2008.

[135] S. A. Biela, Y. Su, J. P. Spatz and R. Kemkemer. Different sensitivity of human endothelial cells, smooth muscle cells and fibroblasts to topography in the nano–micro range. *Acta biomaterialia*, 5(7): 2460–2466. 2009.

[136] T. Lämmermann and M. Sixt. Mechanical modes of 'amoeboid'cell migration. *Current opinion in cell biology*, 21(5): 636–644. 2009.

[137] E. K. Paluch, I. M. Aspalter and M. Sixt. Focal adhesion–independent cell migration. *Annual review of cell and developmental biology*, 32: 469–490. 2016.

[138] X. Trepat, B. Fabry and J. J. Fredberg. Pulling it together in three dimensions. *nature methods*, 7(12): 963. 2010.

[139] D. Lehnert, B. Wehrle-Haller, C. David, U. Weiland, C. Ballestrem, B. A. Imhof and M. Bastmeyer. Cell behaviour on micropatterned substrata: limits of extracellular matrix geometry for spreading and adhesion. *Journal of cell science*, 117(1): 41–52. 2004.

[140] P. Galliker, J. Schneider, H. Eghlidi, S. Kress, V. Sandoghdar and D. Poulikakos. Direct printing of nanostructures by electrostatic autofocussing of ink nanodroplets. *Nature communications*, 3: 890. 2012.

[141] J. W. Goding. Immunofluorescence. In *Monoclonal Antibodies (Third Edition)*, chapter 12, 352 – 399. Academic Press, London, third edition edition. ISBN 978-0-12-287023-1. doi: doi.org/10.1016/B978-012287023-1/50060-2. 1996.

[142] A. Sakaue-Sawano, H. Kurokawa, T. Morimura, A. Hanyu, H. Hama, H. Osawa, S. Kashiwagi, K. Fukami, T. Miyata, H. Miyoshi *et al.* Visualizing spatiotemporal dynamics of multicellular cell-cycle progression. *Cell*, 132(3): 487–498. 2008.

[143] S. Garcia, E. Hannezo, J. Elgeti, J.-F. Joanny, P. Silberzan and N. S. Gov. Physics of active jamming during collective cellular motion in a monolayer. *Proceedings of the National Academy of Sciences*, 112(50): 15314–15319. 2015.

[144] E. Dejana. Endothelial cell–cell junctions: happy together. *Nature reviews Molecular cell biology*, 5(4): 261. 2004.

[145] D. St Johnston and B. Sanson. Epithelial polarity and morphogenesis. *Current opinion in cell biology*, 23(5): 540–546. 2011.

[146] T. E. Angelini, E. Hannezo, X. Trepat, M. Marquez, J. J. Fredberg and D. A. Weitz. Glass-like dynamics of collective cell migration. *Proceedings of the National Academy of Sciences*, 108(12): 4714–4719. 2011.

[147] J. P. Garrahan. Dynamic heterogeneity comes to life. *Proceedings of the National Academy of Sciences*, 108(12): 4701–4702. 2011.

[148] M. Sadati, N. T. Qazvini, R. Krishnan, C. Y. Park and J. J. Fredberg. Collective migration and cell jamming. *Differentiation*, 86(3): 121–125. 2013.

[149] P. Friedl and D. Gilmour. Collective cell migration in morphogenesis, regeneration and cancer. *Nature reviews Molecular cell biology*, 10(7): 445. 2009.

[150] M. Bergert, T. Lendenmann, M. Zündel, A. E. Ehret, D. Panozzo, P. Richner, D. K. Kim, S. J. Kress, D. J. Norris, O. Sorkine-Hornung *et al.* Confocal reference free traction force microscopy. *Nature communications*, 7: 12814. 2016.

[151] M. F. Fournier, R. Sauser, D. Ambrosi, J.-J. Meister and A. B. Verkhovsky. Force transmission in migrating cells. *The Journal of cell biology*, 188(2): 287–297. 2010.

[152] J. D. Humphrey, E. R. Dufresne and M. A. Schwartz. Mechanotransduction and extracellular matrix homeostasis. *Nature reviews Molecular cell biology*, 15(12): 802. 2014.

[153] A. J. Ribeiro, A. K. Denisin, R. E. Wilson and B. L. Pruitt. For whom the cells pull: Hydrogel and micropost devices for measuring traction forces. *Methods*, 94: 51–64. 2016.

[154] J. Fu, Y.-K. Wang, M. T. Yang, R. A. Desai, X. Yu, Z. Liu and C. S. Chen. Mechanical regulation of cell function with geometrically modulated elastomeric substrates. *Nature methods*, 7(9): 733. 2010.

[155] D.-H. Kim, P. P. Provenzano, C. L. Smith and A. Levchenko. Matrix nanotopography as a regulator of cell function. *J Cell Biol*, 197(3): 351–360. 2012.

[156] A. Curtis and C. Wilkinson. Topographical control of cells. *Biomaterials*, 18(24): 1573–1583. 1997.

[157] M. Dembo and Y.-L. Wang. Stresses at the cell-to-substrate interface during locomotion of fibroblasts. *Biophysical Journal*, 76(4): 2307 – 2316. ISSN 0006-3495. doi: 10.1016/S0006-3495(99)77386-8. 1999.

[158] E. P. Canović, D. T. Seidl, S. R. Polio, A. A. Oberai, P. E. Barbone, D. Stamenović and M. L. Smith. Biomechanical imaging of cell stiffness and prestress with subcellular resolution. *Biomechanics and modeling in mechanobiology*, 13(3): 665–678. 2014.

[159] S. R. Polio, K. E. Rothenberg, D. Stamenović and M. L. Smith. A micropatterning and image processing approach to simplify measurement of cellular traction forces. *Acta biomaterialia*, 8(1): 82–88. 2012.

[160] N. Q. Balaban, U. S. Schwarz, D. Riveline, P. Goichberg, G. Tzur, I. Sabanay, D. Mahalu, S. Safran, A. Bershadsky, L. Addadi *et al.* Force and focal adhesion assembly: a close relationship studied using elastic micropatterned substrates. *Nature cell biology*, 3(5): 466. 2001.

[161] P. Galliker, J. Schneider, L. Rüthemann and D. Poulikakos. Open-atmosphere sustenance of highly volatile attoliter-size droplets on surfaces. *Proceedings of the National Academy of Sciences*, 110(33): 13255–13260. 2013.

[162] S. J. Kress, P. Richner, S. V. Jayanti, P. Galliker, D. K. Kim, D. Poulikakos and D. J. Norris. Near-field light design with colloidal quantum dots for photonics and plasmonics. *Nano letters*, 14(10): 5827–5833. 2014.

[163] P. Richner, H. Eghlidi, S. J. Kress, M. Schmid, D. J. Norris and D. Poulikakos. Printable nanoscopic metamaterial absorbers and images with diffraction-limited resolution. *ACS applied materials & interfaces*, 8(18): 11690–11697. 2016.

[164] R. W. Style, R. Boltyanskiy, G. K. German, C. Hyland, C. W. MacMinn, A. F. Mertz, L. A. Wilen, Y. Xu and E. R. Dufresne. Traction force microscopy in physics and biology. *Soft Matter*, 10: 4047–4055. doi: 10.1039/C4SM00264D. 2014.

[165] Y. Iwadate and S. Yumura. Molecular dynamics and forces of a motile cell simultaneously visualized by tirf and force microscopies. *Biotechniques*, 44(6): 739–50. doi: 10.2144/000112752. 2008.

[166] A. F. Mertz, S. Banerjee, Y. Che, G. K. German, Y. Xu, C. Hyland, M. C. Marchetti, V. Horsley and E. R. Dufresne. Scaling of traction forces with the size of cohesive cell colonies. *Phys. Rev. Lett.*, 108: 198101. doi: 10.1103/PhysRevLett.108.198101. 2012.

[167] A. F. Mertz, Y. Che, S. Banerjee, J. M. Goldstein, K. A. Rosowski, S. F. Revilla, C. M. Niessen, M. C. Marchetti, E. R. Dufresne and V. Horsley. Cadherin-based intercellular adhesions organize epithelial cell-matrix traction forces. *Proceedings of the National Academy of Sciences*, 110(3): 842–847. doi: 10.1073/pnas.1217279110. 2013.

[168] G. Bartalena, R. Grieder, R. I. Sharma, T. Zambelli, R. Muff and J. G. Snedeker. A novel method for assessing adherent single-cell stiffness in tension: design and testing of a substrate-based live cell functional imaging device. *Biomedical Microdevices*, 13(2): 291–301. ISSN 1572-8781. doi: 10.1007/s10544-010-9493-3. 2011.

[169] R. Merkel, N. Kirchgeßner, C. M. Cesa and B. Hoffmann. Cell force microscopy on elastic layers of finite thickness. *Biophysical journal*, 93(9): 3314–3323. doi: 10.1529/biophysj.107.111328. 2007.

[170] S. Deguchi, J. Hotta, S. Yokoyama and T. S. Matsui. Viscoelastic and optical properties of four different pdms polymers. *Journal of Micromechanics and Microengineering*, 25(9): 097002. doi: 10.1088/0960-1317/25/9/097002. 2015.

[171] M. Yao and J. Fang. Hydrophilic peo-pdms for microfluidic applications. *Journal of Micromechanics and Microengineering*, 22(2): 025012. doi: 10.1088/0960-1317/22/2/025012. 2012.

[172] R. Hopf, L. Bernardi, J. Menze, M. Zündel, E. Mazza and A. Ehret. Experimental and theoretical analyses of the age-dependent large-strain behavior of sylgard 184 (10:1) silicone elastomer. *Journal of the Mechanical Behavior of Biomedical Materials*, 60: 425 – 437. ISSN 1751-6161. doi: 10.1016/j.jmbbm.2016.02.022. 2016.

[173] W. Loesberg, J. te Riet, F. van Delft, P. Schön, C. Figdor, S. Speller, J. van Loon, X. Walboomers and J. Jansen. The threshold at which substrate nanogroove dimensions may influence fibroblast alignment and adhesion. *Biomaterials*, 28(27): 3944 – 3951. ISSN 0142-9612. doi: 10.1016/j.biomaterials.2007.05.030. 2007.

[174] E. A. Cavalcanti-Adam, T. Volberg, A. Micoulet, H. Kessler, B. Geiger and J. P. Spatz. Cell spreading and focal adhesion dynamics are regulated by spacing of integrin ligands. *Biophysical journal*, 92(8): 2964–2974. doi: 10.1529/biophysj.106.089730. 2007.

[175] J. Schneider, T. Bachmann, D. Franco, P. Richner, P. Galliker, M. K. Tiwari, A. Ferrari and D. Poulikakos. A novel 3d integrated platform for the high-resolution study of cell migration plasticity. *Macromolecular Bioscience*, 13(8): 973–983. ISSN 1616-5195. doi: 10.1002/mabi.201200416. 2013.

[176] A. Jorge-Peñas, A. Izquierdo-Alvarez, R. Aguilar-Cuenca, M. Vicente-Manzanares, J. M. Garcia-Aznar, H. Van Oosterwyck, E. M. de Juan-Pardo, C. Ortiz-de Solorzano and A. Muñoz-Barrutia. Free form deformation-based image registration improves accuracy of traction force microscopy. *PLoS ONE*, 10(12): 1–22. doi: 10.1371/journal.pone.0144184. 2015.

[177] S. J. Han, Y. Oak, A. Groisman and G. Danuser. Traction microscopy to identify force modulation in subresolution adhesions. *Nature methods*, 12(7): 653–656. doi: 10.1038/nmeth.3430. 2015.

[178] S. Munevar, Y.-l. Wang and M. Dembo. Traction force microscopy of migrating normal and h-ras transformed 3t3 fibroblasts. *Biophysical journal*, 80(4): 1744–1757. 2001.

[179] W. R. Legant, J. S. Miller, B. L. Blakely, D. M. Cohen, G. M. Genin and C. S. Chen. Measurement of mechanical tractions exerted by cells in three-dimensional matrices. *Nature methods*, 7(12): 969–971. doi: 10.1038/nmeth.1531. 2010.

[180] L. Trichet, J. Le Digabel, R. J. Hawkins, S. R. K. Vedula, M. Gupta, C. Ribrault, P. Hersen, R. Voituriez and B. Ladoux. Evidence of a large-scale mechanosensing mechanism for cellular adaptation to substrate stiffness. *Proceedings of the National Academy of Sciences*, 109(18): 6933–6938. doi: 10.1073/pnas.1117810109. 2012.

[181] W. R. Legant, C. K. Choi, J. S. Miller, L. Shao, L. Gao, E. Betzig and C. S. Chen. Multidimensional traction force microscopy reveals out-of-plane rotational moments about focal adhesions. *Proceedings of the National Academy of Sciences*, 110(3): 881–886. doi: 10.1073/pnas.1207997110. 2013.

[182] S. S. Hur, Y. Zhao, Y.-S. Li, E. Botvinick and S. Chien. Live cells exert 3-dimensional traction forces on their substrata. *Cellular and Molecular Bioengineering*, 2(3): 425–436. ISSN 1865-5033. doi: 10.1007/s12195-009-0082-6. 2009.

[183] M. Aragona, T. Panciera, A. Manfrin, S. Giulitti, F. Michielin, N. Elvassore, S. Dupont and S. Piccolo. A mechanical checkpoint controls multicellular growth through yap/taz regulation by actin-processing factors. *Cell*, 154(5): 1047 – 1059. ISSN 0092-8674. doi: 10.1016/j.cell.2013.07.042. 2013.

[184] S. Ghassemi, G. Meacci, S. Liu, A. A. Gondarenko, A. Mathur, P. Roca-Cusachs, M. P. Sheetz and J. Hone. Cells test substrate rigidity by local contractions on submicrometer pillars. *Proceedings of the National Academy of Sciences*, 109(14): 5328–5333. doi: 10.1073/pnas.1119886109. 2012.

[185] D. W. Dumbauld, T. T. Lee, A. Singh, J. Scrimgeour, C. A. Gersbach, E. A. Zamir, J. Fu, C. S. Chen, J. E. Curtis, S. W. Craig and A. J. Garcia. How vinculin regulates force transmission. *Proceedings of the National Academy of Sciences*, 110(24): 9788–9793. doi: 10.1073/pnas.1216209110. 2013.

[186] K. T. Bashour, A. Gondarenko, H. Chen, K. Shen, X. Liu, M. Huse, J. C. Hone and L. C. Kam. Cd28 and cd3 have complementary roles in t-cell traction forces. *Proceedings of the National Academy of Sciences*, 111(6): 2241–2246. doi: 10.1073/pnas.1315606111. 2014.

[187] T. Das, K. Safferling, S. Rausch, N. Grabe, H. Boehm and J. P. Spatz. A molecular mechanotransduction pathway regulates collective migration of epithelial cells. *Nature cell biology*, 17(3): 276–287. doi: 10.1038/ncb3115. 2015.

[188] B. Zhao, X. Wei, W. Li, R. S. Udan, Q. Yang, J. Kim, J. Xie, T. Ikenoue, J. Yu, L. Li *et al.* Inactivation of yap oncoprotein by the hippo pathway is involved in cell contact inhibition and tissue growth control. *Genes & development*, 21(21): 2747–2761. doi: 10.1101/gad.1602907. 2007.

[189] S. J. P. Kress, F. V. Antolinez, P. Richner, S. V. Jayanti, D. K. Kim, F. Prins, A. Riedinger, M. P. C. Fischer, S. Meyer, K. M. McPeak, D. Poulikakos and D. J. Norris. Wedge waveguides and resonators for quantum plasmonics. *Nano Letters*, 15(9): 6267–6275. doi: 10.1021/acs.nanolett.5b03051. 2015.

[190] P. Richner, S. J. P. Kress, D. J. Norris and D. Poulikakos. Charge effects and nanoparticle pattern formation in electrohydrodynamic nanodrip printing of colloids. *Nanoscale*, 8: 6028–6034. doi: 10.1039/C5NR08783J. 2016.

[191] R. W. Ogden. Large deformation isotropic elasticity - on the correlation of theory and experiment for incompressible rubberlike solids. *Proceedings of the Royal Society of London A: Mathematical, Physical and Engineering Sciences*, 326(1567): 565–584. ISSN 0080-4630. doi: 10.1098/rspa.1972.0026. 1972.

[192] U. Horzum, B. Ozdil and D. Pesen-Okvur. Step-by-step quantitative analysis of focal adhesions. *MethodsX*, 1: 56–59. 2014.

[193] A. G. Clark, K. Dierkes and E. K. Paluch. Monitoring actin cortex thickness in live cells. *Biophysical Journal*, 105(3): 570 – 580. ISSN 0006-3495. doi: 10.1016/j.bpj.2013.05.057. 2013.

[194] M. Panagiotakopoulou, T. Lendenmann, F. M. Pramotton, C. Giampietro, G. Stefopoulos, D. Poulikakos and A. Ferrari. Cell cycle-dependent force transmission in cancer cells. *Molecular biology of the cell*, mbc–E17. 2018.

[195] M. Beil, A. Micoulet, G. von Wichert, S. Paschke, P. Walther, M. B. Omary, P. P. Van Veldhoven, U. Gern, E. Wolff-Hieber, J. Eggermann *et al.* Sphingosylphosphorylcholine regulates keratin network architecture and visco-elastic properties of human cancer cells. *Nature cell biology*, 5(9): 803. 2003.

[196] C. M. Kraning-Rush and C. A. Reinhart-King. Controlling matrix stiffness and topography for the study of tumor cell migration. *Cell adhesion & migration*, 6(3): 274–279. 2012.

[197] M. Krause and K. Wolf. Cancer cell migration in 3d tissue: Negotiating space by proteolysis and nuclear deformability. *Cell adhesion & migration*, 9(5): 357–366. 2015.

[198] J. K. Mouw, G. Ou and V. M. Weaver. Extracellular matrix assembly: a multiscale deconstruction. *Nature reviews Molecular cell biology*, 15(12): 771. 2014.

[199] P. P. Provenzano, D. R. Inman, K. W. Eliceiri, J. G. Knittel, L. Yan, C. T. Rueden, J. G. White and P. J. Keely. Collagen density promotes mammary tumor initiation and progression. *BMC medicine*, 6(1): 11. 2008.

[200] Z. I. Khamis, Z. J. Sahab and Q.-X. A. Sang. Active roles of tumor stroma in breast cancer metastasis. *International journal of breast cancer*, 2012. 2012.

[201] K. Wolf, M. Te Lindert, M. Krause, S. Alexander, J. Te Riet, A. L. Willis, R. M. Hoffman, C. G. Figdor, S. J. Weiss and P. Friedl. Physical limits of cell migration: control by ecm space and nuclear deformation and tuning by proteolysis and traction force. *J Cell Biol*, 201(7): 1069–1084. 2013.

[202] G. Charras and E. Sahai. Physical influences of the extracellular environment on cell migration. *Nature reviews Molecular cell biology*, 15(12): 813. 2014.

[203] A. Kumar, M. Mazzanti, M. Mistrik, M. Kosar, G. V. Beznoussenko, A. A. Mironov, M. Garre, D. Parazzoli, G. Shivashankar, G. Scita *et al.* Atr mediates a checkpoint at the nuclear envelope in response to mechanical stress. *Cell*, 158(3): 633–646. 2014.

[204] C. Holohan, S. Van Schaeybroeck, D. B. Longley and P. G. Johnston. Cancer drug resistance: an evolving paradigm. *Nature Reviews Cancer*, 13(10): 714. 2013.

[205] M. Lund-Johansen, R. Bjerkvig, P. A. Humphrey, S. H. Bigner, D. D. Bigner and O.-D. Laerum. Effect of epidermal growth factor on glioma cell growth, migration, and invasion in vitro. *Cancer research*, 50(18): 6039–6044. 1990.

[206] P. L. Penar, S. Khoshyomn, A. Bhushan and T. R. Tritton. Inhibition of epidermal growth factor receptor-associated tyrosine kinase blocks glioblastoma invasion of the brain: Experimental studies. *Neurosurgery*, 40(1): 141–151. 1997.

[207] W. Zhang, R. E. Law, D. R. Hinton and W. T. Couldwell. Inhibition of human malignant glioma cell motility and invasion in vitro by hypericin, a potent protein kinase c inhibitor. *Cancer letters*, 120(1): 31–38. 1997.

[208] W. Roth, C. Wild-Bode, M. Platten, C. Grimmel, H. S. Melkonyan, J. Dichgans and M. Weller. Secreted frizzled-related proteins inhibit motility and promote growth of human malignant glioma cells. *Oncogene*, 19(37): 4210. 2000.

[209] A. Corcoran and R. M. Del. Testing the" go or grow" hypothesis in human medulloblastoma cell lines in two and three dimensions. *Neurosurgery*, 53(1): 174–84. 2003.

[210] T. Garay, É. Juhász, E. Molnár, M. Eisenbauer, A. Czirók, B. Dekan, V. László, M. A. Hoda, B. Döme, J. Tímár *et al.* Cell migration or cytokinesis and proliferation?–revisiting the “go or grow” hypothesis in cancer cells in vitro. *Experimental cell research*, 319(20): 3094–3103. 2013.

[211] T. R. Alves, F. R. S. Lima, S. A. Kahn, D. Lobo, L. G. F. Dubois, R. Soletti, H. Borges and V. M. Neto. Glioblastoma cells: a heterogeneous and fatal tumor interacting with the parenchyma. *Life sciences*, 89(15-16): 532–539. 2011.

[212] M. Panagiotakopoulou, M. Bergert, A. Taubenberger, J. Guck, D. Poulikakos and A. Ferrari. A nanoprinted model of interstitial cancer migration reveals a link between cell deformability and proliferation. *ACS nano*, 10(7): 6437–6448. 2016.

[213] S. Cho, J. Irianto and D. E. Discher. Mechanosensing by the nucleus: from pathways to scaling relationships. *J Cell Biol*, 216(2): 305–315. 2017.

[214] L. Cramer and T. Mitchison. Myosin is involved in postmitotic cell spreading. *The Journal of Cell Biology*, 131(1): 179–189. 1995.

[215] A. Lesman, J. Notbohm, D. A. Tirrell and G. Ravichandran. Contractile forces regulate cell division in three-dimensional environments. *J Cell Biol*, 205(2): 155–162. 2014.

[216] L. G. Griffith and M. A. Swartz. Capturing complex 3d tissue physiology in vitro. *Nature reviews Molecular cell biology*, 7(3): 211. 2006.

[217] K. J. Huber-Keener, X. Liu, Z. Wang, Y. Wang, W. Freeman, S. Wu, M. D. Planas-Silva, X. Ren, Y. Cheng, Y. Zhang *et al.* Differential gene expression in tamoxifen-resistant breast cancer cells revealed by a new analytical model of rna-seq data. *PloS one*, 7(7): e41333. 2012.

[218] C. Bonnans, J. Chou and Z. Werb. Remodelling the extracellular matrix in development and disease. *Nature reviews Molecular cell biology*, 15(12): 786. 2014.

[219] S. Marchesi, F. Montani, G. Deflorian, R. D'Antuono, A. Cuomo, S. Bologna, C. Mazzoccoli, T. Bonaldi, P. P. Di Fiore and F. Nicassio. Depdc1b coordinates de-adhesion events and cell-cycle progression at mitosis. *Developmental cell*, 31(4): 420–433. 2014.

[220] C. K. Choi, M. Vicente-Manzanares, J. Zareno, L. A. Whitmore, A. Mogilner and A. R. Horwitz. Actin and α-actinin orchestrate the assembly and maturation of nascent adhesions in a myosin ii motor-independent manner. *Nature cell biology*, 10(9): 1039. 2008.

[221] I. Thievessen, P. M. Thompson, S. Berlemont, K. M. Plevock, S. V. Plotnikov, A. Zemljic-Harpf, R. S. Ross, M. W. Davidson, G. Danuser, S. L. Campbell *et al.* Vinculin–actin interaction couples actin retrograde flow to focal adhesions, but is dispensable for focal adhesion growth. *J Cell Biol*, 202(1): 163–177. 2013.

[222] M. Chrzanowska-Wodnicka and K. Burridge. Tyrosine phosphorylation is involved in reorganization of the actin cytoskeleton in response to serum or lpa stimulation. *Journal of Cell Science*, 107(12): 3643–3654. 1994.

[223] S. F. Retta, S. T. Barry, D. R. Critchley, P. Defilippi, L. Silengo and G. Tarone. Focal adhesion and stress fiber formation is regulated by tyrosine phosphatase activity. *Experimental cell research*, 229(2): 307–317. 1996.

[224] M. C. Frame. Newest findings on the oldest oncogene; how activated src does it. *J Cell Sci*, 117(7): 989–998. 2004.

[225] D. D. Schlaepfer and S. K. Mitra. Multiple connections link fak to cell motility and invasion. *Current opinion in genetics & development*, 14(1): 92–101. 2004.

[226] R. Zaidel-Bar, R. Milo, Z. Kam and B. Geiger. A paxillin tyrosine phosphorylation switch regulates the assembly and form of cell-matrix adhesions. *Journal of cell science*, 120(1): 137–148. 2007.

[227] S. V. Plotnikov, A. M. Pasapera, B. Sabass and C. M. Waterman. Force fluctuations within focal adhesions mediate ecm-rigidity sensing to guide directed cell migration. *Cell*, 151(7): 1513–1527. 2012.

[228] S. Miwa, S. Yano, H. Kimura, M. Yamamoto, M. Toneri, Y. Matsumoto, F. Uehara, Y. Hiroshima, T. Murakami, K. Hayashi *et al.* Cell-cycle fate-monitoring distinguishes individual chemosensitive and chemoresistant cancer cells in drug-treated heterogeneous populations demonstrated by real-time fucci imaging. *Cell Cycle*, 14(4): 621–629. 2015.

[229] S. Duan, A. Wu, Z. Chen, Y. Yang, L. Liu and Q. Shu. Mir-204 regulates cell proliferation and invasion by targeting ephb2 in human cervical cancer. *Oncology Research Featuring Preclinical and Clinical Cancer Therapeutics*, 26(5): 713–723. 2018.

[230] T. L. Chu, M. Connell, L. Zhou, Z. He, J. Won, H. Chen, S. M. Rahavi, P. Mohan, O. Nemirovsky, A. Fotovati *et al.* Cell cycle–dependent tumor engraftment and migration are enabled by aurora-a. *Molecular Cancer Research*, 16(1): 16–31. 2018.

[231] A. H. Mekhdjian, F. Kai, M. G. Rubashkin, L. S. Prahl, L. M. Przybyla, A. L. McGregor, E. S. Bell, J. M. Barnes, C. C. DuFort, G. Ou *et al.* Integrin-mediated traction force enhances paxillin molecular associations and adhesion dynamics that increase the invasiveness of tumor cells into a three-dimensional extracellular matrix. *Molecular biology of the cell*, 28(11): 1467–1488. 2017.

[232] M. J. Moes, J. J. Bijvelt and J. Boonstra. Attachment of hela cells during early g1 phase. *Histochemistry and cell biology*, 136(4): 399. 2011.

[233] S. J. Han, K. S. Bielawski, L. H. Ting, M. L. Rodriguez and N. J. Sniadecki. Decoupling substrate stiffness, spread area, and micropost density: a close spatial relationship between traction forces and focal adhesions. *Biophysical journal*, 103(4): 640–648. 2012.

[234] P. W. Oakes, S. Banerjee, M. C. Marchetti and M. L. Gardel. Geometry regulates traction stresses in adherent cells. *Biophysical journal*, 107(4): 825–833. 2014.

[235] M. Chang. Tamoxifen resistance in breast cancer. *Biomolecules & therapeutics*, 20(3): 256. 2012.

[236] J. M. Harvey, G. M. Clark, C. K. Osborne, D. C. Allred *et al.* Estrogen receptor status by immunohistochemistry is superior to the ligand-binding assay for predicting response to adjuvant endocrine therapy in breast cancer. *Journal of clinical oncology*, 17(5): 1474–1481. 1999.

[237] A. M. Otto, R. Paddenberg, S. Schubert and H. G. Mannherz. Cell-cycle arrest, micronucleus formation, and cell death in growth inhibition of mcf-7 breast cancer cells by tamoxifen and cisplatin. *Journal of cancer research and clinical oncology*, 122(10): 603–612. 1996.

[238] A. Ward, A. Balwierz, J. D. Zhang, M. Küblbeck, Y. Pawitan, T. Hielscher, S. Wiemann and Ö. Sahin. Re-expression of microrna-375 reverses both tamoxifen resistance and accompanying emt-like properties in breast cancer. *Oncogene*, 32(9): 1173. 2013.

[239] R. L. Sutherland, M. D. Green, R. E. Hall, R. R. Reddel and I. W. Taylor. Tamoxifen induces accumulation of mcf 7 human mammary carcinoma cells in the g0/g1 phase of the cell cycle. *European Journal of Cancer and Clinical Oncology*, 19(5): 615–621. 1983.

[240] H. K. Kleinman and K. Jacob. Invasion assays. *Current protocols in cell biology*, 1: 12–2. 1998.

[241] S. Corallino, C. Malinverno, B. Neumann, C. Tischer, A. Palamidessi, E. Frittoli, M. Panagiotakopoulou, A. Disanza, G. Malet-Engra, P. Nastaly *et al.* Author correction: A rab35-p85/pi3k axis controls oscillatory apical protrusions required for efficient chemotactic migration. *Nature communications*, 9(1): 2085. 2018.

[242] B. Vianay, F. Senger, S. Alamos, M. Anjur-Dietrich, E. Bearce, B. Cheeseman, L. Lee and M. Théry. Variation in traction forces during cell cycle progression. *Biology of the Cell*, 110(4): 91–96. 2018.

[243] C. M. Denais, R. M. Gilbert, P. Isermann, A. L. McGregor, M. te Lindert, B. Weigelin, P. M. Davidson, P. Friedl, K. Wolf and J. Lammerding. Nuclear envelope rupture and repair during cancer cell migration. *Science*, aad7297. 2016.

[244] C. D. Paul, P. Mistriotis and K. Konstantopoulos. Cancer cell motility: lessons from migration in confined spaces. *Nature Reviews Cancer*, 17(2): 131. 2017.

[245] B. J. Green, M. Panagiotakopoulou, F. M. Pramotton, G. Stefopoulos, S. O. Kelley, D. Poulikakos and A. Ferrari. Pore shape defines paths of metastatic cell migration. *Nano letters*, 18(3): 2140–2147. 2018.

[246] S. Jurmeister, M. Baumann, A. Balwierz, I. Keklikoglou, A. Ward, S. Uhlmann, J. D. Zhang, S. Wiemann and Ö. Sahin. Microrna-200c represses migration and invasion of breast cancer cells by targeting actin-regulatory proteins fhod1 and ppm1f. *Molecular and cellular biology*, 32(3): 633–651. 2012.

[247] B. van de Water, F. Houtepen, M. Huigsloot and I. B. Tijdens. Suppression of chemically induced apoptosis but not necrosis of renal proximal tubular epithelial (llc-pk1) cells by focal adhesion kinase (fak) role of fak in maintaining focal adhesion organization after acute renal cell injury. *Journal of Biological Chemistry*, 276(39): 36183–36193. 2001.

[248] J. K. Slack-Davis, K. H. Martin, R. W. Tilghman, M. Iwanicki, E. J. Ung, C. Autry, M. J. Luzzio, B. Cooper, J. C. Kath, W. G. Roberts *et al.* Cellular characterization of a novel focal adhesion kinase inhibitor. *Journal of Biological Chemistry*, 282(20): 14845–14852. 2007.

[249] C. Malinverno, S. Corallino, F. Giavazzi, M. Bergert, Q. Li, M. Leoni, A. Disanza, E. Frittoli, A. Oldani, E. Martini *et al.* Endocytic reawakening of motility in jammed epithelia. *Nature materials*, 16(5): 587. 2017.

[250] B. Szabo, G. Szöllösi, B. Gönci, Z. Jurányi, D. Selmeczi and T. Vicsek. Phase transition in the collective migration of tissue cells: experiment and model. *Physical Review E*, 74(6): 061908. 2006.

[251] T. E. Angelini, E. Hannezo, X. Trepat, J. J. Fredberg and D. A. Weitz. Cell migration driven by cooperative substrate deformation patterns. *Physical review letters*, 104(16): 168104. 2010.

[252] J.-A. Park, J. H. Kim, D. Bi, J. A. Mitchel, N. T. Qazvini, K. Tantisira, C. Y. Park, M. McGill, S.-H. Kim, B. Gweon *et al.* Unjamming and cell shape in the asthmatic airway epithelium. *Nature materials*, 14(10): 1040. 2015.

[253] D. Bi, J. Lopez, J. Schwarz and M. L. Manning. A density-independent rigidity transition in biological tissues. *Nature Physics*, 11(12): 1074. 2015.

[254] C. P. Goodrich, S. Dagois-Bohy, B. P. Tighe, M. van Hecke, A. J. Liu and S. R. Nagel. Jamming in finite systems: Stability, anisotropy, fluctuations, and scaling. *Physical Review E*, 90(2): 022138. 2014.

[255] S. M. Zehnder, M. Suaris, M. M. Bellaire and T. E. Angelini. Cell volume fluctuations in mdck monolayers. *Biophysical journal*, 108(2): 247–250. 2015.

[256] M. C. Marchetti, J.-F. Joanny, S. Ramaswamy, T. B. Liverpool, J. Prost, M. Rao and R. A. Simha. Hydrodynamics of soft active matter. *Reviews of Modern Physics*, 85(3): 1143. 2013.

[257] S. M. Zehnder, M. K. Wiatt, J. M. Uruena, A. C. Dunn, W. G. Sawyer and T. E. Angelini. Multicellular density fluctuations in epithelial monolayers. *Physical Review E*, 92(3): 032729. 2015.

[258] S. Sigismund, S. Confalonieri, A. Ciliberto, S. Polo, G. Scita and P. P. Di Fiore. Endocytosis and signaling: cell logistics shape the eukaryotic cell plan. *Physiological reviews*, 92(1): 273–366. 2012.

[259] S. Corallino, M. G. Malabarba, M. Zobel, P. P. Di Fiore and G. Scita. Epithelial-to-mesenchymal plasticity harnesses endocytic circuitries. *Frontiers in oncology*, 5: 45. 2015.

[260] E. Frittoli, A. Palamidessi, P. Marighetti, S. Confalonieri, F. Bianchi, C. Malinverno, G. Mazzarol, G. Viale, I. Martin-Padura, M. Garré *et al.* A rab5/rab4 recycling circuitry induces a proteolytic invasive program and promotes tumor dissemination. *J Cell Biol*, 206(2): 307–328. 2014.

[261] P. Mendoza, J. Díaz, P. Silva and V. A. Torres. Rab5 activation as a tumor cell migration switch. *Small GTPases*, 5(1): 3835–47. 2014.

[262] M. Sadati, A. Nourhani, J. J. Fredberg and N. Taheri Qazvini. Glass-like dynamics in the cell and in cellular collectives. *Wiley Interdisciplinary Reviews: Systems Biology and Medicine*, 6(2): 137–149. 2014.

[263] M. R. Ng, A. Besser, G. Danuser and J. S. Brugge. Substrate stiffness regulates cadherin-dependent collective migration through myosin-ii contractility. *J Cell Biol*, 199(3): 545–563. 2012.

[264] F. Milde, D. Franco, A. Ferrari, V. Kurtcuoglu, D. Poulikakos and P. Koumoutsakos. Cell image velocimetry (civ): boosting the automated quantification of cell migration in wound healing assays. *Integrative Biology*, 4(11): 1437–1447. 2012.

[265] L. Petitjean, M. Reffay, E. Grasland-Mongrain, M. Poujade, B. Ladoux, A. Buguin and P. Silberzan. Velocity fields in a collectively migrating epithelium. *Biophysical journal*, 98(9): 1790–1800. 2010.

[266] A. Palamidessi, E. Frittoli, M. Garre, M. Faretta, M. Mione, I. Testa, A. Diaspro, L. Lanzetti, G. Scita and P. P. Di Fiore. Endocytic trafficking of rac is required for the spatial restriction of signaling in cell migration. *Cell*, 134(1): 135–147. 2008.

[267] D. Franco, F. Milde, M. Klingauf, F. Orsenigo, E. Dejana, D. Poulikakos, M. Cecchini, P. Koumoutsakos, A. Ferrari and V. Kurtcuoglu. Accelerated endothelial wound healing on microstructured substrates under flow. *Biomaterials*, 34(5): 1488–1497. 2013.

[268] E. H. Barriga, K. Franze, G. Charras and R. Mayor. Tissue stiffening coordinates morphogenesis by triggering collective cell migration in vivo. *Nature*, 554(7693): 523. 2018.

[269] J. Escribano, R. Sunyer, M. T. Sánchez, X. Trepat, P. Roca-Cusachs and J. M. García-Aznar. A hybrid computational model for collective cell durotaxis. *Biomechanics and modeling in mechanobiology*, 1–16. 2018.

[270] N. J. Sniadecki, A. Anguelouch, M. T. Yang, C. M. Lamb, Z. Liu, S. B. Kirschner, Y. Liu, D. H. Reich and C. S. Chen. Magnetic microposts as an approach to apply forces to living cells. *Proceedings of the National Academy of Sciences*, 104(37): 14553–14558. 2007.

[271] N. J. Sniadecki, C. M. Lamb, Y. Liu, C. S. Chen and D. H. Reich. Magnetic microposts for mechanical stimulation of biological cells: fabrication, characterization, and analysis. *Review of Scientific Instruments*, 79(4): 044302. 2008.

[272] D. Zeng, A. Ferrari, J. Ulmer, A. Veligodskiy, P. Fischer, J. Spatz, Y. Ventikos, D. Poulikakos and R. Kroschewski. Three-dimensional modeling of mechanical forces in the extracellular matrix during epithelial lumen formation. *Biophysical journal*, 90(12): 4380–4391. 2006.

[273] N. Goedecke, M. Bollhalder, R. Bernet, U. Silvan and J. Snedeker. Easy and accurate mechano-profiling on micropost arrays. *Journal of visualized experiments: JoVE*, 105(105). 2015.

[274] C. A. Lemmon, N. J. Sniadecki, S. A. Ruiz, J. L. Tan, L. H. Romer and C. S. Chen. Shear force at the cell-matrix interface: enhanced analysis for microfabricated post array detectors. *Mechanics & chemistry of biosystems: MCB*, 2(1): 1. 2005.

[275] R. H. Lam, S. Weng, W. Lu and J. Fu. Live-cell subcellular measurement of cell stiffness using a microengineered stretchable micropost array membrane. *Integrative Biology*, 4(10): 1289–1298. 2012.

[276] S. Weng, Y. Shao, W. Chen and J. Fu. Mechanosensitive subcellular rheostasis drives emergent single-cell mechanical?homeostasis. *Nature Materials*, 15: 961 EP –. URL `doi.org/10.1038/nmat4654`. 2016.

[277] K. F. Chu and D. E. Dupuy. Thermal ablation of tumours: biological mechanisms and advances in therapy. *Nature Reviews Cancer*, 14(3): 199. 2014.

[278] R. L. Warters and J. L. R. Roti. Hyperthermia and the cell nucleus. *Radiation research*, 92(3): 458–462. 1982.

[279] M. Nikfarjam, V. Muralidharan and C. Christophi. Mechanisms of focal heat destruction of liver tumors. *Journal of Surgical Research*, 127(2): 208–223. 2005.

[280] F. Rico, C. Chu, M. H. Abdulreda, Y. Qin and V. T. Moy. Temperature modulation of integrin-mediated cell adhesion. *Biophysical journal*, 99(5): 1387–1396. 2010.

[281] Y. Wu, S. Pan, W. Luo, S.-H. Lin and J. Kuang. Hp95 promotes anoikis and inhibits tumorigenicity of hela cells. *Oncogene*, 21(44): 6801. 2002.

[282] L. F. Fajardo, B. Egbert, J. Marmor and G. M. Hahn. Effects of hyperthermia in a malignant tumor. *Cancer*, 45(3): 613–623. 1980.

[283] A. Livne and B. Geiger. The inner workings of stress fibers- from contractile machinery to focal adhesions and back. *J Cell Sci*, 129(7): 1293–1304. 2016.

[284] L. T. Vassilev, C. Tovar, S. Chen, D. Knezevic, X. Zhao, H. Sun, D. C. Heimbrook and L. Chen. Selective small-molecule inhibitor reveals critical mitotic functions of human cdk1. *Proceedings of the National Academy of Sciences*, 103(28): 10660–10665. 2006.

[285] I. Johnston, D. McCluskey, C. Tan and M. Tracey. Mechanical characterization of bulk sylgard 184 for microfluidics and microengineering. *Journal of Micromechanics and Microengineering*, 24(3): 035017. 2014.

[286] O. Du Roure, A. Saez, A. Buguin, R. H. Austin, P. Chavrier, P. Siberzan and B. Ladoux. Force mapping in epithelial cell migration. *Proceedings of the National Academy of Sciences*, 102(7): 2390–2395. 2005.

[287] A. Saez, A. Buguin, P. Silberzan and B. Ladoux. Is the mechanical activity of epithelial cells controlled by deformations or forces? *Biophysical journal*, 89(6): L52–L54. 2005.

[288] M. T. Yang, J. Fu, Y.-K. Wang, R. A. Desai and C. S. Chen. Assaying stem cell mechanobiology on microfabricated elastomeric substrates with geometrically modulated rigidity. *Nature protocols*, 6(2): 187. 2011.

[289] N. Otsu. A threshold selection method from gray-level histograms. *IEEE transactions on systems, man, and cybernetics*, 9(1): 62–66. 1979.

[290] M. K. Cheezum, W. F. Walker and W. H. Guilford. Quantitative comparison of algorithms for tracking single fluorescent particles. *Biophysical journal*, 81(4): 2378–2388. 2001.

[291] M. Botsch, L. Kobbelt, M. Pauly, P. Alliez and B. Lévy. *Polygon Mesh Processing.* AK Peters / CRC Press. URL `https://hal.inria.fr/inria-00538098`. 2010.

[292] S.-W. Cheng, T. K. Dey and J. Shewchuk. *Delaunay Mesh Generation.* Chapman & Hall/CRC, 1st edition. ISBN 1584887303, 9781584887300. 2012.

[293] H. Si. TetGen, a delaunay-based quality tetrahedral mesh generator. *ACM Transactions on Mathematical Software*, 41(2): 1–36. doi: 10.1145/2629697. 2015.

[294] C. Dapogny, C. Dobrzynski and P. Frey. Three-dimensional adaptive domain remeshing, implicit domain meshing, and applications to free and moving boundary problems. *Journal of Computational Physics*, 262: 358–378. doi: 10.1016/j.jcp.2014.01.005. 2014.

[295] M. Pazouki and R. Schaback. Bases for kernel-based spaces. *J. Comput. Appl. Math.*, 236: 575–588. 2011.

[296] B. Fornberg, E. Larsson and N. Flyer. Stable computations with gaussian radial basis functions. *SIAM J. Sci. Comput.*, 33: 869–892. 2011.

[297] A. Mongera, P. Rowghanian, H. J. Gustafson, E. Shelton, D. A. Kealhofer, E. K. Carn, F. Serwane, A. A. Lucio, J. Giammona and O. Campàs. A fluid-to-solid jamming transition underlies vertebrate body axis elongation. *Nature*, 561(7723): 401. 2018.

[298] T. B. Saw, W. Xi, B. Ladoux and C. T. Lim. Biological tissues as active nematic liquid crystals. *Advanced materials*, 30(47): 1802579. 2018.

[299] T. B. Saw, A. Doostmohammadi, V. Nier, L. Kocgozlu, S. Thampi, Y. Toyama, P. Marcq, C. T. Lim, J. M. Yeomans and B. Ladoux. Topological defects in epithelia govern cell death and extrusion. *Nature*, 544(7649): 212. 2017.

[300] G. Duclos, S. Garcia, H. Yevick and P. Silberzan. Perfect nematic order in confined monolayers of spindle-shaped cells. *Soft matter*, 10(14): 2346–2353. 2014.

[301] L. Wagstaff, M. Goschorska, K. Kozyrska, G. Duclos, I. Kucinski, A. Chessel, L. Hampton-O'Neil, C. R. Bradshaw, G. E. Allen, E. L. Rawlins *et al.* Mechanical cell competition kills cells via induction of lethal p53 levels. *Nature communications*, 7: 11373. 2016.

[302] G. Duclos, C. Blanch-Mercader, V. Yashunsky, G. Salbreux, J.-F. Joanny, J. Prost and P. Silberzan. Spontaneous shear flow in confined cellular nematics. *Nature Physics*, 1. 2018.

[303] C. Wang, B. M. Baker, C. S. Chen and M. A. Schwartz. Endothelial cell sensing of flow directionsignificance. *Arteriosclerosis, thrombosis, and vascular biology*, 33(9): 2130–2136. 2013.

[304] V. L. Bautch and K. M. Caron. Blood and lymphatic vessel formation. *Cold Spring Harbor perspectives in biology*, 7(3): a008268. 2015.

[305] F. Orsenigo, C. Giampietro, A. Ferrari, M. Corada, A. Galaup, S. Sigismund, G. Ristagno, L. Maddaluno, G. Y. Koh, D. Franco *et al.* Phosphorylation of ve-cadherin is modulated by haemodynamic forces and contributes to the regulation of vascular permeability in vivo. *Nature communications*, 3: 1208. 2012.

[306] H.-B. Kwon, S. Wang, C. S. Helker, S. J. Rasouli, H.-M. Maischein, S. Offermanns, W. Herzog and D. Y. Stainier. In vivo modulation of endothelial polarization by apelin receptor signalling. *Nature communications*, 7: 11805. 2016.

[307] W. W. Sugden, R. Meissner, T. Aegerter-Wilmsen, R. Tsaryk, E. V. Leonard, J. Bussmann, M. J. Hamm, W. Herzog, Y. Jin, L. Jakobsson *et al.* Endoglin controls blood vessel diameter through endothelial cell shape changes in response to haemodynamic cues. *Nature cell biology*, 19(6): 653. 2017.

[308] J. A. Ukropec, M. K. Hollinger and M. J. Woolkalis. Regulation of ve-cadherin linkage to the cytoskeleton in endothelial cells exposed to fluid shear stress. *Experimental cell research*, 273(2): 240–247. 2002.

[309] M. A. Ostrowski, N. F. Huang, T. W. Walker, T. Verwijlen, C. Poplawski, A. S. Khoo, J. P. Cooke, G. G. Fuller and A. R. Dunn. Microvascular endothelial cells migrate upstream and align against the shear stress field created by impinging flow. *Biophysical journal*, 106(2): 366–374. 2014.

[310] S. McCue, D. Dajnowiec, F. Xu, M. Zhang, M. R. Jackson and B. L. Langille. Shear stress regulates forward and reverse planar cell polarity of vascular endothelium in vivo and in vitro. *Circulation research*, 98(7): 939–946. 2006.

[311] J. T. Butcher, A. M. Penrod, A. J. García and R. M. Nerem. Unique morphology and focal adhesion development of valvular endothelial cells in static and fluid flow environments. *Arteriosclerosis, thrombosis, and vascular biology*, 24(8): 1429–1434. 2004.

[312] K. B. Vartanian, M. A. Berny, O. J. McCarty, S. R. Hanson and M. T. Hinds. Cytoskeletal structure regulates endothelial cell immunogenicity independent of fluid shear stress. *American Journal of Physiology-Cell Physiology*, 298(2): C333–C341. 2009.

[313] R. Steward Jr, D. Tambe, C. C. Hardin, R. Krishnan and J. J. Fredberg. Fluid shear, intercellular stress, and endothelial cell alignment. *American Journal of Physiology-Cell Physiology*, 308(8): C657–C664. 2015.

[314] F. Giavazzi, M. Paoluzzi, M. Macchi, D. Bi, G. Scita, M. L. Manning, R. Cerbino and M. C. Marchetti. Flocking transitions in confluent tissues. *Soft matter*, 14(18): 3471–3477. 2018.

[315] B. De Oliveira, P. Avelino, F. Moraes and J. Oliveira. Nematic liquid crystal dynamics under applied electric fields. *Physical Review E*, 82(4): 041707. 2010.

[316] K. Kawaguchi, R. Kageyama and M. Sano. Topological defects control collective dynamics in neural progenitor cell cultures. *Nature*, 545(7654): 327. 2017.

[317] J.-A. Park, J. A. Mitchel, N. T. Qazvini, J. H. Kim, C. Y. Park, J. P. Butler, E. Israel, S. H. Randell, S. A. Shore, J. M. Drazen *et al.* Compressive stress causes an unjamming transition and an epithelial–mesenchymal transition in the airway epithelium in asthma. *Annals of the American Thoracic Society*, 13(Supplement 1): S102–S102. 2016.

[318] A. Palamidessi, C. Malinverno, E. Frittoli, S. Corallino, E. Barbieri, S. Sigismund, P. P. Di Fiore, G. V. Beznoussenko, E. Martini, M. Garrè *et al.* Unjamming overcomes kinetic and proliferation arrest in terminally differentiated cells and promotes collective motility of carcinoma. *bioRxiv*, 388553. 2018.

[319] B. C. Berk. Atheroprotective signaling mechanisms activated by steady laminar flow in endothelial cells. *Circulation*, 117(8): 1082–1089. 2008.

[320] M. G. Lampugnani, M. Corada, P. Andriopoulou, S. Esser, W. Risau and E. Dejana. Cell confluence regulates tyrosine phosphorylation of adherens junction components in endothelial cells. *Journal of cell science*, 110(17): 2065–2077. 1997.

[321] G. Stefopoulos, C. Giampietro, V. Falk, D. Poulikakos and A. Ferrari. Facile endothelium protection from tnf-α inflammatory insult with surface topography. *Biomaterials*, 138: 131–141. 2017.

[322] G. Stefopoulos, F. Robotti, V. Falk, D. Poulikakos and A. Ferrari. Endothelialization of rationally microtextured surfaces with minimal cell seeding under flow. *Small*, 12(30): 4113–4126. 2016.

[323] S. V. Costes, D. Daelemans, E. H. Cho, Z. Dobbin, G. Pavlakis and S. Lockett. Automatic and quantitative measurement of protein-protein colocalization in live cells. *Biophysical journal*, 86(6): 3993–4003. 2004.

[324] O. Sorkine. Laplacian mesh processing. In *Eurographics (STARs)*, 53–70. 2005.

[325] L. Gurobi Optimization. Gurobi optimizer reference manual. URL `http://www.gurobi.com`. 2018.

[326] M. Buhmann. *Radial Basis Functions: Theory and Implementations*. Cambridge Monographs on Applied and Computational Mathematics. Cambridge University Press. ISBN 9781139435246. 2003.

[327] P. Biscari, M. C. Calderer and E. M. Terentjev. Landau–de gennes theory of isotropic-nematic-smectic liquid crystal transitions. *Physical Review E*, 75(5): 051707. 2007.

F | List of Publications

F.1 Journal Articles

1. Tobias Lendenmann*, Martin Bergert*, Manuel Zündel*, Alexander E. Ehret, Daniele Panozzo, Patrizia Richner, David K. Kim, Stephan J. P. Kress, David J. Norris, Olga Sorkine-Hornung, Edoardo Mazza, Dimos Poulikakos & Aldo Ferrari, "Confocal Reference Free Traction Force Microscopy", *Nature Communications* 7 (2016): 12814.

2. Tobias Lendenmann, Teseo Schneider, Jeremie Dumas, Marco Tarini, Apratim Bajpai, Weiqiang Chen, Dimos Poulikakos, Aldo Ferrari & Daniele Panozzo, "Cellogram: On the Fly Traction Force Microscop", in preparation

3. Tobias Lendenmann, Georgios Stefopoulos, Thomas M. Schutzius, Fabio Giavazzi, Roberto Cerbino, Dimos Poulikakos & Aldo Ferrari, "Bistability of polar liquid crystals in the collective adaptation of endothelia", in preparation

4. Magdalini Panagiotakopoulou, Tobias Lendenmann, Francesca Pramotton, Costanza Giampietro, Georgios Stefopoulos, Dimos Poulikakos & Aldo Ferrari, "Cell cycle-dependent force transmission in cancer cells", *Molecular Biology of the Cell*, 29 (2018) 2528.

5. Julia Gerber, Tobias Lendenmann, Hadi Eghlidi, Thomas Schutzius & Dimos Poulikakos, "Wetting transitions in droplet drying on soft materials" under revision

6. Chiara Malinverno, Salvatore Corallino, Fabio Giavazzi, Martin Bergert, Qingsen Li, Marco Leoni, Andrea Disanza, Emanuela Frittoli, Amanda Oldani, Emanuele Martini, Tobias Lendenmann, Gianluca Deflorian, Galina V. Beznoussenko, Dimos Poulikakos, Kok Haur Ong, Marina Uroz, Xavier Trepat, Dario Parazzoli, Paolo Maiuri, Weimiao Yu, Aldo Ferrari, Roberto Cerbino & Giorgio Scita, "Endocytic reawakening of motility in jammed epithelia", *Nature Materials*, 16 (2017) 587.

7. Patrizia Richner, Patrick Galliker, Tobias Lendenmann, Stephan J.P. Kress, David K. Kim, David J. Norris & Dimos Poulikakos, "Full-Spectrum Flexible Color Printing at the Diffraction Limit" *ACS Photonic*, 5 (2016) 754

8. Anastasios Marmaras, Tobias Lendenmann, Gianluca Civenni, Davide Franco, Dimos Poulikakos, Vartan Kurtcuoglu & Aldo Ferrari, "Topography-mediated apical guidance in epidermal wound healing" *Soft matter*, 8 (2012) 2922

F.2 Conference Presentations

1. Martin Bergert, High resolution live traction force microscopy, *Mechanobiology: mechanisms of force sensation and transduction that control cell behavior in health and disease*, (2016, March) Amsterdam, Netherlands
2. Tobias Lendenmann, Confocal Reference-Free Traction Force Microscopy, *Nanoengineering for Mechanobiology*, (2016, April), Camogli, Italy

F.3 Patents

1. Tobias Lendenmann, Maximilian Fischer, Simone Bottan, Aldo Ferrari, Dimos Poulikakos, Bernhard Winkler, Martin Grapow, "Method for the production of structured cellulose patches or elements and devices made using such a method.", (2016). U.S. Patent Application No. 15/023,215.